ON THE SYNOPTIC AND MESOSCALE ORGANIZATION OF MID-LATITUDE, CONTINENTAL CONVECTIVE SNOW EVENTS

A Dissertation
presented to
the Faculty of the Graduate School
University of Missouri-Columbia

In Partial Fulfillment
of the Requirements for the Degree
of Doctor of Philosophy

---

by

Christopher J. Melick

Dr. Patrick S. Market, Dissertation Supervisor

May 2008

The undersigned, appointed by the Dean of the Graduate School, have examined the dissertation entitled:

ON THE SYNOPTIC AND MESOSCALE ORGANIZATION OF MID-LATITUDE, CONTINENTAL CONVECTIVE SNOW EVENTS

presented by Christopher J. Melick
a candidate for the degree of Doctor of Philosophy
and hereby certify that in their opinion it is worthy of acceptance.

Dr. Patrick S. Market

Dr. Anthony R. Lupo

Dr. Neil I. Fox

Dr. Milon George

Dr. Christopher Wikle

ACKNOWLEDGMENTS

I would like to start out by thanking Dr. Market on so many levels. He has such a kind heart and has been excessively patient with me over the last several years, always willing to give a pep talk on a regular basis and concerned with both my professional and personal development. In addition, Dr. Market has repeatedly been available for consultation on problems with my research and encouraged me to present the results of our investigations at conferences and within peer-reviewed journal papers. Pat has been more than an excellent adviser, whom I respect greatly, he also became my friend as well. As for the rest of my committee, I greatly appreciate their assistance and input along the way in my dissertation work. In particular, I should also note the extra support Dr. Lupo lent in mentoring and encouraging me to get involved in independent research projects.

Several graduate and undergraduate students befriended me through my stay at Mizzou, too many of which to name all right here. In particular, Brian Pettegrew, Steve Lack, and George Limpert deserve particular notice for sharing their technical expertise with various computing issues/programs and the regular bantering I would receive on the side (especially from the latter person). I very much also enjoyed the exciting art of chasing severe weather with the likes of Marc Dahmer, Dan Hinch, Ali Koleiny, Rose Sutton, and Willie Gilmore, which became a favorite and much needed diversion for up and coming meteorologists. I sincerely enjoyed the camaraderie and conversations with the likes of Justin Glisan, Marc Dahmer, Cody Fritz, Colleen Heck, Jeff LaMontia, Ali Koleiny, Ken Leppert, and Amy Schnetzler (to name just a few). Finally, I would also like to specifically acknowledge Kevin Birk and Larry Smith, both of whom became two of my best friends during graduate school.

In conclusion, I could have not made it all the way to my PhD without the love and encouragement of my parents and extended family. I can safely say that my accomplishments are due in large part to them and I hope they know of my deep gratitude. Despite the ups and downs over the course of my education, I ultimately owe my success and perseverance to my deep faith in the Lord Jesus Christ. The ultimate praise goes to God!

Contents

List of Tables

List of Figures

ABSTRACT

An ingredients-based methodology was pursued in order to evaluate the likelihood of thunderstorms occurring in the presence of snowfall (i.e. thundersnow; TSSN) by validating the collective presence of forcing, moisture, and instability in the atmosphere. Since the latter factor has been cited as crucial in distinguishing from typical snowstorms (i.e. non-TSSN), the detailed examination focused on stability characteristics of wintertime convection across the central United States immediately leading up to the onset of the event. Although results from several commonly employed techniques performed successfully, the research primarily analyzed the value of the seldom applied growth rate parameter through initial output fields of the 40-km Rapid Update Cycle model.

The current work substantiated the premise that atmospheres were more unstable in episodes of convective snow. The analyses revealed pronounced forcing mechanisms and greater susceptibility to the produced upward vertical motions, thus, illustrating the positive feedback and strong, crucial connection between the two ingredients. The development of TSSN and any associated banding was correctly and most accurately predicted from trends in plots of the growth rate parameter analyzed at the level at which the highest significant growth rates occurred. An outlook for elevated, cold-season thunderstorms can be more accurately issued by identifying regions where reduced values of equivalent potential vorticity (i.e. small symmetric stability or instability) are collocated with estimates of high growth rates (i.e. where small-scale slantwise perturbations will grow). Given the overall success, it is hoped that some of the conclusions established will be implemented routinely in an operational environment and provide forecasters an additional, essential tool in dealing with nowcasting situations of hazardous winter weather events.

Chapter 1

Introduction

1.1 Background & Motivation

Various aspects of extratropical cyclones (ETC)s within western Europe and North America have been studied extensively over the last century (e.g., Shapiro and Grønås 1999 [and the references therein]). The primary reason for this research is (presumably) due to the impact of the wide range in sensible weather produced, which can vary quite extensively in intensity and duration over relatively short distances. Given the impetus to serve several sectors within society, most notably the protection of both life and property, this has naturally caused a higher level of demand to be placed on producing more accurate and timely predictions of atmospheric processes associated with cyclogenesis. This has led to significant advances in both the observational and numerical weather modeling framework, as well as meant the continued development of empirical methods to identify the ingredients required to initiate and sustain such common weather phenomena. Understanding the underlying processes of synoptic-scale disturbances has thus become not only an intriguing curiosity but a necessity for meteorologists, within both the academic and operational communities.

Branick (1997) found that significant winter-type weather events occur on almost a daily basis from mid-November to March across the contiguous United

States, with heavy snow occurring the most often compared to other types of frozen precipitation. Over the central and eastern part of the country, a review of the literature on synoptic climatologies of heavy snowstorms (e.g., Goree and Younkin 1966; Browne and Younkin 1970; Mote et al. 1997) reveals the recurring presence of common background circulations, most notably a developing ETC in close proximity. In particular, Goree and Younkin (1966) found that the favored location for heavy snow was 5 degrees along and 2.5 latitude degrees to the left of the track of the sea level pressure minima center (i.e., typically north and east). By expanding the selection criteria to also include lightning and any intensity of snow, similar composite characteristics were also obtained by Elkins (1987), Market et al. (2002), and Oravetz (2003). Specifically, thundersnow tended to initiate as a result of dynamical processes in the cold air poleward side of a low pressure system, such that the interaction of various airstreams provided the necessary combination of forcing mechanisms and elevated instability in a nearly saturated environment.

In most of these works just cited, the selection criterion for an event often favored eliminating localized effects and concentrated on systems that could bring hazardous winter weather to a broad landscape and ultimately influence a larger portion of the public. Still, greater intensity snowfalls at one particular moment are often confined to relatively small areas embedded within a much larger zone of light precipitation, thereby stressing the significance of mesoscale processes as well as their accurate representation within short-term forecasts (Branick 1997). Following the suggestions of Branick (1997) and others, the primary motivation of the dissertation will be to develop new forecasting techniques specifically tailored for the nowcasting of significant winter precipitation events, which could hopefully be implemented in an operational environment. More precisely, the research will attempt to provide new insights into the initiation and subsequent maintenance of thundersnow occurrences across the central part of the United

States. By helping meteorologists better predict the time and location of onset of convective snowfall, the ultimate goal is to recommend new guidelines that would succeed more promptly in alerting the general public to any imminent, hazardous winter weather conditions.

1.2 Rationale: Main Objectives

The central objective of the research will be to investigate the multiscale organization of convective, winter precipitation events originating from inside the circulation of several continental ETCs from both an Eulerian and Lagrangian perspective. Despite the recent inquiries into the unique nature of snowstorms which exhibit electrical activity (e.g., Schultz 1999; Smith 2006; Market et al. 2006), Schultz (1999) notes that the research on thundersnow has been lacking for several reasons, the most prominent of these being its rather infrequent occurrence and the corresponding low risk of lightning-related damage, injury, and fatality. The fact that severe weather is not as common in the cold-season with much lower temperature profiles is not surprising considering the usual, greater static stability and relative lack of moisture often observed. Still, hazardous traveling conditions do occur as significant amounts of frozen precipitation accumulate over concentrated regions in a short time period. Furthermore, some evidence (Crowe et al. 2006) has been presented recently that heavier instantaneous rates of snowfall and higher total accumulations are often associated with episodes of thundersnow. Thus, it is hoped that the results will reveal distinct signatures in the four dimensional atmospheric fields of numerous convective snow case studies which differentiate themselves from a dataset of non-thundering snow events.

A traditional ingredients-based methodology is pursued to assess the potential for convection and any ensuing lightning. As with the diagnosis of any type of thunderstorm, the collective action of lift, moisture, and instability must be

present (e.g., Doswell 1987; Johns and Doswell 1992; McNulty 1995; Schultz and Schumacher 1999). Furthermore, both precipitation efficiency and temperature profile should be considered when restricting the scenario to frozen precipitation, such as performed by Wetzel and Martin (2001). For the purposes of this work, while all of these essential elements will be examined to some degree, most of the dissertation will focus on stability regimes and their changing characteristics. Consequently, assessments of gravitational and symmetric instability will be performed utilizing a variety of traditional and relatively newer techniques. Some examples will include the 3-D equivalent potential vorticity (EPV) as derived by McCann (1995), the $M_g - \theta_e$ relationship (with relative humidity) in order to diagnose conditional symmetric instability (CSI; e.g., Bennetts and Hoskins 1979; Bennetts and Sharp 1982; Halcomb and Market 2003), moist Richardson number for slantwise convection (e.g., Sanders and Bosart 1985; Seltzer et al. 1985; Jascourt et al. 1988), and other commonly employed stability indices (e.g., most unstable level for lifting a parcel, most unstable Lifted Index, most unstable Convective Available Potential Energy, middle tropospheric lapse rates). However, most of the focus will be on evaluating the seldom used growth rate parameter (σ^2; Bennetts and Sharp 1982) and its tendency. The significance of these findings will be further made apparent for thundersnow events by comparing results against a set of nonthundering snowstorms.

The identification of instantaneous features at different stages in the lifecycle of an ETC does not provide the best means of visualizing the ever changing flow within various atmospheric conveyor belts. Rather, distinct airstreams are best identified through a trajectory analysis, similar to what was performed by Moore et al. (2005a,b). By following their lead, the work presented here also hopes to highlight how the production of a confined region of relatively heavier snow (with or without lightning) is formed from the interaction and juxtaposition of these different conveyor belts. Once the forcing mechanisms are established

for lifting air parcels to their level of saturation, the collocated presence of diminished stability is crucial to enhancing and constricting the updraft to a smaller horizontal scale (Emanuel 1985). From the point of view of following the fluid parcels, favorable conditions would be determined by assessing momentum and thermodynamic variations between the representative airstreams.

Conceptual models depicting contributing airstreams to the formation of significant snowstorms, sometimes convective, have been approached in the past sometimes utilizing Eulerian diagnostics and following the movement in the analyses over a set period of time (e.g., Nicosia and Grumm 1999; Oravetz 2003). A simpler and more novel surrogate to the Lagrangian methodology will be pursued, such that a comparable outcome will be obtained by utilizing growth rates as a conserved tracer for moist, reversible processes for the time period immediately leading up to convective initiation. Similarities in distinct pattern features can be followed at different pressure levels for the short three hour window in order to:

1. Evaluate the continuity in the σ^2 fields.

2. Highlight any pronounced differences in the parameter magnitudes vertically associated possibly with different airstreams.

3. Perform a forecast verification by noting any errors between where the tracer identifies the most likely place for cloud electrification to where the thundersnow actually occurred.

The aim from this substitute airflow analysis is to hopefully build upon the conceptual models provided by Moore et al. (2005a,b), Nicosia and Grumm (1999), and Oravetz (2003) through determining any discriminating characteristics between snowstorms exhibiting electrical activity versus those that do not. If remarkable differences do exist, then the forecasting community might find these results of great utility in their daily regimen.

1.3 Plan of Work & Statement of Thesis

1.3.1 Statement of Thesis

The presence of instability is crucial in creating an environment favorable for the creation of any thunderstorm. In the last quarter century, a gradual comprehension of wintertime cloud electrification from the background synoptic conditions down to the microphysical scale has occurred. Nevertheless, the theories and measures used in determining the susceptibility of the atmosphere to convection have been limited and unrealistic at times. The dissertation seeks to expand and improve the foundations for more fully gauging the likelihood of thundersnow initiation. A few of the testable issues that the research will investigate are:

1. How substantial are departures from geostrophy in thundersnow events? In other words, is it appropriate or accurate to diagnose the momentum equations of mesoscale features by imposing thermal wind balance on the background environment?

2. Can the approximate location and timing of lightning and thunder in snowstorms be identified immediately beforehand by examining a suite of stability parameters and their trends? Is there general agreement in the various techniques?

3. Along those lines, is it possible to predict banding in these events from the growth rate parameter, such as what was accomplished in Bennetts and Sharp (1982)? What is the best way to do this?

4. What type of instability is most common in convective snowstorms?

5. How much do stability regimes in thundersnow events differ from those in non-thundersnow events? Are there statistically significant thresholds?

6. Does the surrogate airstream analysis offer any significant, additional information on the distinguishing marks of snowstorms with lightning compared to those without?

1.3.2 Plan of Work

Numerous goals will be pursued in this research work in order to fulfill the objectives and hypotheses briefly cited above. These include:

1. Determining the validity and impact of including ageostrophic effects in σ^2 since the original formulation was intended to diagnose CSI, which stipulates that nearly geostrophic conditions are assumed in the along vertical shear direction (e.g., Martin 1998, Schultz and Schumacher 1999). Schultz and Schumacher (1999) contended that the usage of the total wind is inconsistent with the original theoretical development of symmetric instability. Nevertheless, Gray and Thorpe (2001) have presented rigorous, mathematical support for the extension of this premise to a more generalized, three-dimensional basic state which is allowed to evolve and, thus, would not be in strict thermal wind balance.

2. Examining the performance of σ^2 against various observational datasets, with radar analysis being emphasized. The comparison with theory is motivated by the fact that narrow lines of clouds and precipitation are often found in the vicinity of frontal systems, which Bennetts and Hoskins (1979) found could be due to the release of CSI. Bennetts and Sharp (1982) directly applied this principle to the prediction of frontal rainbands and found that the precipitation was almost certainly to be banded for $\sigma^2 \geq 0.2h^{-2}$. Furthermore, positive values for this parameter might represent the presence of some sort of instability (usually CSI) as well as indicate that a disturbance will grow in the given environment (Bennetts and Sharp

1982). As Bennetts and Sharp (1982) recommend, a term by term analysis of σ^2 will be utilized in order to properly distinguish the type of instability present in a particular convective snowfall environment.

3. Examining performance of the tendency in σ^2, which should represent the instantaneous change in the growth rate of the instability. No previous work in this area has been performed to date and would hopefully provide information about the nature of how likely and quickly wintertime convection is expected to develop. Examinations of soundings and cloud-to-ground (CG) lightning data from the National Lightning Data Network (NLDN) will aid in verification efforts.

4. Substantiating results obtained from σ^2 for consistency by correlating results from the other customary approaches discussed previously. The type, strength, and evolution of the stability regime could then be further confirmed. More importantly, the emphasis would be to discover if strong similarity exists between σ^2 and these other independent techniques, such that more reliability can be placed in the results obtained from this relatively new growth rate parameter.

5. Determining how 1) - 4) fit into the operational offerings of Wetzel and Martin (2001) and Moore et al. (2005a,b). Both perspectives discovered through different means the necessary ingredients for the development of significant cold season precipitation events. Although analyses of individual events will be offered, the fact that multiple similarities exist within the dataset supports the aim to refine these preexisting conceptual models.

Chapter 2

Literature Review

Prolonged periods of intense frozen precipitation can disrupt all forms of traffic, services, goods, and communication, thereby crippling daily, vital operations within major metropolitan areas. For instance, snowstorm activity begins as early as October and extends into April across substantial portions of the United States, with the peak typically occurring in the months of January, February, and March when synoptic conditions (e.g., ETC tracks) are the most favorable (Changnon et al. 2006). This high level of incidence can create a multitude of problems, ranging from public safety concerns and property/environment damage to economic losses. As a matter of illustration, the "superstorm" of March 1993, in itself, was responsible for approximately $ 20 billion (2000 dollars) in insured property losses and affected parts of twenty states from Louisiana to Maine (Changnon et al. 2006). Being known as the nation's most widespread winter storm of the last century, 270 people lost their lives as a result of this natural catastrophe. Please refer to Changnon et al. (2006) and references therein for more details on the specific impacts of significant winter events such as these.

Convective snow events typically are rare across the United States compared to other weather observations (Curran and Pearson 1971; Schultz 1999) but occur more frequently than what is commonly perceived. More importantly, some evidence (e.g., Crowe et al. 2006) has been presented recently to support the

anecdotal observation that heavier instantaneous rates of snowfall and higher total accumulations are often associated with snowstorms which feature lightning. As a result, understanding the antecedent conditions leading up to thundersnow initiation is significant. By obtaining common, repeatable features in the observations and model analyses beforehand, more accurate predictors can be utilized by the operational community in the future. The ultimate goal was to achieve greater preparation for significant winter storms by improving upon forecast duration and spatial extent when an outlook was expected to be issued.

In this chapter we review the recent progress of assessing typical environmental characteristics responsible for the occurrence of convective snowfall. Although several factors were described, the crucial stability ingredient will be dealt with in detail. As a result, several different techniques for analyzing instability that have been previously investigated were summarized here. Given that the topic concerned cold-season thunderstorms, the theoretical framework of CSI and the practical means of measuring its influence in the atmosphere were emphasized. From this comprehensive treatment, the study at hand will then apply the varying diagnostics to the specific phenomenon of thundersnow.

2.1 Basic Characteristics of Thundersnow

Thundersnow is considered present whenever lightning is coincident with any intensity of snowfall. Schultz (1999) noted that the historical record of this weather phenomenon varied across the world but extended back approximately thousand years ago in China. Still, the lack of investigation into the subject matter until about thirty years ago is presumably motivated by its infrequent nature. This assertion by Schultz (1999) is supported by the relatively few weather reports retrieved by Curran and Pearson (1971), who were among the first to address the occurrence of thunderstorms with snow and construct composite

soundings. Schultz (1999) also suggested that the lack of interest could also be due to the fewer number of lightning flashes (especially cloud-to-ground) in the cold-season and the associated reduced risk of resultant injuries and property damages. Colman (1990a,b) has shown that gravitational instability is for the most part lacking in wintertime events, which would correspond to the relatively weak vertical circulation patterns present within most snow-bearing ETCs. While the characteristic updraft speeds are marginal at best in meeting the necessary threshold for lightning production (Zipser and Lutz 1994), Colman (1990b) has argued that CSI is a likely mechanism to explain limited electrical activity in the presence of elevated convection. Finally, the number of thundersnow occurrences could be under-reported given that snow tends to absorb more sound and light as well as fewer direct observations in the colder weather as people favor to stay indoors (Schultz 1999).

Aside from pure curiosity, interest in winter thunderstorms increased further in the middle 1990s as a result of providing staff at the Storm Prediction Center insight on how to start the transition process on issuing hazardous weather outlooks year-round (Holle et al. 1998). Although the study by Holle et al. (1998) encompassed the occurrence of any weather conditions, the restriction to examining just convective snow by Curran and Pearson (1971) and Market et al. (2002) indicated similar, specific geographical regions, the central Great Plains repeatedly being one of those locations. Unlike other investigations which narrowed their focus to sections of the United States, such as the Southeast (e.g., Hunter et al. 2001; Mote et al. 1997), the three former climatologies utilized surface reports across the entire country and surrounding regions. Amongst this more extensive search for understanding the typical conditions under which significant frozen precipitation can form, Market et al. (2002) was the only study to develop a classification scheme for thundersnow events utilizing a 30-year (1961-90) data period. From this methodology, most cases of convective snowfall were found to

be embedded within ETCs, where the source of the most unstable parcel was generally found at high altitudes above the more easily identified surface influences (Market et al. 2002, 2006), such as observed in lake effect (Schultz 1999) situations. A review of the ingredient-based approach in foretelling thunderstorm initiation will be addressed in the following sections, with a thorough discussion given to the crucial instability component.

2.2 Ingredient-Based Approach to Convection

2.2.1 General Overview

The generation of deep, moist convection requires the presence and collective interaction of lift, moisture, and instability (e.g., Johns and Doswell 1987; Doswell 1987; McNulty 1995; Schultz and Schumacher 1999). This ingredients-based methodology has traditionally been utilized in order to properly assess the development of warm season thunderstorms. The vertical extent of the generated gravitational (upright) convection through the troposphere will depend upon a set of limiting factors, which as discussed in Johns and Doswell (1992), are dependent upon the strength of the low-level capping inversion, the amount of 1000-500hPa average relative humidity, the value of the lifted index, and the intensity of the lifting mechanism(s) present. Once these are satisfied, the forecaster must then be able to distinguish between regions capable of producing severe thunderstorms from those that are not conducive (e.g., McNulty 1995).

The general lack of positive, buoyant energy during the coldest months of the year in the continental United States would seem to preclude the usage of this technique for the most part. Still, Schultz and Schumacher (1999) assert that the same evaluation process should be extended to include elevated thunderstorms associated with the release of moist, slantwise convection as well. In addition, MacGorman and Rust (1998) also did not confine themselves to specific seasons

and defined the phenomenon of thundersnow more by its electrical nature. As the audible sound of thunder is not commonly heard in the wintertime (e.g., Schultz 1999), the presence of lightning (intracloud or cloud-to-ground) from observation platforms (i.e. National Lightning Detection Network; NLDN) during this season should determine the existence of a thunderstorm. As a result, the task of anticipating substantial convection and its resultant, damaging effects remains unchanged, despite the fact that the detailed impacts are more complex (i.e. mixed-phase precipitation). Thus, the responsible dynamical and thermodynamical processes involved need to be physically understood before development and implementation of conceptual models into the forecasting procedure.

Extensive research into the atmospheric conditions on the mesoscale and synoptic scale contributing to lightning in winter storms had yet been performed by the turn of the 21st century, as noted in MacGorman and Rust (1998). The only published study to bridge this gap was that of Colman (1990 a,b), who utilized a four-year data set (1978-82) to investigate thunderstorms across the conterminous United States which developed above a frontal inversion. Still, the main drawback in this study was that it was all inclusive with respect to precipitation type. Although sleet and freezing rain events occur quite regularly, snow is often the most prominent of the frozen variety observed with thunder, especially when surface temperature are at or below freezing (Holle et al. 1998). By restricting the dataset to just the latter, Market et al. (2002, 2004, 2006) was able to more effectively compile and provide typical 3-D analyses of momentum, mass, and humidity for a specific subset, the distinct information of which would be diminished in the approach applied by Colman (1990 a,b).

2.2.2 Forcing Mechanisms

2.2.2.1 Composite Plots

Evidence from Colman (1990 a,b) shows that nearly all winter season (December through February) thunderstorms occurring east of the Rocky Mountains, except for the Florida peninsula, are of the elevated type (Figs. 2.1 and 2.2). The source of the shallow convection was removed from the colder, more stable, planetary boundary-layer airmass and associated with the surface extension of a strong baroclinic zone. In addition, the background environment shows that these localized features are often organized on the synoptic-scale around an ETC. Relative to the low pressure center, Colman (1990a) and Market et al. (2002) show that the greatest occurrence of reports was displaced to the poleward side, the peak activity only a few hundred kilometers away from the surface system. While the scatter plots in both studies reveal a maximum just off to the north and east, an additional preferred location in Market et al. (2002) produced a bimodal pattern for thundersnow events (compare Figs. 2.3 and 2.4) determined by the point in evolution of the ETC. In particular, reports came generally from the colder air north of the warm front in the developing stages, whereas the maximum shifted off towards the northwest of the low by the time occlusion set in. Similar findings were also obtained from the unpublished thesis of Elkins (1987).

Typical surface characteristics for convective snow episodes in an ETC have been ascertained in the past (Market et al 2002), wherein average, ambient temperatures and dewpoints are found in the composite station model to be below freezing (Fig. 2.5). As would be expected, the prevalence of the arctic airmass is sustained by moderate north-to-northeasterly winds on the order of 15 knots. Above ground level, the flow direction tended to rotate clockwise with height throughout the lower troposphere in situations of elevated thunderstorms. Given the veering shear profile, Colman (1990a) deduced that warm air advection was prevalent by assuming an atmosphere in approximate geostrophic balance. This

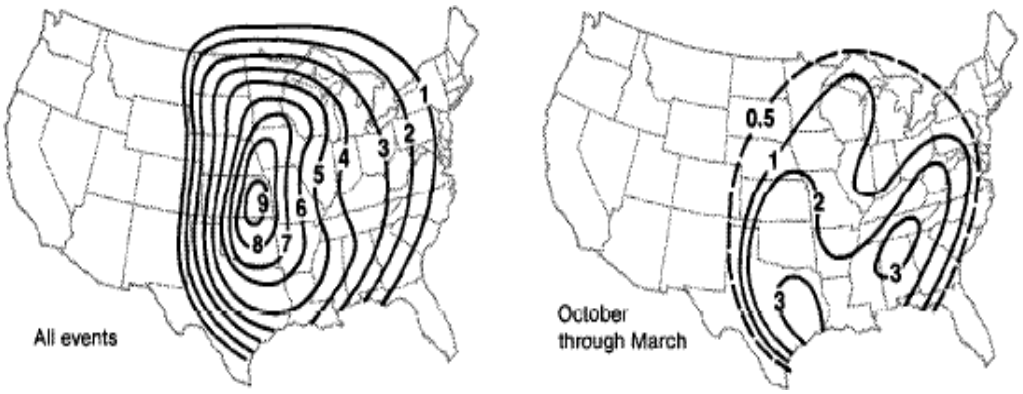

Figure 2.1: The number of elevated thunderstorms (reports/station) identified over the 4-year period (a) from September 1978 through August 1982 and (b) the subperiod October through March. Reproduced from Colman (1990a).

finding was further confirmed by Oravetz (2003), who utilized a spatial subgrid to compile averages and standard deviations for numerous meteorological variables at select isobaric surfaces. The generated composite plots helped in the process of identifying typical atmospheric features and their associated trends leading up to the onset of thundersnow. As suggested by the synoptic setup, Oravetz (2003) discovered that the peak value in upward vertical motions occurred by the time of initiation. As the average cyclone approached from the southwest with the development of convective snowfall, the maximum 850-hPa convergence (Fig. 2.6) coincides favorably with the strongest upper-level divergence at 300-hPa. From application of the quasi-geostrophic theory, the best conditions for producing large-scale ascent were provided by the very high positive differences in absolute vorticity advections between the 850-hPa and 300-hPa levels. Furthermore, typical analyses from Oravetz (2003) indicated the warm air advection acted as additional support as 700-hPa magnitudes (Fig. 2.7) had persisted in intensity for the previous 12 hours (Fig. 2.8). Once the dataset were split into subsets for those events occurring northeast (NEC) and northwest (NWC) of the parent cyclone, Oravetz (2003) found some distinct differences in the analyses.

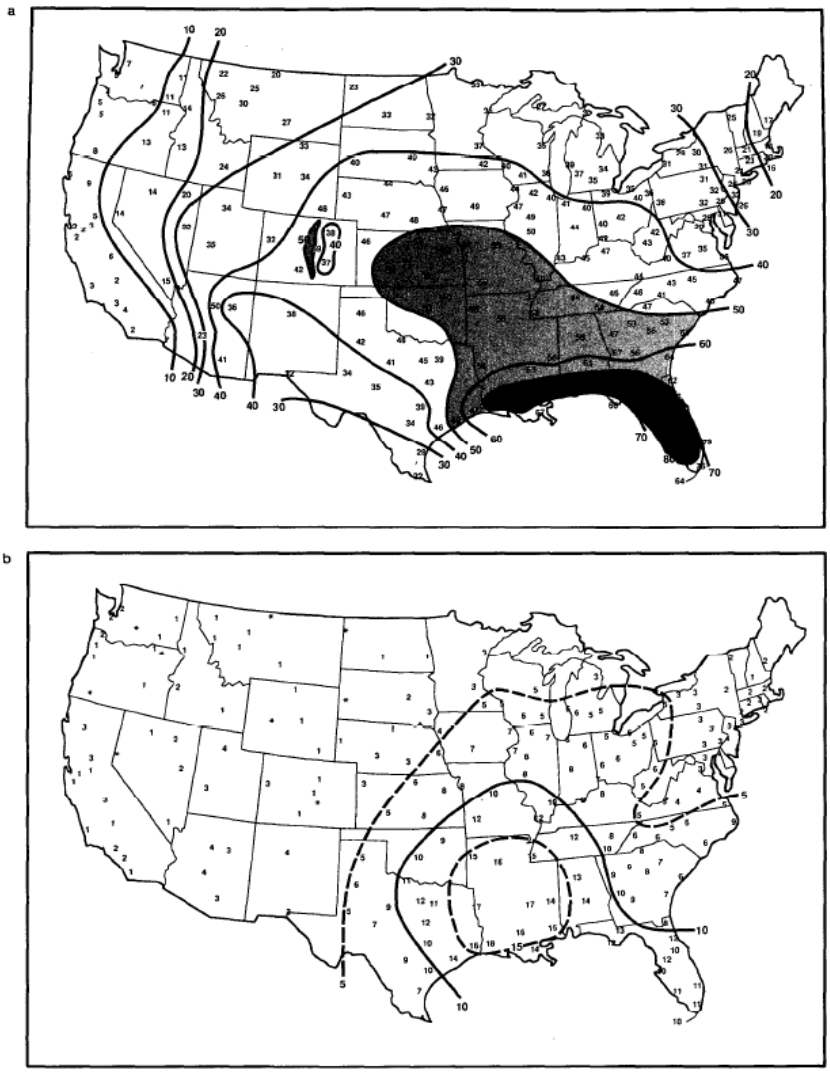

Figure 2.2: (a) The mean annual number of days with thunderstorms of any type, by station, 1951-75. (b) The mean number of days with thunderstorms of any type, by station, 1951-75, for the subperiod October through March (Court and Griffiths 1986). Reproduced from Colman (1990a).

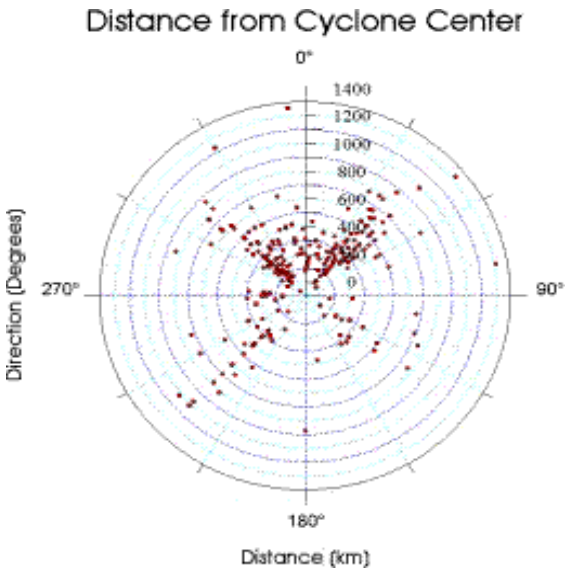

Figure 2.3: Polar plot showing the location of thundersnow events (Category 1: cyclone) relative to the position of the center of the parent low (N=247). Direction is given in the traditional meteorological azimuth (degrees) from the position of the low to the observing station. Range (distance from origin) is given in km. Reproduced from Halcomb (2001) and Market et al. (2002).

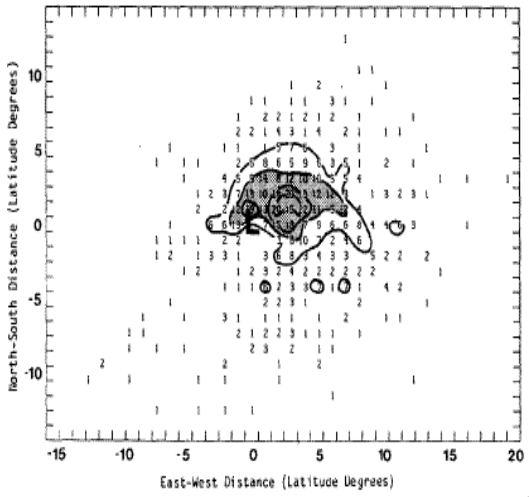

Figure 2.4: The number of reports at a given position with respect to the associated surface low-pressure center (L). The degree of latitude (60 nm, 111.1 km) is used as the unit of distance. Contour interval is 5. Reproduced from Colman (1990a).

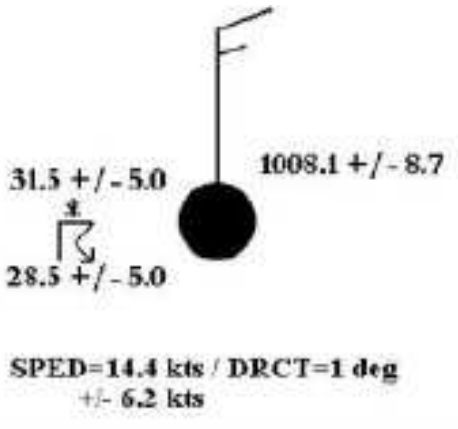

Figure 2.5: Representative station model for the average initial report for all thundersnow events (N=375). Temperature and dewpoint are given in degrees F, the wind speed in knots, and the sea level pressure in hPa. The standard deviation parameters is also represented. Reproduced from Halcomb (2001) and Market et al. (2002).

Conceptual illustrations were constructed as a result and revealed that the primary difference between the two types was that the NEC (NWC) was associated with the open wave (mature) phase of the NCM. Elkins (1987) also obtained similar results with respect to evolutionary stages on the synoptic scale.

2.2.2.2 Frontogenesis

The fact that most near-to-subfreezing, elevated convection occurs in connection with transient ETCs implies the importance of subsynoptic scale processes, as both phenomenon evolve on time periods which can be substantially different (in the extreme, minutes vs. days). While the contributing factors to this type of convection might be external, such as orographic, the prevalence of strong temperature advections in the results of both Colman (1990a) and Oravetz (2003) imply the necessity of narrow baroclinic zones. The paradigm of mid-latitude fronts developing within an ETC first arose from Bjerknes and Solberg (1922); their representation of an incipient disturbance along the polar front progressing through maturity to occlusion and decay has been commonly referred to as

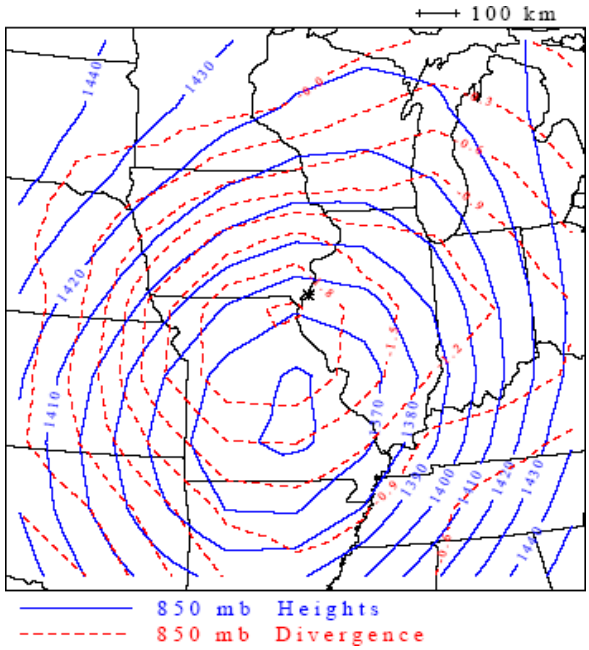

Figure 2.6: The 850-mb heights (gpm) and divergence ($10^{-5}s^{-1}$) fields for ALL cases at T-00. Reproduced from Oravetz (2003).

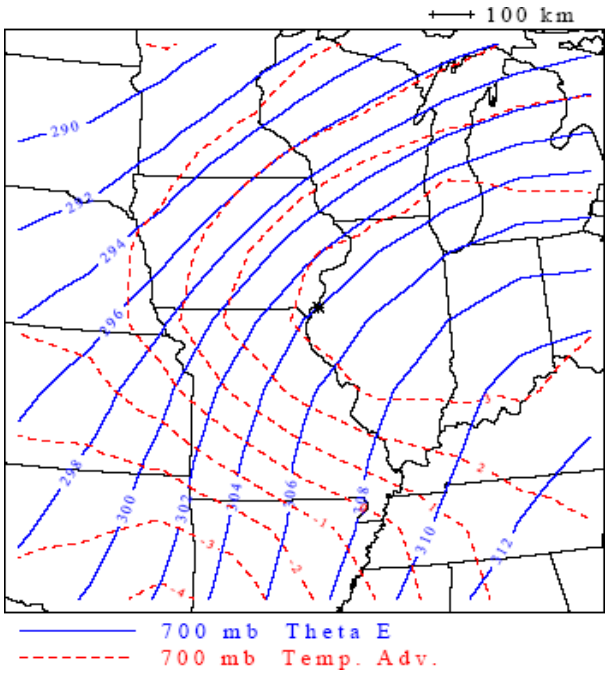

Figure 2.7: The 700-mb θ_e and temperature advection ($10^{-4}Ks^{-1}$) for ALL cases at T-00. Reproduced from Oravetz (2003).

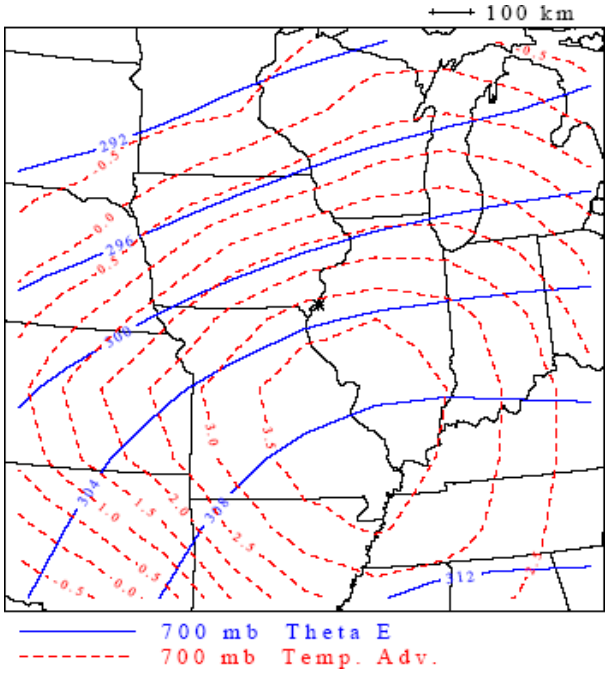

Figure 2.8: The 700-mb θ_e and temperature advection ($10^{-4}Ks^{-1}$) for ALL cases at T-12. Reproduced from Oravetz (2003).

the Norwegian Cyclone Model (NCM; Fig. 2.9). Observations of differing cyclone/frontal structures and evolutions has offset the success of the NCM somewhat in recent years, a review of some of the limitations offered in Schultz et al. (1998). Despite its inadequacy to explain all scenarios, enough commonalities in the physics of cyclogenetic events are evident and no widely acceptable and versatile alternative has been proposed that the fundamental approach has not been abandoned and still remains practical to meteorologists even to this day (Schultz et al. 1998).

Frontogenesis ($\Im$) is defined by the *Glossary of Meteorology* (American Meteorological Society 2000) as the creation of a front or the increase in density (and associated thermal) gradients. Petterssen (1956) formulated a 2-D mathematical expression, given by:

$$\Im = -\frac{1}{2}|\nabla\theta|(F\cos(2\beta) - D), \tag{2.1}$$

where F is the resultant deformation, D is the horizontal divergence, and β is

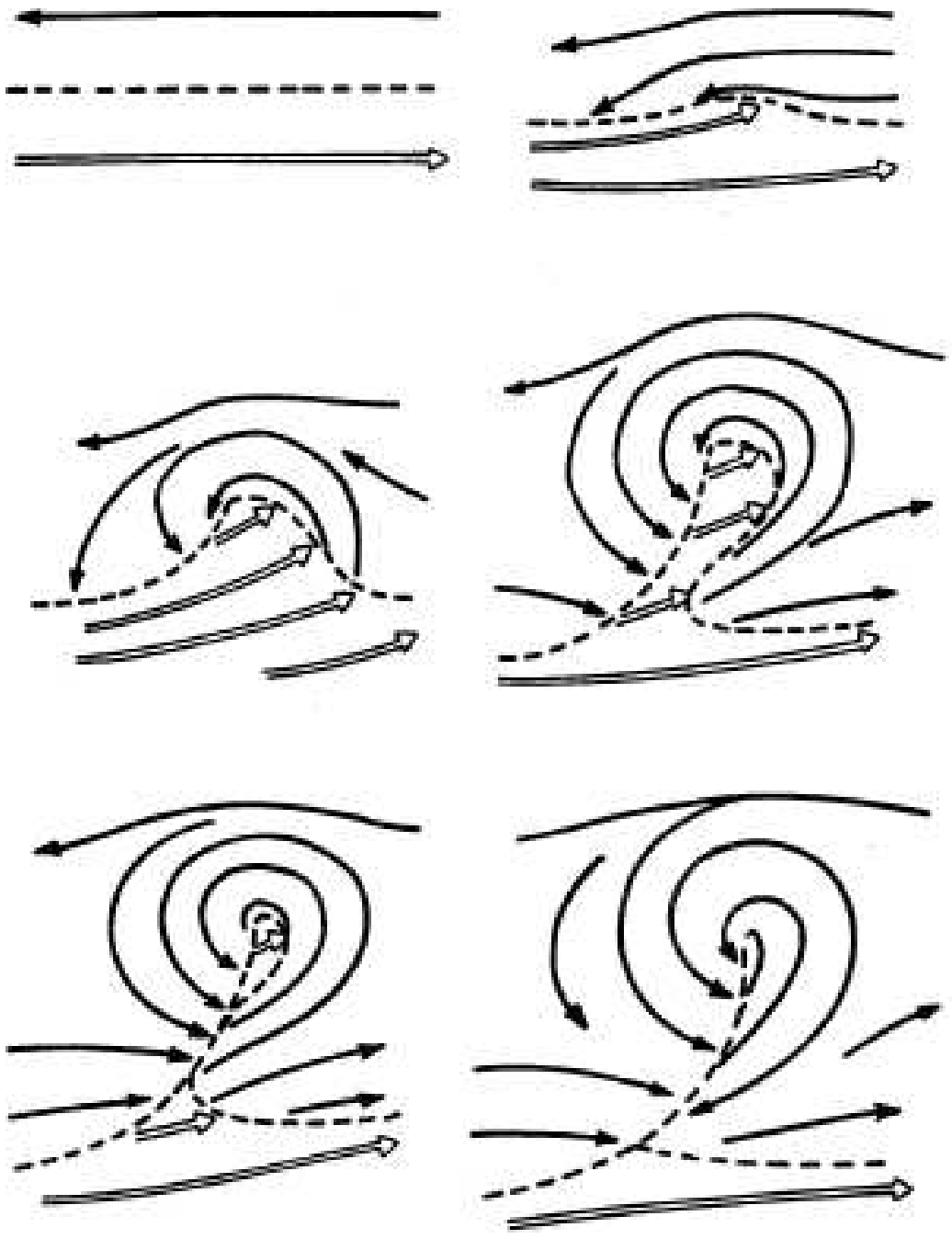

Figure 2.9: The life cycle of an extratropical cyclone (after Bjerknes and Solberg 1922). Solid lines indicate streamlines and dashed lines signify frontal boundaries. Reproduced from Schultz and Mass (1993).

the angle from the axis of dilatation to the isentropes. In the case that β is less than 45 degrees in Eq. 2.1, the potential temperature gradient will be increased (frontogenesis; $\Im > 0$) through deformation (Fig. 2.10). On the other hand, frontolysis ($\Im < 0$) and a relaxing of the thermal gradient will occur if the angle is more than 45 degrees between the dilatation axis and the isentropic surfaces (Fig. 2.11). As for pure convergence (divergence) in the wind field (i.e. only *Dnonzero*), frontogenesis (frontolysis) will result from Equation 2.1. Given this simplified representation for frontogenesis, the horizontal cartesian coordinates are rotated over to a linear field of motion where a measure of the local intensity of the confluence could be obtained (Petterssen 1956). As a result, the physical reasoning states that temporal variations in the distribution of the thermal pattern are solely determined by the momentum field and its orientation with respect to the temperature field. From a QG approximation, $\Im$ offers a means to explain the synoptic and mesoscale production of vertical motions within ETCs.

In particular, Hoskins et al. (1978) developed an alternative method of the omega equation which combines the traditional forcing of temperature advections and differential vorticity advections into one term, the divergence of the Q-vector. The Q-vector ($Q \equiv [-\frac{R}{p}\frac{\partial \vec{V_g}}{\partial x} \cdot \nabla T, -\frac{R}{p}\frac{\partial \vec{V_g}}{\partial y} \cdot \nabla T]$), analogous to $\Im$, represents the rate of change of the horizontal potential temperature gradient forced by geostrophic motion alone (e.g., Hoskins et al. 1978). Other than its compact nature, another primary advantage of this technique is its ability to avoid partial cancellation errors. Additionally, the right-hand side forcing function can be determined from examining only one pressure surface; whereas differential vorticity advection requires two upper-air height fields (Walters 2001).

Numerical modeling by both Hoskins and Bretherton (1972) and Mudrick (1974) evaluated the assumption of geostrophy on the wind field in frontogenetic processes. In the beginning stages of cyclogenesis, deformation is more important and QG is a good first approximation. Still, the kinematic explanation implies a

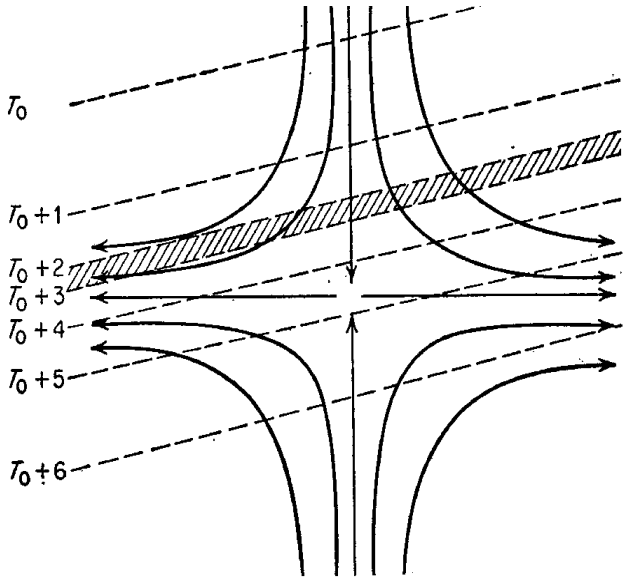

Figure 2.10: Illustrating frontogenesis. The line of frontogenesis (hatched) moves toward the axis of dilatation, while the temperature contrast increases. Reproduced from Petterssen (1956).

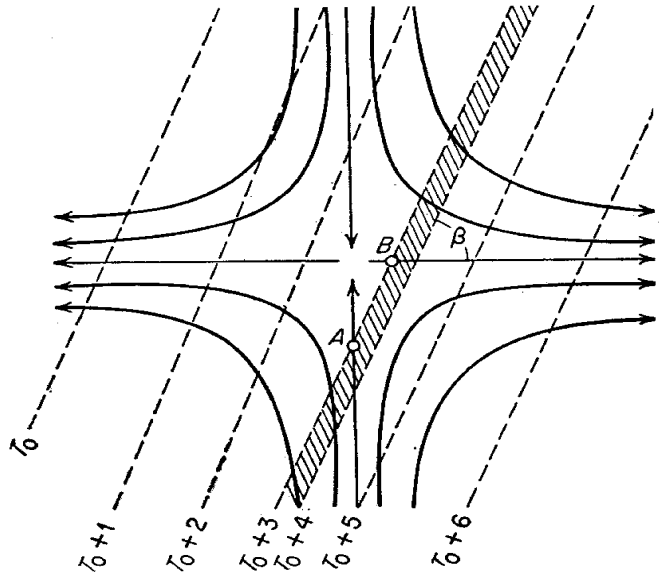

Figure 2.11: Illustrating frontolysis. Reproduced from Petterssen (1956).

rate of frontogenesis that is too slow (e.g., Carlson 1998), in which the temperature field is treated as a tracer in (Eq. 2.1) and does not actively feedback on the wind field, as it should. By utilizing analyzed (observed) winds and a more complete form of the inviscid, adiabatic primitive equations of motion, more realistic frontal structures are permitted as ageostrophic motions and divergence are included. The usual sloping nature of the baroclinic zone and formation of intense temperature gradients in a finite time period were demonstrated (Hoskins and Bretherton 1972; Mudrick 1974). While the emphasis of the dissertation is not on the importance of mesoscale forcing processes, the interaction with the coincident stability regime is crucial to the development of an intense ageostrophic circulation and ensuing convective updrafts sufficient for lightning production (Emanuel 1985; Zipser and Lutz 1994; Schultz and Schumacher 1999).

2.2.3 Instability and Moisture

Instability is a property which prescribes that small perturbations introduced into some steady state flow in the atmosphere, either related to wave or parcel displacements, will increase in magnitude (*Glossary of Meteorology* 2000). On the other hand, the atmospheric response in a stable regime will be to suppress disturbance growth back toward the initial equilibrium state, or at the very least produce a constant periodic oscillation. When considering fluid motions in a horizontal context, most often the relative vorticity is sufficiently small compared to the coriolis parameter that the effects of rotation are stabilizing to the air flow (e.g., Lilly 1986; Holton 2004). Consequently, lateral accelerations require that the absolute vorticity be negative (positive) in the northern (southern) hemisphere, a condition that is rarely met except possibly in strong anticyclonic shear or curvature regions of upper-level jet streams. Other than the work of Schumacher and Schultz (2001), relationships between inertial instability and

severe weather have been lacking, mainly due to the aforementioned infrequency as well as the unclear physical role in the development of these convective events. Rather, more attention has traditionally been given to how the atmosphere reacts to vertical parcel displacements.

The inquiry into the background conditions necessary for thunderstorms has centered primarily on the warm season category, where the ingredients-based methodology has been applied to forecast deep, moist convection. The relevant instability in this case is typically assumed to be associated with the lapse rate definition (i.e. environmental lapse rates between the dry- and moist-adiabatic lapse rates of a conditionally unstable atmosphere), in which the condition terminology refers to the requirement that the air parcels be saturated (e.g., Doswell 1987; Schultz et al. 2000). Johns and Doswell (1992) discussed the limiting factors that need to be assessed in an operational environment in order to determine the depth of the gravitational (upright) circulation. Once these are satisfied, the forecaster must then be able to distinguish between regions capable of producing severe thunderstorms from those that are not conducive (e.g., McNulty 1995).

Monthly distributions of cloud-to-ground (CG) lightning flashes across the contiguous United States were obtained by Orville and Huffines (2001) from a decade long (1989-1998) set of data. Acquired from the NLDN, the observations showed a symmetric maximum centered on July that trailed off to only a few hundred thousand counts between November and February (Fig. 2.12). This latter minimum also coincides with the coldest temperatures of the year and a general increase in stability of the environment, especially within the planetary boundary layer. In addition, as was stated earlier, most soundings in the few winter thunderstorms generally lack convective available potential energy (CAPE; e.g., Curran and Pearson 1971; Colman 1990a,b; Market et al. 2006). This is not to say that conditional instability (CI) is not possible, as has been documented within some individual case studies (e.g., Halcomb and Market 2003; Market

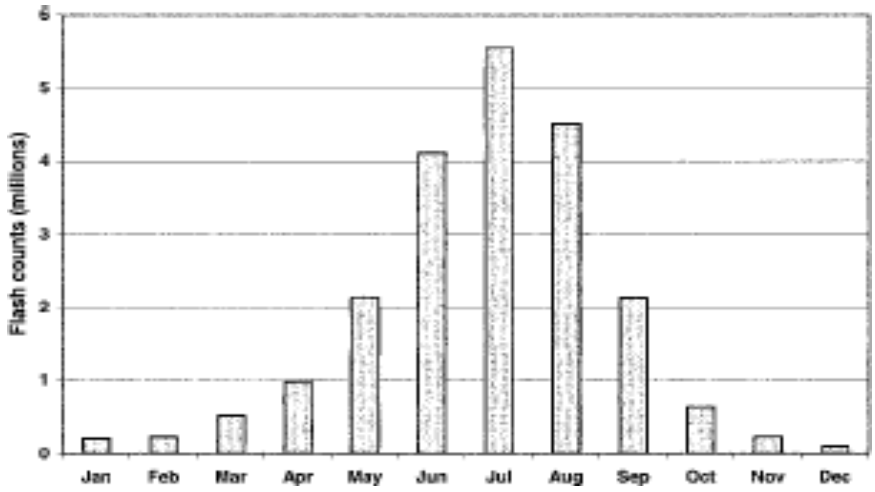

Figure 2.12: The mean monthly flash counts for the decade show symmetry around the maximum in July followed by low values recorded from Nov. through Feb. Reproduced from Orville and Huffines (2001).

et al 2006), but slantwise circulations released from CSI tend to be a more frequent and plausible explanation for these type of events. Thus, characteristics and evaluation techniques of the more unique scenario of CSI will be addressed subsequently.

2.3 Conditional Symmetric Instability

2.3.1 Original 2D Theory

Bennetts and Hoskins (1979) and Emanuel (1983a,b) were probably the first to suggest that the atmosphere could still be susceptible to a combination of horizontal and vertical (i.e. slantwise) motions in a moist, baroclinic environment, despite the fact that conditions for purely buoyant and inertial stability are separately satisfied (Holton 2004). As a result, the assumption of geostrophic and hydrostatic balance requires that the effects of both centrifugal (for the adherence to near-geostrophic balance) and gravitational forces acting on an air parcel be taken into account. Generally speaking, traditional dry (moist) symmetric in-

stability theory simultaneously merges the influences of inertial and dry (moist) gravitational buoyancy in a two-dimensional, semigeostrophic framework with no variation allowed in the along-vertical shear axis (e.g., Schultz and Schumacher 1999; Martin 1998; Snook 1992). In particular, Schultz and Schumacher (1999) note that the term "symmetric" mandates the presence of a basic state flow and perturbations that are independent of a horizontal direction.

CSI is a particular form of moist symmetric instability that requires the atmosphere to be saturated in order for the air parcels to be unstable. Once the convective potential energy is released, the resultant motions take the form of slanted roll circulations oriented parallel to the thermal wind vector (Bennetts and Hoskins 1979). According to Bluestein (1986), the most favorable conditions for the release of CSI include atmospheres that are strongly baroclinic (high vertical shear), have pronounced anticyclonic flow, and low but positive static stability in a nearly saturated environment. These criteria are often met in the vicinity of a warm front and have led researchers like Bennetts and Hoskins (1979), Bennetts and Sharp (1982), and others to suggest that CSI might be a likely contributor to narrow bands of intense precipitation generally found along frontal zones.

Spatial and temporal scaling arguments, such as those found in Emanuel (1986), show that the effects of buoyant and inertial stability are mutually significant for moist slantwise convection. As a result, the two-dimensional motions can be considered unambiguously mesoscale. In particular, horizontal velocities for the parcel typically are comparable to that of the mean flow (approximately 10 ms^{-1}), whereas those for vertical motions range on the order of about tens of cms^{-1} all the way up to a few ms^{-1} (Bennetts and Hoskins 1979; Emanuel 1983a; Wolfsberg et al. 1986). Using reflectivity data from various research field programs, Zipser and Lutz (1994) proposed that a mean updraft speed of 6-7 ms^{-1} was required to sustain or generate the essential sizes and types of hydrometeors

(i.e. raindrops and large ice particles) for electrical discharges within the convective cloud (e.g., Zipser and Lutz 1994; Schultz and Schumacher 1999). Thus, the limited lightning activity in the cold-season established from studies in Japan (e.g., Michimoto 1991, 1993) and the United States (e.g., Orville and Huffines 2001) can be supported partly by the strength of circulations produced by CSI often not reaching the critical intensity. In the cases where the released convection is adequate enough, proximity soundings from Market et al. (2006) revealed that thundersnow cases northeast of an extratropical cyclone appeared to exhibit an environment more favorable to slantwise than upright displacements.

The theoretical description of moist symmetric instability presented here follows that in Emanuel (1983a,b), in which a localized region of the atmosphere is considered. This scenario of considering air parcel motions differs somewhat from the type discussed in Bennetts and Hoskins (1979), wherein the stability of lifting an entire layer to saturation is examined. Instead of infinitesimal displacements, this framework deals with the resistance of isolated two-dimensional small masses of air to finite slantwise displacements. Expanding from this basis, a purely meridional, steady, baroclinic shear flow is assumed to be in geostrophic balance (v_g), thereby constraining the virtual potential temperature (θ_v) to be only a function of x and z. Consequently, the background environment should obey the thermal wind relation represented by:

$$f\frac{\partial v_g}{\partial z} = \frac{g}{\theta_{v0}}\frac{\partial \theta_{vg}}{\partial x}, \tag{2.2}$$

where f is the coriolis parameter and θ_{v0} is a reference virtual potential temperature. Now, consider an infinitely extending small "tube" of air in the y direction and the subsequent atmospheric response to some finite, reversible displacement of this parcel in the $x-z$ plane. By assuming no perturbation or viscous forcing, it then follows that the relevant momentum equations for the secondary circula-

tion are:

$$\frac{du}{dt} = f(M_p - M_g), \tag{2.3}$$

$$\frac{dw}{dt} = \frac{g}{\theta_{v0}}(\theta_{vp} - \theta_{vg}), \tag{2.4}$$

and the subscripts p and g refer to the parcel and geostrophically balanced state, respectively. The variable, M, defined as the pseudo-angular momentum:

$$M = \vec{V} + fx, \tag{2.5}$$

is assumed to be conserved following the fluid motion for conditions of unidirectional vertical shear with no turbulent mixing allowed (e.g., Emanuel 1983a,b). Surpluses (deficits) of M on the right-hand-side of Eq. 2.3 indicate that a parcel will experience an eastward (westward) acceleration. Along the same lines, upward (downward) accelerations are obtained when surpluses (deficits) of θ_v are present on the right-hand-side of Eq. 2.4. Finally, the background flow regime is restricted to be inertially and statically stable (i.e. $\frac{\partial M_g}{\partial x}$ and $\frac{\partial \theta_{vg}}{\partial z}$ are positive) and small disturbances are visualized to proceed slowly enough so that the large-scale environment is undisturbed.

The sign and magnitude of accelerations experienced in the x and z directions can be obtained by noting the net value for M and θ_v, respectively, in Eqns. 2.3 and 2.4. A fluid parcel will move away from its initial position in the direction of the displacement if the left-hand sides of both (2.3) and (2.4) have the same sign as the displacement (Wolfsberg et al. 1986). When the atmosphere is unsaturated, this is equivalent to assessing regions where the slope of the M_g surface are less than those of potential temperature (θ) surface. Without the

implied effects of diabatic heating, however, Bennetts and Hoskins (1979) note that dry symmetric instability is rarely attainable in the atmosphere. On the other hand, slantwise convection is more plausible if the release of latent heat is permitted. The inclusion of moisture in the environment can be accounted for in the previously mentioned condition by utilizing surfaces of equivalent potential temperature (θ_e) (hereafter called the M_g - θ_e relationship). Past authors (Bennetts and Hoskins 1979; Bennetts and Sharp 1982; Halcomb and Market 2003) have employed a threshold of relative humidity greater than 80% as a means to satisfy the final constraint of a saturated environment in the diagnosis of CSI. This methodology avoids the unrealistic overmoistening of the atmosphere, something that unfortunately does occur with the strict usage of saturated equivalent potential temperature (θ_{es}) advocated by Schultz and Schumacher (1999).

2.3.2 Evaluation of CSI

2.3.2.1 M_g - θ_e Relationship

Snook (1992) and Schultz and Schumacher (1999) offer descriptions on the various techniques for the evaluation of CSI. Before some of these are implemented to determine the likelihood of slantwise convection in occurrences of thundersnow, the theory will be reviewed here. The most commonly employed method involves the M_g - θ_e relationship (popularized by Moore and Lambert, 1993), such that a saturated parcel will experience an unstable path upwards and towards the west (tilted back toward the colder air) if the displacement is between the M_g and θ_e surfaces. According to Schultz and Schumacher (1999), the identification of CSI in this manner necessitates that the following assumptions are valid:

1. the geostrophic wind does not change in the along-front direction.

2. the evaluation from a cross-section is taken perpendicular to the vertical shear of the geostrophic wind (i.e. thickness contours).

3. the curvature of the flow is minimized by ensuring that the ageostrophic component is small so that the basic state can be assumed to be in geostrophic balance.

A physical description of assessing parcel instability relevant to CSI from a hypothetical cross-section of M_g and θ_e is set forth in great detail in Sanders and Bosart (1985), with Fig. 2.13 helping to illustrate the diagnosis. Other explanations can also be found in Emanuel (1983a,b) and Wolfsberg et al. (1986), as well as other publications. Suppose that the analysis is performed in an $x-z$ plane that is perpendicular to a southerly, geostrophic wind increasing with height. By applying the thermal wind equation (2.2) for this particular scenario, temperatures (or by similar analogy, θ_e) will increase across the baroclinic zone from left to right, in the positive x direction. Furthermore, the resultant M_g surfaces, evident in Fig. 2.13, would then increase upward and to the right, the latter occurring since f is positive in the northern hemisphere. Similar to Sanders and Bosart (1985), a stable stratification is also chosen, so that larger values of θ_e are found at successively higher altitudes. By comparing the properties of the parcel to that of the environment, Sanders and Bosart (1985) demonstrate that the accelerations in an entirely horizontal direction (point A) or vertical direction (point B) act opposite to the displacements. Corresponding to these conditions, the schematic in Fig. 2.13 emphasizes that these perturbed parcels return to their initial positions, as both rotation and gravity act as restoring forces. On the other hand, a saturated parcel will experience an unstable path upwards and towards the west (tilted back toward the colder air) for the isolated air mass at point C, where the isopleths of θ_e are more vertical than M_g.

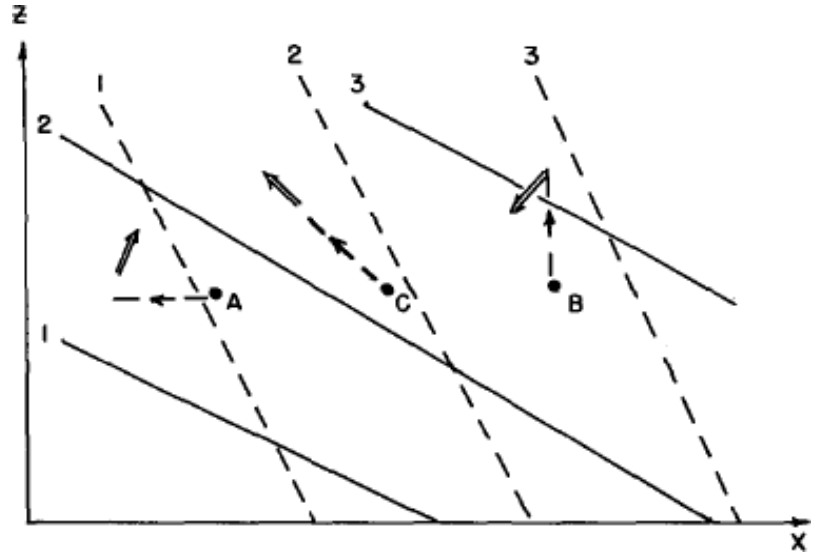

Figure 2.13: Schematic vertical cross section illustrating symmetric instability. Solid lines represent absolute momentum $\bar{M}$ of basic flow. Dotted lines represent equivalent potential temperature. Lettered points show sample displacements (dashed) and accelerations (arrowheads). Reproduced from Sanders and Bosart (1985). Refer to their text for more thorough clarification of concepts.

2.3.2.2 Moist (Equivalent) Potential Vorticity

In their original numerical experiments, Bennetts and Hoskins (1979) explored the "possibility of symmetric instability for two-dimensional flow in an atmosphere which is assumed to be saturated everywhere." An alternative to qualitatively comparing the slope of the absolute vorticity vector to that of potential temperature is to calculate the moist geostrophic potential vorticity (MPV_g), in which either θ_w (wet-bulb potential temperature; Bennetts and Hoskins 1979; Bennetts and Sharp 1982) or θ_e (e.g., Emanuel 1983a; Sanders and Bosart 1985; Schultz and Schumacher 1999, and many others) is employed. The existence of instability is determined by noting regions where the equivalent (q_e; EPV)/wet-bulb (q_w) potential vorticity are less than zero. Upon determining whether convectively stable conditions are present, the criterion of CSI from the M_g - θ_e relationship can be assumed to be satisfied for atmospheric environments with negative MPV_g. While Moore and Lambert (1993) used a two-dimensional form of this diagnostic in their cross-section analysis, the full potential of MPV_g was not realized until recently with the extension to three-dimensions by McCann (1995). In vector form,

$$q_e \equiv - g\vartheta_g \cdot \nabla\theta_e, \tag{2.6}$$

where ϑ_g is the three-dimensional geostrophic absolute vorticity vector, ∇_3 the three-dimensional gradient vector in pressure *(x,y,p)* coordinates, and the remaining variables take on their usual meteorological meanings.

By expanding Eq. 2.6 into component form, McCann (1995) neglects the vertical velocity terms and coriolis parameter in the along-shear direction via scale analysis. Upon carrying out the dot product, the new expression leads to:

$$q_e = g[\frac{\partial\theta_e}{\partial x}\frac{\partial v_g}{\partial p} - \frac{\partial\theta_e}{\partial y}\frac{\partial u_g}{\partial p} - (\frac{\partial v_g}{\partial x} - \frac{\partial u_g}{\partial y} + f)\frac{\partial\theta_e}{\partial p}], \tag{2.7}$$

wherein computations can be easily computed from gridded data in numerical weather models. Upon inspection of Eq. 2.7, the response to a given forcing would be amplified when the:

1. lapse rate for θ_e is negative, indicative of a potentially unstable regime.

2. lapse rate is slightly stable, the vertical shear is strong (i.e. baroclinic), with greater anticyclonic vorticity present. As a result, slantwise convection will be generated from the release of CSI.

Thus, discrimination of the type of instability is not possible from just plan-view plots of q_e since it is possible for both to coexist in cross-sections (Moore and Lambert 1993) and plan-view analyses (McCann 1995). As a result, Moore and Lambert (1993) and McCann (1995) encourage the superposition of the constituent parts on top of fields of q_e

Three major northeastern United States snowstorms were examined by Nicosia and Grumm (1999) in order to diagnose mesoscale mechanisms responsible for the narrow bands of heavy snowfall. Their analysis revealed that frontogenetic forcing and a deep layer of negative q_e were important in constricting the stronger vertical motions to a smaller scale. The resultant increased ageostrophic circulation across the front aided in additional convergence (divergence) in the lower (upper) troposphere and ultimately an increase in thermal gradients. Through a simple conceptual model, Nicosia and Grumm (1999) suggested that the collocation of the mid-level dry tongue jet (DTJ) on the warm side of the mid-level frontogenetic region provided a favorable positive feedback mechanism for lowering q_e (see Fig. 2.14, 2.15). The irrevocable link between baroclinic dynamics and thermodynamics can be demonstrated rather effectively by the response to the Sawyer-Eliassen equation. Emanuel (1985) and Thorpe and Emanuel (1985) provided evidence through numerical modeling experiments that the circulation

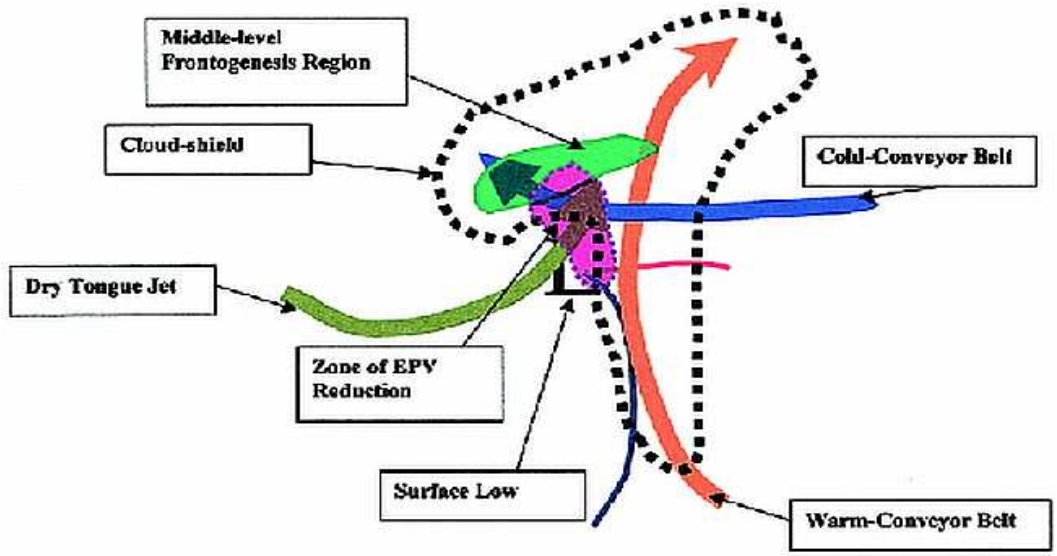

Figure 2.14: Conceptual model depicting the frontogenesis region and zone of equivalent potential vorticity reduction within the context of the major components of a developing extratropical cyclone. Reproduced from Nicosia and Grumm (1999).

produced in the presence of a given frontogenetical forcing was sensitive to variations in the atmospheric symmetric stability. As the MPV_g is diminished on the warm side of the baroclinic zone, the sloping, ascending branch of a thermally direct circulation would be enhanced and constricted to a smaller horizontal scale (Figs. 2.16, 2.17). As for the more stable, cloudless airstream behind the front, the associated downward motions were weaker and more diffuse since the applicable, unsaturated MPV_g is of larger value.

Despite the theoretical and empirical examples showing a close interaction, Schultz and Schumacher (1999) note that assessments of slantwise convection are often made by distinguishing between influences solely due to CSI from those arising because of synoptic or mesoscale forcing processes. The results obtained by Emanuel (1985) in a modeling study and similarly by numerous others through observational work (e.g., Martin 1998, Moore and Blakely 1988, Nicosia and Grumm 1999, Jurewicz and Evans 2004, Moore et al. 2005b) emphasize the

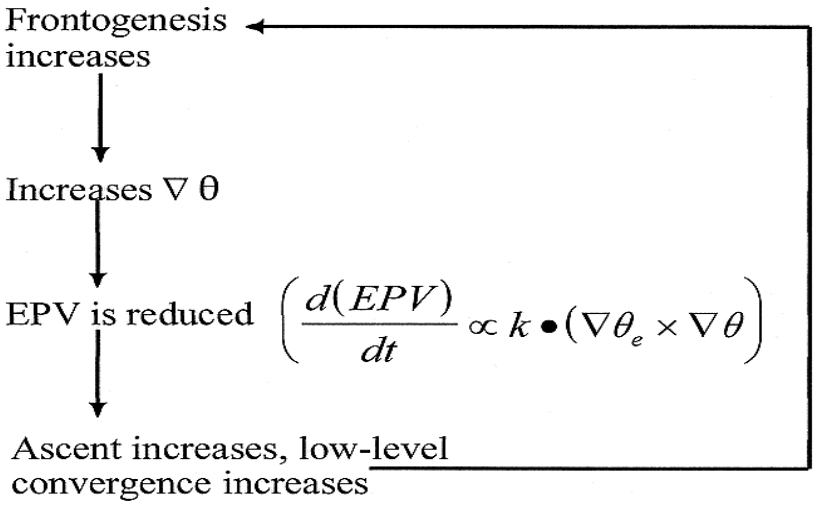

Figure 2.15: Schematic depicting a proposed positive feedback mechanism between frontogenesis and the reduction of equivalent potential vorticity. Reproduced from Nicosia and Grumm (1999)

.

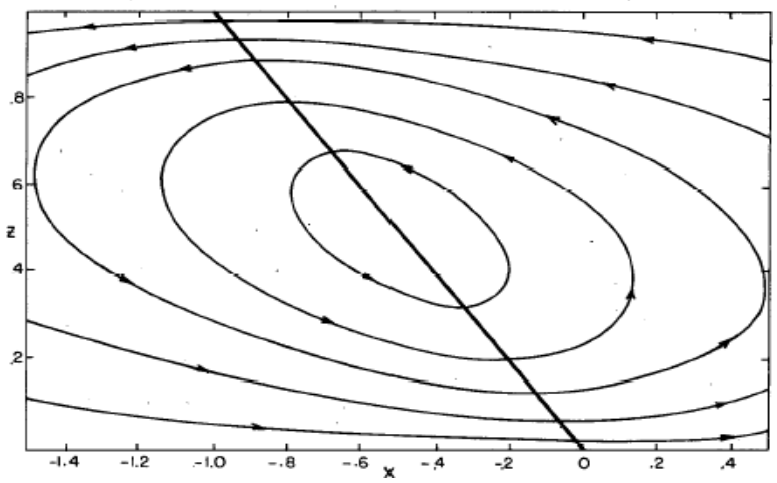

Figure 2.16: The cross-front circulation in physical space for the case that $q_1 =$ 1.0 and $b =$ 5.1. The minimum value of the dimensionless streamfunction if -0.611; contours are at 0.1, 0.3, 0.5, 0.7, and 0.9 times the minimum value. The background dimensionless shear equals b. Heavy solid line denotes the position of the $X = 0$ surface. Reproduced from Emanuel (1985). Refer to associated text.

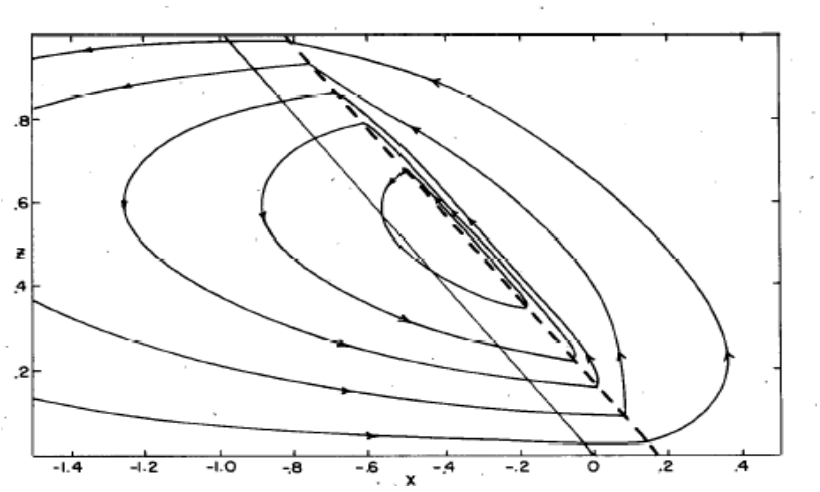

Figure 2.17: As in Fig. 2.16 but for $q_1 = 10^{-2}$. The minimum value of the streamfunction is -1.769 in this case and the heavy dashed line denotes the surface $X = L$. Reproduced from Emanuel (1985). Refer to associated text.

need to properly evaluate all means of lifting parcels to their level of saturation and subsequently releasing any instability present. Thus, the essential, synergistic interaction between frontogenesis and CSI (as diagnosed by MPV_g here) is conducive to the development of narrow bands of clouds and precipitation, something which will be kept in mind in the present study.

2.3.2.3 Richardson Number

The release of CSI will occur physically where the environmental lapse rate along an inclined M_g surface lies between the moist and dry-adiabatic lapse rates (Schultz and Schumacher 1999). In other words, the criterion is met by noting that the traditional relationship in Fig. 2.13 constricts the decrease of M_g in the positive x-direction along a θ_e-surface (Sanders and Bosart 1985). From elementary meteorology, this is analogous to assessing CI in a barotropic environment, except that the absence of vertical shear implies that the absolute vorticity vector is vertical. Thus, the evaluation of distinct atmospheric systems for a wide

range of stability regimes can be ascertained by utilizing something which has information on aspects of both buoyancy and variations in momentum. Emanuel (1986) utilized the customary Richardson number for just such a purpose. He found that since the vertical wind shear is typically slightly larger than the stratification for moist slantwise convection, characteristic values for this metric fall in the intermediate range (readings are less than unity but still greater than 0.25). Similarly, Sanders and Bosart (1985) proposed the extension of qualitatively comparing slopes from a cross-section into a more quantitative diagnostic. Starting from simple geometry, and utilizing Eqns. 2.2 (except for θ_e) and 2.5, they determined that the M_g-surfaces are shallower than the θ_e-surfaces when:

$$\frac{(\partial z/\partial x)_{M_g}}{(\partial z/\partial x)_{\theta_e}} = (\frac{\eta_g}{f})(\frac{\Gamma_d}{\Gamma_m})\frac{g}{\theta_e}\frac{(\partial\theta_e/\partial z)}{(\partial\vec{V_g}/\partial z)^2} \equiv Ri_{sc} < 1, \tag{2.8}$$

where η_g is the vertical component of the geostrophic absolute vorticity, Γ_m represents the moist-adiabatic lapse rate, and Γ_d the dry-adiabatic lapse rate. As a result of the initial assumptions, the basic state is regarded as being in both hydrostatic and near-geostrophic balance. Sanders and Bosart (1985) refer to Ri_{sc} as the "Richardson Number for slantwise convection" and the relationship to the customary Richardson number can be shown to be $Ri_{sc} \equiv (\frac{\eta_g}{f})Ri$ (Seltzer et al. 1985; Jascourt et al. 1988; Byrd 1989). The right-hand-side of Eq. 2.8 can be rewritten in terms of pressure coordinates and simplified for this study by using both the equation of state and hydrostatic balance. From these modifications, Eq. 2.8 becomes:

$$Ri_{sc} = -(\frac{\eta_g}{f})(\frac{\Gamma_d}{\Gamma_m})\frac{RT}{p\theta_e}\frac{(\partial\theta_e/\partial p)}{(\partial\vec{V_g}/\partial p)^2}. \tag{2.9}$$

The ratio of slopes of shear to static stability as given in Eq. 2.8 (or some-

thing very similar) has been studied for a variety of precipitation structures by Bennetts and Hoskins (1979), Byrd (1989), Jascourt et al. (1988), and Seltzer et al. (1985) in order to investigate the importance of conditional symmetric instability or convective-symmetric instability. Overall, results tend to be mixed on the effectiveness of using this parameter with the purpose of discriminating instances of banding from nonbanding. Still, many of the features predicted by symmetric instability for banding, such as preferred orientation and spacing, compare well with observations. Furthermore, Byrd (1989) compared varying degrees of bandedness for winter season "overrunning" events in the southern plains of the United States and obtained some statistically significant differences. The better organized convection was correlated to environments often exhibiting greater instability and much lower means for the minimum values of Ri_{sc}. The category of small values of $Ri_{sc} > 1$, while not quite meeting instability status, are indicative of weak symmetric stability and have been shown to modulate the arrangement of preexisting gravitational circulations (e.g., Jascourt et al. 1988). It should be emphasized that all of these findings were produced with the application of analyzed winds as the approximation for geostrophy. Seltzer et al. (1985) rightly points out that this presumption violates the original linear theory since the empirical analysis deviates occasionally. The highly smoothed shear calculated from height fields would yield an increase in the Ri_{sc}, such that the CSI condition would be met in fewer cases overall (Byrd 1989). While the significance of including curvature in Eq. 2.8 is not going to be investigated, the effects of ageostrophic motions will be dealt with when considering the seldom utilized growth rate parameter.

2.3.2.4 Growth Rate Parameter

Narrow lines of clouds and precipitation are often found in the vicinity of

frontal systems. In order to explain the origin of these banded features, Bennetts and Hoskins (1979) revealed evidence through numerical modeling and observations that CSI might be an important mechanism. In their work on growth rates of slantwise convection, Bennetts and Hoskins (1979) obtained a doubling time (the time required for a convective element to achieve twice its current depth) for CSI on the order of a couple of hours. By assuming very moist conditions and taking into account possible motions around a hypothetical "tube" of air, they were able to formulate an expression for σ^2:

$$\sigma^2 = -\frac{q_w}{N_w^2} = -\frac{\frac{fg}{\theta_o}(\vartheta_g \cdot \nabla_3 \theta_w)}{\frac{g}{\theta_o}\frac{\partial \theta_w}{\partial z}}, \tag{2.10}$$

which represented the ratio of the wet-bulb potential vorticity (q_w) to the moist static stability (N_w^2). In the above expression for Eq. 2.10, θ_o represents a reference potential temperature (283 K, Bennetts and Sharp 1982), ϑ_g the three-dimensional geostrophic absolute vorticity vector, and ∇_3 the three-dimensional gradient vector in cartesian *(x,y,z)* coordinates. The units of σ^2 are inverse time (hours) squared, which will be expressed as h^{-2}, with positive (negative) values expected to indicate growth (decay) of a disturbance introduced into the prescribed environment.

Bennetts and Sharp (1982) directly applied Eq. 2.10 to the relevance of CSI and the occurrence of mesoscale frontal rainbands and found that the growth rate parameter was more useful in the prediction of banded precipitation than in identifying occasions where the rainfall was uniform. In particular, the structure of any frontal precipitation was considered to be almost certainly banded for $\sigma^2 \geq 0.2h^{-2}$. However, in their evaluation of 44 case studies by the United Kingdom radar network, Bennetts and Sharp (1982) found less successful performance

Table 2.1: Growth rate parameter σ^2 in unites of h^{-2} calculated from the rectangle forecast model. Reproduced from Bennetts and Sharp (1982).

	Non-banded precipitation predicted	Banded precipitation predicted				
	$\leq$ -0.1	-0.1 to 0.0	0.0 to 0.1	0.1 to 0.2	0.2 to 0.3	$>$ 0.3
Non-banded precipitation observed	4	5	4	1	0	0
Banded precipitation observed	2	7	11	3	3	4

Observations from the U.K. radar network.

of this parameter for values lower than the previous cited criterion (see Table 2.1). In situations where small positive or negative growth rates were obtained, discrimination of banded from non-banded precipitation was difficult, and approximately half of the events fell into either category. Since there are multiple causes for banded precipitation, the presence of banded structures does not necessarily mean that the cause is associated with the release of CSI and/or the destabilization of the background atmospheric environment. Rather, the existence of such mesoscale features can be justified through several other dynamical theories (e.g., Parsons and Hobbs 1983) which are not discussed in the current work. Thus, caution will be observed when correlating elongated patterns in the radar reflectivity against regions of high σ^2 values.

From a physical standpoint, a common belief might be that an unstable environment is likely to be encountered when the growth rate is positive. While there is some validity to this statement, it should be kept in mind that there is a remarkable difference between *stability* and its *predicted tendency*. Even though it might be expected that small perturbations will increase in magnitude within

the near future, the atmospheric response to vertical or slantwise displacements at that instant could very well be stable. The two pieces of information are independent; the former represents a prognostic quantity with the latter expressing something of a more diagnostic nature. In order to gain more instructive insight, Eq. 2.10 can be rewritten by expanding q_w into its vertical and horizontal components and utilizing the thermal wind relationship, as was done in Bennetts and Sharp (1982). Upon converting from height to pressure coordinates and eliminating density through the equation of state, an alternative form for the development of small amplitude disturbances is obtained:

$$\begin{array}{rcccc} \sigma^2 = & -f\eta_g & - & \dfrac{RT}{p\theta_o}\dfrac{\nabla_h\theta\cdot\nabla_h\theta_w}{\dfrac{\partial\theta_w}{\partial p}}, & \\ & (\mathbf{A}) & & (\mathbf{B}) & \end{array} \tag{2.11}$$

where ∇_h is the horizontal gradient vector. In the case of σ^2, an examination of Eq. 2.11 shows that several constituents contribute to the magnitude and sign of this prognostic variable. As a result, a particular value for the growth rate parameter will not be able to identify type(s) of instability, let alone assure that any is present. Consequently, for this purpose, Bennetts and Sharp (1982) advocate that an evaluation of the individual terms in Eq. 2.11 as well as an analysis of the corresponding synoptic pattern is required.

Bennetts and Sharp (1982) noted that conditions favorable for the development of CSI occur in regions where the two main right-hand-side terms in Eq. 2.11 are of similar magnitude. Still, this equation also predicts positive values for σ^2 in atmospheres characterized by other types of instability. For instance, an inertially unstable environment exists in situations when term (A) ≥ 0 and when term (A) $\gg$ term (B). Whereas term (A) is comprised of just an inertial contribution ($-f\eta_g$), term (B) can be separated into three more elements. The first of these (hereafter referred to as term B1), given by $\dfrac{RT}{p\theta_o}$, represents thermal

properties of the fluid since R, p (usually 700-hPa), and θ_o are all constants. As for the second contribution (hereafter referred to as term B2), $\nabla_h\theta \cdot \nabla_h\theta_w$ corresponds to the orientation of the moisture gradient with that of the temperature gradient. Alternatively, this is equivalent to the projection of one gradient onto the other, in which the term will be most effective when the two vectors are aligned. A result of zero, however, will be obtained when one is perpendicular to the other. Furthermore, the dot product stipulates that a positive (negative) sign for this particular contribution can only be obtained when the gradients point in the same (opposite) direction, such as when relatively warm air is coincident with moist (dry) air.

The last of the elements (hereafter referred to as term B3) represents the moist static stability of the environment ($\frac{\partial\theta_w}{\partial p}$) and generally plays a significant role in σ^2 as the atmosphere tends toward a convectively unstable state ($\frac{\partial\theta_w}{\partial p} \rightarrow 0$). Still, as was previously mentioned, it should also be made clear that upright convection released in an environment characterized purely by CI (i.e. B3 > 0) does not automatically guarantee a positive response for σ^2. In particular, a positive value for $\frac{\partial\theta_w}{\partial p}$ would signal the existence of convective instability sufficient for supporting vertical accelerations and upright convection, which will become the dominant mode due to its faster growth rate (e.g., Bennetts and Sharp 1982; Weismuller and Zubrick 1998). This is a condition outside the purview of σ^2 as this parameter predicts how rapidly a small-amplitude disturbance will grow in a conditional symmetrically unstable environment. In summary, growth or decay of a disturbance will be determined ultimately by considering all contributing terms and their associated signs and magnitudes collectively within Eq. 2.11.

2.3.3 Extension to 3D Theory

The development of frontal convection from symmetric instability has been

explained so far in terms of an non-evolving, inviscid state, under which the geostrophic shear is unidirectional. From this context, pure CSI would produce circulations oriented parallel to the thermal wind and be infinite in length. While this 2D context is a good first approximation to the characteristics of precipitation bands, modeling experiments (e.g., Jones and Thorpe 1992) and observations (e.g., Byrd 1989, Gray and Thorpe 2001, Seltzer et al. 1985, Wolfsberg et al. 1986) show that these structures are more complex and variations along the supposed independent axis do regularly occur. Despite the discouragement of Schultz and Schumacher (1999), the extension to the third dimension for assessing moist, slantwise convection has been rigorously considered by Jones and Thorpe (1992) and Gray and Thorpe (2001). Their purpose was to account for more realistic features, such as the confined, localized, and modifying aspects of CSI, something which the long established, simple framework devised by Bennetts and Hoskins (1979) and Emanuel (1983a,b) was not capable of rendering.

Investigations into the use of substituting the analyzed or total wind for the geostrophic value in various evaluations of CSI have been made by Seltzer et al. (1985), Byrd (1989), Gray and Thorpe (2001), and Clark et al. (2002), to name just a few. The idea is to treat the environmental flow regime as one in which a variety of balanced states (e.g., gradient, semigeostrophy) are entirely plausible for releasing slantwise convection. However, ambiguities exist as to when and what type of partition should be performed (Schultz and Schumacher 1999). Instead, the aim here is to ascertain the implications of neglecting departures from geostrophy within σ^2. This can be achieved by computing the ratio of the relative accelerations to that of the coriolis force, where the Rossby number (R_o) condition is approximated by the fraction of the ageostrophic influences to the entire (or extended) growth rates:

$$R_o \equiv \frac{dV/dt}{fV} = \frac{|\sigma^2_{ag}|}{|\sigma^2_{\dot{e}}|} \tag{2.12}$$

The extended formulation (σ_e^2) is identical to Eq. 2.10 except that ϑ_g is replaced by ϑ, the three dimensional observed absolute vorticity. By partitioning the flow into a geostrophic (σ^2) and ageostrophic (σ_{ag}^2) constituents, the modification to Eq. 2.10 yields:

$$\sigma_e^2 \equiv \sigma^2 + \sigma_{ag}^2 \tag{2.13}$$

where the first right-hand-side term has been derived already in Eq. 2.11 and $\sigma_{ag}^2 = -f\zeta_{ag} - \frac{(f[\partial V_{ag}/\partial p]) \cdot (\nabla\theta_w)}{(\partial\theta_w/\partial p)}$. The units for σ_e^2 are the same as σ^2 (in terms of h^{-2}) and results from Eq. 2.13 include the full three dimensional shear through MPV (or similarly EPV), such that all baroclinic and barotropic effects are accounted for within the atmosphere. Clark et al. (2002) applied a similar technique to diagnose the applicability of the geostrophic momentum approximation during a case study of banded snowfall. The criterion for validation required that the R_o number be much less than unity, where the ratio in their study was simply that of ageostrophic motion to the observed winds. Very small estimates of 0.3 to 0.5 were obtained near the snowbands, thus justifying the fact that the pressure gradient and coriolis forces were nearly in equilibrium. For the present case studies of convective snowfall, the appropriateness of following the customary 2D theory is determined by Eq. 2.12. It is a matter of conjecture that the alternate version of σ_e^2 should be more accurate in diagnosing stability tendencies in situations of strong curvature.

2.4 Sounding Characteristics

2.4.1 Traditional Stability Indices

Market et al. (2006) analyzed parameters derived from proximity soundings

associated with both thundering and non-thundering snowstorms. A select set of standard stability indices were tested to find specific metrics that would be statistically significant discriminators for the presence of lightning. Results showed that distinct differences existed in the 700-500hPa lapse rates, the most unstable level for lifting a parcel (MULPL), and to a slightly lesser degree the most unstable lifted index (MULI). In the case of the first, temperatures typically decreased with height more rapidly for thundersnow events ($6.5 \pm 1.3 K km^{-1}$) compared to non-thundersnow episodes ($5.5 \pm 0.7 K km^{-1}$) at a confidence level of $p = 0.03$. A substantial pressure difference in the MULPL was also obtained, such that the least resistance to vertical motion was located at a lower altitude when electrical activity occurred (mean of 671 hPa versus 632 hPa; $p = 0.01$). The corresponding MULI produced estimates of 1.3 ± 3.4 and 3.8 ± 3.3, respectively, these also being favorable indicators. The statistical test revealed a value of $p = 0.06$, thereby narrowly failing the accepted benchmark of significance. As a result, Market et al. (2006) repeatedly discovered the expected lowering of static stability in the presence of convective snow by utilizing simple temperature and moisture data from individual upper-air stations.

The three ideal stability parameters identified by Market et al. (2006) for the climatological period stretching from 1961-1990 are examined for more recent cases of thundersnow in the central United States. For the most part, CAPE has not been present in the subfreezing environment, especially when dealing with parcels lifted from a level close to the surface. This assessment has been reached by alternate sources from Curran and Pearson (1971) and Colman (1990a,b). Certain exceptions to this rule, however, have been offered; in their reassessment of the sounding profile in Curran and Pearson (1971), Market et al. (2006) noted the existence of elevated CI based upon the most unstable (MU) parcel lifted from 800 hPa. From this level, on average, a benefit of $55 J kg^{-1}$ of CAPE was available for the thundersnow environment (Fig. 2.18). In their own composite, Market et

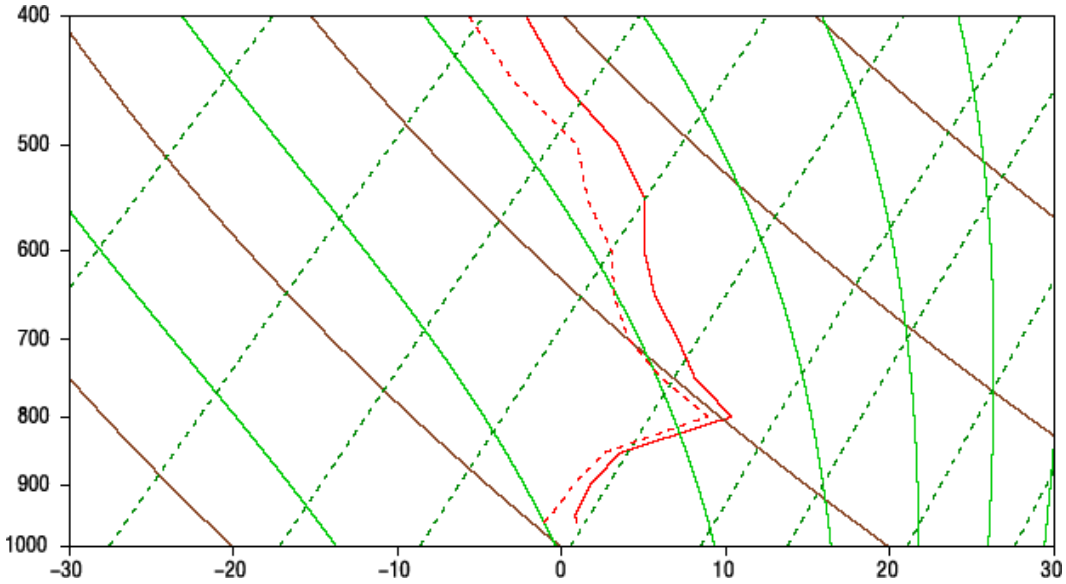

Figure 2.18: Reanalyzed skew-T log$p$ diagram of sounding data taken from Curran and Pearson (1971). Reproduced from Market et al. (2006).

al. (2006) reached an almost identical result ($54 Jkg^{-1}$) from an elevated source by making a small, reasonable adjustment to the feature-preserving approach proposed by Brown (1993). Thus, the MUCAPE will also be calculated and included in the tabular information at the convective initiation sites. Finally, the more novel assessment in this study will be a mesoscale spatial diagnosis of the stability indices, something that can be realized by fine-scale gridded data from a numerical weather model.

2.4.2 Bulk Physics of Lightning

A review of cloud physics and microscale processes for the development of thunderstorms accompanying snowfall can be found in Elkins (1987). Similarly, MacGorman and Rust (1998, pp. 286-292) also cover the essentials of cloud electrification of winter thunderstorms. The fundamental processes in the production of precipitation in such a situation are related to the collective action

of diffusional growth, aggregation, and accretion. The conversion of water vapor into the ice phase, however, is often slow and generally requires temperatures to be significantly below freezing. As a result, most of the precipitation formed in the cloud was presumed to be the result of the latter two methods. Specifically, the mechanism of accretion or riming, whereby supercooled droplets are captured by ice crystals, is found to be important in the relatively warmer, lowest levels of the atmosphere. As for the other process, the collision and clumping together of these ice crystals was also taken into consideration, with the composition of the typical aggregate snowflake often consisting of numerous dendrites, needles, and other various shapes.

In terms of electrical discharges, the presence of riming in the clouds has also been widely viewed as determining whether sufficient charge separation would develop. The standard dipole configuration (positive polarity above negative center) for thunderstorms has been accepted to occur year round in some instances (MacGorman and Rust 1998), the key charge carriers being ice crystals and relatively heavier graupel. Still, with weaker updrafts in the mixed-phase part of the cloud occurring in the winter, the shallower depth to the cloud means that the greatest concentration for supercooled droplets would commonly be located at a lower elevation (e.g., Elkins 1987). From experiments conducted by Takahashi (1978), the electric sign of graupel that forms is highly dependent on the cloud water content and temperature of the ambient environment (Fig. 2.19). Given the charge reversal temperature of -10^0C for modest amounts of moisture ($1 - 2gm^{-3}$) in Fig. 2.19, an additional lower positive polarity might result from riming occurring at warmer temperatures than what might be observed in stronger cells in the spring or summertime (e.g., Elkins 1987, Takahashi 1978). Consequently, another paradigm would allow for a tripole arrangement to the charge centers during the cold-season, such that positive cloud-to-ground flashes might result.

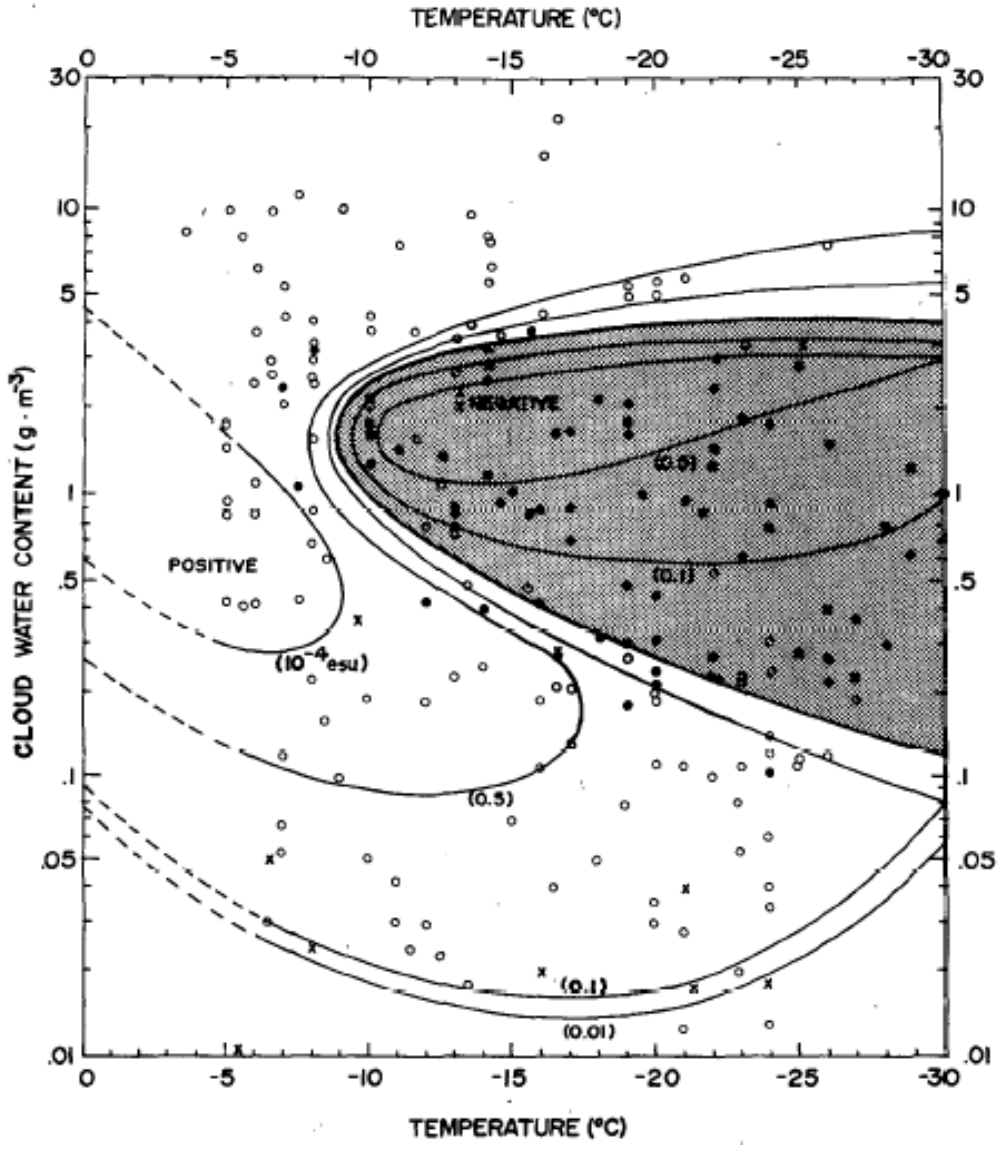

Figure 2.19: Electrification of rime with respect to temperature and cloud water content. Open circles show positive charge, solid circles negative charge, and crosses represent uncharged cases. The electric charge of rime per ice crystal collision is shown in units of $10^{-4}esu$. Reproduced from Takahashi (1978).

An in-depth, microphysics investigation of lightning generation within snowstorms is beyond the scope of the dissertation. Nevertheless, the approximate properties required for cloud electrification can be supplied by some bulk quantities that can be retrieved from standard measured variables in radiosondes or numerical weather models. Michimoto (1993) observed that the production of lightning discharges within convective clouds is influenced by the altitude of the -10^0C level above the surface; the height should be at least 1.4 km above ground level (with an altitude of 1.8 km being ideal) for precipitation particles to become electrified and discharges to occur. Another criteria that has been specified (Bright et al. 2005; Van Den Broeke et al. 2005) is the temperature being warmer than -10^0C at the MULPL for an adequate low-level supply of moisture in the form of supercooled cloud water into the updraft. Both of these parameters have been successfully applied by Market et al. (2006) and Smith (2006) to delineate ordinary snowstorms from those that are accompanied by thunderstorms.

In this study, an alternative means of examining flash data and the type of polarity is explored through Eq. 2.9 and the combined affects of vertical wind shear and moist static stability. The correlation between the fraction of positive CG lightning and the vertical wind shear was investigated by Brook et al. (1982) in several winter thunderstorms in Japan and was found to be strongly proportional with a correlation coefficient of 0.95. From their least squares fit line, the data suggested a threshold value of $1.5ms^{-1}km^{-1}$, below which all the flashes would bring just negative charge down to the ground (Fig. 2.20). Since the normal bipolar configuration was observed, it was proposed that the increase in the strength of the flow above the surface allowed for a substantial horizontal displacement between the charge centers to facilitate the discharge of a positive streamer from high within the cloud. Thus, the hope is to find other benchmarks for describing properties of lightning from a simple measure of both momentum

and thermodynamic data.

In summary, the cursory treatment of CG flash attributes in freezing precipitation systems was dealt with via the means of a bulk parameter derived from the RUC-2 model gridded data. In order to accomplish the task at hand, the Ri_{sc} diagnostic was selected as it realistically coupled the influences of both inertial and gravitational processes sometimes present in cold-season situations. This technique served to discern whether or not the updated version of the Richardson number might be a suitable proxy in predicting the severity and type of lightning activity. In effect, any relationship was established by utilizing a qualitative analysis as well as linear correlation coefficients.

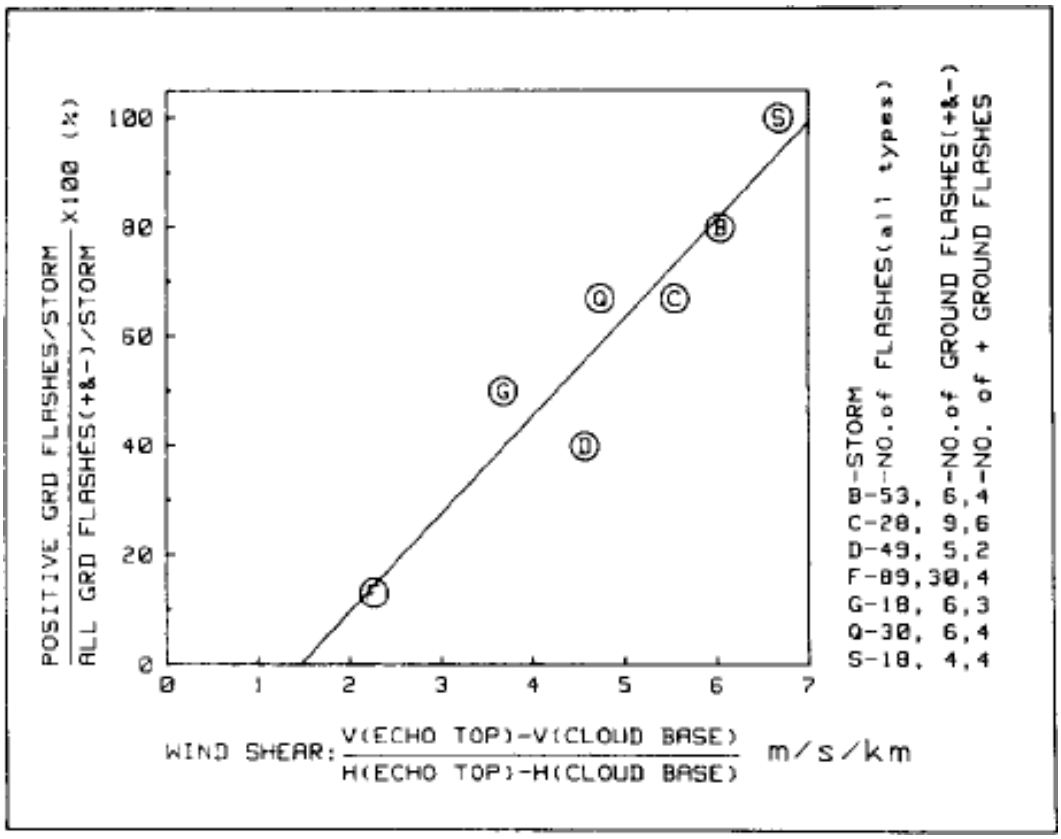

Figure 2.20: Plot of the fraction of positive strokes per storm versus wind shear in the cloud layer. The radar echo top was used to define the upper limit of the cloud. The data used in this plot include all the storms studied. It was possible to obtain stroke polarity from the field change records even if the data were unsuitable for use in obtaining charge magnitude and position. The straight line represents a least squares fit with a correlation coefficient of 0.95. Reproduced from Brook et al. (1982).

Chapter 3

Data and Methodology

3.1 Data

Traditional surface reports, individual/composite radar images, and cloud-to-ground (CG) lightning flashes from the National Lightning Detection Network (NLDN) served to provide the majority of the observational data network for the research project. A thorough analysis of elevated stability characteristics down to the mesoscale, however, required a relatively dense but still realistic portrayal of the atmospheric state above the surface. Gridded model fields from the 40-km Rapid Update Cycle (RUC-2; Benjamin et al. 1998) served to fulfill a substantial portion of this objective as this platform has been proven to provide high-quality analyses and short range forecasts (Benjamin et al. 2004 a,b). From the hourly initialization, the RUC-2 grids contain the fundamental variables of geopotential height, temperature, dewpoint, wind speed, and wind direction. From these measurements, calculations of derived parameters at each grid point could then be determined. Ultimately, the criterion for lightning generation in winter storms can be more firmly ascertained from employing a variety of techniques in the examination, the selection of which will be explained later in this chapter.

3.1.1 Data Sources and Format

Most meteorological information is available for archiving within the Atmospheric Science Program by means of the Unidata Local Data Manager (LDM) feed into the computer cluster in the Weather and Visualization Lab. Data are either saved out in ASCII or in the GEneral Meteorological PAcKage (GEMPAK; desJardins et al. 1991) format. Several internet sites were relied upon in order to retrieve either missing data or information not originally saved. These sources come mainly from the National Climatic Data Center, such as the National Operational Model Archive & Distribution System (NOMADS; `http://nomads.ncdc.noaa.gov/`) and the Hierarchical Data Storage System (HDSS) Access System (`http://hurricane.ncdc.noaa.gov/pls/plhas/has.dsselect`) for radar level II reflectivity patterns. The WSR-88D Algorithm Testing and Display System (WATADS; WATADS 2000) and the Warning Decision Support System - Integrated Information (WDSS-II; Lakshmanan et al. 2007) were relied upon in order to display this type of radar data. Archived numerical weather model data (RUC-2) was also requested through the Atmospheric Radiation Measurement (ARM) port from the Department of Energy.

3.2 Rapid Update Cycle

3.2.1 Assimilation and Domain

The RUC is one of a suite of weather models running operationally at the National Centers for Environmental Prediction (NCEP) since 1994 (Benjamin et al. 2004b). From its inception, the goal was to provide 3-D high-resolution analyses and short-range (12 h) forecasts continuously updated with mesoscale observations, beyond what numerical weather prediction systems traditionally had been implementing up to that point. In the original design, RUC-1 (60

km) output was produced from a forward intermittent assimilation cycle every 3 h utilizing the previous 3-h forecast as a background to represent a new approximation of atmospheric fields. Through this approach, the 3-D multivariate forecast error field (i.e., analysis increment) is generated by the residuals resulting from the difference between observations and forecast variables. The new analysis for the RUC is then acquired by adding the analysis increment to the given "background" estimate.

Since the first major upgrade to the RUC in 1998, this cycling process has increased to be hourly (Fig. 3.1), the most frequent of all forecast models in use at NCEP (Benjamin et al. 1998, Benjamin et al. 2004b). Multimonth verification statistics were subsequently performed to check the associated accuracy in predicting weather phenomena from the assimilation of the most recent observations. These results (Benjamin et al. 2004b) show that the RUC nowcasts provided an overall improvement over persistence and longer-range forecasts valid at the same time. Consequently, interpretation of numerical weather guidance from the RUC can be tailor-made to deal with short-lead time issues, such as year-round severe weather (convective storms, winter precipitation) and aviation (clear air turbulence, downbursts, icing, low ceiling and visibility) hazards.

The horizontal domain (151 x 113 grid points; Fig. 3.2) of the RUC-2 has higher resolution (40 km) and extends farther in all directions, covering 50% more area of the combined North American continent and surrounding oceans, compared to its predecessor the RUC-1 (Benjamin et al. 1998). The mesh is rectangular on a Lambert conformal projection and the exact grid length is 40.635 km at 35^o N, but varies latitudinally from this value to 33 km at the northern boundary due to the map-scale factor. The shapes of coasts, lakes, and other topographic features are better defined from the increase in resolution. In addition, unlike the RUC-1, the "surface envelope" topography is implemented to determine surface elevation. As a result, this upgrade allows for better depiction

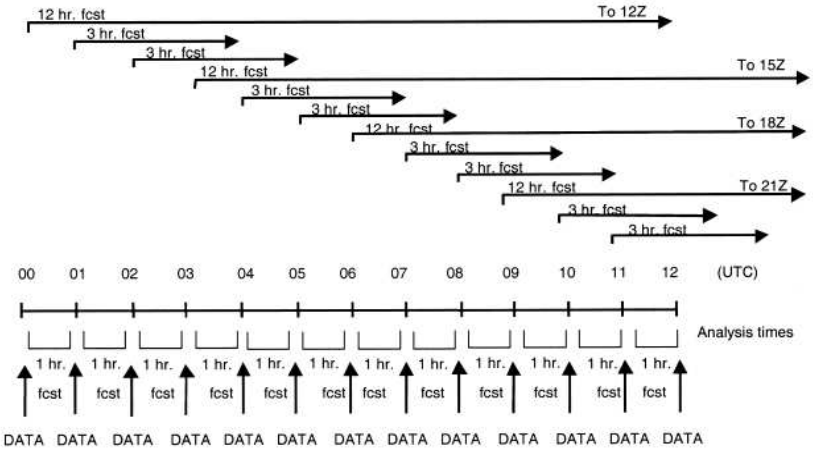

Figure 3.1: Schematic of 1-h Rapid Update Cycle operational configuration at NCEP in early 2003. Reproduced from Benjamin et al. (2004b).

of orographically induced circulations (e.g., mountain waves, sea breezes). Finally, the skill in forecasts from this regional mesoscale model was bolstered by changes to the data input along the boundaries of the domain. To be more compatible with the RUC, the lateral boundary conditions were switched from being specified by the Nested Grid Model (NGM) at 6-h intervals to that of the North American Mesoscale (NAM)/Eta Model (Black 1994), which is interpolated to the RUC-2 grid from the more frequent 3-h output.

3.2.2 Data Types

In addition to traditional surface and rawinsonde reports, the RUC-2 is capa-

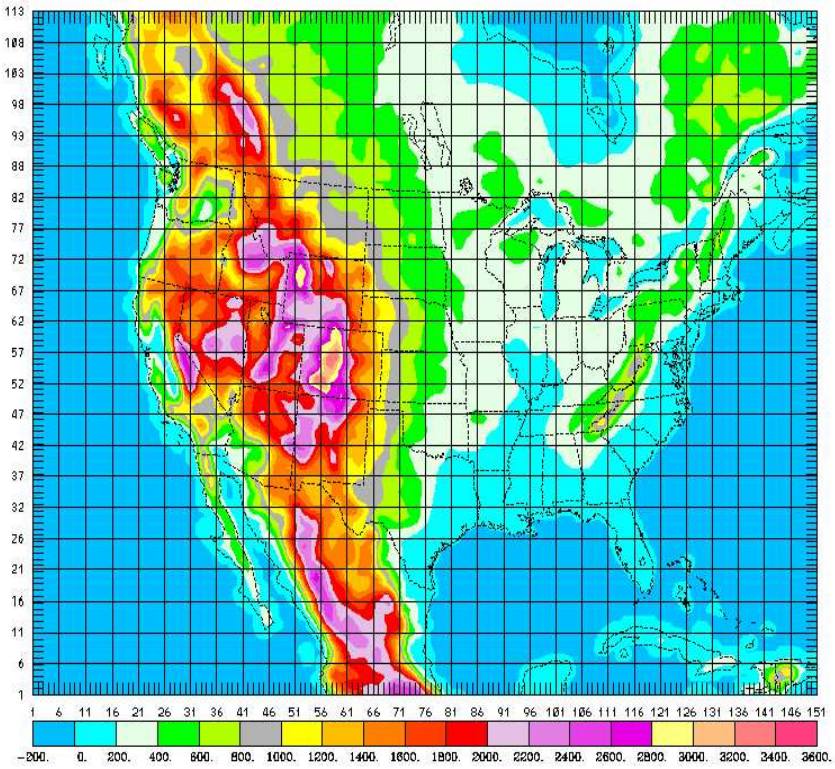

Figure 3.2: RUC-2 (40-km) domain and terrain elevation (m). Reproduced from Benjamin et al. (1998).

ble of incorporating a wide variety of other asynoptic observations, as described in Benjamin et al. (1998). These sources include measurements from buoys, high-resolution commercial aircraft reports (ascending and descending), profiler winds, velocity-azimuth display (VAD) wind profiles derived from radar, and reconnaissance dropwindsonde data. In addition, cloud drift winds estimated from satellites (Geostationary Observational Environmental Satellite (GOES)), integrated precipitable water retrievals from the GOES and the Special Sensor Microwave Imager (SSM/I), and virtual temperatures from the Radio Acoustic Sounding System (RASS) are utilized. Despite their irregular coverage in space and time, the availability of these data networks, often down to an hour, favorably matches to the high frequency assimilation cycle in the RUC-2, thereby helping to provide improved short-range forecasts.

3.2.3 Vertical Coordinate and Numerics

The other unique feature of the RUC-2 is its application of a hybrid isentropic-sigma ($\theta - \sigma$) coordinate set within a generalized vertical coordinate (s) system. For each grid column and dynamical time step, a two-step criteria, described in Benjamin et al. (2004a), is applied to precisely determine whether the grid point pressure is prescribed to be either θ or σ. Working from the ground up, the troposphere is defined more by the use of σ levels in warmer areas and less so within colder regions. Still, a substantial portion of the lower and middle troposphere is identified by the use of potential temperatures. In particular, the native grid has 40 vertical levels extending a greater depth into the lower stratosphere compared to the original version. Starting at the lower boundary of 224K and spanning to an upper limit of 450K, the minimum spacing between isentropes is 2K (Benjamin et al. 1998). The unified analysis framework can also be adapted to permit solutions either from optimal interpolation or 3-D variational tech-

niques, the latter operational as of 2003. The exact steps in the RUC-2 analysis procedure are given in Benjamin et al. (1998). From this framework, observations are acquired, processed routinely, with suspicious observations flagged via a quality control method of "buddy check" between neighboring observations. As for other numerics, the hydrostatic, primitive equations utilized are prescribed for the generalized vertical coordinate s, upon which horizontal and temporal derivatives are evaluated. The grid is staggered in the horizontal (Arakawa C), but non-staggered in the vertical. The Arakawa C option employed acts to improve numerical accuracy by offsetting the u and v wind components from the mass points (Benjamin et al. 1998). Consult Benjamin et al. (2004) for an updated version of the set of governing equations and how they are solved within the RUC.

The benefits in using the hybrid selection of $\sigma - \theta$ in the RUC include the capability of having sharp resolution of atmospheric variables near fronts and the tropopause while eliminating the problem of constant or decreasing entropy by transitioning to terrain-following surfaces within the planetary boundary layer (e.g., Benjamin et al. 2004a). In addition, processes are considered to be conserved to a first approximation as a substantial portion of the flow is captured on sloping adiabats. With vertical motion perpendicular to the largely θ coordinates being minimized, there is a favorable reduction in artificial numerical dispersion as vertical advection is essentially nonexistent (e.g., Benjamin et al. 2004a). By conducting experiments using case studies in different seasons and comparing against the employment of just σ surfaces, Benjamin et al. (2004a) showed that this transport across coordinates is lowered considerably for the $\theta - \sigma$ counterpart whether or not diabatic physics are included. Still, it should be addressed that one of the main problems with the RUC is the handling of the interface between the coordinates. Despite the application of a "cushion" function to alleviate discontinuities in the slopes of θ and σ, inaccuracies in vertical mixing can still be

pronounced in a deep, daytime boundary layer scenario.

3.2.4 Physical Parametrizations

The effects of subgrid scale processes are accounted for in the RUC by use of physical parametrizations common to most regional mesoscale models (Benjamin et al. 2004a). More realistic upgrades to the algorithms initially implemented are summarized here. The explicit mixed-phase bulk cloud microphysics package is the "level 4" scheme of Reisner et al. (1998) applied in the fifth-generation Pennsylvania State University-National Center for Atmospheric Research (PSU-NCAR) Mesoscale Model (MM5; Grell et al. 1994). Forecasts of clouds, icing, and precipitation, previously inferred by supersaturation in the relative humidity fields, are improved by including the advection of mixing ratios of five different hydrometeors: cloud water, rain water, snow, ice crystals, and graupel. Spin-up problems in the RUC-2 are reduced as moisture variables are cycled each hour, meaning that there are initial cloud fields for each run (Benjamin et al. 1998). The influence of convective activity on large-scale variables, such as heat, moisture, and momentum, is dealt with through the Grell (1993) convective parametrization scheme. This procedure is unique in its inclusion of downdrafts, thereby producing much finer details in RUC-2 warm season precipitation patterns over other similar mesoscale models which do not incorporate such realistic features (e.g., Betts-Miller-Janjic in the NAM/Eta model; Benjamin et al. 1998).

Other changes, found in Benjamin et al. (1998), include an overhaul in the treatment of atmospheric radiation in the RUC, for which no consideration was given prior to 1998. For this reason, the MM5 package (Dudhia 1989, Grell et al. 1994) is utilized and modified to also account for attenuation and scattering by all hydrometeor types. This radiation parametrization is a broadband design with separate components for longwave and shortwave radiation. The RUC-1

simulated turbulent mixing at all levels through the level 2 scheme of Mellor and Yamada (1982). Better representations of boundary fluxes are obtained in the 40-km version, however, from using explicit forecasts of turbulent kinetic energy in the equations derived by Burk and Thompson (level 3; 1989). In addition, surface processes in RUC-1 were crudely illustrated using a single surface slab with constant soil moisture availability in the first installment of the model. Low-level atmospheric conditions are more accurately predicted in the RUC-2 by the more sophisticated use of a 6-layer soil/vegetation/snow component. In this complex procedure, the heat and moisture transfer equations are solved at 6 subsurface levels (soil) at each grid point in conjunction with the ground surface, with a complex design also attributed to snowfall accumulations and melting within the model (Benjamin et al. 1998). From this and other physics details not fully explained here, Benjamin et al. (1998) concluded that: "the RUC-2 surface package provides surface temperature and dewpoint forecasts that are clearly superior to those of the RUC-1 due to improved surface heat and moisture fluxes."

3.3 Methodology - Convective Snow

3.3.1 Selection criterion for thundersnow case studies

METAR and SPECI observations from surface weather stations across the United States were scanned routinely during the winter months (October-April) of 2003-04 and 2004-05. In order to document the occurrence of thundersnow during this time period, reports of thunder with various intensities of snowfall (SN) were counted, such that the lightning was either observed near the surface station (TSSN or VCTSSN) or at some distance away (LTG DSNT). From this dataset, only events associated with an extratropical cyclone (ETC) occurring in the region between the Rocky and Appalachian Mountain ranges (i.e., the central part of the country, see Fig. 3.3 as an example) were investigated further.

Following the methodology applied in Market et al. (2002), twenty-nine separate case studies with corresponding initiation sites were identified by employing an appropriate temporal and spatial criterion for mesoscale processes. Specifically, the identification of distinct events was accomplished by checking whether either of the two following conditions was met: the separation distance at *different* stations for simultaneous thundersnow reports had to be more than 1100 km or more than 6 hours had to pass with consecutive reports at the *same* station. This procedure was selected by Market et al. (2002) as a reasonable means of discriminating TSSN episodes given the sufficiently unique characteristics of the individual flow regimes.

3.3.2 Lightning flashes from the NLDN

In order to further substantiate the existence of thundersnow in these case studies, cloud-to-ground (CG) lightning flash data were obtained from the National Lightning Detection Network (NLDN). While a large portion of the lightning that results from cold season, elevated convection is intracloud, Smith et al. (2005a) utilized the NLDN as a means to provide additional, solid evidence that lightning activity occurred within half of the archived snowstorms from the 2003-04 season. Furthermore, a more accurate identification of initiation was determined at times by plotting CG-lightning flashes from the NLDN in conjunction with surface weather conditions from nearby METARs, despite the fact that a report of thundersnow was lacking from the individual observations. It is worth noting that the change-over to automated observing stations in the mid-1990s made thundersnow observations less reliable and likely reduced the detection rate. The current methodology helped to obtain additional precision in determining the location and onset of convective snowfall, something which Smith et al. (2005a) emphasized would be important to operational forecasters

and their capacity to notify the general public in a timely manner of approaching hazardous weather. By applying this evaluation scheme to the current work, results from this examination will be specifically restricted to the seventeen selected thundersnow cases, these being episodes where lightning flashes could be verified from the NLDN (one event was left out due to the relatively low amount of moisture present in the sounding profile since the growth rates would require near-saturated conditions).

CG flashes from the NLDN were chosen near convective initiation to satisfy the purpose of the microphysics section in the investigation. Of all the lightning present in the convective events, a total count of 48 flashes were identified for inclusion, 38 (10) of which were of negative (positive) polarity (Fig. 3.3). Along with its justification, the selection process adheres to the following criteria:

1. From the 17 convective snow episodes, the lightning report(s) sometimes occurred at some distance away from the surface stations reporting TSSN and often did not occur at exactly when the latest analyses from the RUC-2 model were issued. Since the purpose of the study was to concentrate on the associated mesoscale aspects near the first instance of activity, the CG flashes should occur within 30 minutes of the nearest top of the hour (e.g., 0335-0430 for 0400 UTC) and at least within 100 km radius of the initiation site. From these specifications, this allowed for multiple observations from the NLDN, which were relatively close proximity in time and/or space, to be included in the evaluation.

2. Near surface temperatures had to be $< 36^{o}$F from the 2-m RUC-2 analysis and standard observation reports, this threshold being approximately similar to that in Heppner (1992) and Market et al. (2002). Precipitation is determined to be present and in the form of snow, which can be deduced from a combination of METARs and radar. These particular re-

quirements come straight from Smith et al. (2005a), in which their TSSN events represent a subset of the ones identified currently.

3. The RUC-2 850-700-hPa partial thickness values must be < 1560 m at the location for each CG flash, corresponding to an average temperature $< +1^{o}$C for that upper-level layer. Heppner (1992) examined the effectiveness of precipitation-type forecasts from surface and radiosonde data at two cities (Pittsburgh, PA and Albany, NY) during three winters (1989-92). Among the variety of parameters utilized as discriminators in that study, the most persuasive and vital evidence was supported by critical values for the depth of lower-tropospheric layers (1000-850hPa and 850-700hPa). Snow was rarely observed to occur with 850-700-hPa thicknesses > 1550 m. In higher terrain situations, such as in the western plains, greater values for the critical line between frozen and liquid precipitation would be expected. Furthermore, in such regions, usage of the 1000-850-hPa layer would not be a practical factor to consider since it would reside below ground level. Still, it is possible and acknowledged that some melting of the snow crystals near the initiation site could be present in a few events. This is supported by an inspection of 850-hPa temperatures by themselves. Although the average for all CG flashes was only -1.1^{o}C, the large standard deviation (2.7^{o}C) allowed for substantial above freezing conditions. However, it is interesting to note that the inversion from the composite sounding in Curran and Pearson (1971) also had a pronounced warm bias (Fig. 2.18), much more so than the mean profile in the more recent collection of thundersnow events here (Fig. 3.4).

3.3.3 Tendency of σ^2

Instantaneous changes in σ^2 with respect to time have never been explored before. This prognostic quantity represents stability tendency rates and a math-

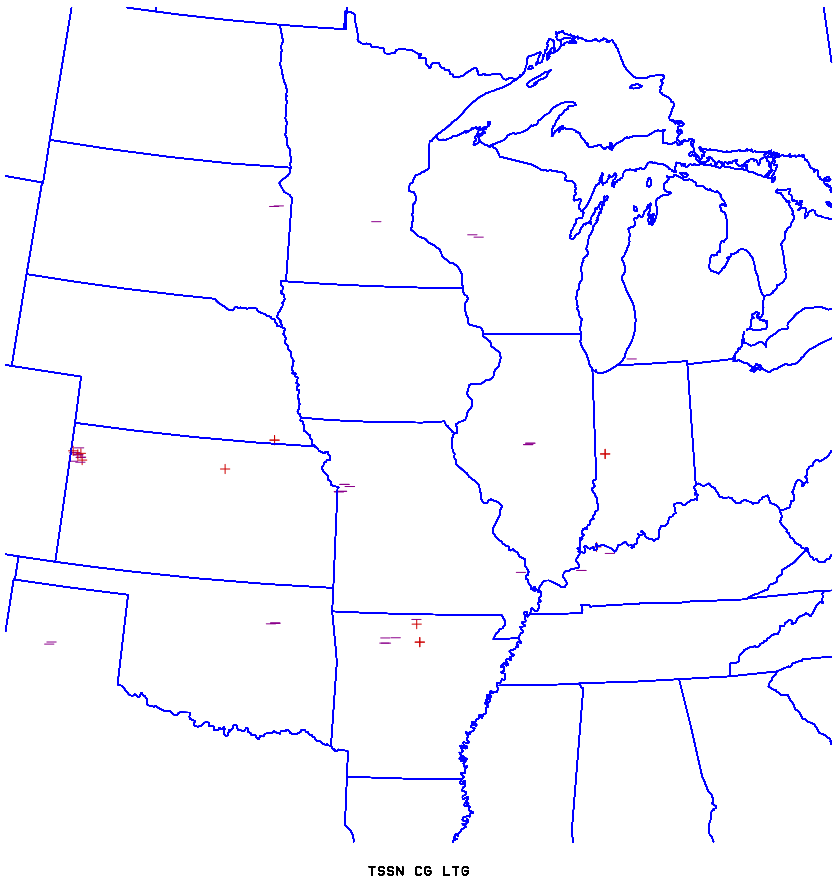

Figure 3.3: CG lightning flashes selected for use near the time of TSSN initiation in all 17 events. The criteria applied for identifying the 48 flashes (38 negative, 10 positive) is explained within the text.

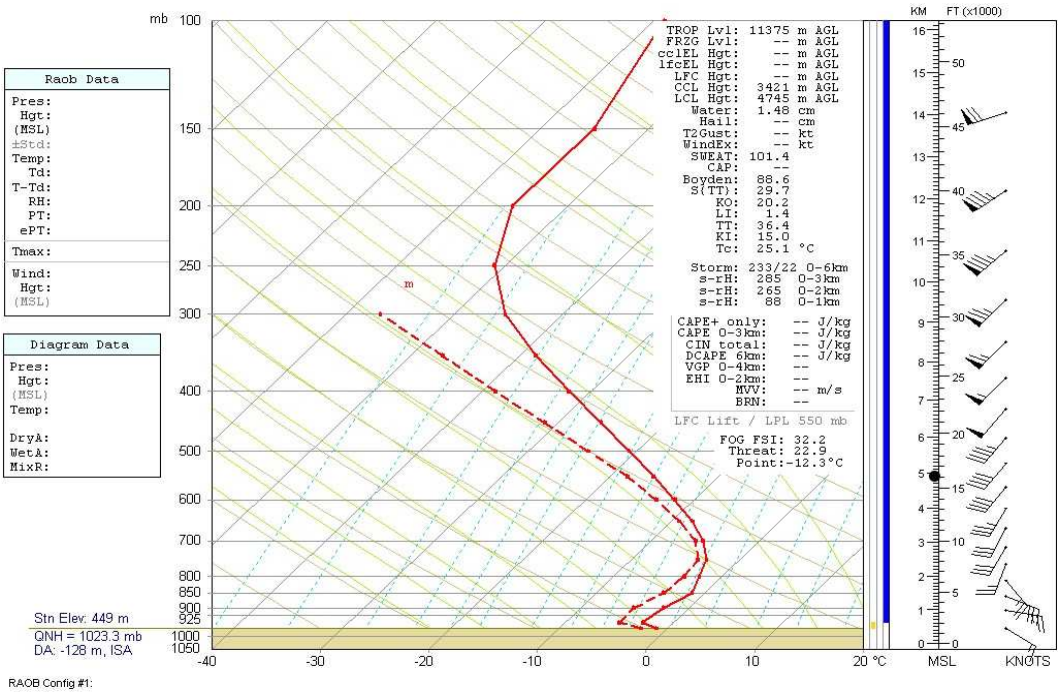

Figure 3.4: Composite sounding shows simple average temperature (solid) and dew point (dashed) from thundersnow events during the 2003-04 and 2004-05 winter seasons. The mean wind speed is plotted on the median wind direction shaft. This method of construction follows that of Market et al. (2006). The upper-air data (every 50 hPa) and surface information (pressure, 2-m temperature, 2-m dew point, 10-m wind direction, and 10-m wind speed) were derived from the RUC-2 model.

ematical derivation can be developed by taking $\frac{\partial}{\partial t}$ of Eq. 2.11:

$$\frac{\partial(\sigma^2)}{\partial t} \equiv \frac{\partial}{\partial t}[-f\eta_g - \frac{RT}{p\theta_o}\frac{\nabla_h\theta \cdot \nabla_h\theta_w}{\frac{\partial\theta_w}{\partial p}}], \tag{3.1}$$

which upon applying the product rule several times to Eq. 3.1 leads to:

$$\begin{aligned}\frac{\partial(\sigma^2)}{\partial t} = \quad & \underset{(\mathbf{C})}{-f\frac{\partial\zeta_g}{\partial t}} \quad - \quad \underset{(\mathbf{D})}{[\frac{(RT/p\theta_o)}{(\partial\theta_w/\partial p)}(\frac{\partial}{\partial t}[\nabla_h\theta]\cdot[\nabla_h\theta_w] + [\nabla_h\theta]\cdot\frac{\partial}{\partial t}[\nabla_h\theta_w])]} \\ & \underset{(\mathbf{E})}{-[\frac{\nabla_h\theta\cdot\nabla_h\theta_w}{\frac{\partial\theta_w}{\partial p}}\frac{R}{p\theta_o}\frac{\partial T}{\partial t}]} \quad + \quad \underset{(\mathbf{F})}{[\frac{(RT/p\theta_o)(\nabla_h\theta\cdot\nabla_h\theta_w)(\frac{\partial}{\partial t}\frac{\partial\theta_w}{\partial p})}{(\frac{\partial\theta_w}{\partial p})^2}]}.\end{aligned} \tag{3.2}$$

Units for $\frac{\partial(\sigma^2)}{\partial t}$ are in terms of h^{-3}. Nearly geostrophic conditions still are the rule for the basic state since that was the theory originally associated with development of σ^2 in Bennetts and Hoskins (1979). Positive values for Eq. 3.2 correspond to an atmosphere becoming more destabilized while negative values correlate to an environment tending toward greater stabilization. Temporal changes in geostrophic relative vorticity (ζ_g), dry/moist frontogenesis ($\frac{\partial}{\partial t}[\nabla_h\theta], \frac{\partial}{\partial t}[\nabla_h\theta_w]$, temperature tendencies, and moist static stability tendencies are represented by terms (C), (D), (E), and (F), respectively. Furthermore, each of these represent dynamic and thermodynamic mechanisms within the atmosphere responsible for altering the growth rates. Thus, Eq. 3.2 emphasizes that properties of stability are closely linked to the same forcing mechanisms which encourage vertical motions (e.g., frontogenesis), thereby providing more solid proof of the synergistic relationship between the ingredients for thunderstorms (e.g., Schultz and Schumacher 1999).

Anticipating increases in σ^2 at a specific pressure level can be deduced from these individual contributions, where the first is the simplest to identify; favorable responses for (C) occur when the flow is becoming more anticyclonic. The other three components are more complicated but some reasonable assumptions

can be utilized to simplify the problem at hand. For example, the thermal and moisture gradients are usually oriented in the same direction since relatively warm, moist (cool,dry) air tends to be collocated. Furthermore, conditions for CSI over CI are more likely to be found as convectively stable regimes exist over large spatial domains. Based off of these specific restrictions, positive results for the left-hand-side of Eq. 3.2 can be associated with frontogenesis, warming of the environment, and/or a lessening of the moist static stability. The final sign, however, would also be dependent on the relative magnitudes of (C), (D), (E), and (F). Nevertheless, departures to the set of ideal approximations made here do occur and would require a more quantitative analysis of each term to get an idea of the atmospheric fields and associated changes to σ^2.

3.3.4 Analysis Routine

Each of the right-hand-side terms in Eqns. 2.1, 2.7, 2.9, 2.11, 3.2, and 2.13 were calculated utilizing GEMPAK (desJardins et al. 1991) software (version 5.7.2p2), with the initial analysis from the RUC-2 model grid providing the necessary input data. Calculations were performed every 50 hPa in the model from 950 hPa to 550 hPa and second-order finite differencing was utilized to evaluate vertical derivatives. Temporal derivatives in Eq. 3.2 were solved through the discrete process of backward differencing, whereby the prior time frame relied upon the previous hourly RUC-2 analysis in each case study. This approach does produce some noise in the analyses of σ^2, as expected (Barnes et al. 1996). Comparison to results of 2.11 from a filtered, 80-km RUC file from the same time produce nearly identical (although smoother) patterns. Still, application of the geostrophic wind at such a fine resolution is most likely not appropriate. Thus, a simple Gaussian filter was applied to significantly dampen artificial structures at the shortest wavelengths in the raw fields while still retaining true small-scale fea-

tures. The degree of filtering chosen acted to substantially decrease wave amplitude for length scales below 240 km, thereby mostly eliminating information that would be considered noise in an atmosphere that is in approximate geostrophic balance. Alternatively, this approach was not needed for ageostrophic processes, whether the representation was explicit or the use of the analyzed wind denoted an implicit presence. Thus, as an illustration, the filter was appropriate for σ^2 but not for σ_{ag}^2 in Eq. 2.13.

The RUC-2 numerical model (Benjamin et al. 1998) is unique in its frequent hourly assimilation of the most recent observations, thus providing valuable short-range forecasts and ensuring better confidence when monitoring current conditions. This advantage is important in examining and noting short-term trends in stability characteristics of thundersnow events, especially considering that such phenomena have horizontal dimensions in the meso-β scale range and typically exhibit a timescale on the order of just a few hours (e.g., Emanuel 1986; Market et al. 2002). Moreover, Curran and Pearson (1971) noted that traditional indices would often not produce accurate estimates of instability at the time of the proximity sounding given the fact that convection has already begun. As a result, this study not only investigates the time of initiation, but also takes into account preconditioning of the environment three hours beforehand.

In order to remain consistent with Bennetts and Sharp (1982), calculations of σ^2 were initially performed at 700 hPa and considered significant only in regions where the relative humidity (RH) exceeded 80%. This latter criterion was applied to ensure sufficient moisture in the atmosphere, a necessary condition, as mentioned earlier, in diagnosing the presence of CI or CSI. Indeed, a standard RH of 80% represents a saturated condition with respect to ice for temperatures that support dendrite growth (8.6^{o}F to -0.4^oF). However, given the natural variability in synoptic conditions which exist from one case study to the next, evaluating the likelihood of wintertime convection from one set pressure level is

not the best approach. For this reason, an alternative technique was pursued by obtaining separate estimates of σ^2 at the level with the highest significant growth rates (LHSGR) present, which ordinarily was different than 700 hPa. In this way, it is believed that a more plausible measure of the source and nature of elevated thunderstorms would generally be obtained at the elevation experiencing the least resistance to destabilization. One of the criteria for the LHSGR was that the assessment did not begin until above 850 hPa in order to make certain that the analysis was above ground level, as well as avoid spurious results near the surface. In the rare situation where two different levels have the same value for σ^2, the lowest value for EPV is utilized as a discriminator. The use of the word *significant* in the acronym was the final crucial factor, and again meant that ample moisture had to be present for the parcel instability to be realized. The pressure level for the LHSGR three hours before and at the time of initiation is documented.

3.3.5 Cross-Sections

For the usual $M_g - \theta_e$ relationship, as described in Snook (1992) and Schultz and Schumacher (1999), a saturated parcel would experience an unstable slantwise path, toward the colder air, if the displacement is between the M_g and the more steep θ_e surfaces. Following Moore and Lambert (1993), a cross-section is constructed at the seventeen times of TSSN initiation by first identifying the orientation of the baroclinic zone from the 850-300-hPa thickness field. Further assessment of CSI is only attempted if the three assumptions stated by Schultz and Schumacher (1999) are satisfied (as summarized in section 2.3.2.1), something which generally is ascertained subjectively. Although the effects of curvature should be minimized, most often their influence is present to some degree in all of the RUC-2 analyses generated. Nevertheless, the ageostrophic

component of the flow is judged to be sufficiently small in a few instances from the configuration of the thickness contours near the site of convective snow development. In these particular case studies, the endpoints for the cross-section are subsequently taken across the midtropospheric frontal zone, such that the area of interest is approximately the midpoint. As a result, values of M_g, θ_e, and RH greater than 80% are plotted, and an example is shown from the 2004 November 24 case study in Fig. 3.5. Regardless of whether the presence of CSI can adequately be determined, though, profiles of θ_e can also be utilized to reveal the existence of CI. Ultimately, these procedures help to qualitatively analyze the type of instability evident in each of the TSSN events.

3.3.6 Model Verification

In this section, an attempt is made to assess the accuracy of the output from the RUC-2 fields that are the foundation of the larger study. Given that the RUC has been designed and coded to assimilate many of the available operational datasets in real time, it is difficult to find an independent observed data set that might be used for comparison. However, a number of rawinsonde flights were made during a field campaign in the central United States during the late winter of 2005, with some of the initial results presented in Smith et al. (2005b); these data were *not* assimilated into the RUC model. Although this is a small sample, with fewer than 30 flights for comparison, each one was flown in a snowing environment that was similar to the kind addressed by the larger investigation here. In fact, one of the cases in this study was also a field campaign case (18 March 2005). What we offer here is a brief statistical analysis of the differences between the observed atmosphere in these snowstorms and the initial fields from the RUC model.

We begin by examining the mean and standard deviation values for the differ-

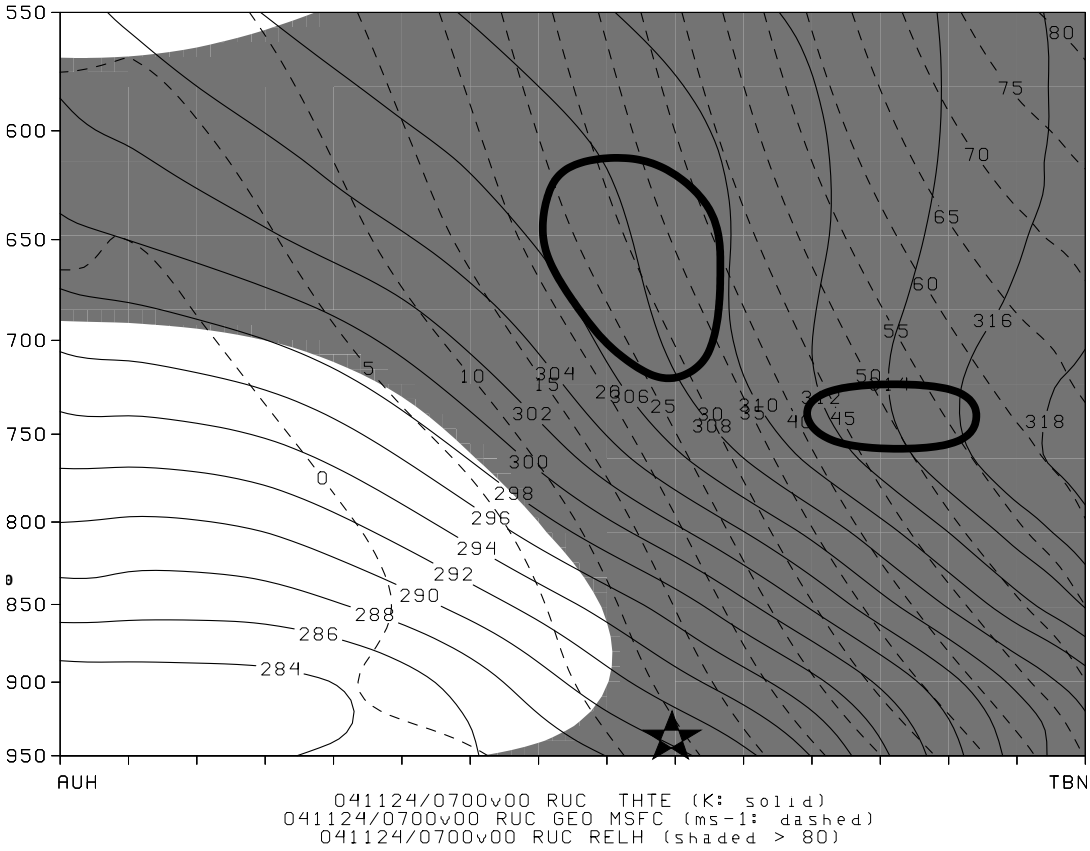

Figure 3.5: 40-km RUC cross-section analysis of geostrophic pseudo-angular momentum (M_g; ms^{-1}, dashed lines), equivalent potential temperature (θ_e; K, solid lines), and relative humidity greater than 80% (shading) valid at 0700 UTC 24 November 2004. The cross-section extends from Aurora, NE (KAUH) to Fort Leonard Wood, MO (KTBN) with temperatures increasing to the right and the star representing approximate location of Kansas City, MO. Solid black circle highlights atmospheric region deemed susceptible to the release of CSI.

ences between the observed data and the RUC output (Table 3.1). The mean and standard deviation of the difference in temperatures and dew point temperatures in the lower troposphere (850 hPa and 700 hPa) are modest, with the dew point temperature showing more serious errors with height than the ambient temperature. The u and v wind components feature higher mean difference as well as broader standard deviation values, which is common for kinematic fields. There is also not as clear a pattern of increasing error with height as there was with the thermodynamic variables. However, the absolute value of the mean differences tends to be less than $1.5ms^{-1}$, with standard deviations that are generally less than $4.0ms^{-1}$.

Table 3.1: Mean average and standard deviation [μ (s)] of differences between rawinsonde observed values and RUC numerical model initial field values of temperature ($\mathbf{T}$; ^{o}C), dew point temperature ($\mathbf{D}$; ^{o}C), and the $\boldsymbol{u}$ and $\boldsymbol{v}$ wind components (ms^{-1}) for the 850-hPa, 700-hPa, 500-hPa, and 300-hPa levels. All raw differences were computed as "observed value - RUC value".

		850 hPa	**700 hPa**	**500 hPa**	**300 hPa**
$\mathbf{T}_{OBS} - \mathbf{T}_{RUC}$	(N=27)	-0.0 (0.6)	+0.3 (0.7)	-0.3 (1.1)	-1.3 (0.6)
$\mathbf{D}_{OBS} - \mathbf{D}_{RUC}$	(N=27)	+0.3 (0.9)	-0.0 (1.5)	-2.2 (4.8)	+1.5 (4.0)
$u_{OBS} - u_{RUC}$	(N=24)	-0.1 (3.6)	+0.8 (2.9)	-1.2 (6.3)	+1.1 (3.5)
$v_{OBS} - v_{RUC}$	(N=24)	-2.2 (3.80	+0.3 (2.1)	-0.9 (4.6)	+1.2 (3.5)

Of perhaps greater interest is the tendency toward lower error profiles at the 700-hPa level, which is representative of the level where many of the calculations are made in the larger study. Indeed, the observed and modeled values at that level are very well correlated at that level (Table 3.2), with the exception of the v wind component. When one considers that many of the stability expressions are influenced largely by thermodynamic variables, these statistical results encourage a greater level of reliance on RUC-2 output in the larger study, especially in the lower- to mid-troposphere where our calculations of σ^2 and other parameters

Table 3.2: Pearson correlation coefficients between the rawinsonde observed values and RUC numerical model initial field values of temperature (T), dew point temperature (D), and the ***u***- and ***v***-wind components.

		850 hPa	**700 hPa**	**500 hPa**	**300 hPa**
T	(N=27)	0.78	0.97	0.92	0.99
D	(N=27)	0.67	0.88	0.59	0.51
u	(N=24)	0.84	0.93	0.80	0.97
v	(N=24)	0.85	0.54	0.52	0.94

tend to be made.

3.3.7 Grid Navigation Errors

Another source of error that might possibly affect the RUC results arises from the use of two grid analysis schemes, one for when the model was archived through the LDM and another for when the data had to be retrieved remotely. In order to evaluate, two TSSN events (2003 Dec 10 0400 UTC; 2004 Nov 24 0700 UTC) were selected for which both types of navigations were available and differences in some of the basic upper-level variables, such as geopotential height, temperature, wind [u- and v-components], and relative humidity, are calculated at 850 hPa, 700 hPa, 500 hPa, and 300 hPa. From this output at each grid point in the RUC domain at all four pressure levels, mean absolute values (MAV) are determined as well. Upon comparison against the standard precision of such measurements from rawinsondes (NOAA 2008), the results are concluded to be insignificant as the MAV differences are less than 1 gpm, 0.1^{o}C, 1 ms^{-1}, and 1%, respectively (not shown). Thus, this investigation shows that variations between episodes of convective snow should be substantially more dependent upon the actual synoptic setting than on the means for interpolating the observations to the grid.

3.3.8 Snowband Classification Scheme

The development of most synoptic-scale and embedded mesoscale precipitation structures is often related to the evolution of airstreams within ETCs. While this observation has been known implicitly since the days of the Norwegian Cyclone Model (NCM) developed by Bjerknes and Solberg (1922), the explicit representation of three main conveyor belts and their associated interactions is more recent (e.g., Carlson 1980). Within the extensive zone of weaker ascent in the warm conveyor belt (WCB), enhanced and constricted updrafts are often contained over regions spanning tens to a few hundred kilometers wide. Intense precipitation from these larger mesoscale areas tends to take on structures sufficiently elongated that an orientation can be assigned. Frequently referred to as bands, the length to width ratio are defined to be at the very least 2:1 (e.g., Houze et al. 1976; Hane 1986; Byrd 1989; Browning 1990; Novak et al. 2004). Furthermore, Wallace and Hobbs (1977) cite typical horizontal areas covered by these banded features to be on the order of 10^3-$10^4 km^2$. Although common lifetimes for such events are noted to be on the order of hours, the exact duration tended to be less restrictive in some observational work (e.g., Byrd 1989) than in others (e.g., Bennetts and Sharp 1982; Novak et al. 2004). Furthermore, Browning (1990) also indicates that the wide mesoscale precipitation bands generally have an orientation parallel to the vertical wind shear within the middle troposphere, with any embedded convection often developing above the more stable surface layer. Still, within the context of being able to identify a moving radar reflectivity pattern for a set period of time, no widely accepted lower limit is present in the literature. Consequently, because of these varying degrees of ambiguity, a subjective criteria method for (identifying) banded precipitation was formulated.

The resultant classification scheme deals strictly with defining cold-season precipitation band areas without reference to the type or number present (single or multiple). The comparisons of individual observed radar features against the theoretical fields generated by the mesoscale model are not expected to correspond perfectly to one another, the amount of variation particularly dependent upon differences in the resolution. Like the case study of heavy banded snowfall by Martin (1998), the current work also employs a grid-point spacing of 40 km which is too coarse to explicitly represent CSI circulations (let alone those caused by CI). However, like Martin (1998), the author is only interested in evaluating those regions of the atmosphere wide enough to be identifiable in model output and meet the necessary conditions for elevated instability and destabilization. In other words, the desired goal is to examine whether there is general agreement in the patterns in reflectivity data and major areas of precipitation with those of σ^2, as advanced by Bennetts and Sharp (1982). Consequently, it is expected that the finer details will not be captured, such as multiple bands being present within a broad region of positive growth rates. As a result, the criteria will be that the bands are greater than 200 km in length, possess a width of approximately 50 to 100 km, and are coherent structures with a minimum intensity of 25 dBZ maintained throughout a majority of their length for at least an hour. These standards are comparable to the transitory banded category of Novak et al. (2004) and the banded (B) or weakly banded (WB) categories defined by Byrd (1989). The constraint of consistent movement throughout the entire evolution by Bennetts and Sharp (1982) will be applied in instances where the midtropospheric mean flow is aligned with the band of precipitation, something which could realistically occur northwest of a surface cyclone.

3.3.9 Identification of Non-Thundering Snowstorms

The combination of surface observations and the NLDN allowed the ability to select snowstorms associated with an ETC *but without* the presence of lightning. The process, established by Smith (2006) and Market et al. (2006), is similar in many respects to determining episodes of thundersnow. The idea was to diminish both orographic and lake-effect influences by restricting the domain to the same interior portion of the country and picking cases that had snowfall accumulations and rates comparable to the convective snow subset in the climatology of Market et al. (2006). More precisely, observed visibility had to be less than or equal to $\frac{1}{4}$ mile for an extended time frame, such that the midpoint was defined as the time of balloon flight (1200/0000 UTC). Besides the dearth of CG flashes from the NLDN, the *absence* of lightning was further bolstered by the fact that human observers were frequently present at the station locations. For the purpose of the current work, the identical set of non-thundersnow (non-TSSN) events decided in Smith (2006) was evaluated. So as to keep differences between TSSN and non-TSSN limited to just physical mechanisms in the atmosphere, the analysis routine is kept consistent. The RUC-2 is relied upon once again for computations and synopses, with the acquisition of results from some of the techniques previously explained also explored. Following the format established in the other set of events, seven non-TSSN events (encompassing four winter seasons from 2002-2005) are documented.

3.4 Investigation Techniques

3.4.1 Point Value Statistics

The examination of stability characteristics will be pursued in two different fashions. The first will be more quantitative and entail compiling averages

and standard deviations for point values of all stability parameters in each case study. To be more precise, these statistics are derived from the individual initiation (TSSN) or midpoint (non-TSSN) sites and provide some idea of the expected sign and magnitude for the metrics diagnosed at the place of interest. Since each station identifier or pair of latitude and longitude coordinates demarks a specific position not exactly matching the grid points in the RUC-2 model, significance of the results is limited to some extent by the utilization of bilinear interpolation. Furthermore, while some effort has been devoted to show that statistical significance has been achieved for some stability indices (e.g., Market et al. 2006), the precision needed for anticipating activity at specific point locations is generally unattainable. Rather, some practical benefit could be attained by utilizing pattern recognition.

3.4.1.1 Sounding Characteristics

Individual sounding characteristics, such as midlevel lapse rates and most unstable parameters, were obtained from the national version of the Skew-T Hodograph Analysis and Research Program (NSHARP; Hart and Korotky 1991) for both TSSN and non-TSSN events. Statistics were generated in each dataset for the two time periods, with the diagnosis of thermodynamic stability indices within NSHARP taking into account the virtual temperature correction. The composite sounding shown in Fig. 3.4 was produced utilizing RAwinsonde OBservation (RAOB) program, version 5.6 (`http://www.raob.com/`). The construction of a mean profile followed the process established in Market et al. (2006), where the RUC-2 provides the original input data for this part of the study as well. Also, similar to Market et al. (2006), the MULPL was determined to be the pressure level at which the lowest value of the lifted index (i.e. MULI) occurred if no CAPE was found within the sounding.

3.4.2 Composites

Plots of of atmospheric properties, whether they are directly observed or indirectly derived, are also pursued and help to complement the tabular results already established. Instead of inspecting each case study individually for this objective, discrete spatial composites are produced for both TSSN and non-TSSN situations through means of a moving grid. The size of the subdomain (31 x 31 grid points) in this study was sufficiently large (1200 x 1200 km) to capture the background (meso-α to synoptic-scale) aspects associated with both types of snowstorms. Seeing that the origin in the spatial framework has been known to track many analyzed meteorological phenomenon (e.g., Mote et al. 1997; Moore et al. 2003; Oravetz 2003), the scheme here establishes two separate storm-relative composites by centering on the initiation sites of TSSN in one and the midpoint locations for non-TSSN in the other, where the *nearest* grid point in the RUC-2 model represented the centroid. It should be stressed that the calculation of σ^2 and other expressions discussed in the text occurred before compositing for the strict intention to avoid additional, artificial smoothing in creating averaged and standard deviation fields.

3.4.2.1 Mann-Whitney Rank-Sum Test

Tracking the development and progression of stability features should be instrumental in establishing a region that is more conducive for constricted and enhanced updrafts. Although Smith (2006) observed no substantial distinction in the plan view analyses for TSSN events, the dataset has since been expanded for the current work and more parameters are considered. The author has often noted that spatial distributions will reveal an axis of relatively reduced stability

in conjunction with situations of convective snow. For a more rigorous assessment of the composites, a statistical procedure is applied for σ^2 (and other indices) to measure the importance of the results in the horizontal region encompassing the TSSN report compared to a similar winter environment except with no lightning activity. In this case, though, the theoretical distribution of atmospheric data is often not known beforehand. As a result, nonparametric methods can be utilized to formally tests hypotheses, also known as significance testing (e.g., Davis 2002; Wilks 1995).

In the classical technique, mathematical formulas are constructed for the experiment such that the distribution is insignificant. In particular, the Mann-Whitney rank-sum test (e.g., Davis 2002; Wilks 1995) checks for equivalence of the medians of two samples, and thus, the premise that both subsets come from the same population. This is accomplished by combining the two samples and sorting the observations from smallest to largest, where the smallest is assigned a rank of one. The ordering of values is dependent on the stability parameter considered. For instance, in the case of growth rates, the ordering starts with the maximum positive value (greatest destabilization) and decreases to the smallest outcome denoted by the highest negative magnitudes (greatest stabilization). In cases of ties, where two or more data points have the same values, a rank is assigned equal to their average rank. Then, the test statistic for the Mann-Whitney technique is achieved by summing the ranks of the smaller group (W_x). For larger sample sizes, such as in this study, W_x is approximately Gaussian and can be tested using normal tables. Following (Davis 2002), the expected mean ($\overline{X}$) and standard deviation (s) are then defined, respectively, to be:

$$\overline{X} = \frac{nm}{2}, \tag{3.3}$$

and

$$s = \sqrt{\frac{nm(n+m+1)}{12}}, \tag{3.4}$$

where n and m are the two sample sizes. By converting the test value W_x into standardize form, the Z-score can be calculated using the equation:

$$Z = \frac{W_x - \overline{X}}{s}. \tag{3.5}$$

Either one-sided (one sample is expected to be larger or smaller than the other) or two-sided (no prior information is given on which one should be larger) alternative hypotheses are possible (e.g., Wilks 1995). Since many factors (e.g., grid point spacing, positioning of the subset domains, spatial extent and orientation, etc.) would influence the results from the numerical analysis, two-tailed p-values were utilized as a priori assertion to coincide with no outcome being assumed on the stability pattern.

Chapter 4

Results - Statistical Findings

4.1 The Growth Rate Parameter

4.1.1 Standard Geostrophic Approximation

Reflectivity data with the best resolution available (most often 1 km; obtained from `http://hurricane.ncdc.noaa.gov/pls/plhas/has.dsselect`) were examined from WSR-88D radar stations in each of the thundersnow events. Only the 5 March 2004 case study presented a scenario where no suitably close level II radar data were available, so the more coarse 6 km level III composite information was evaluated instead utilizing GEMPAK for the purpose of identifying precipitation banding. The typical range in the level of highest significant growth rates (LHSGR) for TSSN and non-TSSN was estimated from the separate lists of corresponding events. Regardless of the time period examined, a comparison between the two in Table 4.1 revealed comparable results. The pressure level of the LHSGR often varied between 550-700 hPa in each dataset, with the mean at a slightly higher elevation at initiation in TSSN-events (635 hPa) compared to the midpoint of non-TSSN case studies (671 hPa). Nevertheless, the main aspect that should be emphasized was that the vertical location of the best growth rates was found to fluctuate (Table 4.1).

Table 4.1: Statistics of the LHSGR(hPa) in TSSN and non-TSSN events for the two time periods utilized, such that μ(s) represents the average (standard deviation). Calculations are based off of the RUC-2 model and are valid at thundersnow onset location and time period. Results are also provided for 3-hours prior to convective initiation. In the case of non-TSSN events, values are determined for the midpoint location where and when the radiosonde balloon flight occurred in conjunction with snow falling.

LHSGR(hPa)	Initiation/Midpoint	Prior
TSSN	635(79)	672(102)
Non-TSSN	671(95)	664(107)

Table 4.2 provides a diagnosis of mesoscale banding from the observational evidence, and also presents corresponding results for σ^2 (conventional as well as from the LHSGR). An initial inspection of the tendencies from σ^2 reveals considerable variations in both sign and magnitude from one episode to another, especially for the numerous nonbanded events observed (Table 4.2). The progression and sometimes intensification of already robust radar reflectivity returns (usually $>$ 30 dBZ) into the area of interest corroborated the nowcast that wintertime convection might transpire in the near future. This increase in intensity is further supported by the upward trend in average values for σ^2 compiled in Table 4.3, when comparing the time the event commenced to that from three hours prior, regardless of whether the conventional method advocated by Bennetts and Sharp (1982) or the application of the LHGSR was applied.

However, more favorable conditions were obtained with higher σ^2 values for both time periods at the LHSGR (compare Table 4.3A to 4.3B), which was typically close to the 650-hPa level (Table 4.1). More formal support for this conclusion was reached by computations of 3-D EPV (McCann 1995), the statistical results of which are also shown in Table 4.3. Although a substantial number of the thundersnow cases exhibited evidence of weak stability to insta-

bility within the vertical profiles, the averages and large standard deviations for EPV showed that values varied substantially (Table 4.3). Again, results from this metric revealed that less opposition (i.e. slightly positive to negative estimates) to elevated thunderstorm development was offered at the LHSGR. Along these lines, average values for σ^2 at the time of initiation increased from -0.01 h^{-2} to 0.30 h^{-2} when the more novel approach was used (Table 4.3b). This latter value corresponds to a σ equal to 0.55 h^{-1} or a doubling time for the disturbance every 1.8 hours, which is approximately consistent with the established time scale (f^{-1}) for moist slantwise convection generated from the release of CSI (e.g., Bennetts and Hoskins 1979; Emanuel 1986).

Table 4.2: The counts of banded and non-banded occurrence are binned according to value ranges in the filtered growth rate parameter (σ^2; h^{-2}) calculated from the RUC-2 model. This is accomplished at thundersnow onset location and time period and performed at both (A.) 700 hPa and (B.) the LHSGR(hPa). When comparing against the observational evidence in each case study, the existence of mesoscale banded areas of precipitation near time of initiation is determined from the classification scheme described in the text.

A.	Predicted Non-Banded		Predicted Banded		
700 hPa σ^2	$<$ -0.1	-0.1 to 0	0.01 to 0.1	0.11 to 0.19	$\geq$ 0.2
Non-Banded Observed	8	3	0	0	1
Banded Observed	1	0	1	0	3

B.	Predicted Non-Banded		Predicted Banded		
LHSGR σ^2	$<$ -0.1	-0.1 to 0	0.01 to 0.1	0.11 to 0.19	$\geq$ 0.2
Non-Banded Observed	1	4	3	1	3
Banded Observed	0	0	0	0	5

Table 4.3: Average and standard deviation [μ (s)] values of filtered equivalent potential vorticity (EPV; $10^{-6}Kkg^{-1}m^2s^{-1}$) and growth rate parameter (σ^2; h^{-2}) for all TSSN events. Values were calculated from the RUC-2 model and valid at thundersnow onset location and time period, with calculations performed at (A) 700 hPa and the (B) LHSGR(hPa). Results are also provided for 3 hours prior to convective initiation. Since the atmosphere needed to be nearly saturated, statistical evaluation does not include those case studies in which the RH $<$ 80%.

(A) 700 hPa	Initiation	Prior
σ^2	0.01 (0.33)	-0.43 (1.16)
3-D EPV	0.46 (0.77)	0.25 (0.49)

(B) LHSGR	Initiation	Prior
σ^2	0.30 (0.59)	-0.01 (0.12)
3-D EPV	-0.03 (0.25)	0.25 (0.65)

Five of the seventeen thundersnow events examined at the time of initiation met the criteria for banded structures developed for the current work (Table 4.2). While the width was typically on the order of 50 km, lengths varied from 200 to 700 km and the precipitation bands lasted for periods of 1 to 3 hours. Reflectivity magnitudes within the colder area of precipitation generally ranged from 25-40 dBZ, with much higher values occurring in a few instances. However, in these rare occurrences, the presence of a strong elevated warm nose in RUC-2 soundings and thickness (the depth of a layer bounded by two isobaric surfaces) analyses indicated that some of the precipitation reaching the surface was probably of the mixed variety. For all five banded precipitation areas identified in the observations, the evaluation of horizontal, 2D plots and vertical profiles of σ^2 compared well in each instance. In this regard, Table 4.2 also reveals that more favorable results were again obtained by selecting the LHSGR, where the stability tendencies more easily surpassed the $0.2h^{-2}$ criterion. In fact, at this

particular level, all of the observed instances of precipitation banding were associated with growth rates greater than this value. A consultation of the statistical analysis of just these five events (Table 4.4) provided supporting evidence of the substantially large magnitudes at the time of initiation.

However, high values of the growth rate parameter are not a sufficient condition for banded precipitation. From this particular vantage point, banded precipitation areas were expected to occur in eight convective snow events (Table 4.2) as the growth rates were sufficiently high, positive values although only five were predicted correctly. Alternatively, the potential for amplification of small parcel perturbations in the midlevels of the atmosphere could also be observed by the fact that negative LHSGR EPV estimates occurred in this specific subset of events (not shown). As a means of comparison between banded (Table 4.4) and nonbanded (Table 4.5) TSSN events, statistics revealed similar trends in the parameters over the three-hour period with the existence of relatively more stable conditions being inferred from the sample of the latter. In spite of this contrast in 3-D EPV averages, the large standard deviations at the LHSGR in cases of nonbanding affirmed that the sign was also negative in some instances in this dataset. As for the observations, consultation of the reflectivity pattern showed that banded structures did not occur in nearly half of the eight cases where the growth rate was large, with three time periods failing to meet the standards required in the classification scheme. Yet even with these particular exceptions, the radar analysis indicated that the convection more typically was organized as discrete cells, something which the RUC-2 model fields corroborated fairly well as the regions of higher value growth rates tended to be more circular in shape. Again, it is acknowledged that individual features in the fine resolution reflectivity data can not be exactly correlated to the much coarser RUC-2 grids. Thus, individual grid point values should not be the sole source of predicting the type of precipitation structure to expect. Potentially more useful methods

will be explored with composites and case study analyses in the next couple of chapters.

Finally, accuracy in anticipating nonbanded snowfall was dependent upon how the evaluation was accomplished. If the growth rates are analyzed at 700 hPa (Table 4.2A), values less than zero for σ^2 captured all but one occurrence. By progressing vertically to the LHSGR (Table 4.2B), however, a much wider range of results are present for these 12 events. This larger spread is also evident by the examination of the relevant averages and corresponding standard deviations (Table 4.5). The one encouraging sign was that both approaches showed the probability of banding decreased as a function of decreasing growth rate, something also advanced by other measures of the typical response to σ^2 computed just for the subcategories (Tables 4.4 and 4.5). While the current sample size is too small to allow firm conclusions to be drawn for the general findings, the data tends to confirm the results of Bennetts and Sharp (1982).

Table 4.4: As in Table 4.3 except for just the banded TSSN events.

(A) 700 hPa	Initiation	Prior
σ^2	0.28 (0.39)	-0.02 (0.11)
3-D EPV	-0.05 (0.56)	0.13 (0.43)

(B) LHSGR	Initiation	Prior
σ^2	0.4 (0.25)	0 (0.12)
3-D EPV	-0.25 (0.19)	0.13 (0.27)

Table 4.6 shows a similar list of parameters but for the alternate group of non-TSSN events. Characteristic results of σ^2 (3-D EPV) increased (decreased) over the three hour period ending at the midpoint of the storm for both at 700 hPa

Table 4.5: As in Table 4.3 except for just the nonbanded TSSN events.

(A) 700 hPa	Initiation	Prior
σ^2	-0.1 (0.23)	-0.5 (1.26)
3-D EPV	0.67 (0.77)	0.27 (0.51)

(B) LHSGR	Initiation	Prior
σ^2	0.26 (0.69)	-0.01 (0.12)
3-D EPV	0.06 (0.22)	0.32 (0.76)

(Table 4.6A) and the LHSGR (Table 4.6B). The latter method was once again associated with relatively reduced stability and elevated growth rates over the former. As was the scenario for TSSN, a large range in values is evident in Table 4.6 as standard deviations were about on the same order as the averages. Despite this resemblance, the obvious distinction is the larger 3-D EPV and smaller σ^2 statistics in winter storms lacking CG-lightning (contrast Tables 4.3 and 4.6). In fact, an evaluation of Eqns. 2.11 and 2.7 in Table 4.6B ($-0.06 \pm 0.11h^{-2}$ and $0.24 \pm 0.3910^{-6}Kkg^{-1}m^2s^{-1}$) versus that of Table 4.3B ($0.30 \pm 0.59h^{-2}$ and $-0.03 \pm 0.2510^{-6}Kkg^{-1}m^2s^{-1}$) indicated that the signs for the left-hand-side expressions at the LHSGR and the later time period had a tendency to be opposite to those for TSSN. As a result, the correlation between the two datasets advanced some evidence that instability and destabilization of the environment was more prevalent for instances of cold-season moist convection.

4.1.2 Term Contributions and Stability Regime Diagnosis

The task of partitioning σ^2 can be a useful exercise in establishing the ideal conditions under which small disturbance growth is maximized. By making reasonable assumptions for each scenario, the type of instability present can

Table 4.6: As in Table 4.3 except for non-TSSN events, with calculations valid at the midpoint location and time period as well as 3 hours prior.

(A) 700 hPa	Midpoint	Prior
σ^2	-0.11 (0.11)	-0.13 (0.09)
3-D EPV	0.72 (0.71)	0.84 (0.61)

(B) LHSGR	Midpoint	Prior
σ^2	-0.06 (0.11)	-0.08 (0.11)
3-D EPV	0.24 (0.39)	0.53 (0.58)

subsequently be assessed. As was briefly mentioned in the formal discussion of concepts, a large, positive response to the left-hand-side of Eq. 2.11 is best achieved from the first contribution (term A) when the area of interest is located in high latitudes (larger values for f) and the flow tends to be anticyclonic to the point that $\eta_g < 0$. Although theoretically possible, it is much more plausible that the absolute vorticity remains positive but the magnitude be reduced to diminish the opposition. From this realistic adjustment, the sign of the entire expression resides upon the second and third components to term (B). With the large proportion of constants, the minor variations resulting from (B1) are the result of the pressure level chosen and to a lesser extent the thermal properties of the environment. If the atmosphere is convectively stable ($\frac{\partial \theta_w}{\partial p} < 0$), growth of the instability is best achieved by assuring the temperature and moisture gradients lie in the same direction and that values of $\nabla_h \theta$ and $\nabla_h \theta_w$ are both simultaneously substantial (such as in a baroclinic zone). More importantly, estimates for σ^2 are amplified most effectively by a near zero contribution in the denominator, making division by term (B3) huge. Physically, this would translate to a very weakly stable environment, most prominently associated with CSI. On the other hand, the sign placement would be opposite for situations of buoyant convection, with the influence of term (B2) being minimized. In

practice, however, a negative response for $\nabla_h\theta \cdot \nabla_h\theta_w$ is unlikely for these types of precipitation event as the conjunction of a warm, moist flow within the WCB is often evident within the lower-middle troposphere (e.g., Oravetz 2003; Moore et al. 2005a,b).

The actual findings for the term-by-term diagnosis agreed rather well with the reasonable expectations from the mathematical and physical analysis of Eq. 2.11. Nevertheless, discriminating the type of stability present just from the point values calculated from each separate part can be problematic due to the associated ambiguity. Several factors have to be considered especially when classifying what constitutes characteristics of CSI and how they differ from weak symmetric stability (WSS: isentropic surfaces are nearly parallel to or slightly less vertical than those of momentum) or for that matter a very stable regime. Furthermore, it should be emphasized that the calculations of σ^2 and the sum of its constituents at the initiation sites will not match exactly. This is due to the fact that the coordinates are not collocated with any of the grid points and interpolation must be performed separately.

For the limited number of TSSN events compiled, the results at the time of the first CG flash have a wide distribution, as shown in Table 4.7. With respect to horizontal shear effects, the 2-D flow is essentially laminar ($\zeta_g = 0$) when the inertial contribution scales to f^2. The average latitude for the TSSN events compiled is approximately 40^oN and translates to a coriolis parameter of $9.4 * 10^{-5}s^{-1}$, this a standard representation of mid-latitude systems. This leads to the conclusion that the result in term (A) usually indicates weak relative cyclonic vorticity at both 700 hPa and the LHSGR (Table 4.7). While the large standard deviation allows for the possibility of anticyclonic conditions, inertial instability does not occur in any of the episodes of TSSN. Mean lapse rates in θ_w increased only on the order of 1^oC over the 100-hPa layers calculated, implying a tendency towards weak, moist static stability. The lower statistic for

term (B3) obtained at the LHSGR in Table 4.7 also suggests air parcels more susceptible to vertical displacements in a saturated atmosphere. Furthermore, the fact that the numerator was always positive for the entire set of case studies often meant a favorable sign in the diagnosis. As there was a regular and adequate counterbalancing influence within σ^2, WSS or CSI would be preferred. Although the process of distinguishing a state capable of slantwise convection from one that is slightly resistant is not all that precise, it seems some explanation can be found in Bennetts and Sharp (1982). If the values for (A), (B1), (B2), and (B3) are similar, the crucial indicator would be on the final sign for the expression 2.11.

Table 4.7: Individual contributions to σ^2 from terms (A; $10^{-9}s^{-2}$), (B1; $10^{-3}m^3 kg^{-1}K^{-1}$), (B2; $10^{-10}K^2m^{-2}$), and (B3; $10^{-4}K\ ms^2kg^{-1}$) for the TSSN events at initiation time. The statistic format is once again utilized at 700 hPa and LHSGR(hPa).

	Term (A)	Term (B1)	Term (B2)	Term (B3)
700 hPa	-16.7(7.5)	3.9(0)	3.5(2.6)	-1.6(1.3)
LHSGR(hPa)	-15.6(7.7)	4.3(0.4)	2.5(3.3)	-0.5(0.9)

Table 4.8 summarizes the tallies present for each type of stability depicted through the scheme described above. As there were occasional changes in stability with increasing altitude, the dominant regime was identified for the convective initiation site as well. As can be seen, some combinations of classifications occurred, such as when term (B3) or σ^2 were very close to zero. Whereas WSS (10) was prevalent at 700 hPa in the TSSN case studies, more instances of CSI (6) were evident at the LHSGR (Table 4.8). Even so, the distribution was spread throughout all the categories established and the borderline instances were probably associated with nearby transitions in the grid point domain. Assuming nearly geostrophic conditions, moist slantwise displacements would be most preferred if considering which influence is paramount at the locations selected (Table

4.8). Although the entire vertical profile is not ascertained through this perspective, the term-by-term approach can be modified to inspect each pressure level. Furthermore, the horizontal pattern of the constituent parts, essential to a complete diagnosis, will be explored in the composite analysis of Chapter 5. The process illustrated here is nonetheless another valuable device available in order to identify the particular stability regime present in convective precipitation.

Table 4.8: Type of stability depicted through the term-by-term analysis of σ^2 and the scheme described in the text. Tallies are performed for each category at 700 hPa, LHSGR(hPa), and the dominant of the two in all of the TSSN events at initiation time.

	Stable	WSS	WSS/CSI	CSI	CSI/CI	CI	Inertial
700 hPa	1	10	0	3	1	2	0
LHSGR(hPa)	1	3	2	6	4	1	0
Dominant	1	3	2	6	3	2	0

An examination comparing banded against non-banded convective snow was also performed and the findings presented in Table 4.9. Standard deviations were comparable for all terms in each subset and when compared against the total compilation of TSSN episodes (Table 4.7). However, the similarities tended to end when considering the average values. This evaluation of the individual elements showed that the banding subset had a slightly lower inertial component and lapse rate in θ_w, with a greater contribution from term (B2) compared to the rest of the dataset. In fact, the estimates of these factors in Eq. 2.11 were discovered to be $14.5 * 10^{-9} s^{-2}, 3.1 * 10^{-10} K^2 m^{-2}, and - 0.2 * 10^{-4} K m s^2 kg^{-1}$ at the LHSGR(hPa). Moreover, the latter two values indicated that a relatively warm, moist airmass was present, stronger baroclinicity suggested from the increased θ and θ_w gradients, and a stratification very close to neutrality (Table 4.9A). As a result, this particular collection of ingredients is more conducive to a symmetrically unstable environment and cooperated together to give greater

(and more often positive) growth rates in snowstorms where precipitation bands were present (compare Table 4.4 to Table 4.5).

Table 4.9: As in Table 4.7 except broken up into [A] Banded and [B] Non-banded categories.

[A] Banded	Term (A)	Term (B1)	Term (B2)	Term (B3)
700 hPa	-14.8(7.9)	3.9(0)	4.1(1.5)	-0.7(0.9)
LHSGR(hPa)	-14.5(7.4)	4.1(0.3)	3.1(0.6)	-0.2(0.3)

[B] Non-Banded	Term (A)	Term (B1)	Term (B2)	Term (B3)
700 hPa	-17.5(7.6)	3.9(0)	3.2(2.9)	-2.0(1.3)
LHSGR(hPa)	-16.0(8.0)	4.3(0.5)	2.3(3.9)	-0.7(1.1)

4.1.3 Tendency of σ^2

Instantaneous changes in growth rates were estimated via backward finite differences utilizing the high frequency, hourly-updated observations from the RUC-2. Tabular results were compiled for the convective snow case studies and showed positive (negative) tendencies three hours prior to (at the time of) the first CG lightning flash (Table 4.10). The earlier (later) upward (downward) trend corresponded to a predicted destabilization (stabilization) of the environment, this in agreement with the actual modification in the average values of σ^2 during the three hour period (Table 4.3) and the presumed convective adjustment which generally follows the release of instability. Both the 700-hPa level and LHSGR were comparable in this finding as each has the same sign for the average statistic (Table 4.10). The very large variability between the events resulted primarily from the existence of nearly neutral, moist static stability that resulted in only a couple of instances. In actuality, most of the magnitudes were small and only on the order of 0.01 to 0.1 h^{-3}. The distinction of these calculations to just thunderstorm development in cold-season precipitation episodes

were analyzed by obtaining separate estimates of σ^2 tendencies for the non-TSSN occurrences. An inspection of Table 4.11 revealed averages that were nearly zero and regularly less than the opposing dataset (Table 4.10), with values never surpassing 1.0 h^{-3}.

Verification of the predictions from Eq. 3.2 were accomplished by examining a couple of observation datasets. Mean lapse rates in θ_w were assessed easily from temperature and dew point information, this diagnostic proving to be significant in establishing the nature of stability in the atmosphere as well as its impact upon the four terms within the relevant mathematical expression (Eq. 3.2). For the snowstorms that include (exclude) lightning activity, values of $-1.6(-3.0) * 10^{-4} K m s^2 kg^{-1}$ at 700 hPa and $-0.5(-1.7) * 10^{-4} K m s^2 kg^{-1}$ at the LHSGR were noted at the convective initiation (midpoint) time period. Again, the innovative technique was reliable in producing more favorable results as related to reduced stability. More importantly, the lower lapse rates in TSSN events matched expectations and partially helped to maximize the response to σ^2 tendencies (Table 4.10).

Further diagnosis of the data from the NLDN appeared to provide little additional correlation to theory, aside from the fact that greater magnitudes resulted in Table 4.10 when lightning existed. From the selected CG flashes identified in Chapter 3, however, discrimination of statistical results within the individual TSSN case studies was not very valuable, as the observations were predominately associated with minimal activity (only 1 or 2 flash counts). While it is possible that greater contrasts might transpire with a larger sample size, past work (e.g., Colman 1990a,b, Zipser and Lutz 1994, Schultz and Schumacher 1999, Orville and Huffines 2001) has shown that the colder environment in winter weather precipitation would still only be marginally conducive to electrical discharges. Thus, the findings suggested that growth rates of small perturbations generally increased immediately leading up to the onset of convection. More precisely, the

identification was more unique and remarkable for the very large tendencies (e.g., $> 1.0h^{-3}$), in which the moist static stability played a greater role, as vertical profiles of θ_w were often nearly constant with height. While destabilization of the atmosphere was preferred during the three-hour period, discretion ought to be observed when trying to predict whether or not thunderstorms will occur when magnitudes of σ^2 tendencies are quite small considering the large standard deviations and the overlap in values associated with the non-TSSN dataset (compare Table 4.10 to Table 4.11).

Table 4.10: Average and standard deviation [μ (s)] values of filtered σ^2 tendencies (h^{-3}) calculated from the RUC-2 model and valid at thundersnow onset location and time period, with calculations performed at 700 hPa and the LHSGR(hPa). Results are also provided for 3 hours prior to convective initiation. Since the atmosphere needed to be nearly saturated, statistical evaluation does not include those case studies in which the RH $< 80\%$.

σ^2 tendency	Initiation	Prior
700 hPa	-0.23 (1.08)	58.21 (209.94)
LHSGR	-25.67 (106.2)	0.37 (1.09)

Table 4.11: As in Table 4.10 except for non-TSSN events.

σ^2 tendency	Midpoint	Prior
700 hPa	0.01 (0.05)	0 (0.04)
LHSGR	0.04 (0.11)	0.02 (0.06)

4.1.3.1 Relationship to Forcing Within Convective Snow

The notion that all thunderstorms result from the presence of three fundamental ingredients is widely accepted amongst the meteorological community (e.g., Johns and Doswell 1992; Schultz and Schumacher 1999). Throughout the current work, the focus primarily was on analyzing the role of instability (in all

its forms). Some attention, though, will be focused briefly on the forcing aspect in wintertime convective precipitation, on account of the positive feedback expected between mechanisms producing ascent and the response to that vertical motion. For example, the existence of $\frac{\partial[\nabla_h \theta]}{\partial t}$ on the right-hand-side of Eq. 3.2 in term (D) and the associated production of $\frac{\partial(\sigma^2)}{\partial t}$ on the left-hand-side of the expression illustrated the coupling of frontogenesis and temporal variations of the growth rate parameter. Application of the Petterssen expression (Eq. 2.1) provided a typical means to realistically approximate adjustments to the temperature gradient. Geostrophic conditions were assumed for these calculations such that there was adequate agreement with the theory in deriving Eq. 3.2.

Results from both term (D) and the incorporated, representation of frontogenesis were determined, with values shown in Table 4.12. Averages of the latter revealed minor increases to the above-surface baroclinicity of the environment at convective initiation. In any case, the spread of 0.5 $K100km^{-1}3h^{-1}$ was sufficient in the standard deviations to allow for a considerable presence of frontolysis as well in the TSSN events examined. Given the general trend of relatively warm and humid conditions being collocated in the area of interest and a weak, convectively stable atmosphere (see Table 4.7), term (D) should be opposite in sign to $\frac{\partial[\nabla_h \theta]}{\partial t}$ if frontogenesis and moist frontogenesis for the most part do not offset one another in the same region. While the judgment offered in Table 4.12 appeared to be validated from a comparison of the mean values, the rationale from event to event was not as dependable based upon the fact that Eq. 2.1 was just an estimation of temporal finite differencing of the thermal gradient expressed within diagnostic form. Regardless, the more important discovery was that mesoscale, baroclinic forcing demonstrated by term (D) mainly acted to raise growth rates, a conclusion best supported by the results obtained at the LHSGR (Table 4.12B). In looking at the aggregate tendencies of σ^2 at the beginning of the TSSN event (Table 4.10), other contribution(s) had to have

sufficiently offset this one portion to produce the negative results generated.

Interpretation of the remaining factors suggested that changes in growth rates were generally negligible due to the result of heating/cooling of the environment (term (E)) as values were repeatedly $<< 0.01h^{-3}$. The statistics shown in Table 4.12 also indicate that term (C), while being similar in magnitude to the resultant tendencies, was nearly equally divided in signifying a flow pattern becoming more cyclonic as opposed to one evolving to a more anticyclonic nature. By the process of elimination, stabilization of the environment and the nearly constant values of θ_w with height were the predominant reasons for the accentuated downward trend in σ^2 at the time of convective initiation, something especially asserted by analysis at the LHSGR (compare Table 4.10 to Table 4.12B). Even so, this reasoning did not apply to all events of TSSN seeing that lapse rates were not always so favorable. The very large range in the estimates of term (F) appeared to support instances where frontal and shear dynamics were more significant (Table 4.12).

A similar partitioning was further performed immediately prior to the development of lightning activity, the results also presented in Table 4.12. The examination displayed resemblance to the later time period with respect to $\Im > 0$ and the reduction in $\dfrac{\partial \theta_w}{\partial p}$ maximizing the response to growth rate tendencies. The last contribution was the most substantial at 700 hPa, whereas in this case, predicted increases in the development of small disturbances was facilitated by the general decrease in moist static stability (Table 4.12A). Once more, minor portions of the response in Eq 3.2 were often attributed to the statistics of terms (C) and (D), with the latter being less influential compared to the time that the first CG flash occurred. Thus, this technique illustrated that the prevalent, neutral stratification of the atmosphere acted to amplify changes in σ^2, with greater (less) susceptibility to CI or CSI leading up to (after) the onset of convection usually associated with an atmosphere characterized by destabilization

(stabilization).

Table 4.12: Average and standard deviation [μ (s)] values of filtered geostrophic, Petterssen frontogenesis (GEO FRNT; $K100km^{-1}3h^{-1}$) and the contribution to σ^2 tendencies from terms (C), (D), and (F) in units of h^{-3}) as determined from the RUC-2 model. Results are valid at thundersnow onset location and time period, with calculations performed at (A) 700 hPa and (B) LHSGR(hPa). Results are also provided for 3 hours prior to convective initiation. Since the atmosphere needed to be nearly saturated, statistical evaluation does not include those case studies in which the RH $< 80\%$. Analysis of term (E) was not included since it was at least a couple of magnitudes smaller than the other contributions on a regular basis.

(A) 700 hPa	Initiation	Prior
GEO FRNT	0.2 (0.5)	0.2 (0.4)
Term (C)	0 (0.05)	-0.02 (0.04)
Term (D)	-0.01 (0.09)	0.07 (0.28)
Term (F)	-0.22 (1.01)	58.15 (209.65)

(B) LHSGR	Initiation	Prior
GEO FRNT	0.1 (0.5)	0.1 (0.5)
Term (C)	0 (0.06)	0 (0.03)
Term (D)	-0.28 (0.8)	-0.01 (0.07)
Term (F)	-25.71 (105.3)	0.38 (1.11)

4.1.3.2 Partitioning into Banding and Nonbanding Episodes

Equivalent analyses as in Tables 4.10 and 4.12 were accomplished specifically for the types of precipitation structures identified within the convective snowfall dataset. From this particular classification, approximately constant values for σ^2 were predicted on average at 700 hPa (Table 4.13) for both time periods for those reflectivity patterns exhibiting banded features. On the other hand, by moving generally upwards towards the LHSGR (Table 4.13), typical magnitudes for growth rate tendencies were positive when the first CG flash occurred as well as 3 hours prior. The latter statistic was verified against the assessment

of Eq. 2.11 (Table 4.4B) and again proved to be useful in correctly identifying the observed increase in calculations. For the construction of Table 4.14, the processes responsible for adjustments to σ^2 were ascertained as they pertain to just the banded TSSN events. Before the lightning activity ensued, mean estimates of terms (C) and (D) were similar in scale (0.01 h^{-3}) but counteracted one another in their eventual contributions. Differences with altitude, however, were obtained for the static stability tendency factor as higher, more favorable tendencies were found at the LHSGR, principally for when thunderstorm development began. Upon contrast against the total 17 events (Table 4.12), this inferred destabilization appeared to be unique for occurrences of banding at this stage. Even though evaluations of Petterssen frontogenesis marginally acted to increase temperature gradients in these types of TSSN case studies (Table 4.14), dry and moist baroclinic dynamics (represented by term (D)) offered a reduced role in raising growth rates in just these types of TSSN case studies (compare Tables 4.12 and 4.14). Above all, though, some degree of skepticism was acknowledged in these findings as the standard deviations were predominantly on the same scale as (if not larger than) the averages.

Table 4.13: As in Table 4.10 except just for the banded TSSN events.

σ^2 tendency	Initiation	Prior
700 hPa	0 (1.07)	-0.1 (0.04)
LHSGR	0.28 (1.48)	0.03 (0.15)

The identical inquiry into instances of nonbanding TSSN was then established in order to effectively distinguish the previous results. An inspection of Table 4.15 against that of Tables 4.10 and 4.13 revealed the evolution in $\frac{\partial(\sigma^2)}{\partial t}$ was much more distinct in signifying an environment additionally (much less) responsive to CSI at the earlier (later) time frame. By separating out the influences into the four elements already discussed (Table 4.16), reduction in static stability

Table 4.14: As in Table 4.12 except just for the banded TSSN events.

(A) 700 hPa	Initiation	Prior
GEO FRNT	0.2 (0.5)	0.3 (0.4)
Term (C)	0.02 (0.07)	-0.03 (0.01)
Term (D)	0.01 (0.1)	-0.05 (0.04)
Term (F)	-0.03 (1.09)	-0.03 (0.01)

(B) LHSGR	Initiation	Prior
GEO FRNT	0.1 (0.7)	0.2 (0.4)
Term (C)	0.01 (0.09)	-0.01 (0.02)
Term (D)	-0.02 (0.15)	-0.02 (0.07)
Term (F)	0.29 (1.42)	0.05 (0.09)

followed by strengthening of this process was accentuated during the course of the 3 hours examined. In the attempt to explain this difference, the compiled statistics for term (B3) in the nonbanding episodes were revisited. While this analysis indicated relatively larger lapse rates compared to the remaining archive of TSSN case studies (compare Tables 4.9A and 4.9B), greater occurrences were found with the denominator being significantly reduced (i.e. $\frac{\partial \theta_w}{\partial p} \approx 0$). Thus, the procedure of squaring this portion of term (F) in Eq. 3.2 was apparently responsible for the very high, aggregate value of -437.7h^{-3} in one lone case study at the LHSGR (not shown). This ultimately resulted in the two orders of magnitude increase in mean σ^2 tendencies at convective initiation found in the comparison of Table 4.13 against Table 4.15.

Furthermore, the investigation also showed that the average, earlier effects of frontolysis (i.e. 0.09h^{-3} at 700 hPa; Table 4.16A) and subsequent frontogenesis (i.e. -0.38h^{-3} at the LHSGR; Table 4.16B) suggested greater impact in generating growth rate tendencies than in the presence of precipitation bands (Table 4.14). Nevertheless, comparison of results from the Petterssen formulation showed very similar values amongst the two datasets. As for the part of vorticity changes,

term (C) was typically insignificant as near-zero contributions were evident in Table 4.16. In turning to the observations from the NLDN, it was interesting to note that the precedent, amplified destabilization of the environment was associated with the two highest counts of CG flashes (7,13) just from this subset. At any rate, this correlation could have been an artifact of the specific sample utilized for those occasions where precipitation banding was absent and was not all that strong as lightning activity was otherwise widely unsubstantial.

Table 4.15: As in Table 4.10 except just for the nonbanded TSSN events.

σ^2 tendency	Initiation	Prior
700 hPa	-0.33 (1.11)	68.81 (228.23)
LHSGR	-36.48 (126.37)	0.52 (1.3)

Table 4.16: As in Table 4.12 except just for the nonbanded TSSN events.

(A) 700 hPa	Initiation	Prior
GEO FRNT	0.3 (0.6)	0.2 (0.5)
Term (C)	-0.01 (0.03)	-0.01 (0.04)
Term (D)	-0.02 (0.09)	0.09 (0.31)
Term (F)	-0.3 (1.02)	68.73 (227.91)

(B) LHSGR	Initiation	Prior
GEO FRNT	0.1 (0.5)	0 (0.6)
Term (C)	0 (0.04)	0 (0.03)
Term (D)	-0.38 (0.94)	0 (0.07)
Term (F)	-36.54 (125.27)	0.53 (1.33)

4.1.4 Extension to Ageostrophic Influences

The development of frontal convection from symmetric instability has been explained so far in terms of a very simplified 2D framework. From this context,

pure CSI would produce slanted circulations oriented parallel to the thermal wind and be unrealistic in their supposed infinite length. This was the theoretical framework, which Bennetts and Hoskins (1979) and Bennetts and Sharp (1982) applied to the development and later diagnosis of σ^2. Still, this was only a good first approximation to the characteristics of precipitation bands in ETCs and observations often showed more complex features. Along these lines, the aim of the current work was also to ascertain the implications of neglecting departures from geostrophy by incorporating ageostrophic terms in the original expression for σ^2. As with the traditional approach, equivalent analyses were subsequently applied to the resultant expression (Eq. 2.13), which now accommodated for the full three-dimensional shear through moist potential vorticity. First, the LHSGR for just the extended growth rates ($LHSGR_e$) was also determined for TSSN and non-TSSN occurrences and the statistics presented in Table 4.17. Analogous to Table 4.1, both sets of snowstorms were consistent in their depiction of averages and standard deviations. While the vertical extent was characterized by a 100-hPa layer in the midtroposphere, the pressure level was usually (once more) close to 650 hPa. This methodology (Table 4.17) also indicated that the mean values exhibited a slightly lower elevation at initiation in TSSN-events (671 hPa) compared to the midpoint of non-TSSN case studies (650 hPa). Thus, both distributions verified that more advantageous results were encountered in contrast to the prescribed practice of Bennetts and Sharp (1982).

Table 4.17: As in Table 4.1 except for statistics of the LHSGR(hPa) in the calculations of the extended growth rate parameter (known from herein as $LHSGR_e$).

$LHSGR_e$(hPa)	Initiation/Midpoint	Prior
TSSN	671 (87)	647 (83)
Non-TSSN	650 (91)	671 (99)

The initial investigation of banded precipitation and comparison of observations against predictions from the customary 2D σ^2 values was revisited for the more complete estimates from σ_e^2. For all five relevant case studies, the relationship of the reflectivity patterns was again robust with the revised, RUC-2 gridded fields. More specifically, an inspection of Table 4.18 indicated that the corresponding results from Eq. 2.13 exceeded the $0.2h^{-2}$ threshold at the $LHSGR_e$, whereas the outcome was less desirable at 700 hPa. Turning to the remaining archive, a more even spread emerged in the classification bins for the extended growth rates; decay of instability (i.e., negative σ_e^2) was implied from the vertical profile (e.g., 10 at 700 hPa; Table 4.18A) in several nonbanding TSSN events. Of these twelve time periods, however, very high predictions from theory incorrectly identified the precipitation structure in four. The explanation for this discrepancy was obtained by returning to the corresponding finding for the geostrophic approximation, in which the shape of the features (e.g., cellular) matched fairly well in the spatial analyses. Fundamentally, the repeatable implication from the results was the direct correlation of σ_e^2 to the possibility of mesoscale banding as the likelihood increased (decreased) for a greater (reduced) response from this rarely applied stability index. Thus, the agreement between Tables 4.2 and 4.18 was fairly compatible in several aspects.

Other types of evaluations were provided (i.e. Tables 4.19 and 4.20) to highlight the importance of ageostrophic processes. The extension to a more complete prognosis of all dynamic mechanisms was presumed to produce substantial anomalies especially for situations of strong curvature. First, the contrast of σ^2 against that of σ_e^2 signified elevated averages for the latter regardless of the elevation leading up to and including convective initiation. Results from Table

Table 4.18: As in Table 4.2 except for the counts of banded and non-banded occurrence are binned according to value ranges in the extended growth rate parameter (σ_e^2; h^{-2}).

A.	Predicted Non-Banded		Predicted Banded		
700 hPa σ_e^2	$<$ -0.1	-0.1 to 0	0.01 to 0.1	0.11 to 0.19	$\geq$ 0.2
Non-Banded Observed	6	4	1	0	1
Banded Observed	0	1	0	1	3

B.	Predicted Non-Banded		Predicted Banded		
$LHSGR_e$ σ_e^2	$<$ -0.1	-0.1 to 0	0.01 to 0.1	0.11 to 0.19	$\geq$ 0.2
Non-Banded Observed	1	3	3	1	4
Banded Observed	0	0	0	0	5

4.19 suggested that the atmosphere was more conducive to slantwise perturbations and was unique in providing beneficial preconditioning of the environment. In addition, the slightly larger value of 0.35 h^{-2} at the $LHSGR_e$ (Table 4.19 translated to a σ of 0.59 h^{-1} and a comparable doubling time for the ensuing convection (1.7 hours) amongst the two approaches. From just the context of statistics described thus far, the inequalities were deceptively inappreciable on first glance. Instead, a more accurate and quantitative portrayal was demonstrated from the calculations of R_o in Table 4.20. This approach illustrated that sizable fluctuations occurred quite often, such that the neglect of curvature within the atmosphere was not reasonable. For instance, the constraints of geostrophic balance applied the best for the smallest ratios (i.e. $R_o \leq 0.1$) calculated, this classification being rare amongst TSSN reports compared to a combination of the other categories. Alternatively, certainly greater occurrences of convective snowfall matched up to the intermediate value range at both 700 hPa (9 at convective initiation; Table 4.20A) and LHSGR (8 at 3 hours prior; Table 4.20B). Assuming such simplifications upon the background environment for this situation would be partially justified and corresponded to the R_o estimates

in Clark et al. (2002). For much stronger flow regimes, within ETCs, however, the validity became very questionable on the upper end of the R_o criterion. This especially was accurate for the quarter to third of TSSN events found in Table 4.20 associated with R_o numbers greater than or equal to unity.

The uniqueness of the conclusions to just conditions of convective snowfall was determined by performing the same tests as in Tables 4.19 and 4.20 but for the collection of non-TSSN events. Unlike the former dataset, the diagnosis from Table 4.21 revealed all mean values of σ_e^2 to be negative and appeared to have the greater case for negligible deviations away from the original σ^2. Still, this analysis also showed results from case to case were not so uniform and was substantiated by further testing the modification to allow non-geostrophic mechanisms. In spite of the smaller sample, the presence of $R_o \geq 1.0$ was recurrent at each level and time period in Table 4.22, this evidence testifying to the presence of strong curvature somewhere within non-TSSN events. In summary, the extraordinary technique of extending to the entire growth rates produced somewhat distinctive conclusions depending upon whether lightning was present or not. In either scenario, the restrictions considered by Bennetts and Hoskins (1979) and Bennetts and Sharp (1982) were rudimentary and had some definite advantages but ultimately failed to completely resolve all contributions to the stability regime.

Table 4.19: Average and standard deviation [μ (s)] values of the extended growth rate parameter (σ_e^2; h^{-2}) for all TSSN events. Values were calculated from the RUC-2 model and valid at thundersnow onset location and time period, with calculations performed at 700 hPa and the $LHSGR_e$(hPa). Results are also provided for 3 hours prior to convective initiation. Since the atmosphere needed to be nearly saturated, statistical evaluation does not include those case studies in which the RH $< 80\%$.

σ_e^2	Initiation	Prior
700 hPa	0.08 (0.35)	0.17 (0.86)
$LHSGR_e$	0.35 (0.48)	0.2 (0.75)

4.2 Other Stability Diagnostics

4.2.1 M_g - θ_e Relationship

Further confirmation of the stability regime in the convective snow events was obtained through the traditional means of the M_g - θ_e relationship (Table 4.23). Utilizing the 850-300hPa thickness fields, the amount of flow curvature was ascertained qualitatively to be weak enough in about 29.4% (47.1%) of the case studies at (3 hours prior to) the beginning of the first CG flash. In this particular collection, the methodology described in Section 3.3.5 allowed for the inspection of CSI within the atmosphere. As for the remaining majority, the analysis of stability type was restricted to the lapse rates of θ_e. The two time periods provided in Table 4.23 also established a cursory examination into the evolution of the dominant stability regime during the short interval progressing towards the development of TSSN activity. In order to comply with the *conditional* part of CSI or CI, the lack of a nearly saturated environment in several of the earlier soundings meant that the release of slantwise or upright convection could only be characterized as *potentially* occurring. As a result, the corresponding possibilities would be potential symmetric instability (PSI) or potential instability (PI), respectively.

Table 4.20: The counts of TSSN events are binned according to value ranges in the Rossby number (R_o) condition approximated by the ageostrophic influences to the extended growth rates. This is performed at (A) 700 hPa and the (B) LHSGR at the time of convective initiation and 3 hours prior. Tallies do not necessarily total to 17 due to undefined ratios resulting from dividing by zero and the exclusion of events when the RH < 80%.

(A) 700 hPa	$R_o < 0.1$	$0.1 \leq R_o < 0.5$	$0.5 \leq R_o < 1.0$	$R_o \geq 1.0$
Initiation	1	9	3	3
Prior	2	4	3	3

(B) LHSGR	$R_o < 0.1$	$0.1 \leq R_o < 0.5$	$0.5 \leq R_o < 1.0$	$R_o \geq 1.0$
Initiation	4	4	4	5
Prior	1	8	3	3

Table 4.21: As in Table 4.19 except for non-TSSN events.

σ_e^2	Midpoint	Prior
700 hPa	-0.11 (0.08)	-0.11 (0.1)
$LHSGR_E$	-0.07 (0.07)	-0.04 (0.14)

Smith (2006) utilized a similar procedure as described here and discovered classes roughly coinciding to that in Table 4.23. Disagreements with this study were possibly due to the expected ambiguities from one judgment to the next, the reduced sample size he based his conclusions upon, and the fact that he employed a finer resolution of the RUC with the 20-km version (see Tables 4.8.1 and 4.8.2 in Smith 2006). The current results showed that CSI was detectable for less than 20% of the dataset during the first TSSN reports but this conformed to the relatively small number of instances that the diagnosis could be acquired from the M_g - θ_e relationship. With less pronounced ageostrophic influences, however, the preceding analyses from Table 4.23 were associated with a greater proportion of CSI. Otherwise, the subjective investigation showed little

Table 4.22: As in Table 4.20 except for non-TSSN events.

(A) 700 hPa	$R_o < 0.1$	$0.1 \leq R_o < 0.5$	$0.5 \leq R_o < 1.0$	$R_o \geq 1.0$
Midpoint	1	2	2	2
Prior	1	3	2	1

(B) LHSGR	$R_o < 0.1$	$0.1 \leq R_o < 0.5$	$0.5 \leq R_o < 1.0$	$R_o \geq 1.0$
Midpoint	0	1	3	3
Prior	0	3	3	1

discernible shift in the evolution of stability characteristics. Some resemblance in the identifications from the term-by-term examination of σ^2 (Table 4.7) was noticed but to an extent differed because of the automatic premises implied from Bennetts and Hoskins (1979) and Bennetts and Sharp (1982). Following the conclusions of Smith (2006), both techniques of determining type of instability here revealed that CI transpired for about two to four case studies. From a quantitative inspection of $\theta_e - p$ plots utilizing an alternate collection of convective snow events, Market et al. (2006) discovered an average 1.5 K decrease over shallow depths and the tendency toward greater instability (see their Fig. 4b). While this meant that conditions susceptible to upright displacements were infrequent here, the presence of weakly stable to near-neutral stratification (i.e. very small θ_w and θ_e lapse rates) dominated the environmental profiles. By taking into account this setup and the more realistic descriptions of three dimensional symmetric instability by Jones and Thorpe (1992) and Gray and Thorpe (2001), localized, moist slantwise updrafts might still be favored at the time of convective initiation.

Table 4.23: Diagnosis of the M_g - θ_e relationship for each TSSN event is presented at the time of convective initiation and 3-hours prior. In those flow regimes where curvature was determined to be pronounced, the analysis of stability type was restricted to the profiles of θ_e. From these two techniques, the dominant type of instability above 850 hPa was identified and displayed in terms of percentages to the total sample of case studies. For those profiles where the RH was $< 80\%$, potential symmetric instability (PSI) or potential instability (PI) was possible.

M_g - θ_e	WSS	CSI/PSI	CI/PI	Curvature		
θ_e profile				Stable	Weakly Stable-Neutral	CI/PI
% - Initiation	11.8	11.8/0	5.9/0	5.9	52.9	11.8/0
% - Prior	29.4	11.8/0	5.9/0	5.9	35.3	5.9/5.9

4.2.2 Richardson Number for Slantwise Convection

4.2.2.1 Discrimination of TSSN versus Non-TSSN events

Scaling arguments, such as those found in Emanuel (1986), were applied to investigate physical traits of discrete meteorological phenomenon (i.e. snowstorms featuring lightning). Aspects consisting of centrifugal and buoyancy forcing were dealt with in detail by way of Eq. 2.9 and this study adhered to the linear theory by substituting the relevant height pattern in for the wind observations. Upon calculating the Ri_{sc} from the RUC-2 data, the lowest response from the pressure layer of 800-550hPa was selected so as to maximize any beneficial contribution. Thus, following the rationale for the LHSGR, the level at which the minimum value (LMV;hPa) of Ri_{sc} was retained for this particular diagnostic in each TSSN and non-TSSN event and the summary of the information presented in Table 4.24. In the vertical, the LMV usually was documented to be around 600 hPa (650 hPa) in both datasets at the earlier (later) time frame, although standard deviations of 50-100hPa were evident. The associated MV was subsequently presented as tallies occurring in specific ranges of the Ri_{sc} (Tables 4.25 and 4.26).

If the slope of θ_e was steeper compared to those of M_g, interpretation of the

approach meant that some type of instability was inferred to be present. From the results for TSSN, this translated to an evolution of nine instances decreasing to seven. By dividing up the $Ri_{sc} < 1$ category further, negative (positive) solutions attested to the development of moist, upright (slantwise) convection released from CI (CSI). From Table 4.25, this roughly equal separation showed that both types of instability characterized convective snow about as often. In regards to those readings where the shear was smaller than the stratification, weak resistance to symmetric stability (i.e. WSS) provided the predominant bias during the span of this specific analysis (Table 4.25). Moreover, the exclusive nature of these results to snowstorms exhibiting lighting activity was explored by performing calculations of the Ri_{sc} MV for the non-TSSN collection, with the findings presented in Table 4.26. The criterion was adequately satisfied for a relatively small(er) fraction of case studies in this sample, thus reiterating the lack of *all* three ingredients essential to thunderstorm development.

Table 4.24: Statistics of the level at which the minimum value (LMV;hPa) of filtered, Richardson number for slantwise convection (Ri_{sc}) in TSSN and non-TSSN events for the two time periods utilized, such that μ(s) represents the average (standard deviation). Calculations are based off of the RUC-2 model and are valid at thundersnow onset location and time period. Results are also provided for 3-hours prior to convective initiation. In the case of non-TSSN events, values are determined for the midpoint location.

LMV(hPa)	Initiation/Midpoint	Prior
TSSN	641 (82)	613 (87)
Non-TSSN	657 (79)	592 (58)

Table 4.25: The counts of TSSN events are binned according to ranges in the minimum value (MV) Ri_{sc} from the LMV(hPa) at the time of convective initiation and 3-hours prior. Estimates of the MV required that the RH > 80%.

MV	$Ri_{sc} < 0$	$0 \leq Ri_{sc} < 1$	$1 \leq Ri_{sc} < 10$	$Ri_{sc} \geq 10$
Initiation	4	3	8	2
Prior	5	4	6	1

Table 4.26: As in Table 4.25 except for non-TSSN events.

MV	$Ri_{sc} < 0$	$0 \leq Ri_{sc} < 1$	$1 \leq Ri_{sc} < 10$	$Ri_{sc} \geq 10$
Midpoint	0	2	5	0
Prior	0	2	3	2

4.2.2.2 Discriminator in Banded vs. Nonbanded Episodes

The exact and detailed nature of Eq. 2.9 over that in Section 4.2.1 made it appealing in the identifications of stability regimes. Application of this approach has been effectively studied by Seltzer et al. (1985) and Byrd (1989) for a variety of precipitation bandedness. The results from the latter investigation were more appropriate to the current diagnosis given the overlapping focus areas, the comparable definitions for classifying precipitation bands, and the research motivation in Byrd (1989) as dedicated to the relevance of CSI theory to overrunning precipitation events during the winter season. The main differences in Byrd (1989) were the neglect of the $\frac{\eta_g}{f}$ in Eq. 2.8, the higher RH criterion of 95% in order for the atmosphere to be adequately categorized as saturated, and the previously discussed use of analyzed winds instead of the more theoretical relevant geostrophic values. Following his lead, the MV Ri_{sc} results were partitioned within Table 4.27 into frequency of occurrence of the parameter by degree of bandedness (i.e. only for banding and nonbanding here) at the time of convective initiation for the TSSN events.

The critical stability condition ($Ri_{sc} < 1$) was satisfied in under half of all TSSN occurrences at the time of convective initiation (Tables 4.25 and 4.27). Upon separating the dataset up into banding and nonbanding episodes, Table 4.27 showed the criterion exceeded in 60% and 33.4% of the corresponding subsets, respectively. However, it should be recognized that the size of the two subsets were not entirely comparable, wherein the use of the classification scheme produced to an extent few (i.e. five) instances of bands within the winter season precipitation. Despite this contradiction, the percentages did suggest preference of lower Ri_{sc} for these features. As was performed in Byrd (1989), the method of calculating the mean MV for this parameter was also included in Table 4.27 and additionally illustrated the discrepancy in the two categories. The much lower (higher) solution for banding (nonbanding) was substantially modified by the occurrence of the maxima (minima) extreme of 34.33 (-268.39). So as to minimize the magnitude contribution from the outliers, determination of the median complemented the analysis rather effectively. For either statistic, the MV Ri_{sc} results (mean, median; Table 4.27) obtained for banding regimes (-52.74, 0.65) were lower than their counterpart (5.18, 1.55) as well as for those values computed for *all* TSSN case studies (-11.85, 1.15). The percentage comparisons would have possibly been more foretelling if the overall sample size was larger, in which case a sound basis for exploring statistical significance could have been made. Byrd (1989) accomplished such a task and found that his strongly banded and banded categories were remarkably different compared to the nonbanded results in the same context as established here. Even with these encouraging signs, he did rightfully caution the reader to a particular discriminator, as situations of $Ri_{sc} < 1$ occurred frequently regardless of the degree of bandedness from the observations. Thus, the findings in Table 4.27 showed that Ri_{sc} was useful in descriptively conveying the combined affects of inertial and gravitational instability for a variety of convective structures diagnosed from the radar imagery.

In particular, those events exhibiting evidence of banding *tended* to some extent to be more susceptible to the release of CSI and the development of slantwise circulations.

Table 4.27: Percentage occurrence of MV Ri_{sc} for each bin range as determined for banding and nonbanding TSSN events at the time of convective initiation. Mean and median MV Ri_{sc} was also given and the same procedure performed for *all* case studies for completeness.

% MV	$Ri_{sc} < 0$	$0 \leq Ri_{sc} < 1$	$1 \leq Ri_{sc} < 10$	$Ri_{sc} \geq 10$	Mean	Median
Banding	40.0	20.0	40.0	0.0	-52.74	0.65
Nonbanding	16.7	16.7	50.0	16.7	5.18	1.55
All	23.5	17.6	47.1	11.8	-11.85	1.15

4.2.2.3 Comparison against LTG Characteristics in TSSN events

The customary Richardson number has been used as a means to forecast convective storms, whereby the dimensionless value dictated whether the flow would become dynamically unstable and turbulent (American Meteorological Society 2000). The updated expression (Eq. 2.9) accommodated conditions of CSI and the possibility of electrical discharges in the presence of elevated, slantwise circulations (e.g., Colman 1990b; Zipser and Lutz 1994; Schultz and Schumacher 1999). The MV Ri_{sc} was compared against a couple characteristics from the NLDN, namely polarity and flash count, in order to discover whether any empirical relationships existed. The rank of the MV Ri_{sc} was substituted for the actual solution since the order of magnitude varied substantially and might possibly mask any connection. This ranking began with the most favorable (or smallest) results.

First, the positive fraction of CG flashes (CG_P) was attained from those selected observations defined in Section 3.3.2 and represented in Fig. 3.3. With

a majority of the lightning being of negative polarity, this fraction was rarely above zero in the TSSN case studies (Table 4.28). The relationship was very weak between the MV Ri_{sc} as the correlation coefficient (r) was only 0.24. Still, the negative trendline (not shown) suggested that the higher CG_P tended to occur with the best rankings in Table 4.28. Next, the *null* observations from the non-TSSN events were inserted in the hope to more accurately consider the total count of CG flashes (CG_T). Regardless of the response obtained from Eq. 2.9, limited lightning activity generally transpired near the time and location of convective initiation (Table 4.29). Thus, any supposed association with the position of the MV Ri_{sc} (r=0.16) was again less than inspiring. However, this investigation did reveal at least one very interesting and promising outcome; the nine lowest and most advantageous results from the diagnostic, which happened to satisfy the instability criterion, predominantly ensured the presence of thunderstorms. In summary, the bulk microphysics analysis provided some mixed results and was rudimentary in nature. Nevertheless, some attention was deserved despite being somewhat beyond the scope of the dissertation.

Table 4.28: The relationship between the fraction of positive CG flashes (CG_P) and the rank of the MV Ri_{sc} at the time of convective initiation as determined through categorizing each TSSN event appropriately. The ranking begins with the lowest value of the MV Ri_{sc}.

	$CG_P = 0$	$0 < CG_P < 0.5$	$0.5 \leq CG_P < 1$	$CG_P = 1$
Rank < 4	2	0	0	1
$4 \leq$ Rank < 7	2	0	1	0
$7 \leq$ Rank < 10	1	1	0	1
$10 \leq$ Rank < 13	2	0	1	0
$13 \leq$ Rank < 16	2	1	0	0
Rank ≥ 16	2	0	0	0

Table 4.29: As in Table 4.28 except for the relationship between the total number of CG flashes (CG_T). The associated *null* results from the non-TSSN events at the midpoint time period were also included for completeness.

	$CG_T = 0$	$0 < CG_T \leq 2$	$2 < CG_T \leq 5$	$5 < CG_T \leq 10$	$CG_T > 10$
Rank < 5	0	4	0	0	0
$5 \leq$ Rank < 9	1	3	0	0	0
$9 \leq$ Rank < 13	2	0	1	1	0
$13 \leq$ Rank < 17	1	3	0	0	0
$17 \leq$ Rank < 21	1	2	0	0	1
Rank ≥ 21	2	1	1	0	0

4.2.3 Sounding Characteristics

Some updated data dealing with standard stability indices was offered and served the recommendations of Smith (2006), whose analysis was confined to one season worth of TSSN occurrences. Further, this representation of conditions within wintertime convection would hopefully assist in justifying the value of σ^2. As with Market et al. (2006) and Smith (2006), the noticeable departures in a few of the customary methods (i.e. midlevel lapse rates, MULPL, and MULI) against those associated with no lightning reports was duplicated here. In particular, consultation of the relevant information from Tables 4.30 and 4.31 demonstrated the MUCAPE to be intermittent, small in magnitude (e.g., $7 \pm 30\ Jkg^{-1}$) and, as a rule, not crucial for TSSN to develop. The scarcity of favorable positive buoyancy from this measure in both sets of case studies, however, might be the effect of the coarse resolution in the RUC-2, the possible neglect of the slantwise contribution (i.e. SCAPE, Emanuel 1983a,b) in the detailed consideration of CSI, or that convective overturning was already underway.

Interpretation of the lower estimation in average MULI for thunderstorm situations, the value reduced by approximately 0.5 compared to the *typical* snowstorm, alluded to an environment comparatively less stable. The standard de-

viations for this parameter in Tables 4.30 and 4.31 meant that values tended to reside in the 0 to 2 (^oC) range for all cold-season episodes at both time periods, but it is interesting to note that the lone negative MULI transpired in the TSSN subset. Although the contrast obtained here was not as sizable as that in Market et al. (2006) and Smith (2006), the disagreement was inevitably influenced by the comparison procedures and the choice of the MULPL. With regards to the latter, the pressure level was typically about 50 hPa greater in the other two studies for TSSN, and thus, the most unstable parcel resided at a somewhat lower elevation. Nevertheless, the current results also captured the fact that the distribution varied between 700-550 hPa (Table 4.30), whereas the same computations in non-TSSN events depicted an MULPL restricted to the 550-hPa level (Table 4.31). This distinction appeared to be more pronounced upon examination of the midlevel lapse rates as given by the 1.3 Kkm^{-1} to 1.5 Kkm^{-1} variations in the means. The nearly moist adiabatic lapse rate for convective snow at the time of initiation and three hour prior complied with the findings of both Market et al. (2006) and Smith (2006).

In addition, trend analyses in all of the indices revealed generally constant stability conditions over the three hour period, this being in opposition to the increase in growth rates from the geostrophic (Tables 4.3 and 4.6) and extended approaches (Tables 4.19 and 4.21). This inconsistency could be explained by the fact that the assessment of instability in the recent examination only was concerned with the gravitational aspects of convection and does not incorporate the affects of shear as was accomplished in σ^2 and Ri_{sc}. More importantly, though, the traditional stability indices corroborated with the other seldom employed techniques on the notion that the environments in TSSN events had greater instability compared to non-TSSN events.

Table 4.30: Standard stability indices for TSSN events derived from RUC-2 soundings in NSHARP. Averages and standard deviations (μ(s)) were calculated for the MULPL (hPa), MULI, MUCAPE (Jkg^{-1}), and the midlevel (700-500hPa) lapse rates (Kkm^{-1}) at the time of initiation as well as 3-hours prior.

Sounding parameter	Initiation	Prior
MULPL (hPa)	611(72)	609(78)
MULI	0.9(0.8)	0.8(1.2)
MUCAPE (Jkg^{-1})	0(1)	7(30)
Midlevel lapse rates (Kkm^{-1})	6.2(0.9)	6.3(0.9)

Table 4.31: As in Table 4.30 except for non-TSSN events.

Sounding parameter	Midpoint	Prior
MULPL (hPa)	550(0)	564(24)
MULI	1.4(1.1)	1.0(0.8)
MUCAPE (Jkg^{-1})	0(0)	0(0)
Midlevel lapse rates (Kkm^{-1})	4.9(1.5)	4.8(1.4)

Chapter 5

Results - Composites

5.1 Plot Descriptions

5.1.1 Synoptic Forcing

Forcing mechanisms attributed to snowstorms with electrical activity were considered with the intent to give a brief synopsis of the physical, background environment that engenders the typical stability pattern. The inclusion of analyses from the non-thundering dataset aided in identifying whether there existed any unique characteristics. Accordingly, standard upper air charts of measured or easily derived variables (e.g., heights, θ_e, geostrophic winds, absolute vorticity, and temperature advection) were presented for the two corresponding time periods for TSSN events in Figs. 5.1 and 5.2 as well as for non-TSSN events in Figs. 5.3 and 5.4. Panels (a), (b), (c), (d) correspond respectively to the 900-hPa, 700-hPa, 500-hPa, and 300-hPa pressure levels, this selection following the average fields constructed from the 30-year climatology in Oravetz (2003) and Market et al. (2004). The background maps are shown as reference only and, at best, symbolize the representative area of interest for the case studies.

Many of the basic synoptic features observed in the recent compilation of convective snow occurrences were present in Oravetz (2003) composite classification of *all* cyclones (e.g., compare Fig. 5.2 to Figs. 4.49, 4.51, and 4.52 in

Oravetz, 2003). The warm air advection at 900 hPa was strongest just ahead and to the right of the track of a closed low as it advanced off to the northeast (Figs. 5.1a and 5.2a). While the maximum was slightly displaced from the convective initiation site, this feature was collocated at 700 hPa (Figs. 5.1b and 5.2b). The θ_e analysis also showed an upstream, subtle ridge extending up from the warm sector that became more pronounced by the time of convective initiation. Over the course of the three hours, development of a trowal at 700 hPa and the lowering of heights and positive vorticity advection at 500 hPa (compare Fig. 5.1c to Fig. 5.2c) in the center of the domain coincided with the intensification of the near-surface ETC. This disturbance was eventually positioned as close as a couple hundred kilometers equatorward of the location where wintertime thunderstorms developed. Furthermore, the jet streak emerged within the southwesterly flow along the southern periphery of the domain (Figs. 5.1d and 5.2d) and the favorable left exit region was situated over the low pressure system in support of mesoscale circulations. All of these thermodynamic and dynamic features implied an atmosphere suited for substantial upward vertical motions. The difference in details in the upper air analyses between here and the other set of case studies utilized in Oravetz (2003) and Market et al. (2004) was to be expected as both sample sizes were relatively small and allowed for substantial variations in the diagnostics. Nevertheless, as was intended by Market et al. (2004), pattern comparisons and recognition revealed that the similarities were noticeable.

Routine charts gave a comprehensive picture of the state of the atmosphere in snow producing ETC systems. However, the exclusive nature of these patterns to just thunderstorms required equivalent analyses to be performed for those winter episodes that do no exhibit CG lightning. In this respect, the results from Figs. 5.3 and 5.4 appeared initially to put forward moderate variations. For instance, the central pressure of the ETC was deeper but took on more of a

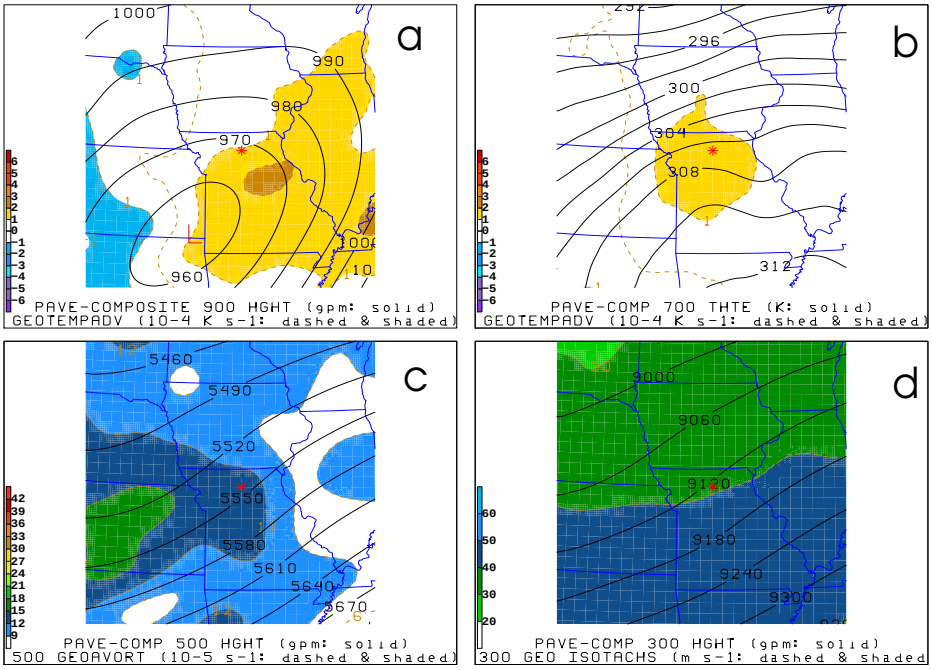

Figure 5.1: Spatial average composites for TSSN events and showing standard upper air charts valid for three-hours prior to convective initiation from the initial analysis of the 40-km RUC model. Panel (a) corresponds to 900-hPa height (gpm, solid lines) and geostrophic temperature advection ($10^{-4}Ks^{-1}$, dashed lines and color shading). Panel (b) corresponds to 700-hPa equivalent potential temperature (θ_e; K, solid lines) and geostrophic temperature advection ($10^{-4}Ks^{-1}$, dashed lines and color shading). Panel (c) corresponds to 500-hPa height (gpm, solid lines) and geostrophic absolute vorticity ($10^{-5}s^{-1}$, dashed lines and color shading). Panel (d) corresponds to 300-hPa height (gpm, solid lines) and geostrophic isotachs (ms^{-1}, dashed and color shading). While often not realistic, the assumption of geostrophy adhered to the theory of CSI and the subsequent formulation of σ^2. The background map is utilized as reference only and the asterisk denotes the approximate position for the average (or typical) TSSN initiation site.

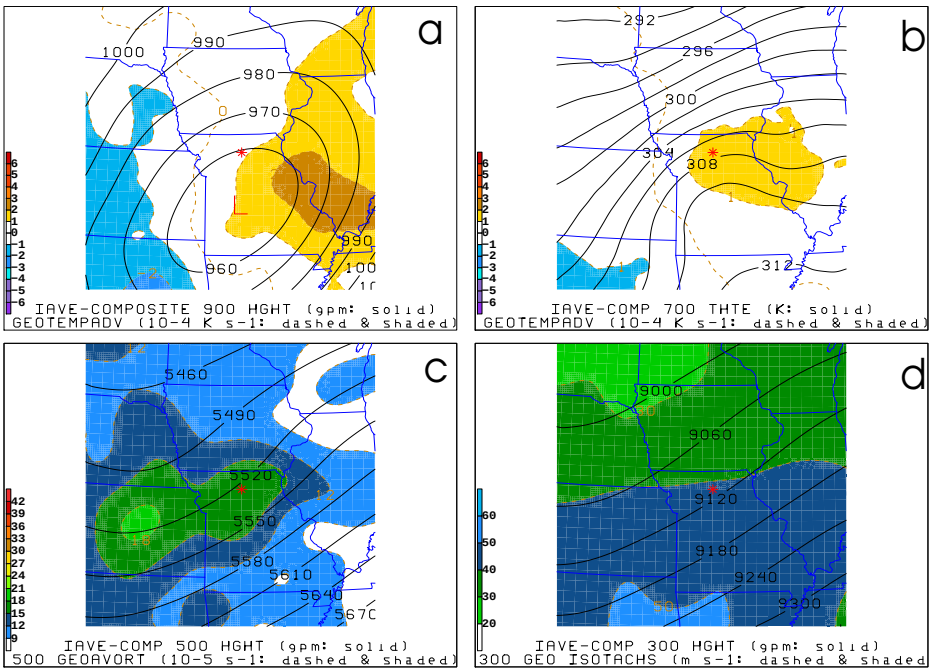

Figure 5.2: Same as in Fig. 5.1 except valid at convective initiation.

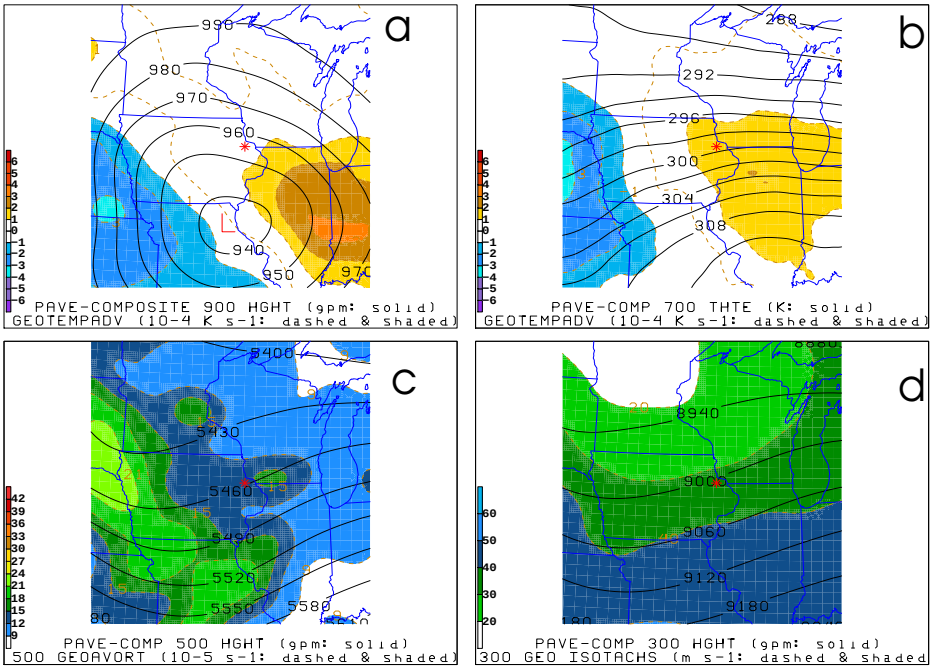

Figure 5.3: Same as in Fig. 5.1 except valid for three-hours prior to the midpoint time period in non-TSSN events.

zonal path in the non-TSSN composites (compare panels (a) in Figs. 5.1 and 5.2 to that in Figs. 5.3 and 5.4). In addition, slightly weaker temperature advections at 900 hPa were also observed in these non-TSSN instances. This signature accompanied less discernible features in the other mean fields examined, such as the much flattened axis of higher θ_e in the midlevels and the broader 500-hPa to 300-hPa trough as seen in panels (b), (c), and (d) of the updated Figs. 5.3 and 5.4. The definitive signs from the depictions will next be substantiated by comparing plots of differing stability indices utilizing the composite methodology.

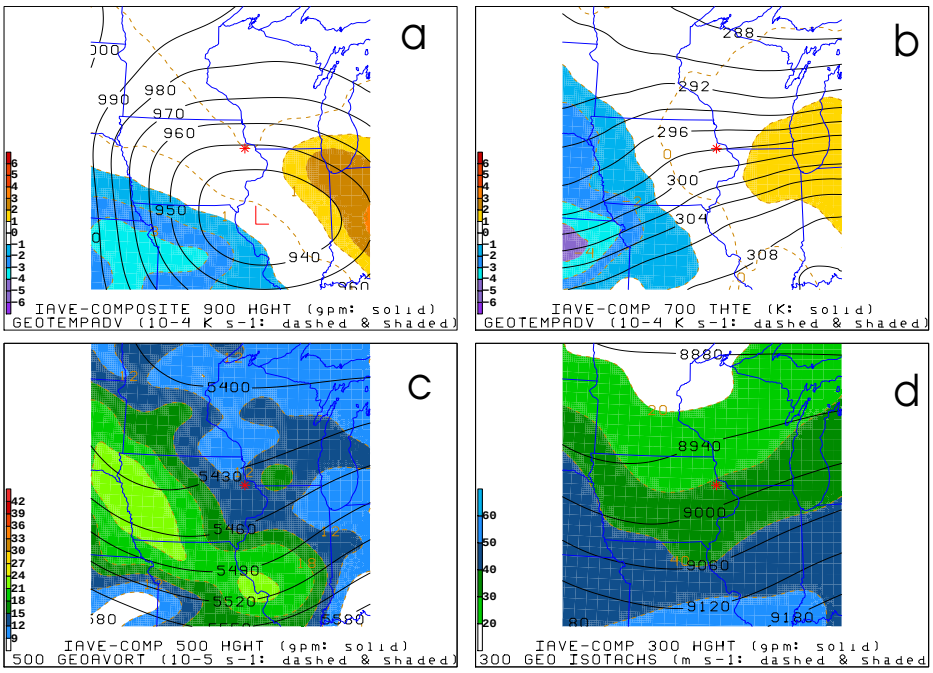

Figure 5.4: Same as in Fig. 5.2 except valid at the midpoint time period in non-TSSN events.

5.1.2 Growth Rate Parameter and 3D-EPV

The composite plots produced here complemented the profile results from a single location. The analyses offered a way to inspect the spatial distribution of stability characteristics and visually track their movement with respect to the most intensive part of the snowstorm (whether or not lightning was present). Averages of σ^2 (h^{-2}) and 3-D EPV ($10^{-6} K kg^{-1} m^2 s^{-1}$) were obtained for each grid point in the smaller domain and combined together to refine the forecast area deemed susceptible to convective development. Since the mean pressure level for the LHSGR was not a standard 50 hPa as in a numerical weather model, the closest approximation for both datasets and time periods was determined to be 650 hPa for the composites. The addition of standard deviations gave value ranges for the two stability parameters near the area of interest.

Figure 5.5 shows σ^2, 3-D EPV, and RH calculated from the RUC-2 model for the set of previously identified convective snow case studies in this study. The smoothed fields show a small area of instability along the southern border (Fig. 5.5 a,c) that expanded a little northward by the time the first CG-lightning occurs(Fig. 5.5 b,d). A larger, surrounding region of slightly stable conditions extended farther into the polar airmass and near the TSSN initiation site. This information is revealed by the orange (red) shaded extent of 3-D EPV values of less than 0.25 (less than zero). The release of either CI or CSI was permitted given the collocation of a nearly saturated atmosphere. While there are some variations in the 3-D EPV pattern depending upon time frame or pressure level selected, the contoured plots of growth rates vary much more. Pockets of higher, positive σ^2 propagate closer to the centroid over the course of the three hours, with panels (c) and (d) in Fig. 5.5 indicating that the LHSGR exhibited the most favorable increase in values. Consequently, as would be expected, the typical atmosphere near thunderstorm development in winter precipitation events is one that shows signs of destabilization.

The standard deviation plots for TSSN events, shown in Fig. 5.6, revealed that variations in values of both σ^2 and 3-D EPV were noticeable amongst the time periods and pressure levels (700 hPa and LHSGR). The shaded regions of growth rates near the area of interest indicated that the range was on the order of the averages established in Fig. 5.5. However, the greatest concentration of darker shading, cellular features tended to be displaced towards the south. This pronounced signature was most likely the result of the often localized and spotty nature of convectively unstable air-masses within the warm sector of synoptic scale disturbances, where lapse rates in θ_w (i.e. term B3) tend to be less (and more often approach conditions of neutrality) than locations poleward of the ETC. On the other hand, the standard deviations in 3-D EPV were not as substantial and never approached in the spatial analysis an order of magnitude larger than the associated mean values shown in Fig. 5.5. The trends in the RUC-2 patterns leading up to convective initiation (compare panels b,d to a,c in Fig. 5.6) were somewhat ambiguous, as the assessment depended on the selected parameter and spatial coordinates, which can be prescribed by horizontal distance relative to initiation site as well as vertical placement. This complexity is not surprising with respect to σ^2 as the regions of greatest magnitude are present over a very confined domain that can often change in size, orientation, shape, and precise location with respect to initiation site as there was a natural evolution in the synoptic environment from one event to the next. While it is true that the mean fields in the composites (Fig. 5.5) would be more representative of *all* thundersnow occurrences if the relatively limited number of events collected were expanded, it is speculated that some of the variability prevalent in Fig. 5.6 might be inherent to the unique combination of factors influencing the diagnosis of growth rates in the atmosphere.

The similarity in synoptic-scale features (e.g., transient ETC) for both sets of snowstorms meant that the necessary dynamic and thermodynamic forcing

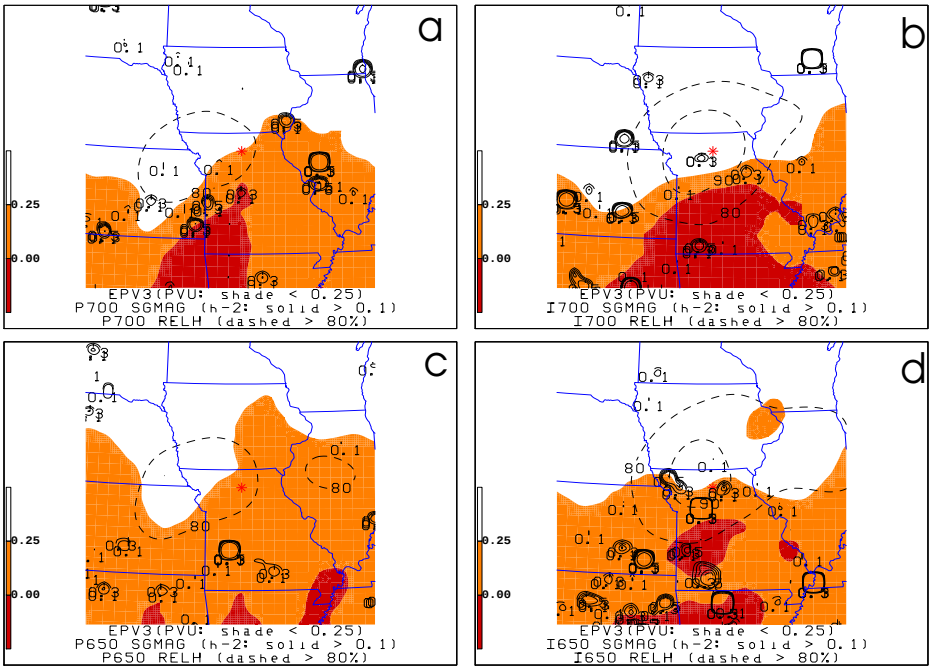

Figure 5.5: Spatial average composites of σ^2 (h^{-2}; solid lines > 0.1), 3-D EPV ($10^{-6} K kg^{-1} m^2 s^{-1}$; orange shading < 0.25 and red shading < 0), and RH (dashed lines for 80% and higher) from the 40-km RUC model. Panels (b) and (d) represent the time of initiation, whereas panels (a) and (c) represent three hours prior. Plots at the 700-hPa level (a, b) and the LHSGR (approx. 650 hPa; c, d) are presented. The background map is utilized as reference only and the asterisk denotes the approximate position for the average (or typical) TSSN initiation site.

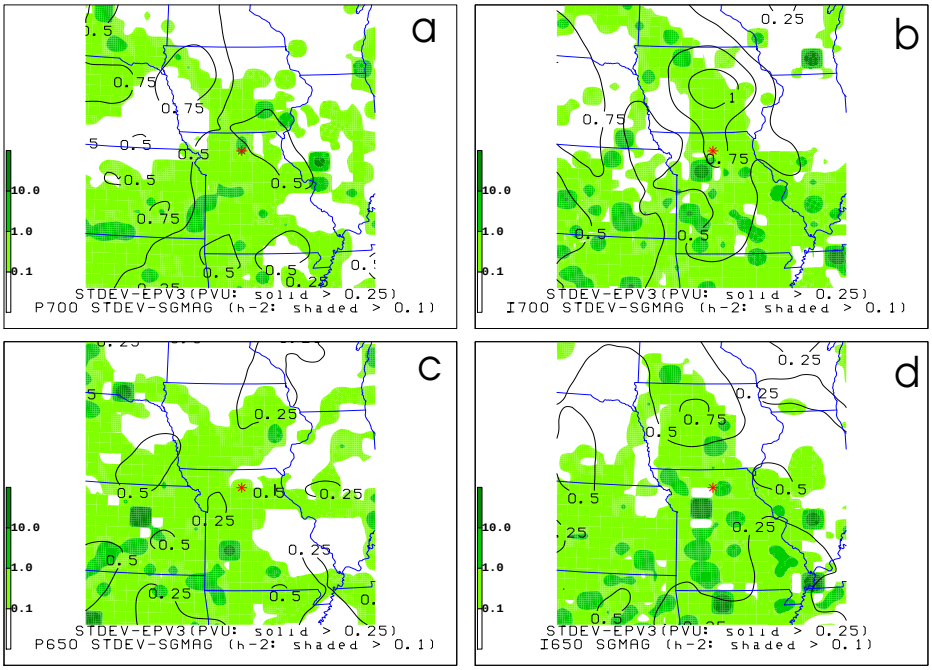

Figure 5.6: Spatial standard deviation composites of σ^2 (h^{-2}; light green shading > 0.5; moderate green shading > 1.0; dark green shading > 10.0) and 3-D EPV ($10^{-6} K\ kg^{-1} m^2 s^{-1}$; solid lines > 0.25) from the 40-km RUC model. Panels and background map are same as that in Fig. 5.5.

mechanisms are present in either case (not shown). In order to effectively identify discrepancies, other ingredient factors for thunderstorm development must be considered. For this purpose, composites of non-TSSN events are displayed in Fig. 5.7. Zones of σ^2 greater than zero were displaced farther equatorward compared to Fig. 5.5, with the lower 3D-EPV estimates not as evident within the domain. Although high RH values near the midpoint site suggest an atmosphere saturated enough for the production of precipitation, these plots indicate the stability regime was insufficient for the development of moist convection in the snowstorm (Fig. 5.7). The smaller number of case studies utilized in the identification process compared to its counterpart would often lead one to conclude that the spatial distribution of standard deviations are greater. An inspection of the statistics in Figs. 5.8 against those in 5.6 corroborates this assumption at least for 3-D EPV in and around the area of interest. In fact, the continuity in the contoured field was more discernible and made tracking the progression and intensification of the maxima for this stability diagnostic much easier. As for σ^2, however, the variations in all time frames and elevations (Fig. 5.8) were diminished overall throughout the domain. This is to be expected since the constituent environment of non-TSSN events is generally colder compared to those snowstorms that feature lightning [e.g., see Fig. 3 in Market et al. (2006)] and, thus should be displaced farther away from an atmosphere prone to upright or slantwise displacements in almost all instances.

5.1.3 Term Contributions to σ^2

Isolation of factors responsible for σ^2 and explaining the resultant, favorable patterns given in Fig. 5.5d required generating model fields for the individual contributions for when the first report of TSSN occurred. Consideration of term (B1) in this manner was deemed not suitable as the corresponding statistics

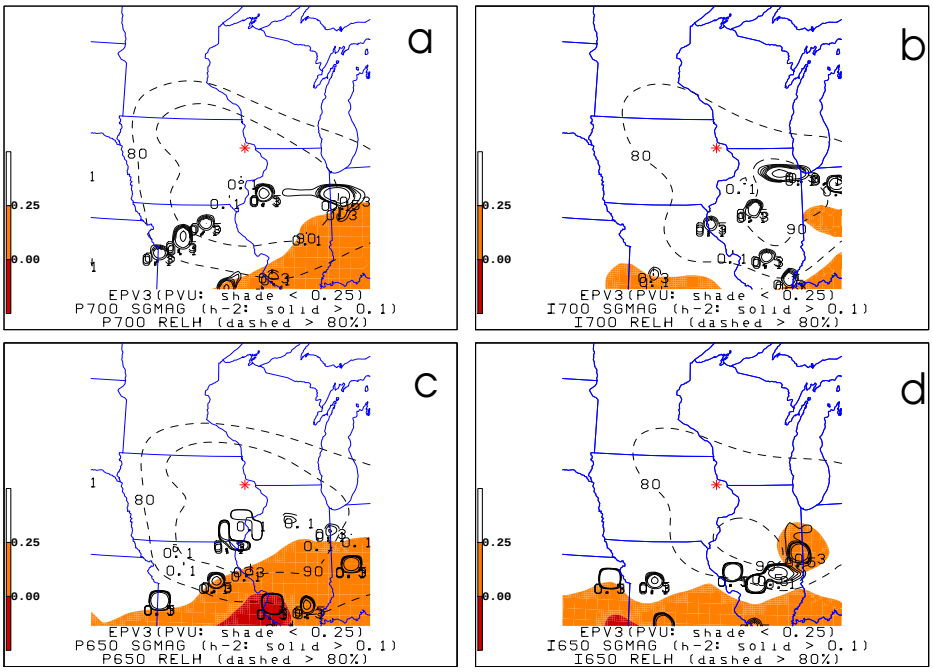

Figure 5.7: Same as in Fig. 5.5 except for non-TSSN events compiled. The asterisk denotes the approximate position for the average (or typical) non-TSSN midpoint site.

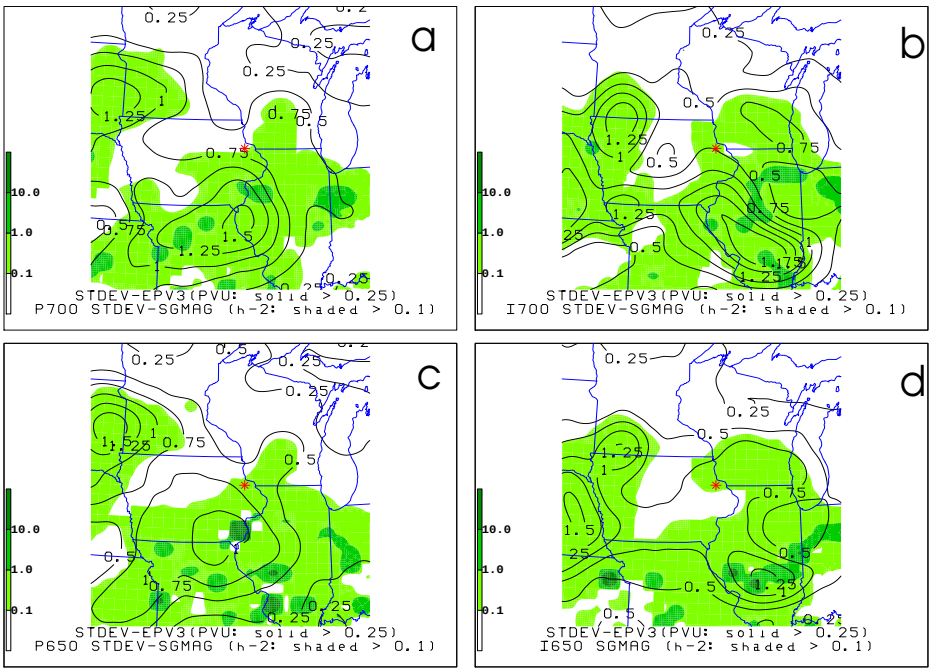

Figure 5.8: Same as in Fig. 5.6 except for non-TSSN events compiled.

revealed the substantial influence of constants within the expression (Table 4.7). As a result, both mean and standard deviation composites were generated for the other three contributions at the LHSGR (i.e. 650 hPa). First, the evaluation of panel (a) in Fig. 5.9 indicated relatively, greater cyclonic flow oriented southwest to northeast and positioned near the representative initiation site. Moreover, the magnified negative response (i.e. -16*$10^{-9}s^{-2}$) in the average values suggested a general opposition to the affects of horizontal shear within the area of interest. Still, this plot (Fig. 5.9a) also advanced some evidence that large case by case fluctuations exist, which allowed for the possibility of more favorable conditions in the analysis of inertial instability.

The counterbalance of term (A) so as to produce the high, positive σ^2 results in the center of the domain appeared to be fulfilled by features in terms (B2) and (B3) of Figs. 5.9b and 5.9c, respectively. In the case of the former, positive values were present over the RUC-2 grid and the maximum axis was located just west and upstream of where the first signs of wintertime convection emerged. Along with the examination of some simple thermodynamic properties, such as temperature and dewpoint at 650 hPa (not shown), the adjoining strong gradients in the diagnostics implied the existence of an elevated frontal zone. On the other hand, the juxtaposition of comparable magnitudes (2 to 3 $10^{-10}K^2m^{-2}$) in the standard deviations also indicated that there were occasions in which term (B2) had a negligible role in the production of growth rates (Fig. 5.9b).

Within the warm sector of the synoptic scale system, the last component concerning moist static stability portrayed conditions for which reduced resistance to vertical displacements existed. More specifically, the zone of less than 1 Kkm^{-1} lapse rates of θ_w in Fig. 5.9c extended a short distance poleward of the surface ETC to barely encompass the centroid position. Farther north, the analysis of term (B3) showed a sharp transition to atmospheres much less susceptible to the development of convection. As was already explained, profiles approaching

moist neutrality would particularly amplify the response to σ^2, something which the results bear out. This hypothesis was reinforced by the appropriately placed large stretch of greater than 0.1 h^{-2} from the total response in Fig 5.5d. Additionally, these numerous isolated structures occurred largely equatorward and in the midst of magnitude errors equating to a positive extreme in term (B3) and conveyed the notion that elevated PI was most probable along the southern periphery of the domain, as suggested by and Nolan (formalized in Schultz and Schumacher (1999)). Finally, the overlapping areas of high averages in term (B2) and weak but negative statistics of term (B3) close to the location of TSSN development not only facilitated the amplification of small-amplitude disturbance but also the presumption of CSI from the evaluation of individual contributions (Fig. 5.9).

5.1.4 Tendency of σ^2

The distribution of average tendencies in σ^2 were scrutinized in the vicinity of the centroid from the composites in Fig. 5.10. Besides utilizing positive values of this parameter instead of 3-D EPV, panels (a), (b), (c), and (d) portray identical fields in TSSN occurrences as to what was given in Fig. 5.5. The relevant shaded regions, which were sporadic and irregular in time and space, represented instantaneous increases in growth rates that sometimes became magnified by two or more orders of magnitude. The combination of the seldom employed parameter and its temporal derivative demonstrated that the beneficial development of instability and further destabilization of the environment coexisted largely ahead of the advancing upper-level trough (Fig. 5.10). Despite the necessary positive values in this portion of the domain, the limited moisture content from the analyses violated the sufficient criterion for CSI in σ^2.

As for locations closer to the convective initiation site within the colder airmass, this shortcoming was avoided by the high RH revealed in Fig. 5.10. It

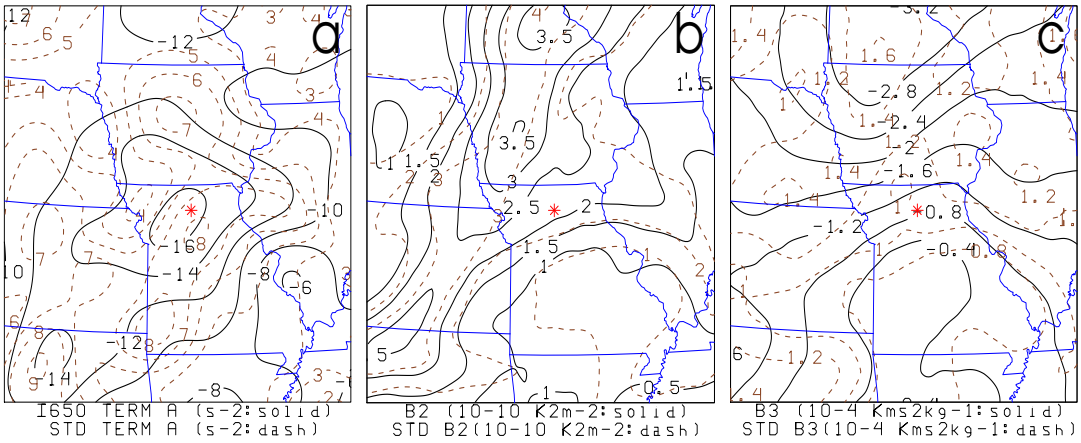

Figure 5.9: Spatial composites of the term contributions to σ^2 for the LHSGR (approx. 650 hPa) and valid at TSSN onset. Panels (a), (b), and (c) represent, respectively, average (solid lines) and standard deviation (dashed lines) fields of term (A; $10^{-9}s^{-2}$), term (B2; $10^{-10}K^2m^{-2}$), and term (B3; $10^{-4}Kms^2kg^{-1}$). Term (B1; $10^{-3}m^3kg^{-1}K^{-1}$) was ignored in this investigation.

was also interesting to note that the evolution in typical results from Eq. 2.11 obtained in the area of interest accurately verified the predictions of Eq. 3.2 from the previous three hours. More precisely, computations greater than 0.1 h^{-2} for growth rates at the latter time period (Fig. 5.10b,d) supported the upward trend assessment of 0.1-10.0 h^{-3} from the earlier time frame (Fig. 5.10a,c). This illustration, nonetheless, would not be complete without taking into account the standard deviation horizontal plots presented in Fig. 5.11. As the regions of largest variations generally matched the highest average σ^2 tendencies, some uncertainty in the conclusions has to be acknowledged as there would most likely not be duplicate features in every TSSN case study. Finally, the value of this investigation was reached again by constructing equivalent diagnostics for those snowstorms where lightning activity was absent (i.e. Figs. 5.12 and 5.13). Unlike its counterpart, resistance to vertical motions was much stronger near the representative location for non-TSSN events as the best structures in the mean attributes of the growth rate parameter were displaced a greater distance to the south. Thus, while nearly saturated conditions existed in these particular occasions, the unshaded regions identified represented locales where Eq. 3.2 was either a small positive value or < 0 and suggested the unlikely probability of wintertime thunderstorm formation in the near future (Fig. 5.12). Relatively minor fluctuations in this select sample were also noted in the northern and central areas of the grid in Fig. 5.13, thereby revealing a more uniform nature in the results compared to the TSSN dataset.

5.1.4.1 Relationship to Forcing within Convective Snow

The findings from Table 4.12 supported the basis that adjustments to the stability regime emerged from a mix of physical mechanisms in the atmosphere. As was established in that strategy, objectively analyzed charts also accommodated the venture into understanding the role of the individual contributions to

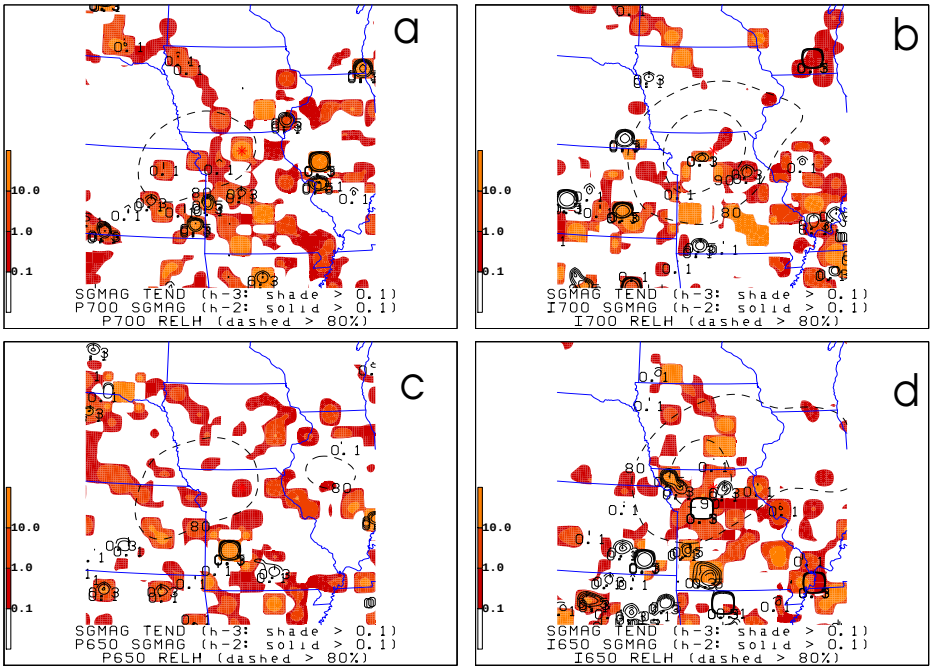

Figure 5.10: Spatial average composites of σ^2 (h^{-2}; solid lines > 0.1), σ^2 tendencies (h^{-3}; red shading > 0.1; orange-red shading > 1.0; orange shading > 10.0), and RH (dashed lines for 80% and higher) from the 40-km RUC model. Panels and background map are same as that in Fig. 5.5.

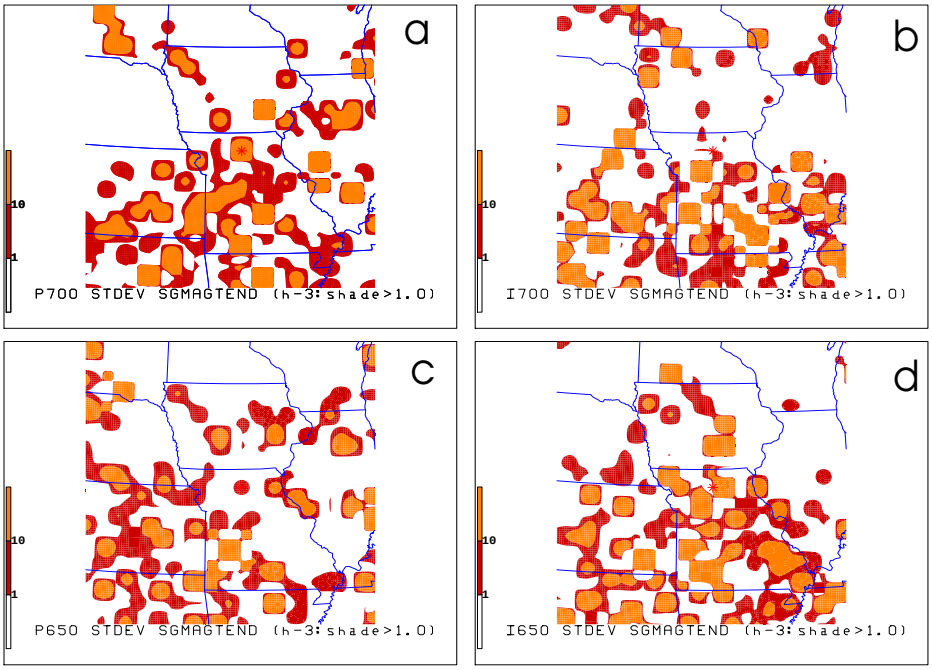

Figure 5.11: Spatial standard deviation composites of σ^2 tendencies (h^{-3}; red shading > 1.0; orange shading > 10.0).

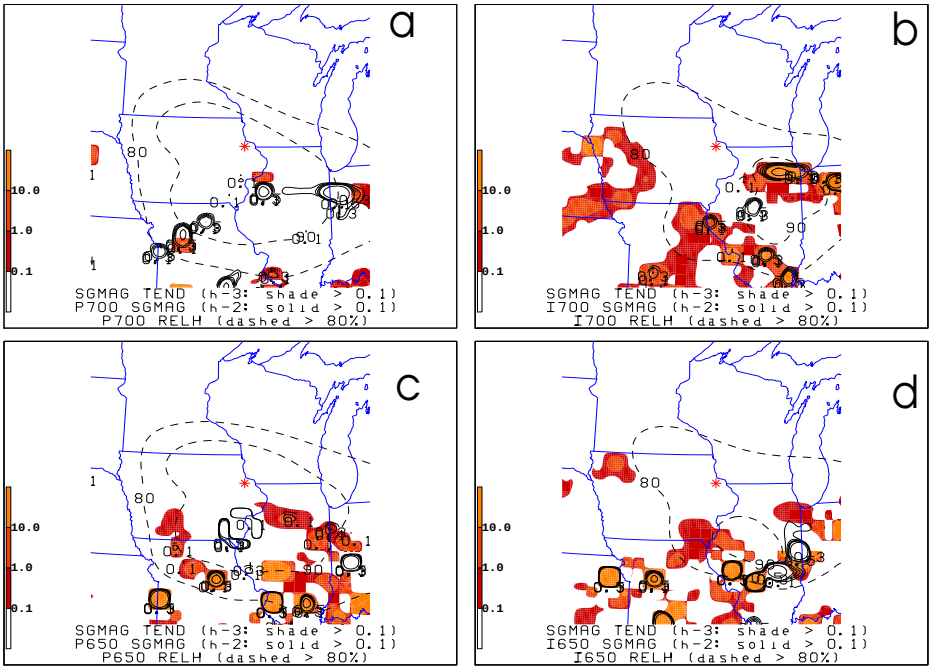

Figure 5.12: As in Fig. 5.10 except for non-TSSN events compiled.

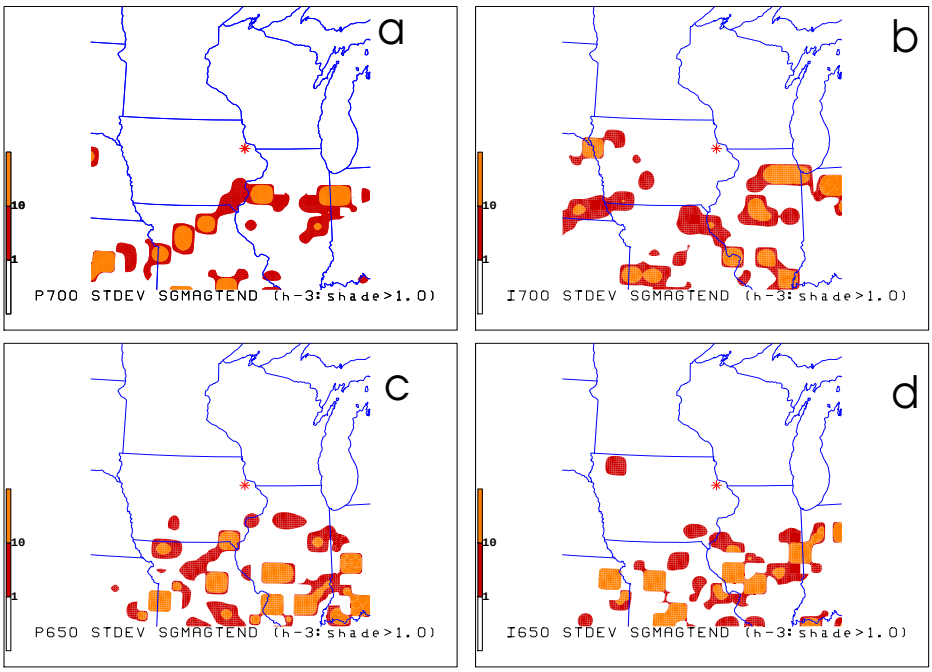

Figure 5.13: As in Fig. 5.11 except for non-TSSN events compiled.

σ^2 tendencies in the vicinity of the area of interest and leading up to the onset of convection. Since modification of growth rates resulting from term (E) was initially determined to be much smaller than those computed from (C), (D), and (F), only averages of the latter three were incorporated in the composites. In order to just isolate positive responses to Eq. 3.2 , Fig. 5.14 only portrayed the combined layout of dry/moist frontogenesis, increases in anticyclonic vorticity, and lessening of the moist static stability. First, the shaded regions identified matched in large part to the shape, placement, and amplitude of the aggregate results from Fig. 5.10. In effect, the magnified tendencies corresponded to very small values of $\frac{\partial \theta_w}{\partial p}$ and an upward progression in $\frac{\partial}{\partial t}\frac{\partial \theta_w}{\partial p}$. This setup would act to overturn θ_w (or for that matter θ_e) surfaces, something which both Bennetts and Hoskins (1979) and Emanuel (1983a; see his Fig. 5) mentioned as favorable in strong growth of the instability and an atmosphere more prone to gravitational convection. Furthermore, the prominent role of this term (F) was evident throughout the central and southern portions of the domain during the short term evolution examined (Fig. 5.14). Still, both panels (a) and (c) of Fig. 5.14 showed the greatest increases of 1.0-10.0 h^{-3} occurred right over the convective initiation site three hours prior to the first report of TSSN. As a result, the destabilizing component properly preconditioned the environment for lightning generation within the cold-season precipitation.

The other feature of note is the greater impact of term (D) by the end of the three hour period, despite the observation that these averages were generally an order of magnitude or smaller compared to the static stability tendency (compare panels (b),(d) in Fig. 5.14 to those of panels (a),(c)). Similar to the point statistics offered in section 4.1.3.1, forcing from elevated frontogenesis was more instrumental closer to the time and location of convective initiation, as illustrated at either pressure level in Fig. 5.14b,d. While these results assert that thermodynamic processes were essential to changes in σ^2, the contoured area of term

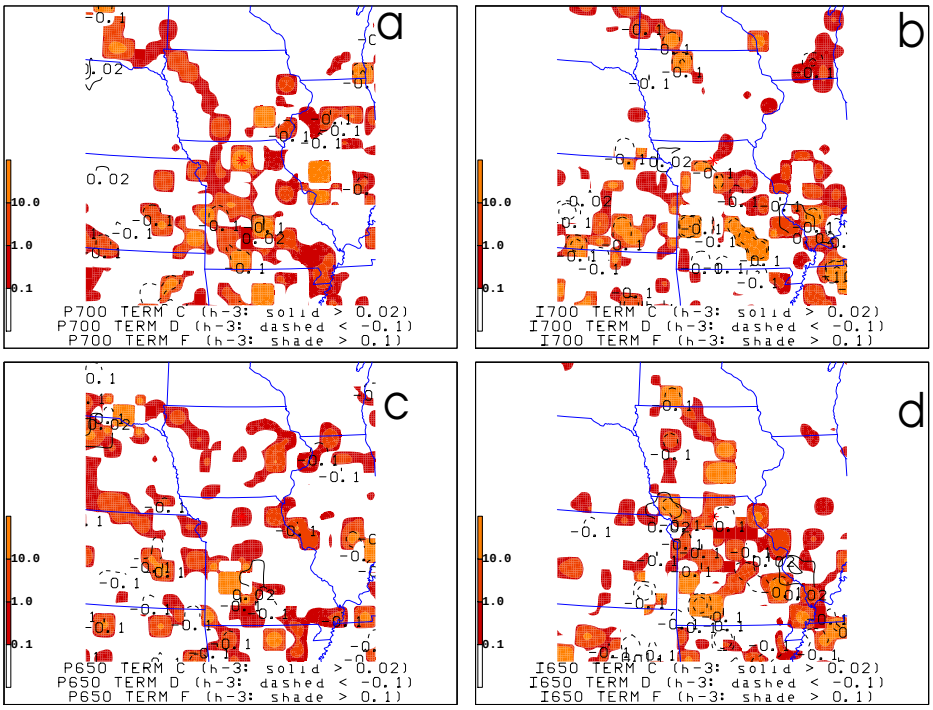

Figure 5.14: Spatial average composites of the term contributions to σ^2 tendencies from fields of term (C; h^{-3}, solid > 0.02), term (D; h^{-3}, dashed < -0.1), and term (F; h^{-3}, red shading > 0.1; orange-red shading > 1.0; orange shading > 10.0). Term (E; h^{-3}) was ignored in this investigation.

(C) representing decreases for $\frac{\partial \zeta_g}{\partial t}$ were minor in regions covered, usually small in value, and displaced at some distance away from the centroid of the composite region. Thus, it should be restated that the combined terms produced positive contributions on the left-hand-side of Eq. 3.2 to a greater (lesser) extent in and around the TSSN report area at the earlier (later) time frame.

5.1.5 Extension to Ageostrophic Influences

The groundwork for σ^2 in Bennetts and Hoskins (1979) presumed an approximately saturated atmosphere and the processes associated with symmetric instability. From this quasi-geostrophic (QG) framework, where $R_o < 0.1$, the most appropriate synoptic setup would be one of weak cyclogenesis and a less amplified trough structure. In stronger flow regimes, however, the strict constraints imposed become less plausible and more complex forcing mechanisms must be included. By essentially replacing the geostrophic wind shear in the evaluation of growth rates with that of analyzed or observed values, an "extension" of QG diagnostics in the example of Eq. 2.13 was able to accommodate for more realistic structures while also retaining the simplified 2D expression of Eq. 2.11. Such an approach has been utilized by Tsou et al. (1987) with regard to height changes from the height tendency equation and by Melick (2003) in his comparison of vertical motions obtained from different forms of the omega equation.

Assimilation of σ_e^2 into the composite domain for convective snow episodes was pursued to identify remarkable features duplicated or possibly missing from the original plots, such as that from Fig. 5.5. The highest resultant averages are displayed in Fig. 5.15 and showed the contoured regions to be largely positioned in identical locations corresponding to σ^2. Still, there was some displacement in the patterns and in some situations isolation in the positive growth rates. The extended estimates were also generally amplified in magnitude, this being evident for example by the sometimes 0.1 h^{-2} increase in and around the TSSN activity. On the other hand, the exact difference between the zones of best values was difficult to resolve as the variations were abrupt over a short distance in the plots. Coincidentally, this was the main reason for the small spectrum of growth rates displayed in either Fig. 5.5 or Fig. 5.15. In spite of the discrepancy, the presence of a (less) more favorable signal at the (earlier) later time period and

the preference of the $LHSGR_e$ (once again near 650 hPa) over that of 700 hPa corroborated the conclusion obtained in the geostrophic approximation (compare Fig. 5.15 to Fig. 5.5).

Inspection into the significance of ageostrophic shear was also aided by the spatial illustration of R_o (as given by Eqns. 2.12 and 2.13), for which no clear, discernible trend was discovered vertically or over the three hour period (Fig. 5.15). Besides the erratic nature in the shaded portion of the domain, the smallest departures from geostrophy ($R_o < 0.1$) were present only to a limited extent. The intermediate range in this parameter was more prominent but was still often displaced to the periphery of the composite field. Near the convective initiation site, however, the ratio easily surpassed unity on average and would thus classify the attendant flow as mesoscale (Fig. 5.15). Although the idealized balanced state of σ^2 provided an appropriate first pass to describing the stability regime, this method was incapable of describing the more accurate 3D aspects of growth rates. More precisely, these findings were not necessarily attributed to each TSSN event seeing that standard deviations in σ_e^2 and R_o were quite substantial from Fig. 5.16. Regardless of pressure level or whether considering the time of initiation or prior to lightning development, calculations around the area of interest were 1.0-10.0 h^{-2} and greater than 0.1, respectively. As these results were on the same order of scale as, if not larger than, the mean statistics, Fig. 5.16 illustrated that the affects of curvature were not consistent in each scenario and depended upon the type and strength of the synoptic-scale system present.

The set of non-TSSN case studies were also examined in respect to the significance of net accelerations within the fluid flow, with the representative analyses shown in Fig. 5.17 and Fig. 5.18. The comparison of instability growth utilizing σ^2 (Fig. 5.7) versus that of σ_e^2 provided a similar conclusion to that reached in the sample of snowstorms featuring lightning flashes. By neglecting the occasional noticeable differences, the subjective evaluation revealed once again that

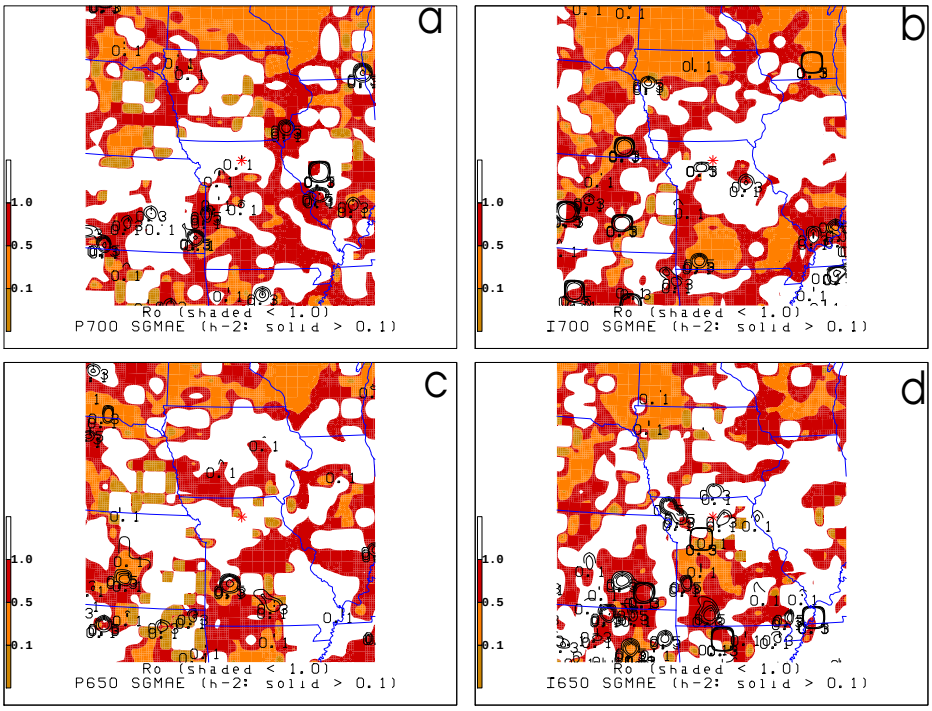

Figure 5.15: Spatial average composites of σ_e^2 (h^{-2}; solid lines > 0.1) and R_o (red shading < 1; orange shading < 0.5; dark orange shading < 0.1) for the TSSN events. The panels represent the same pressure levels and time periods as in Fig. 5.5.

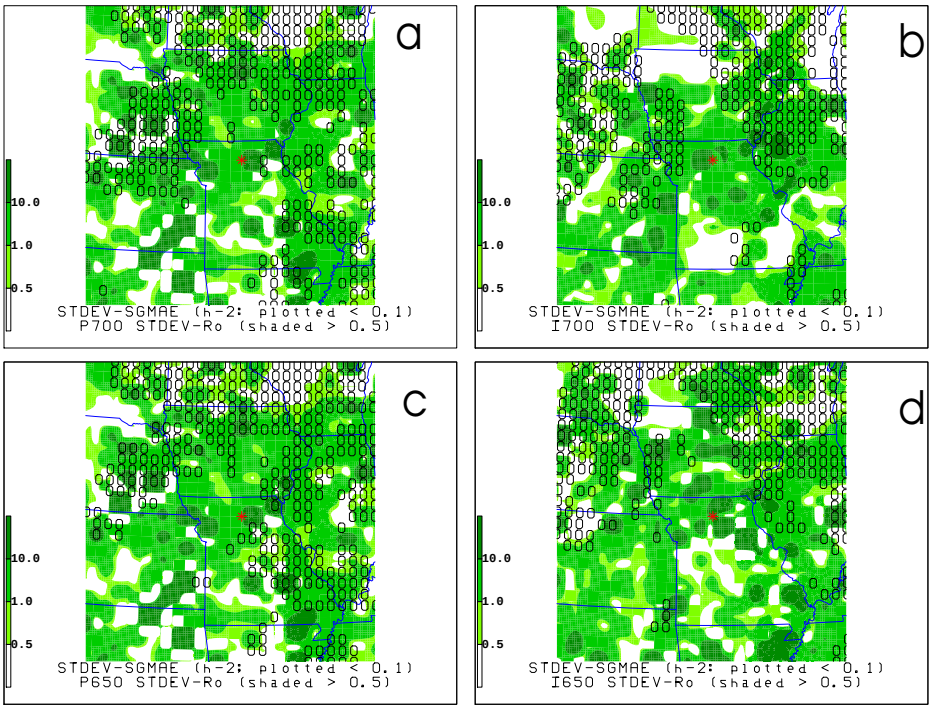

Figure 5.16: Spatial standard deviation composites of σ_e^2 (h^{-2}; values plotted $<$ 0.1) and R_o (light green shading > 0.5; moderate green shading > 1.0; dark green shading > 10.0) for the TSSN events. The panels represent the same pressure levels and time periods as in Fig. 5.5.

the geostrophically balanced state was reasonably accurate in identifying regions susceptible to intensification of small atmospheric disturbances. Furthermore, the extended approach showed that the most pronounced instability features in the diagnosis were shifted away from the center of the grid and towards the south and east, something that was contrary to the occurrences of wintertime convection (compare Figs. 5.15 and 5.17). The impact of non-geostrophic processes, given by the parameter R_o, revealed substantial values around the area of interest. Consequently, these additional results further advanced the fact that strong flow curvature occurred at someplace in the vicinity of the cold-season precipitation inspected whether or not thunderstorms were observed. This judgment was not entirely surprising by taking into account the methodology of selecting only those events associated with ETC and the associated upper-level dynamics. Finally, the standard deviation patterns calculated from Eqs. 2.13 and 2.12 were also generated in Fig. 5.18 and exhibited a less considerable range compared to TSSN distributions (Fig. 5.16), especially for that of R_o.

5.2 Other Stability Techniques

5.2.1 Richardson Number for Slantwise Convection

Evaluation of the ratio in slopes pertaining to the effects of shear and stratification was ascertained for both TSSN and non-TSSN episodes in order to substantiate the diagnosis reached in σ^2. Based upon the averages in Table 4.24, spatial maps of Ri_{sc} at the 600 hPa (650 hPa) level were supposed to represent the LMV at the earlier (later) time period given the closest, standard increment to be 50 hPa in the RUC-2 model (similar to the reasoning in the LHSGR). The seclusion of grid points with solutions less than 10 in Fig. 5.19 supported the identification of atmospheres only affected by WSS ($1 < Ri_{sc} < 10$), CSI ($0 < Ri_{sc} < 1$), and CI ($Ri_{sc} < 0$). It was interesting to note the usual conditions in convective snow case studies to be quite stable at the TSSN initiation

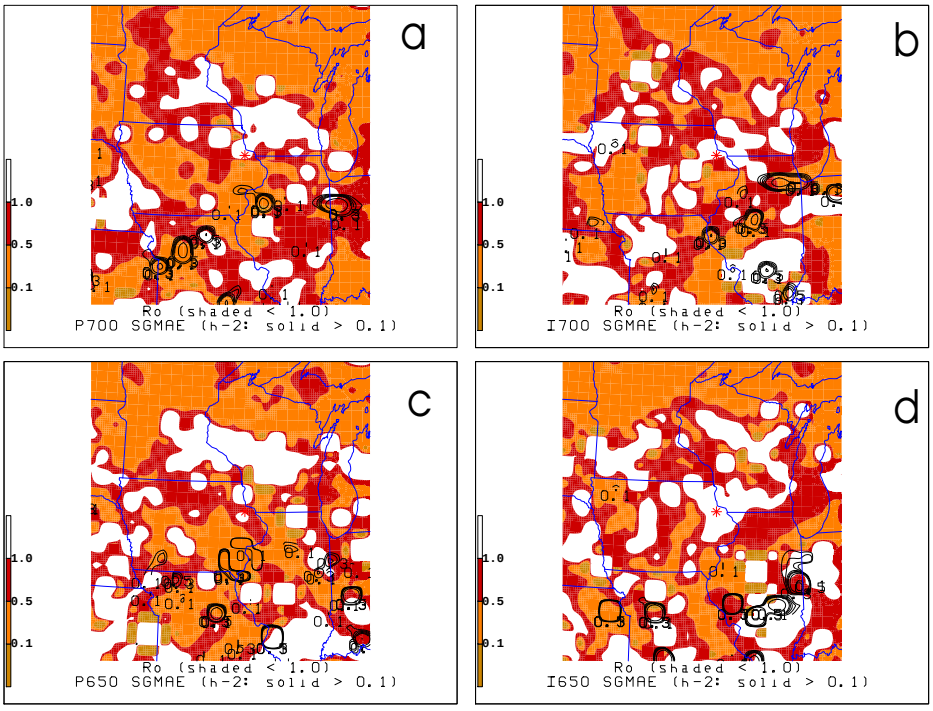

Figure 5.17: Same as in Fig. 5.15 except for non-TSSN events compiled.

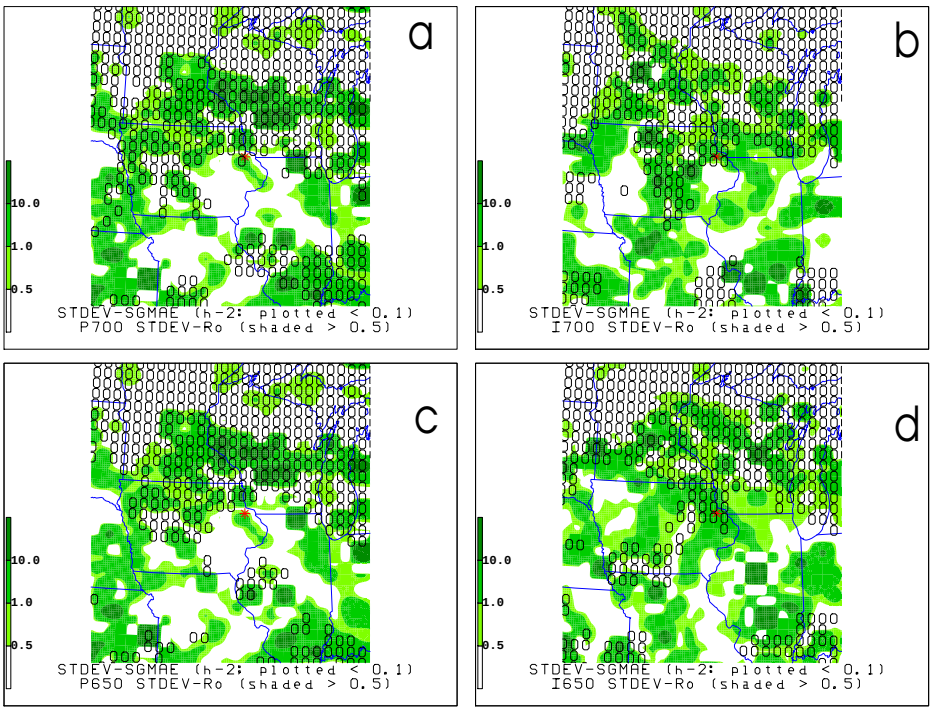

Figure 5.18: Same as in Fig. 5.16 except for non-TSSN events compiled.

site (Fig. 5.19) with more advantageous results situated a couple of grid points away horizontally and elevated vertically by 50-100hPa (not shown). The latter, apparent disagreement in the LMV at the centroid with the statistics presented in Chapter 4 was more the result of interpolation (i.e. numerical nature) and less of a physical concern. Furthermore, there was continuity in the features of this diagnostic with time and a zonal shift in the regions of weakest stability to instability. In particular, WSS was present southeastward immediately prior to TSSN development (Fig. 5.19a) while another elongated zone of WSS and CI progressed closer from the west (Fig. 5.19b). In the middle of these two latter types of regimes, the absence of grid points exhibiting conditions of CSI related to a sharp transition zone that the resolution of the RUC-2 could not resolve properly using the Eq. 2.9.

Support for this type of response to synoptic-scale and mesoscale forcing was assessed by looking back at the term-by-term diagnosis of σ^2 in Fig. 5.9. These techniques proved to be inconsistent in the lack of overlapping patterns but this was presumably due to the substantial difference in scale analysis of the two stability parameters (with a general 2 to 3 magnitude order increase in Ri_{sc}) and the resultant greater smoothing of anomalies associated with growth rates. Along these lines, this was also likely the reason for the very large standard deviations in Fig. 5.19 taking up the sizable, non-shaded portion of the composite domain. While the mean results for Ri_{sc} never dropped below unity right at the *ideal* location for TSSN initiation, the variations (approximately to the degree of 10-1000) were sufficiently substantial for the instability criterion to be met from event to event. Furthermore, the analysis revealed a slight downward trend in this parameter which happened to mutually agree with the increase in σ^2 (compare Fig. 5.5 to Fig. 5.19).

The analogous calculations of the Ri_{sc} in the subset of snowstorms lacking lightning CG flashes was presented in Fig. 5.20. While similar tendencies were

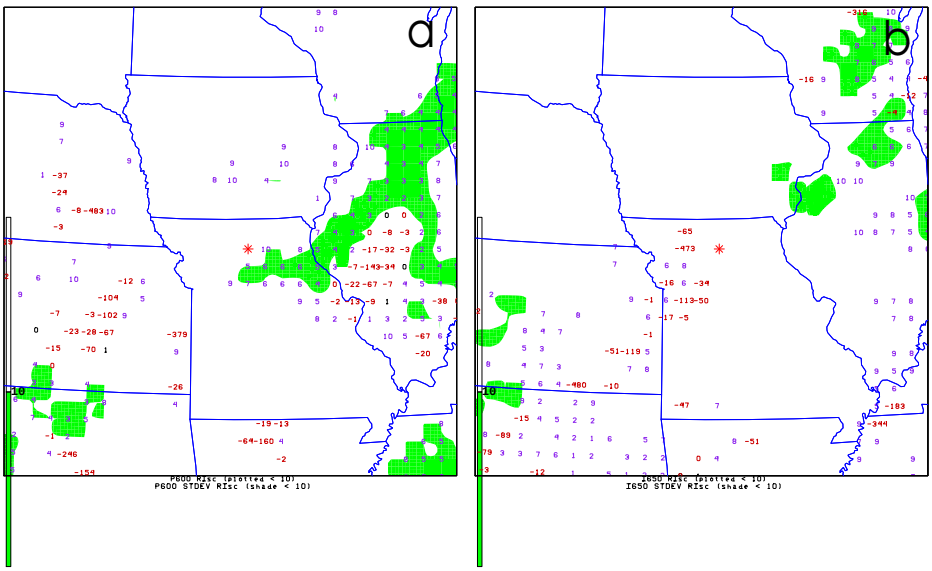

Figure 5.19: Spatial average composites of Ri_{sc} (1 < values plotted < 10, purple; 0 < values plotted < 1, black; values plotted < 0; red) along with standard deviations (green shading < 10) of this parameter in the sample of TSSN events.

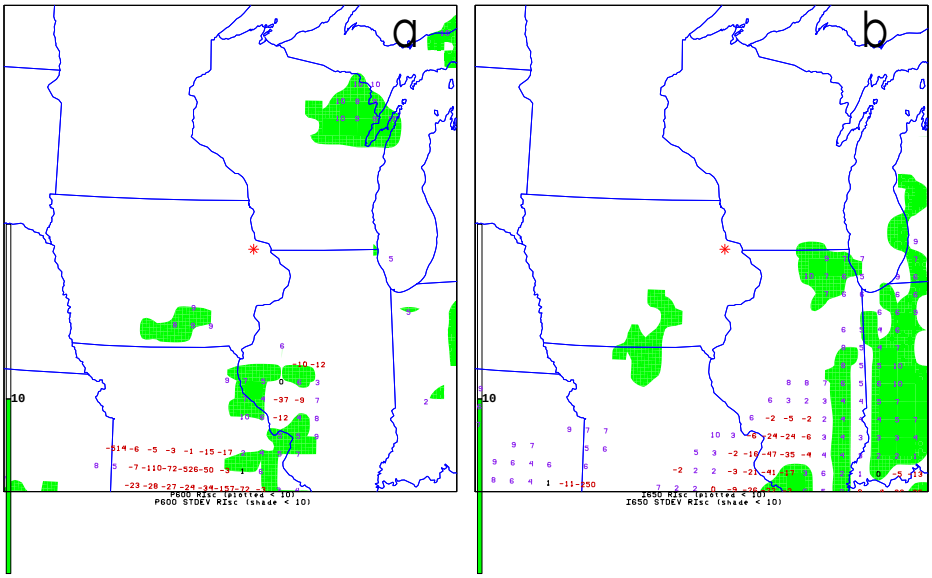

Figure 5.20: As in Fig. 5.19 except for non-TSSN events compiled.

noted over the short duration, the non-TSSN averages indicated conditions of greater stability compared to the TSSN statistics (compare Fig. 5.19 to Fig. 5.20). Similar to the interpretation of the growth rates obtained in the plots (Figs. 5.7 and 5.17), the best computations for this metric were positioned principally in the warm sector and farther away from the subfreezing airmass and precipitation (e.g., Figs. 5.3 and 5.4). Again, the range in Ri_{sc} was very impressive across a considerable region in Fig. 5.20. Yet, by also considering the results from Tables 4.25 and4.26, both approaches suggested overall more instances of greater susceptibility to slantwise (low positive response) and upright (negative response) convection in atmospheres characterized by TSSN reports.

5.2.2 Traditional Stability Indices

In the works of Market et al. (2006) and Smith (2006), a select few traditional stability indices have shown to be of some utility in the determination of wintertime thunderstorms associated with snowfall. These associated studies, along with the information conveyed in Chapter 4, specified the following key indicators to be that lapse rates were approximately moist adiabatic in the middle troposphere, values for the MULPL occurring in the 700-600hPa range, and a low but possibly still positive MULI (i.e. estimates less than 1). Furthermore, the addition of small amounts of CAPE at some elevation in the corresponding soundings (i.e. MUCAPE) would be desired but not crucial in the production of lightning. Yet, these findings were assessed locally and could not illuminate on characteristics in all dimensions. Thus, the evaluation will be expanded from the vertical treatment at the ideal location to portray the plan-view arrangement of these conventional stability metrics.

The detection process of the most unstable characteristics in GEMPAK involved searching every 50 hPa from 800 hPa to 550 hPa for all the TSSN and non-TSSN events. This meant that there was a neglect of boundary layer influences, these being substantial enough to override statistics obtained further aloft at certain grid points. With elevations much higher in the western Plains, though, results would be artificial in nature as pressure surfaces considered to represent near surface conditions (e.g., 1000 hPa, 950 hPa) in many locations would actually reside below ground level. The exclusion of this potential inaccuracy issue helped to clarify the details of elevated instability distinctive to thunderstorms forming in the central United States during the winter season (e.g., Colman 1990 a,b; Market et al. 2006). Following the process laid out in Market et al. (2006), the MULPL was set at the same level with the best CAPE, or if not present, the lowest LI. Once this value was set, construction of gridded fields for the three MU indices (i.e. MULPL, MUCAPE, MULI) was possible.

Along with the midlevel lapse rates, average and standard deviation plots were than finally generated separately for the snowstorms featuring lightning as well as for those that do not exhibit any CG flashes.

5.2.2.1 Midlevel Lapse Rates

Midlevel (700-500hPa) lapse rate fields were constructed from the compositing process of the 17 TSSN case studies, with averages and standard deviations both represented in Fig. 5.21. The nearest grid points surrounding the convective activity exhibited estimates near -6 Kkm^{-1} with little change in this measure of stability. The discriminating threshold of -6.5 Kkm^{-1}, particularly asserted in Market et al. (2006), had more of an influence in the plots at the earlier time frame. To be more exact, regions of PI/CI and the attendant axis of higher average magnitudes was oriented from southwest to northeast and extended into the subfreezing air mass (Fig. 5.21a). By the point that the first CG flashes occurred, however, this feature was practically nonexistent and the opposing trough of reduced lapse rates positioned poleward became enhanced from the previous three hours (Fig. 5.21b). The affiliated standard deviations were 0.5 to 1.5 Kkm^{-1} within the horizontal distribution but remained a little less than 1 Kkm^{-1} near the site of interest.

An inspection of the snowstorms that featured no lightning activity revealed greater gradients of mean $\frac{\partial T}{\partial z}$ in Fig. 5.22 compared to that in Fig. 5.21. The associated plots indicated typical calculations to be in the range of -4.5 Kkm^{-1} to -5.0 Kkm^{-1} for the area associated with the ideal radiosonde station. As with the TSSN subset, the progression in lapse rate patterns during the short time interval was similar. In this scenario, however, the least advantageous results were amplified with the affected region growing larger in extent and becoming almost coincident with the center of the domain (Fig. 5.22). Although the standard deviations were greater than 0.5 Kkm^{-1} in Fig. 5.22 near the representative

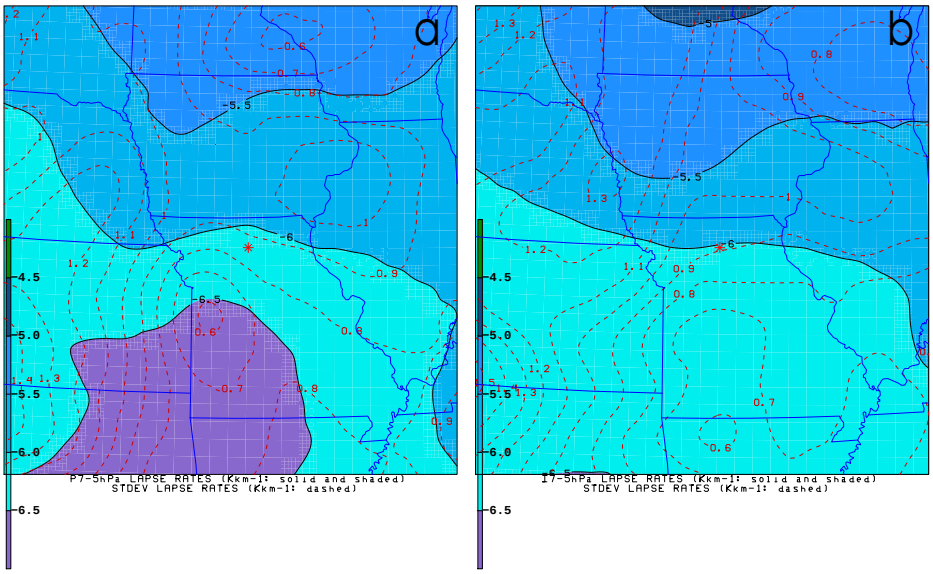

Figure 5.21: Spatial composites of midlevel (700-500hPa) lapse rates (Kkm^{-1}) for the TSSN events using GEMPAK, with both averages (solid lines and color shading) and standard deviations (dashed lines) displayed. Panel (b) shows the time of convective initiation while panel (a) indicates the period three hours prior.

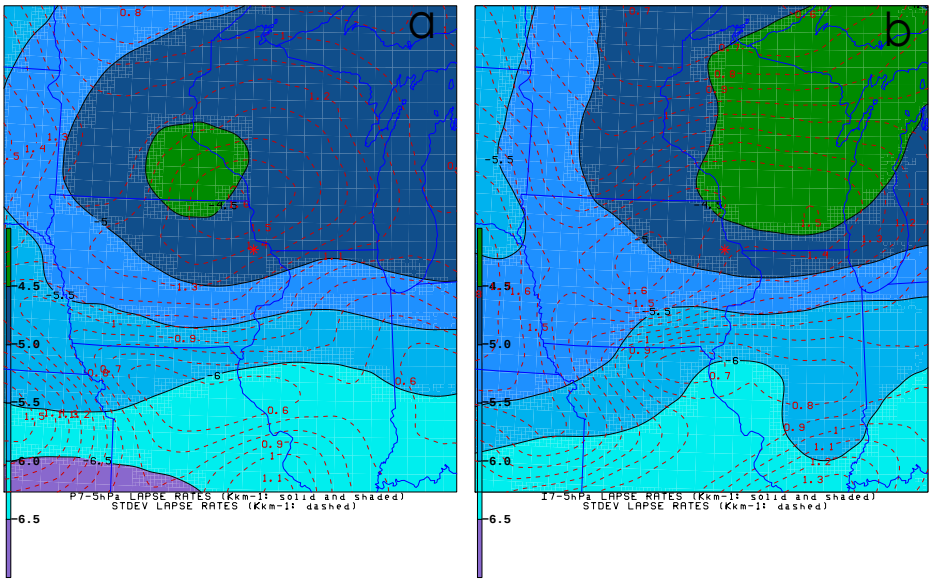

Figure 5.22: As in Fig. 5.21 except for the non-TSSN events compiled. Panel (b) represents the midpoint time frame whereas panel (a) shows the period three hours prior.

composite location, the difference between maxima and minima in this field was approximately similar to that in Fig. 5.21. Overall, the use of this particular stability diagnostic in this manner was not only unique but also reiterated the remarkable differences previously described in Market et al. (2006) and Smith (2006).

5.2.2.2 MULPL

The MU parcel generally originated at higher (lower) altitudes by progressing

poleward (equatorward) regardless of whether dealing with TSSN (Fig. 5.23) or non-TSSN (Fig. 5.24) composites. In either scenario, the mean MULPL extended from an upper limit of 550 hPa to a lower limit of about 725-735hPa. Moreover, Figs. 5.23 and 5.24 resembled one another in terms of the standard deviations being on the order of 50-100hPa, specifically near the area of interest. However, the similarities between the two datasets for this stability parameter ends when comparing averages near the centroid of the domains. Whereas the MULPL increased immediately leading up to convective onset in Fig. 5.23, Fig. 5.24 showed a corresponding decline over a three hour period in the wintertime precipitation exhibiting no thunderstorm reports. In the former, the expansion and northward progression of the region of values greater than 650 hPa became almost coincident with the initiation site, which physically could be connected to the coincident warm air advection and amplification of the θ_e ridge (compare Figs. 5.1b and 5.2b to Figs. 5.23a and 5.23b). On the other hand, these thermodynamic features tended to be less prominent in the non-TSSN events (Figs. 5.3b and 5.4b). In this case, the middle of the MULPL plots exhibited a source region elevated about 50 hPa above that in the TSSN horizontal distribution, indicative of a colder and more stable regime (compare Fig. 5.23 to Fig. 5.24).

5.2.2.3 MULI

The average MULI fields were similar for both TSSN and non-TSSN instances in terms of the axis of lowest averages being positioned in close proximity to the studied meteorological phenomenon, the latter having a slightly larger value nearer to 2 for both time periods (compare Fig. 5.25 to Fig. 5.26). The discernible attribute for the non-TSSN case studies in Fig. 5.26 was the sharper transition to greater stability (and larger MULI) just poleward of the center grid point, this being particularly pronounced by the later time period. The alternate pattern of Fig. 5.25 actually displayed a narrower spectrum of results with val-

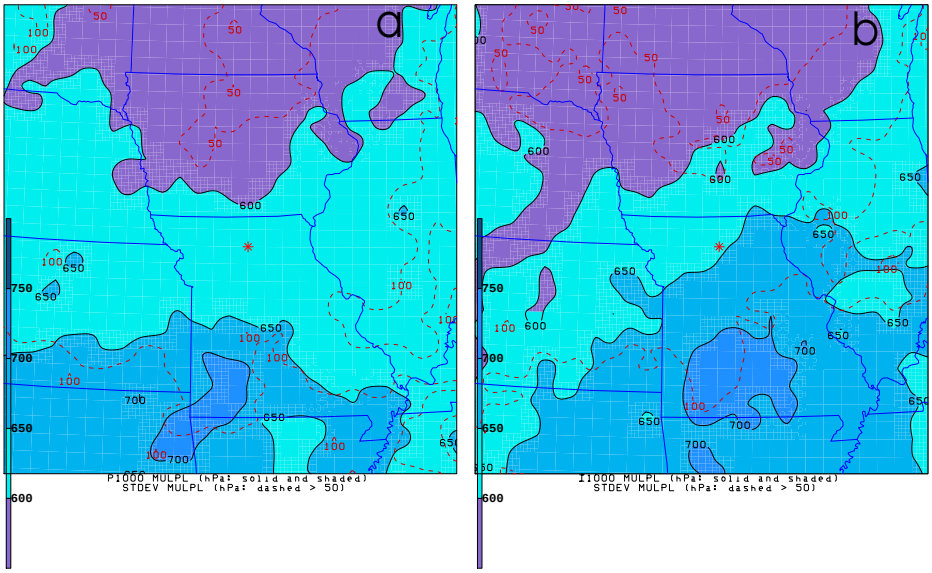

Figure 5.23: Spatial composites of the most unstable level for lifting a parcel (MULPL; hPa) for the TSSN events by examining the elevated layer of 800-550hPa using GEMPAK. The average results were displayed using solid lines and color shading, with the standard deviations revealed by dashed lines.

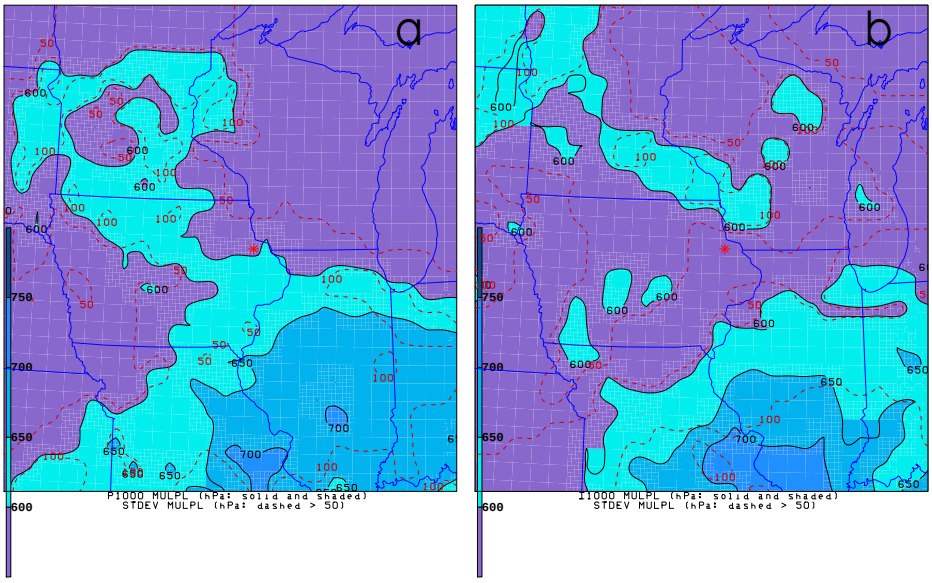

Figure 5.24: As in Fig. 5.23 except for the non-TSSN events compiled.

ues of 1-3 covering a generous portion of the composite area. Regardless of the presence of CG lightning flashes in snowstorms, fluctuations from event to event were generally on the order of the averages or less for a substantial number of grid points. Even so, the area of standard deviations greater than 3 was somewhat more widespread in the non-TSSN plots (Fig. 5.26) compared to those in the TSSN grouping (Fig. 5.25). Finally, the subtle discrepancy in these statistics against the sounding point values presented in section 4.2.3 was apparently due to the greater precision employed in computing parameters in GEMPAK over that of NSHARP. This observed lack of continuity was more noticeable in the handling of MUCAPE, which will be discussed shortly. The exact cause for the problem with this stability index, however, was unclear from the documentation provided at Unidata (`http://www.unidata.ucar.edu/software/`) but might be the result of how the constituent terms were diagnosed in GEMPAK compared to NSHARP.

5.2.2.4 MUCAPE

The virtual temperature correction, as employed in section 4.2.3, was incorporated in the formula for CAPE here. The associated MU average and standard deviation patterns were displayed in Figs. 5.27 and 5.28 for both sets of snowstorms. In the case of TSSN reports, the statistics revealed typical solutions of 15-20 Jkg^{-1} at the centroid, with variations decreasing by about 30 Jkg^{-1} during the three hour period. This contribution, although minimal, was unlike the absent positive buoyancy obtained in nearly all case studies in NSHARP. Furthermore, the best results for the MUCAPE surpassed the 100 Jkg^{-1} threshold along the southwestern periphery and shifted eastward as the first signs of convection developed (Fig. 5.27). The scale of the maximum value was about the same in Fig. 5.28, yet the decline in values to the north was more considerable in the plan-view perspective for non-TSSN events. More importantly, the mean

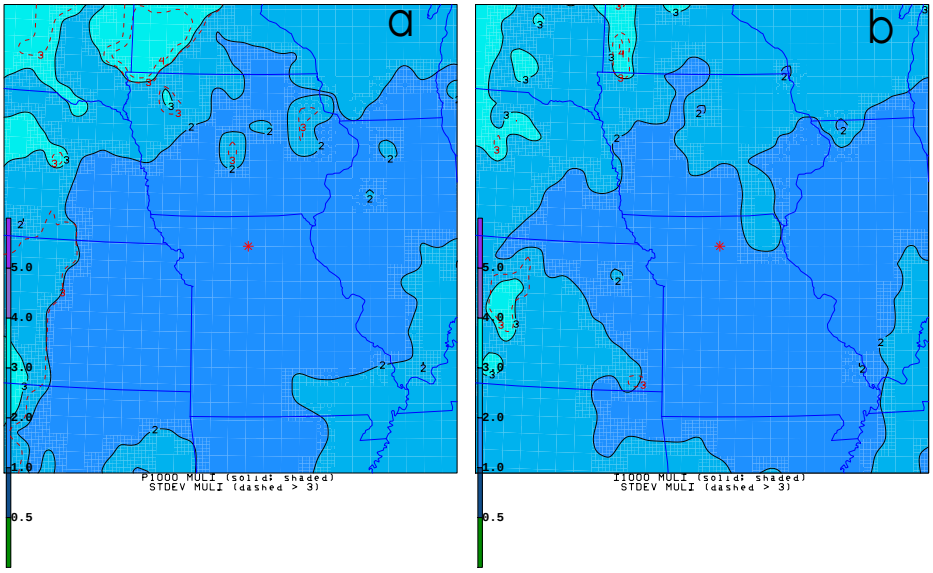

Figure 5.25: As in Fig. 5.23 except for the most unstable lifted index (MULI) based off of the MULPL. Standard deviations greater than 3 were given as dashed lines.

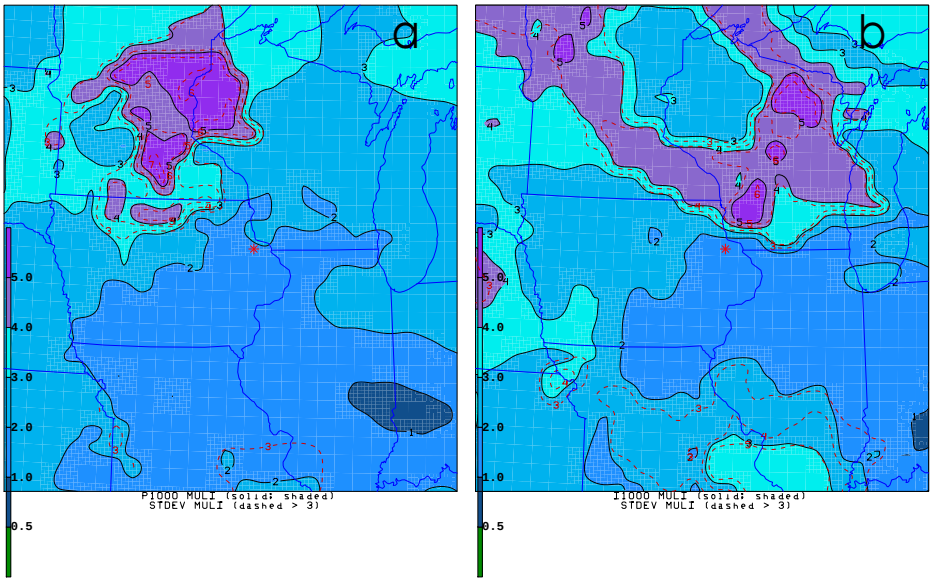

Figure 5.26: As in Fig. 5.25 except for the non-TSSN events compiled.

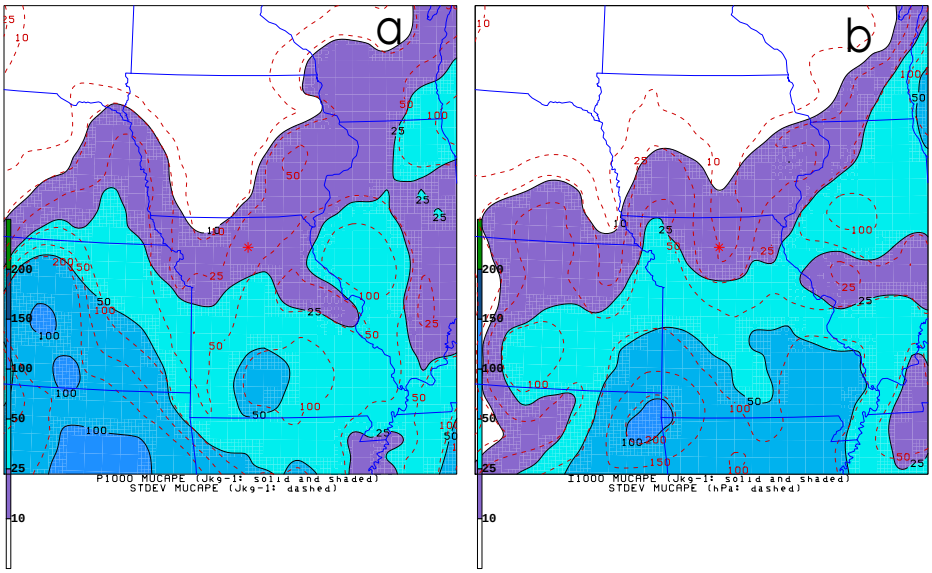

Figure 5.27: As in Fig. 5.23 except for the most unstable convective available potential energy (MUCAPE; Jkg^{-1}) based off of the MULPL. Only regions with values greater than 10 Jkg^{-1} were identified.

response to MUCAPE in this subset of *typical* snowstorms at the center grid point was only a little above (below) 10 Jkg^{-1} in the earlier (later) time period, with hardly any variations in the composite plots in this location. Thus, the category of TSSN reports tended to show relatively greater convective instability compared to those cases where no CG lightning flashes were detected.

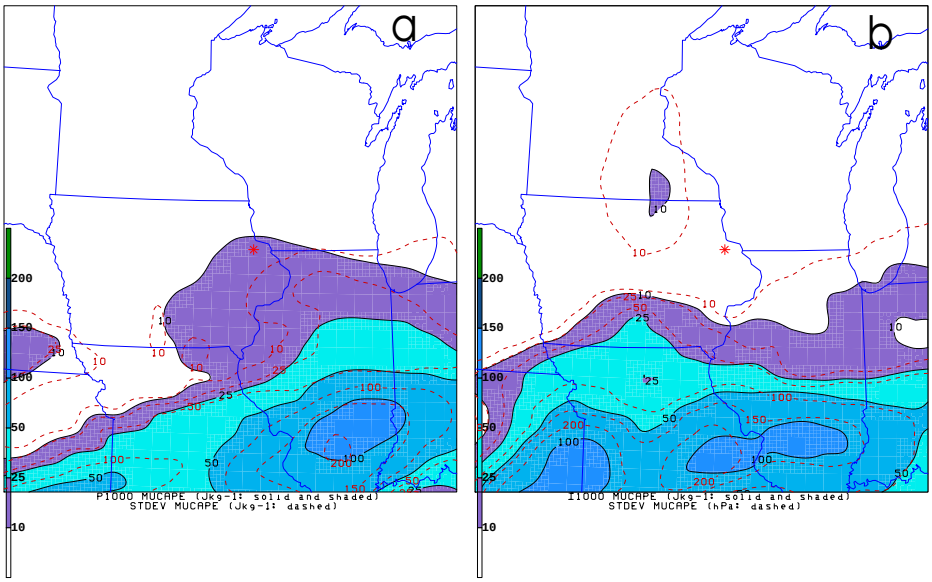

Figure 5.28: As in Fig. 5.27 except for the non-TSSN events compiled.

5.3 Banding and Nonbanding Composites

The diagnosis presented thus far has been a comparison of typical atmospheric conditions occurring within TSSN and non-TSSN events. Yet, it is recognized that subdivisions to these categories are possible and would contribute internal variations to the patterns examined. In this regard, Chapter 4 introduced the influence of bandedness in precipitation onto the degree and type of stability within instances of convective snowfall and statistical results at the initiation site supported this to be a definitive factor. Given that the distinct signal in the spatial representations were masked in the aggregate dataset (e.g., σ^2 in Fig.

5.5), separate composite fields were also designed exclusively for the five banding and twelve nonbanding TSSN events. Upon properly dividing up the case studies utilizing the classification scheme in section 3.3.8, similar sized domains (as in section 3.4.2) were produced by once again utilizing the convective initiation site as the focal point. As a result, the centering process for the unique groupings naturally led to different placements in the average position for TSSN onset in banding and nonbanding situations.

The role of CSI in controlling the organization of frontal convective precipitation has been illustrated already through the application of σ^2 point values. In Table 4.9, the term-by-term technique suggested evidence of increased baroclinicity, greater anticyclonic shear, and relatively reduced static stability values in banding versus nonbanding episodes. The single interpolated estimates, in themselves, were not capable of discriminating the type of convective structures to expect. In an attempt to recognize patterns in the 2-D analyses of σ^2, however, the average representation in Fig. 5.5 would be composed of many different shapes from the individual distributions. For example, Melick et al. (2008) showed that the linear configuration in the growth rates at the LHSGR for an individual convective snow event (24 November 2004) closely matched the location and orientation of the precipitation band in the radar analysis despite the discrepancy in resolution (compare Fig. 6 to Figs. 1 and 4 in Melick et al., 2008). These details would be hidden from the evaluation of Fig. 5.5 but might be represented somewhat in the following partition of banding and nonbanding composites. Although the LHSGR was not exactly the same in the smaller subsets, the 650-hPa level was again selected in order to effectively contrast against that of the original plots.

Figure 5.29 shows σ^2, 3-D EPV, and RH equivalent to that displayed in Fig. 5.5 except just for the banding TSSN events. The averaged fields showed the atmosphere to be moistening over the 3-hour period as the stability reduced more

substantially and a greater increase in growth rates occurred near the initiation site as opposed to *all* instances of snowstorms with lightning. In this scenario, the translation of the best signals for the potential of wintertime convection was farther northward. This assertion is asserted by the fact that the shaded area of negative EPV values was almost situated, if not encompassing, the area of interest by the time of the first report of TSSN (compare Fig. 5.29b,d to Fig. 5.5b,d). Right over this desired location, the regions of positive σ^2 were closely aligned at either pressure level but tended to be most pronounced at the 700-hPa level, where there was some evidence of a discernible southwest to northeast banded structure. This remarkable distinction closely resembled the nature of the higher reflectivity returns in three of the five case studies (not shown) and approximately lined up parallel with the mean midtropospheric thermal wind vector (Fig. 5.30). Accordingly, identification of slanted roll circulations released from pure CSI not only requires the atmosphere to be nearly saturated but also a two-dimensional, semigeostrophic framework with no variation allowed in the along-vertical shear axis (e.g., Bennetts and Hoskins 1979; Schultz and Schumacher 1999; Martin 1998; Snook 1992). As a result, the technique outlined in section 3.3.5 was applied in order to create vertical cross-sections and assess several appropriate diagnostics. The characteristic sea level pressure pattern and 850-300hPa thickness field, for this purpose, was given in Fig. 5.30.

Following Moore and Lambert (1993), the cross-section was taken across the midtropospheric frontal zone with endpoints located about three grid points northwest and southeast from the representative origin in TSSN banding composites (Fig. 5.30). Values of filtered geostrophic, Petterssen frontogenesis (GEO FRNT) greater than 0.1 $K100km^{-1}3h^{-1}$, Ri_{sc} less than 10, and RH greater than 80 % were plotted on the derived x-z plane in Fig. 5.31. A sloping zone of frontogenesis stretched upward from 850 hPa to 600 hPa and toward the colder air, with the greatest magnitudes positioned near the convective initiation site and

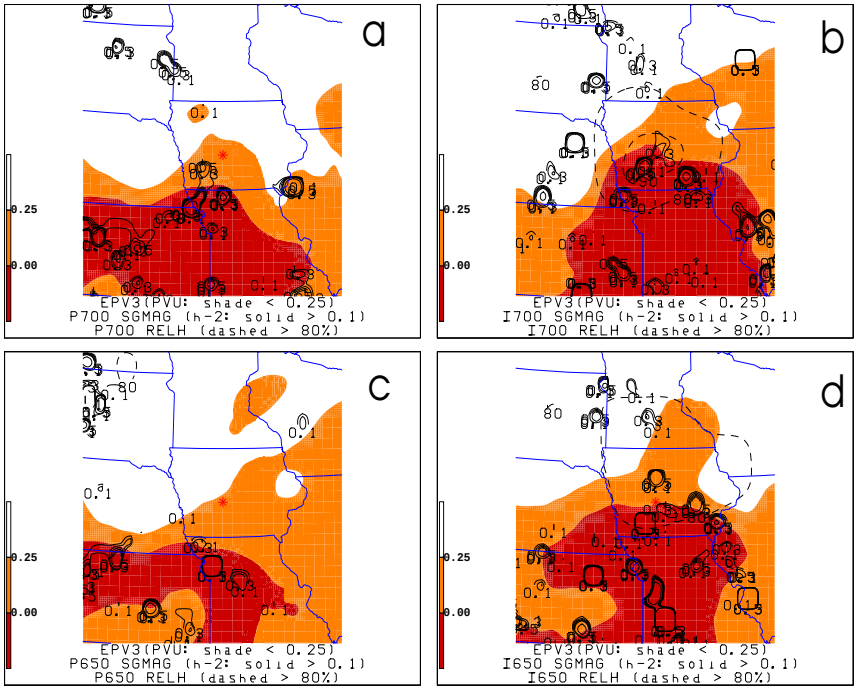

Figure 5.29: As in Fig. 5.5 except just for the banding portion of TSSN events.

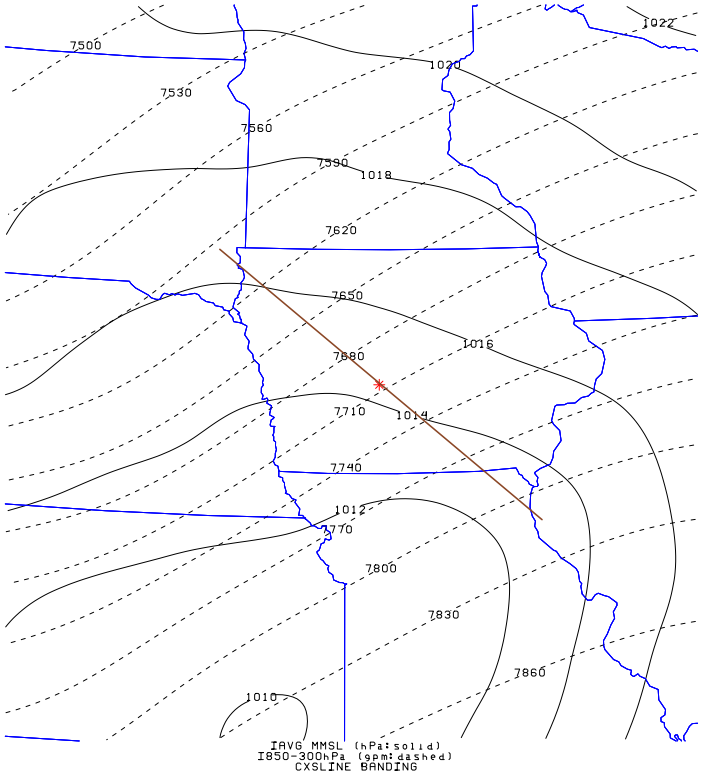

Figure 5.30: Spatial average composites of sea level pressure (hPa; solid lines) and 850-300hPa thickness (gpm; dashed lines) for the banding portion of TSSN events. Bold line denotes cross-section line in Figs. 5.31 and 5.32.

underneath a 200-250hPa deep layer of WSS ($1 < Ri_{sc} < 10$) and CI ($Ri_{sc} < 0$). The juxtaposition of a nearly saturated profile in the presence of mesoscale forcing allowed for the convective energy to be released once the air parcels were lifted sufficiently high enough (Fig. 5.31). In terms of justifying the type of stability, an evaluation of the M_g - θ_e relationship (not shown) revealed that there was a mismatch in the amplified, negative response from Eq. 2.9 and the latter qualitative diagnosis, in which θ_e surfaces only doubled over towards the right of the cross-section and into the warm sector. This greater amount of detail obtained from the highly derived Ri_{sc} parameter was also evident even in the smoothing process of creating composites for 3-D EPV and σ^2. Variations in the elevated symmetric stability occurred across the baroclinic zone (Fig. 5.32), such that the overlapping region of negative EPV estimates with high, positive growth rates was favorably constricted in the shallow 700-650hPa layer. Although the M_g - θ_e approach portrayed conditions of WSS in the middle of the 2-D profile, the signature in Fig. 5.32 demonstrated an atmosphere conducive to slantwise motions characteristic of CSI, something which Melick et al. (2008) argued in the convective snow banding case study from 24 November 2004. In support of this notion, the core of the upward vertical velocities took on a tilted nature in the same cross-section with the greatest magnitudes ($8-12\mu b\ s^{-1}$) appropriately positioned in satisfying the ingredients-based methodology for thunderstorm development (Fig. 5.32).

An identical set of images were also designed for the nonbanding set of TSSN events (Figs. 5.33, 5.34, 5.35, and 5.36) with the purpose of properly distinguishing this dataset from its counterpart. First, an inspection of plan-view 3-D EPV and σ^2 values revealed the usual evolution as there was an increase (decrease) in the averages of the latter (former). In other words, both parameters depicted a favorable progression in the best regions for moist convection, with the environment becoming sufficiently saturated immediately leading up to the first signs of

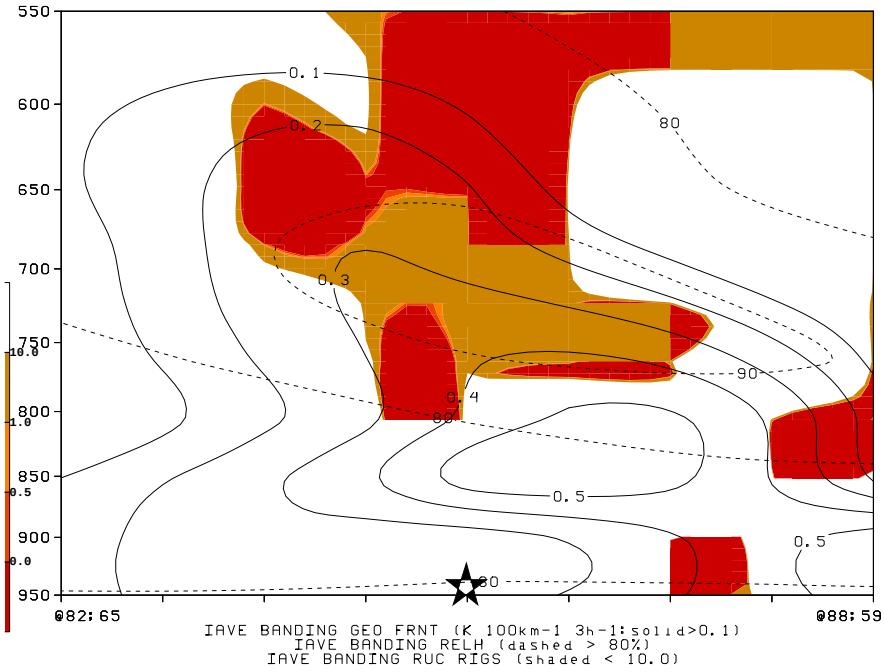

Figure 5.31: 40-km RUC vertical cross-section analysis of average GEO FRNT ($K100km^{-1}3h^{-1}$; solid lines > 0.1), RH > 80 % (dashed lines), and Ri_{sc} (color shading < 10). The extent of the cross-section is based off of the solid line representation shown in Fig. 5.30 with temperatures increasing to the right and the star representing approximate location for the typical convective initiation site.

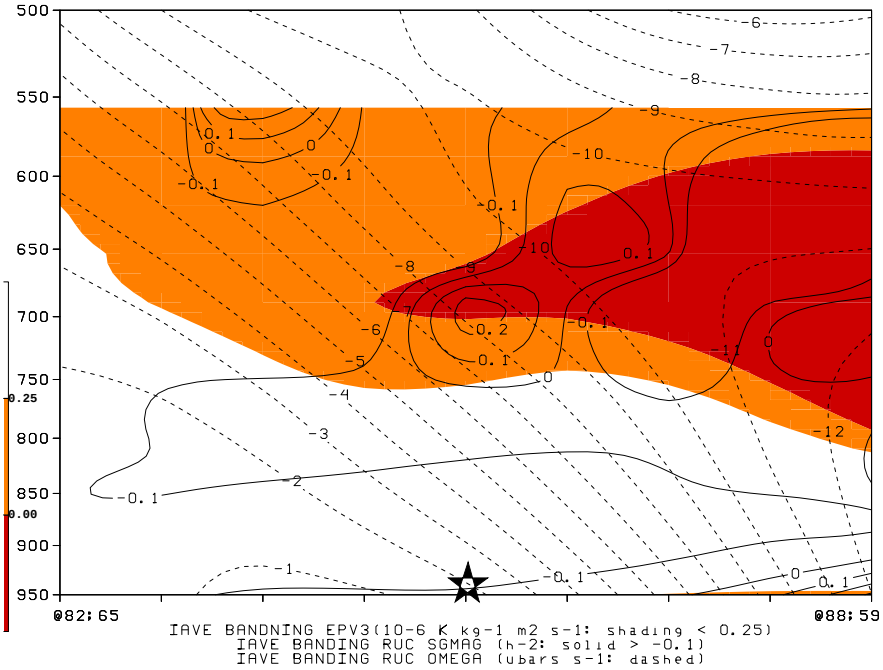

Figure 5.32: As in Fig. 5.31 except for σ^2 (h^{-2}; solid lines > -0.1), isobaric vertical velocity ($\mu bars\ s^{-1}$; dashed lines), and 3-D EPV ($10^{-6} K kg^{-1}\ m^2 s^{-1}$; color shading < 0.25).

electrical activity (Fig. 5.33). Still, one of the major differences of these composites against those exhibiting precipitation bandedness was the fact that the symmetric stability results, while only weakly positive, were greater and thus less desirable in nature. Regardless of whether employing the 700-hPa or 650-hPa levels, the shaded zones of EPV were displaced farther away from the area of interest and restricted within close proximity to the synoptic scale disturbance (Fig. 5.34). In addition, other distinctions would be the typical TSSN position residing northwest (northeast) of the surface cyclone and the attendant shallower (deeper) layer thicknesses in the nonbanding (banding) dataset portion (compare Fig. 5.30 to Fig. 5.34). Despite marginally more robust mesoscale forcing in the cross-section of Fig. 5.35 compared to that of Fig. 5.31, the elevated baroclinic feature was not as discernible and impressive in the corresponding plan-view perspectives. Although the vertical profile certainly portrayed the necessary high levels of RH, the absence of identifiable regions of relatively low Ri_{sc} supported the interpretation that these particular types of convective snow events were generally more resistive to both upright and slantwise displacements (at least from what the coarse 40-km grid point spacing of the RUC-2 was capable of resolving).

The same conclusion could also be supported in the similar approach to analyzing both EPV and growth rates, in which neither suggested the presence of an unstable and/or destabilizing environment above or horizontally close within the cross-section (Fig. 5.36). In addition, the strength of the constituent, slanted updraft (less than $10\mu b\ s^{-1}$) was not as impressive in the nonbanding TSSN composites (compare Fig. 5.32 to Fig. 5.36). From all of this information, the RUC-2 evaluation advanced some clear 3-D spatial variations of dynamic and thermodynamic factors within the overall, cold-season convective episodes. In general, results from diagnostics (e.g., stronger ageostrophic circulation, positive σ^2, reduced EPV and Ri_{sc}) that were more conducive to lightning production transpired more often in those occurrences where precipitation bands developed

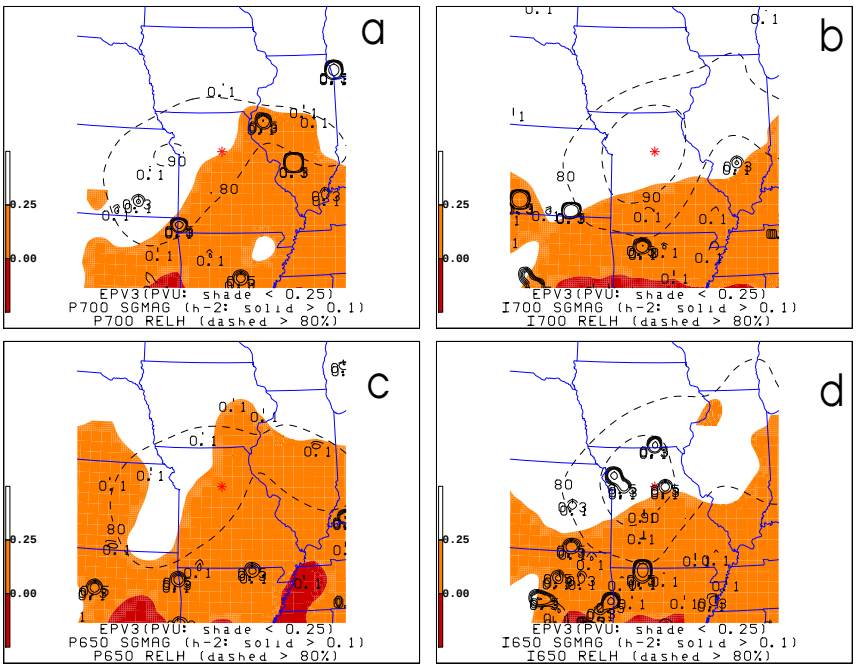

Figure 5.33: As in Fig. 5.5 except just for the nonbanding portion of TSSN events.

as opposed to those where they did not appear.

5.4 Mann-Whitney Rank-Sum Evaluation

Two separate domain regions were created from the grid point data in order to evaluate the significance of the spatial distribution of stability diagnostics computed from the convective snow composites. One field was supposed to represent the approximate location and vicinity where the responsible vertical circulation pattern produced the observation of TSSN, also characterized throughout the text as the "convective area of interest". By analogy, an equivalent spatial rep-

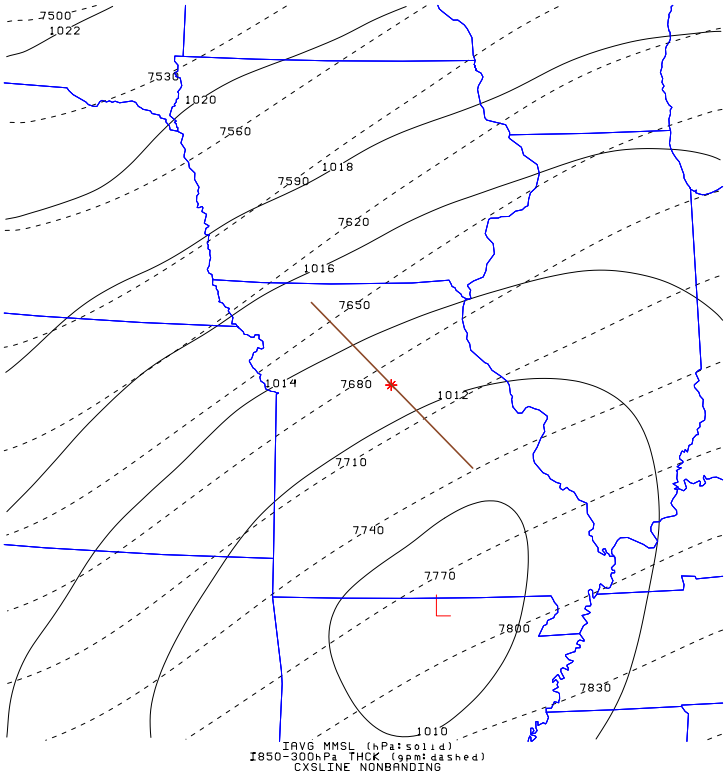

Figure 5.34: As in Fig. 5.30 except just for the nonbanding portion of TSSN events.

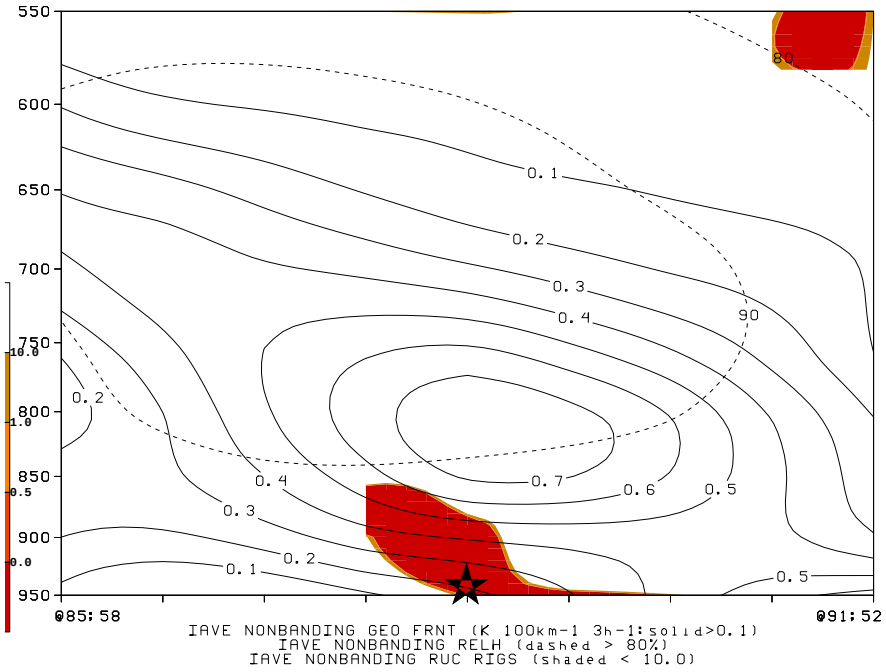

Figure 5.35: As in Fig. 5.31 except just for the nonbanding portion of TSSN events.

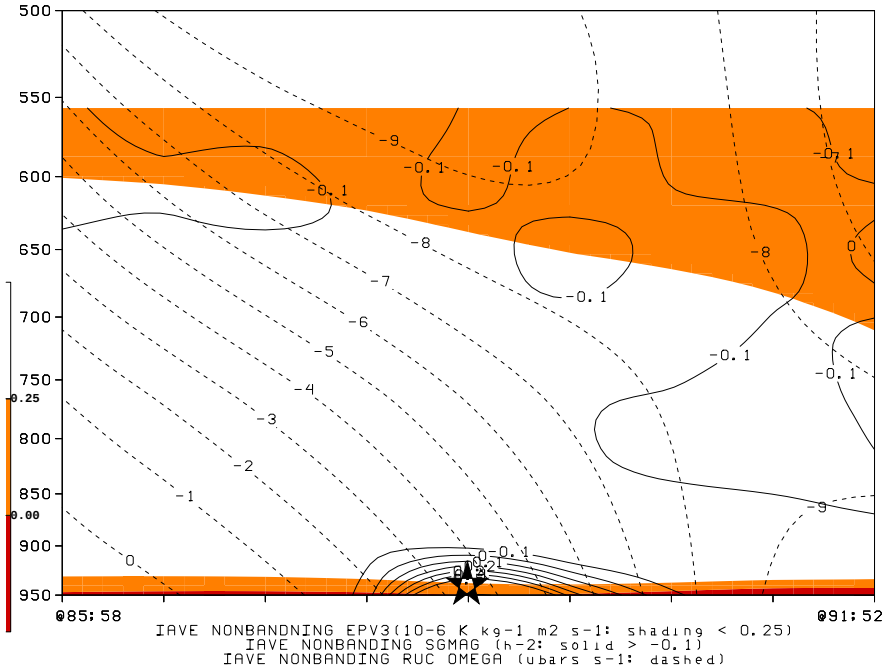

Figure 5.36: As in Fig. 5.32 except just for the nonbanding portion of TSSN events.

resentation could then be constructed independently in order to consider the localized conditions in a typical non-TSSN atmosphere. Given that there was no strict physical means of determining the exact specifications of the spatial data subsets, the author realized that some ambiguity was inherent and would influence any results obtained from the Mann-Whitney test statistic. Despite this potential setback, a few assumptions were made on the size and orientation of the domains and then modified later in order to expose any distinguishing differences in the numerical analysis. Analogously, some liberty was also taken in considering which parameters should be utilized in the more rigorous analysis. In order to narrow down multiple regions which might have similar, favorable results, appropriate combinations of stability measures were employed so as to mask out surface based convection and/or atmospheres with insufficient moisture.

In all instances, the grid point closest to the first report of snow with lightning (or equivalently, the midpoint site in non-TSSN situations) was again identified to be the center of the domains. The identical two time periods utilized throughout the work so far were examined here . In terms of the first merger investigated, averages of σ^2 at the LHSGR (650 hPa) were multiplied by the corresponding RH response. For those grid points where the mean RH was less than 80 %, the lowest rank was applied by substituting an effective default value (i.e. -9999.00). Consequently, this approach accurately placed substantial weight on evidence of a saturated atmosphere in testing the significance of the growth rates. For the sake of comparison, an alternative attempt of the Mann-Whitney analysis was also offered by inspecting the aggregate of midlevel lapse rates and MULI, such that the desired effect was that the product lean towards higher, positive results. The latter traditional stability index was utilized with the intention of eliminating the strong bias in positive buoyancy present in the warm sector and refining the focus to elevated instability. Initially, 6 $\triangle n$ (7 x 7) boxes were chosen since

the lateral extent was small enough to capture the smallest wavelengths. As a result, the mesoscale evaluation was obtained for the portions of the RUC-2 analysis framework displayed in Figures 5.37 and 5.38. After the Mann-Whitney rank-sum, W_x , was then calculated for the "convective area of interest", the standardize statistic was obtained via Eqns. 3.3, 3.4, and 3.5. All of these results, along with the two-tailed p-value, were presented in Table 5.1.

The results showed that significant differences existed between the two fields (TSSN and non-TSSN) for both time periods for the combination of σ^2 and RH (Table 5.1). Since the p-value was substantially less than any reasonable alpha value (e.g., 0.01), the medians of the samples were dissimilar enough to refute the null hypothesis that they came from the same population. Instead, given the stipulated boundaries, this quantitative analysis provided the *unexpected* evidence that the "convective area of interest" was actually relatively more stable than an equivalent area representing the non-TSSN atmosphere. The other test of combining more commonly utilized stability indices (i.e. MULI and 700-500hPa lapse rates) produced an almost identical outcome (Table 5.1). A simple inspection of one of the plots for these specific diagnostics (not shown) suggests the analysis was sensitive to the spatial constraints and the rank-sum might deviate if the methodology was allowed to vary.

In the next variation for creating Table 5.2, the motivation was to adjust the RUC-2 spatial subset areas based off of a more meteorological foundation. The strongest midlevel temperature gradients were elongated in a southwesterly to northeasterly fashion across the west-central portion of the TSSN composites (e.g., see Fig. 5.9b), with the length to width ratio assumed to be at the very least 2:1. Along these lines, enhanced reflectivity patterns from the radar network would most likely be constricted to the aforementioned baroclinic zone. In order to incorporate these practical guidelines, the "convective area of interest" was rotated in the direction of the frontal axis and defined by a rectangular shape

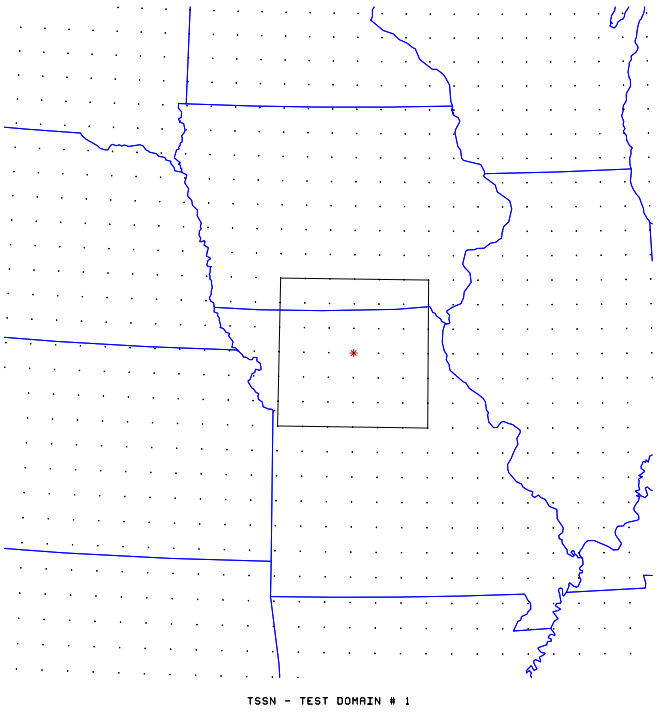

Figure 5.37: Zoomed in RUC-2 analysis domain represented by grid points. Box indicates subset region in Mann-Whitney statistical test corresponding to "convective area of interest". The center grid point (highlighted by asterisk) in this domains designates closest one to the typical observation of TSSN.

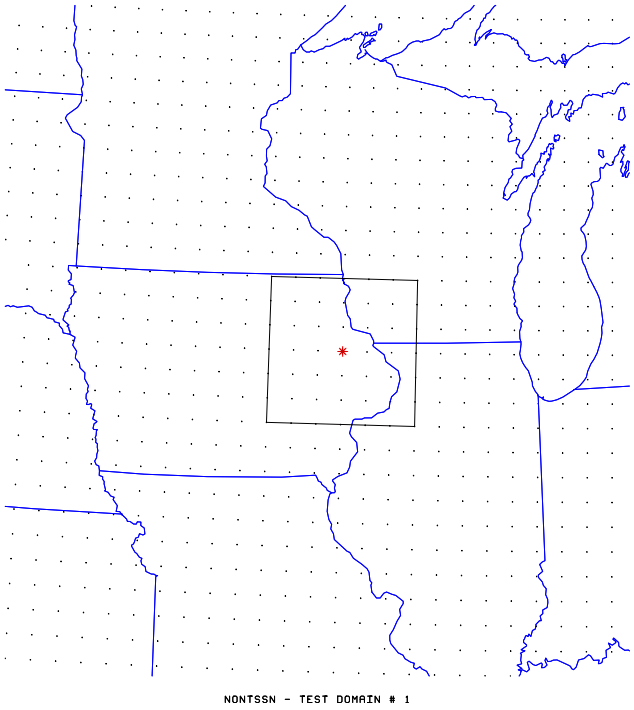

Figure 5.38: Same as in Fig. 5.37 except for the non-TSSN composites, with the domain centered on grid point nearest to the average midpoint site.

Table 5.1: The Mann-Whitney rank-sum test for the composite subdomains displayed in Figs. 5.37 and 5.38. The first evaluation was applied to the combined influence of stability parameters, namely the average patterns of LHSGR σ^2 multiplied with RH $>$ 80 % (650hPa-sigrh) and MULI multiplied with 700-500hPa lapse rates (MULI-Lapse). The statistics for TSSN are valid at convective initiation (I) and for the three hours prior (P) time frame. Refer to section 3.4.2.1 for an explanation of the calculated terms.

	W_x	$\overline{X}$	s	Z-score	2-tailed p-value
P 650hPa-sigrh	2687	1200.5	140.74	10.562	≈ 0.00
I 650hPa-sigrh	2696	1200.5	140.74	10.626	≈ 0.00
P MULI-Lapse	2739.5	1200.5	140.74	10.935	≈ 0.00
I MULI-Lapse	2593	1200.5	140.74	9.894	≈ 0.00

spanning an area on the order of $10^4 km^2$ (12 $\triangle n$ x 6 $\triangle n$; Fig. 5.39). In a similar fashion, this ideology was extended to the opposing dataset with no CG lightning flashes. As a result, Fig. 5.40 shows a more zonal configuration to match up with the characteristic thermal pattern (e.g., Fig. 5.4). By accomplishing this, however, the nonparametric analysis produced almost identical findings to the original methodology, with again unusually high values for W_x and the related $Z - score$ statistics. Furthermore, the difference in the combination of stability parameters was negligible from this quantitative standpoint in all four evaluations (Table 5.2). Overall, while there is some range in the rankings with all the diagnostic factors (including time period and region tested), the most important and unfortunate conclusion was reached through the constant, near zero $p-value$ (compare Tables 5.1 and 5.2).

In the entirety of the approaches utilized for assessing this statistical test, unexpected results were obtained as the hypothesized axis of instability was not revealed through the rigorous study of the patterns of atmospheric parameters. Rather, the combinations of σ^2 with RH and midlevel lapse rates with MULI were found to be not impressive in or near the initiation site of TSSN for either set

Table 5.2: As in Table 5.1 except for the RUC-2 subset domains illustrated in Figs. 5.39 and 5.40.

	W_x	$\overline{X}$	s	Z-score	2-tailed p-value
P 650hPa-sigrh	10751.5	4140.5	355.37	18.603	≈ 0
I 650hPa-sigrh	7892	4140.5	355.37	11.926	≈ 0
P MULI-Lapse	8378.5	4140.5	355.37	11.926	≈ 0
I MULI-Lapse	8713	4140.5	355.37	12.867	≈ 0

of regions defined. Still, this discovery was dependent to some degree upon the subjective specifications decided upon for this examination. For instance, other logical modifications to the RUC-2 fields might produce more favorable results, such as possibly relocating the center grid point in the domains to a position where the nearest instability maximum was positioned (this location slightly displaced sometimes from where the first report of convective snow developed). It should also be noted that both sample sizes were assumed to be of the same size. This restriction to comparable domains would probably, thus, not allow the subset under examination (i.e. winter precipitation with lightning flashes) to stand out. From this understanding, the non-TSSN dataset could be expanded to encompass a synoptic-scale, background regime. Still, the ambiguity still remains as to exactly how much larger this particular region should become to accomplish this task appropriately. As a result, given the unexpected results, the original technique of pattern recognition from a qualitative assessment needs to be explored first. In many instances, this perspective might be more informative and provide the only true practical means of diagnosing the spatial distribution of stability characteristics during these types of elevated, convective episodes.

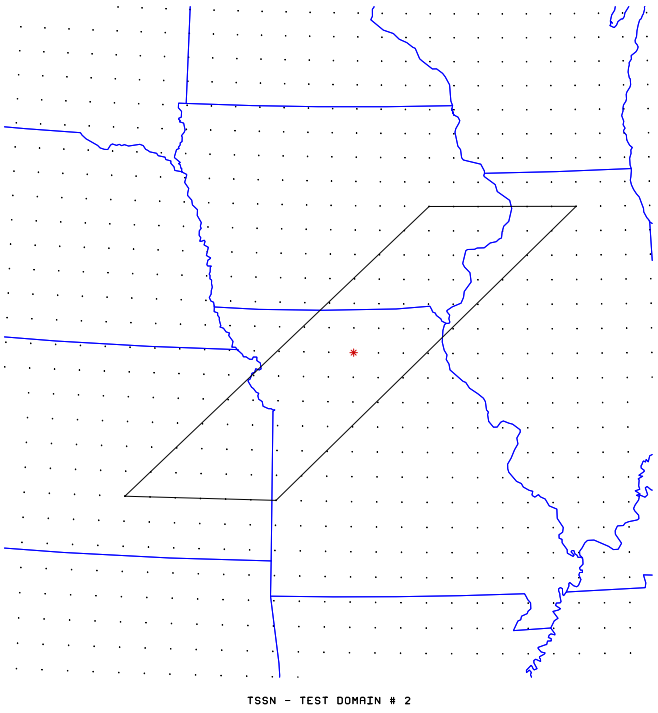

Figure 5.39: As in Fig. 5.37 except for changes applied to the orientation, shape, and size of the domains as described within the text.

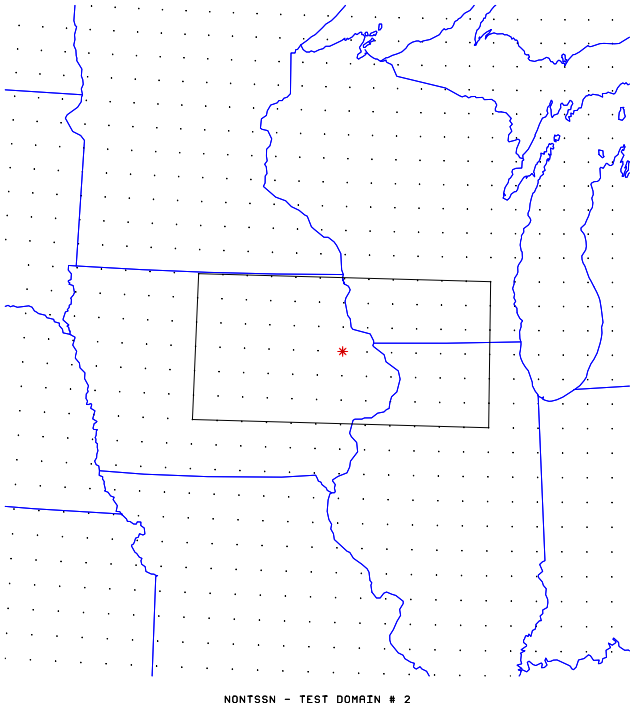

Figure 5.40: As in Fig. 5.39 except for those changes applied to the non-TSSN composite.

Chapter 6

Case Studies

Bennetts and Sharp (1982) utilized horizontal distributions of σ^2 from one case study and matched up the distinguishing features to precipitation regions within frontal systems identified by the radar data. This capability, however, was not practical using the averaged fields obtained from the compilation of several events. Instead, this goal was accomplished by means of four, individual case studies external to the climatologies cited up to this point. While the two TSSN occurrences identified came from the 2006-07 winter season, the complementary non-TSSN episodes were obtained from the subset given in Market et al. (2006; see their Table 2) that was *not* specifically utilized by Smith (2006). Consequently, these selections provided an important, independent check to the statistical results reached in the preceding two chapters.

Regardless of whether any lightning occurred, cooperative snowfall accumulations were obtained through the U.S. Snow Monitoring site (`http://www.ncdc.noaa.gov/oa/climate/research/snow/`) maintained through the National Climatic Data Center (NCDC). Much of the past weather observations for the non-TSSN events were missing and needed to be obtained externally. For instance, the archived satellite data was retrieved from the University of Wisconsin-Madison's Space Science and Engineering Center (SSEC) through the method specified by Unidata (`http://www.unidata.ucar.edu/data/unirec.html`). In

addition, level III radar information from the individual WSR-88D sites was also obtained through NCDC (`http://www.ncdc.noaa.gov/nexradinv/`), with a mosaic manually generated for the immediate area surrounding the midpoint location for non-TSSN. Finally, the extensive collection of past weather reports at the Iowa State University Department of Agronomy (`http://mesonet.agron.iastate.edu/archive/`) helped to often fill in the gaps (e.g., surface METARs).

6.1 TSSN Events

6.1.1 30 November 2006

6.1.1.1 Synopsis: Surface, upper-air, and radar analysis

The first case study focused on the early major winter storm of 2006-07 which brought moderate to heavy frozen precipitation to portions of TX, OK, KS, MO, IL, WI, and MI during 30 November to 1 December. Numerous lightning flashes were reported in the midst of the snowfall, most often coincident to the region experiencing the heaviest rates of precipitation and eventually the highest accumulations (e.g., Figs. 6.1 and 6.2). Utilizing an upgraded version of the NLDN, which also allowed detection of in-cloud flashes, Pettegrew et al. (2007) noted evidence of this remarkable electrical activity for the approximate time frame residing towards the cold air side of the precipitation zone. Their work established the existence of convective snow for a 36-hour period with a trend analysis of the dataset showing a distinct diurnal oscillation (see Fig. 2b in Pettegrew et al. 2007). While their analysis provided some corroboration and a summary of the evolution, the current investigation primarily dealt with the genesis of TSSN and the corresponding diagnostics.

From the synoptic setup, the analysis in Figs. 6.3 and 6.4 showed an incipient, unorganized area of low pressure situated in western TX sliding southeastward over the three hours leading up to 0300 UTC 30 November 2006. Water vapor

imagery indicated atmospheres of greatest moisture content slightly downstream and oriented primarily along the surface frontal boundary, the same narrow region for which high radar returns and surface METARs (Figs. 6.5 and 6.6) revealed intense precipitation of the mixed-phase and liquid variety. The prevalence of associated thunderstorms was supported by the overwhelming portion of cloud-to-ground count from the NLDN in the vicinity. However, Fig. 6.2 also portrayed *only* one lightning flash at 0240 UTC close to Amarillo, TX (KAMA) where surface observations and RUC-2 surface temperatures (upper teen/lower 20^0F range) along with 850-700hPa partial thickness values (near 1530-gpm) were cold enough to support the production of snowfall. In addition, the customary 5400-gpm transition line (from the 1000-500hPa thickness pattern) was suitably positioned equatorside across the TX panhandle (Figs. 6.3 and 6.4) and corresponded to the progression and development of an elongated axis of enhanced reflectivities oriented southwest to northeast (Figs. 6.5 and 6.6).

This well-defined snowband easily met the criteria of the classification scheme (section 3.3.8) and had embedded cells on the order of 35-45 dBZ intensity, an example of a time frame represented in Fig. 6.6 near the synoptic hour and right after the first instance of lightning activity (Fig. 6.2). The juxtaposition of distinct, low-topped convective clouds was suggested by the moderate but relatively brighter shading in the satellite depiction (Figs. 6.3 and 6.4). Within this region, the zoomed in examination from Fig. 6.2 identified a matching zone of elevated snow accumulations (e.g., the 6 inch depth at KAMA associated with TSSN). This favorable relationship with wintertime convection was partially motivated by the work of Crowe et al. (2006), but was only analyzed briefly near convective initiation for the dissertation.

Standard upper air charts of measured or easily derived variables (e.g., heights, θ_e, geostrophic winds, absolute vorticity, and temperature advection) were presented at 0300 UTC in Fig. 6.7. Panels (a), (b), (c), (d) corresponded re-

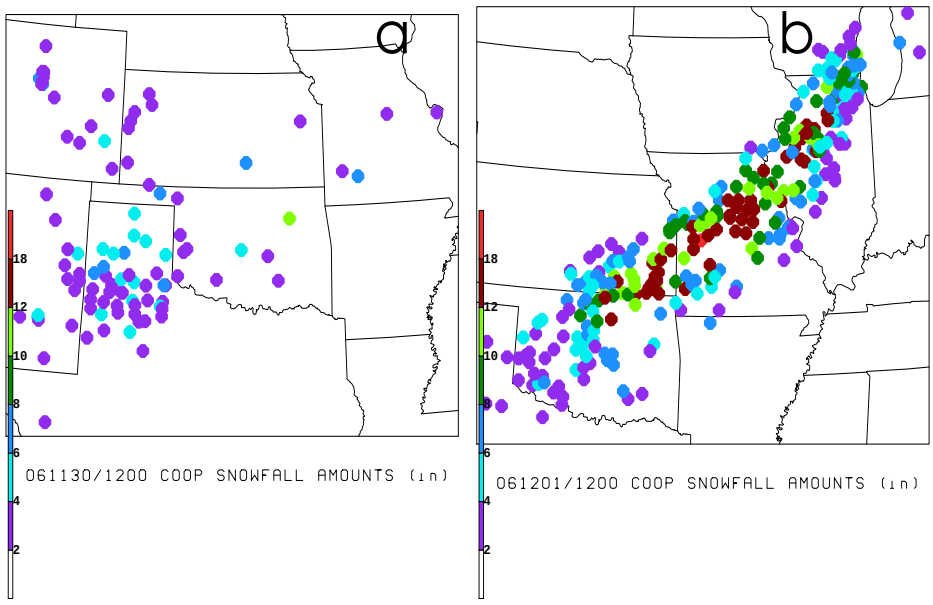

Figure 6.1: Cooperative (24-hr) snowfall accumulations ending at approximately 1200 UTC on (a) 30 November 2006 and (b) 01 December 2006, with color coded circles representing plotted value ranges beginning at 2 inches.

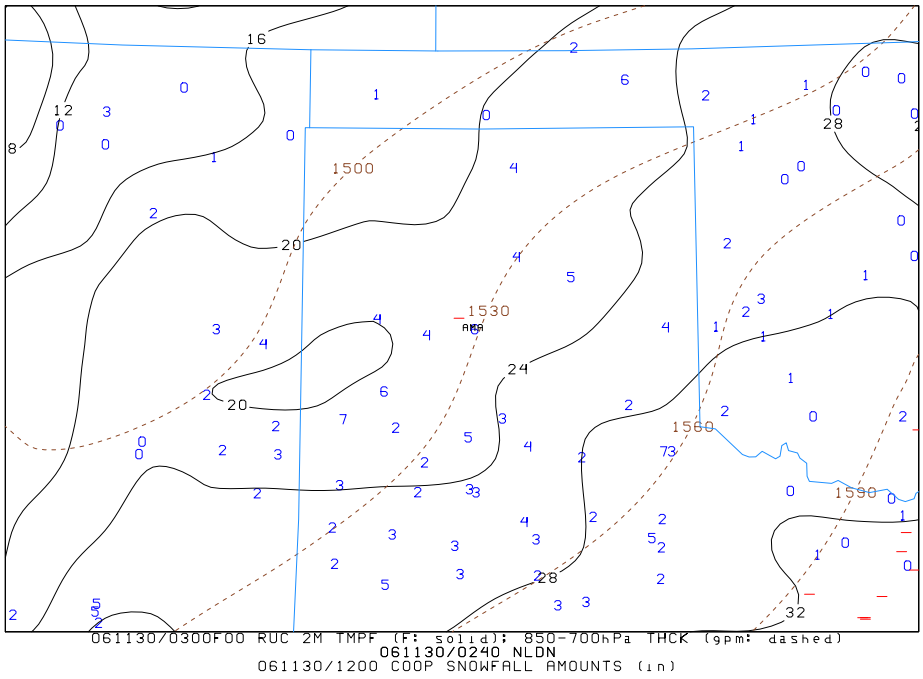

Figure 6.2: Cooperative (24-hr) snowfall accumulations ending at approximately 1200 UTC on 30 November 2006 and 0300 UTC 40-km RUC 2-meter temperature (^0F, solid lines) with 850-700hPa thickness (gpm, dashed lines). The National Lightning Detection Network (NLDN) analysis of cloud-to-ground lightning flashes valid at 0240 UTC 30 November 2006.

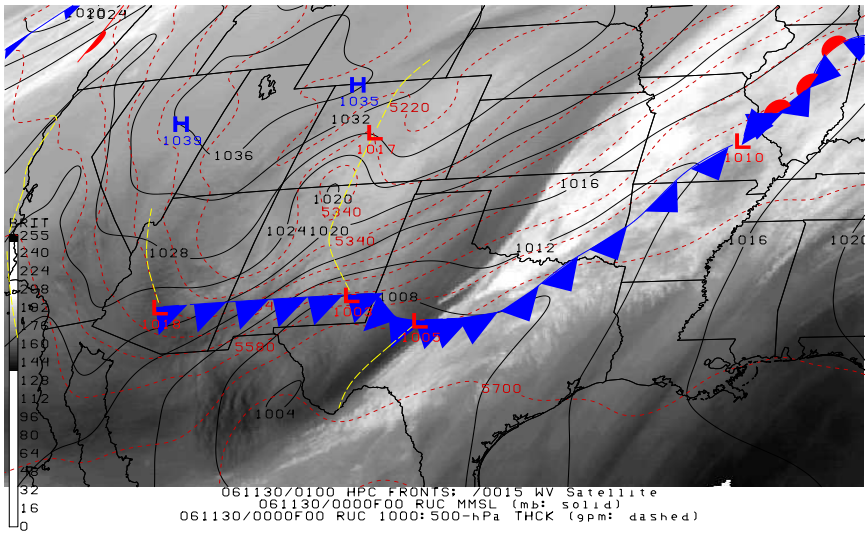

Figure 6.3: Satellite and surface analysis valid for about 0000 UTC 30 November 2006. A composite of 0100 UTC HPC frontal depictions, 0015 UTC water vapor imagery, and 0000 UTC 40-km RUC sea level pressure (hPa; solid lines) with 1000-500hPa thickness (gpm; dashed lines).

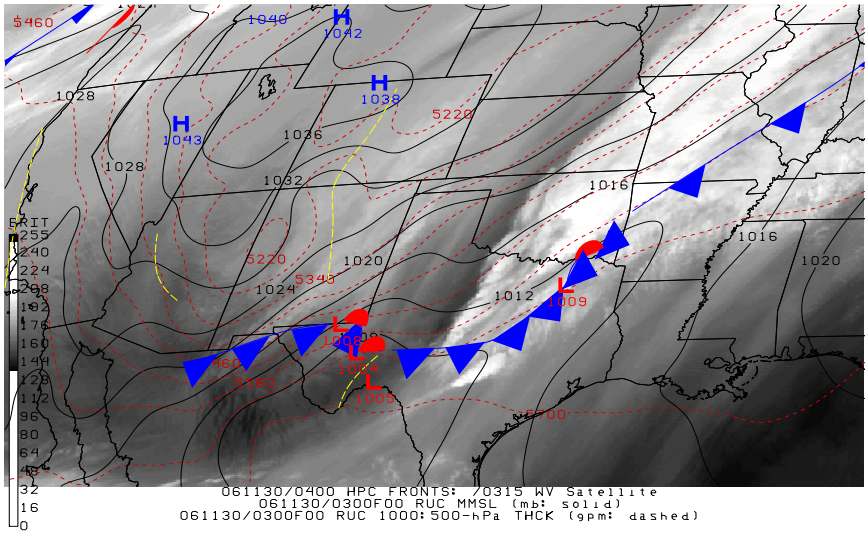

Figure 6.4: Satellite and surface analysis valid for about 0300 UTC 30 November 2006. A composite of 0400 UTC HPC frontal depictions, 0315 UTC water vapor imagery, and 0300 UTC 40-km RUC sea level pressure (hPa; solid lines) with 1000-500hPa thickness (gpm; dashed lines).

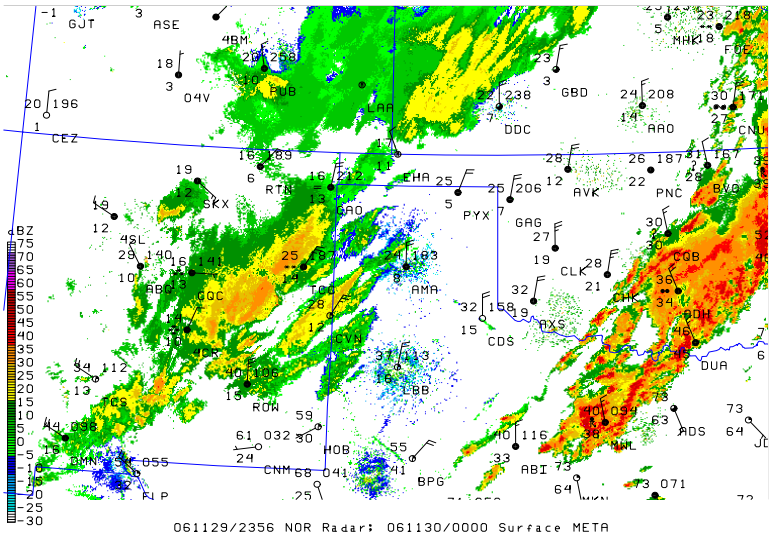

Figure 6.5: Radar analysis and surface weather plot valid for about 0000 UTC 30 November 2006. The level III, 1-km reflectivity mosaic pattern (0.5^0 tilt) displayed via GEMPAK and valid at 2356 UTC 29 November 2006. Standard plotted METAR observations valid at 0000 UTC 30 November 2006.

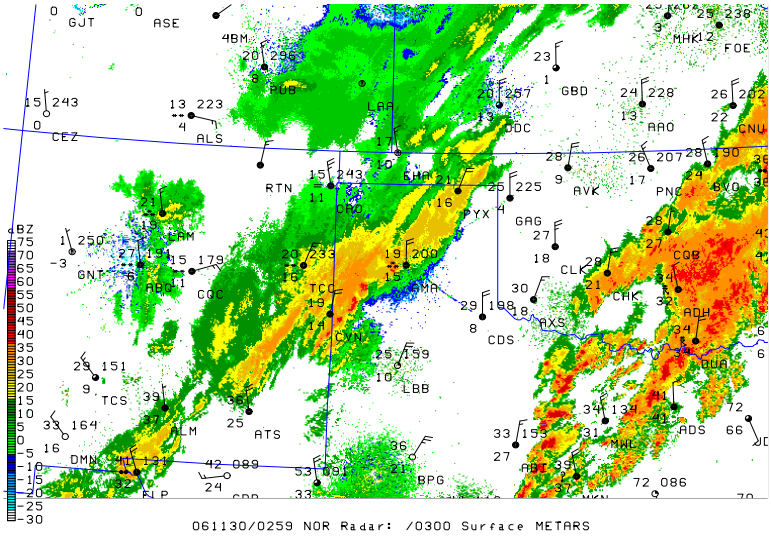

Figure 6.6: Radar analysis and surface weather plot valid for about 0300 UTC 30 November 2006. The level III, 1-km reflectivity mosaic pattern (0.5^0 tilt) displayed via GEMPAK and valid at 0259 UTC 30 November 2006. Standard plotted METAR observations valid at 0300 UTC 30 November 2006.

spectively to the 900-hPa, 700-hPa, 500-hPa, and 300-hPa pressure levels, this selection following the average fields constructed for TSSN events in Chapter 5 and originally employed by Oravetz (2003) and Market et al. (2004). The rationale was to identify the specific forcing mechanisms responsible for producing winter precipitation. Many *but not all* of the basic synoptic features observed in this case study were present in the composites for convective snow occurring north of a surface cyclone (compare Fig. 6.7 to Fig. 5.2) as well as those in Oravetz (2003). The cold air advection at 900 hPa was strongest just poleward of an intense closed low and near the initiation site (Fig. 6.7a) and transitioned to warm air advection with height (Fig. 6.7b). While the analysis at the lowest level implied downward motions, some of the evaluation over the TX panhandle was unrealistic since it resided below ground surface. The 700-hPa analysis also showed a subtle θ_e ridge extending up from the warm sector and cyclonically wrapping around the low level system from west to east just south of the area of interest. Despite the early stages of cyclogenesis, the latter feature demonstrated some initial justification for the emergence of a trowal airstream.

The inferred thermodynamic ascent was also assisted by the basic, dynamic structures displayed in the 500-hPa and 300-hPa perspectives. The slight positive tilt in the middle to upper troposphere troughs was apparent as well as the positive vorticity (Fig. 6.7c) and pronounced wind maxima (Fig. 6.7d) rounding its base. As a result, cyclonic vorticity advection and the left exit region of a curved jet streak were favorably positioned near the area of interest. The difference in details in the upper air analyses between this specific case and in a typical TSSN event was to be expected as there was a natural loss of information which occurred in the compositing process. Nevertheless, as was intended by Market et al. (2004), pattern comparisons and recognition revealed that the similarities were noticeable.

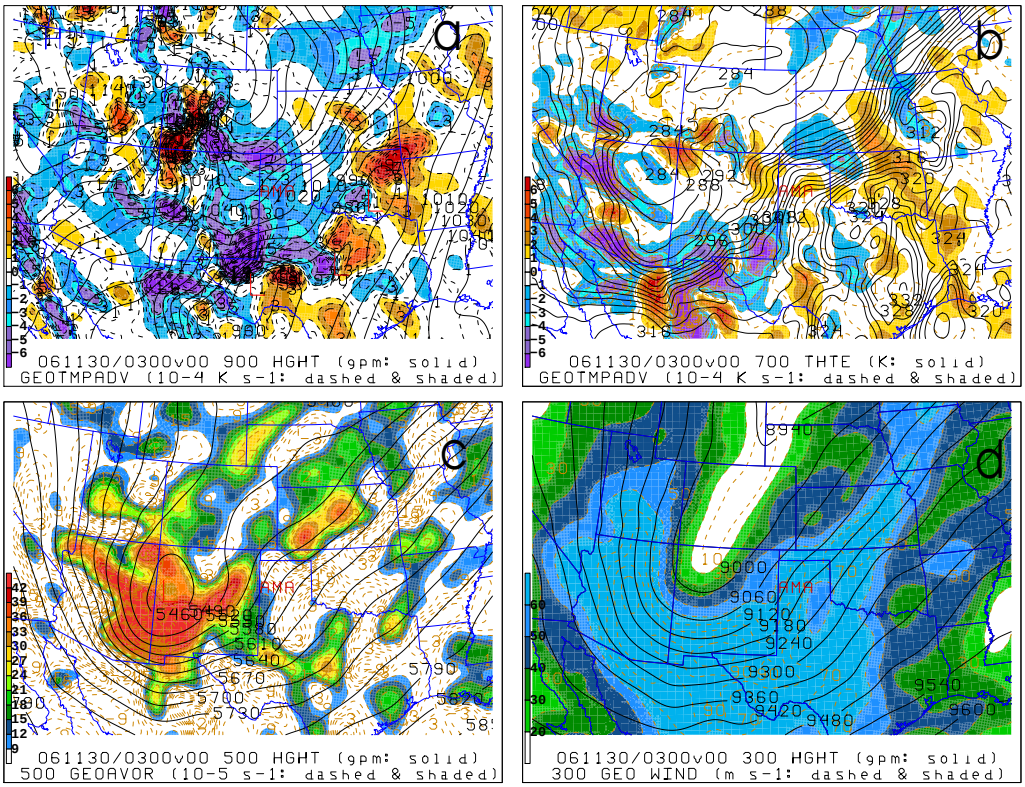

Figure 6.7: Standard upper air charts valid at 0300 UTC 30 November 2006 from the initial analysis of the 40-km RUC model. Panel (a) corresponds to 900-hPa height (gpm, solid lines) and geostrophic temperature advection ($10^{-4} K s^{-1}$, dashed lines and color shading). Panel (b) corresponds to 700-hPa equivalent potential temperature (θ_e; K, solid lines) and geostrophic temperature advection ($10^{-4} K s^{-1}$, dashed lines and color shading). Panel (c) corresponds to 500-hPa height (gpm, solid lines) and geostrophic absolute vorticity ($10^{-5} s^{-1}$, dashed lines and color shading). Panel (d) corresponds to 300-hPa height (gpm, solid lines) and geostrophic isotachs ($m s^{-1}$, dashed and color shading). Location of initiation site is represented by surface station identifier KAMA (Amarillo, TX).

6.1.1.2 Growth rates, sounding examination, and type of instability

The findings for σ^2 in this case study were consistent with previous studies (Bennetts and Hoskins 1979; Bennetts and Sharp 1982) in accurately anticipating elevated convection, the type of storm structure, and identifying the source of the instability released in the background environment. A plot of the growth rates three hours prior to initiation (Fig. 6.8a) showed the highest values southeast and southwest of the region of interest. This pattern matched up reasonably well but not precisely with the intense activity from the radar occurring in approximately the same locale. As this area of elevated magnitudes progressed northward by 0300 UTC, the RUC-2 analysis at the LHSGR (700 hPa; Fig. 6.8b) had the northern extent of the $0.2h^{-2}$ zone just a couple grid points away and the corresponding pattern of σ^2 organizing into more of a linear, elongated configuration compared to the preceding RUC-2 analysis, with adequate saturation of the environment in and around the KAMA region. Despite the limitations in the resolution of the model framework, the banding pattern in the radar reflectivities was reasonably reproduced by applying the growth rates at the level for which they maximized (compare Fig. 6.8 with Figs. 6.5 and 6.6). Thus, this prognostic appeared to be reliable in identifying spatial extent and determining expected movement of possible convective development.

The presence of both low EPV values (small positive to negative) and high relative humidity (Fig. 6.8a) identified a moisture rich environment and instability over portions of eastern NM, and southeastern CO initially, where temperatures were low enough for precipitation to fall as snow. Subsequently, this area progressed into the central United States and expanded to encompass the panhandle of TX (Fig. 6.8b). While all of the essential ingredients were in place for convection to develop, the addition of the growth rate parameter in Fig. 6.8 offered a means to refine the forecast area. The downward trend in stability (positive values of σ^2) occurring in an atmosphere already prone to ver-

tical/slantwise displacements of air parcels suggested that the most likely area for mesoscale updrafts (possibly on a scale too small to be resolved in the RUC-2) capable of producing lightning in the near future to be west to southwest of the Amarillo. Indeed, 16 CG flashes were recorded just in the comparable, narrow corridor stretching 100-150 km towards the Farwell, TX/Clovis, NM vicinity in a 50 minute period spanning 0240-0330 UTC on the 30^{th} of November (not shown). By overlapping the NLDN with the level III radar (1 km resolution) data in GEMPAK, these same CG flashes occurred often in conjunction with embedded cells (35-45 dBZ) on the southern portion of the snowband previously mentioned (e.g., Fig. 6.6).

The approach of combining several factors on a map to fine tune an area of concern is often followed during the spring and early summer when severe weather is a concern over the central United States. While thunderstorms and their attendant precipitation are generally less frequent in the wintertime, many including Schultz and Schumacher (1999) and Wetzel and Martin (2001) advocate using an ingredients methodology to diagnose and predict their existence. Although substantial dynamics and moisture must be present in such situations (e.g., Johns and Doswell 1992, Schultz and Schumacher 1999), the stability to air parcel displacements is often the discriminator in determining the potential for enhanced snowfall rates from convection, primarily slantwise in nature (e.g., Market et al. 2006). Thus, similar to what was accomplished in the composites, growth rates could be superimposed on top of EPV (in a near real-time fashion) to facilitate the process of estimating the likely location and timing of heaviest snowfall, as well as assess the potential for banding.

Figure 6.9 presented the skew-T analysis for KAMA valid at 0300 UTC 30 November 2006, with profiles of vertical velocities and θ_e displayed on the left side and inset of the illustration, respectively. In addition, as evident on the other side of the image, NSHARP calculates commonly derived sounding param-

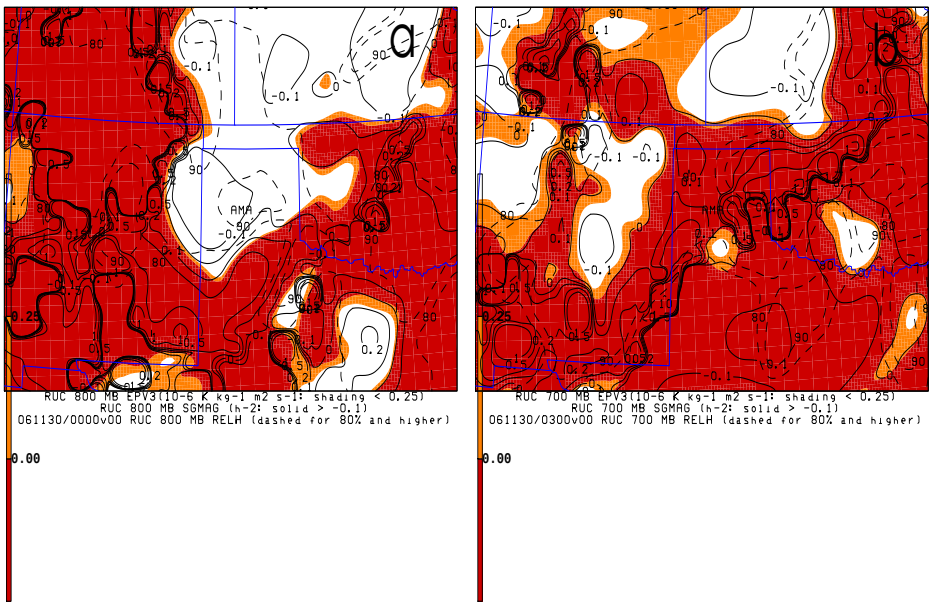

Figure 6.8: Initial analysis of the growth rate parameter (σ^2; h^{-2}, solid lines > -0.1), 3-D equivalent potential vorticity (EPV; $10^{-6} K kg^{-1} m^2 s^{-1}$, color shading < 0.25), and relative humidity (dashed for 80% and higher) from the 40-km RUC model. Panels (a) and (b) correspond to the LHSGR. The left panel (a) is valid at 0000 UTC 30 November 2006 while the right panel (b) is valid at 0300 UTC 30 November 2006. Location of initiation site is represented by surface station identifier KAMA (Amarillo, TX).

eters and presents the generated information in a text format. The examination demonstrated modest ascent throughout the depth of the troposphere with some of the best upward motions (approximately -5 $\mu bars\ s^{-1}$) centered around 700 hPa. Appropriate synergistic interaction between the other two essential ingredients was supported by the low dewpoint depressions stretching from the surface up to 600 hPa and the co-existence of a near neutral (e.g., at the LHSGR) to slightly negative (e.g., at the MULPL; 650 hPa) stratification (Fig. 6.9). Above the midlevel frontal inversion, the rapid, considerable drying and strong environmental lapse rates (e.g., 700-500hPa layer: $6.9 K km^{-1}$) most likely encouraged the onset of CI positioned above CSI. The former type of instability was determined from vertical changes in θ_e and the additional existence (albeit minor; 1 Jkg^{-1}) of elevated CAPE. On the other hand, slantwise convection released from the latter was presumed from the combination of positive growth rates and negative EPV (Fig. 6.8b), as well as a weak, convectively stable atmosphere at 700 hPa (Fig. 6.9). Further confirmation, however, was acquired from the usual cross-section analysis of the M_g - θ_e relationship perpendicular to the midtropospheric baroclinic zone (not shown). Along with the fact that the MULI was near zero and that temperatures were entirely below freezing, all of these particular signatures fell into the accepted range of values for convective snow established by Market et al. (2006) and also earlier in the present study (e.g., section 4.2.3 and Fig. 3.4). Thus, the sounding approach also advanced the fact that electrical activity in the significant snowstorm should be expected near the KAMA site.

6.1.2 28 February 2007

6.1.2.1 Synopsis: Surface, upper-air, and radar analysis

The second case study of TSSN that will be discussed occurred in the late winter over the Upper Midwest, where the first report was associated once again with the open wave phase of cyclone development. Over the course of a period

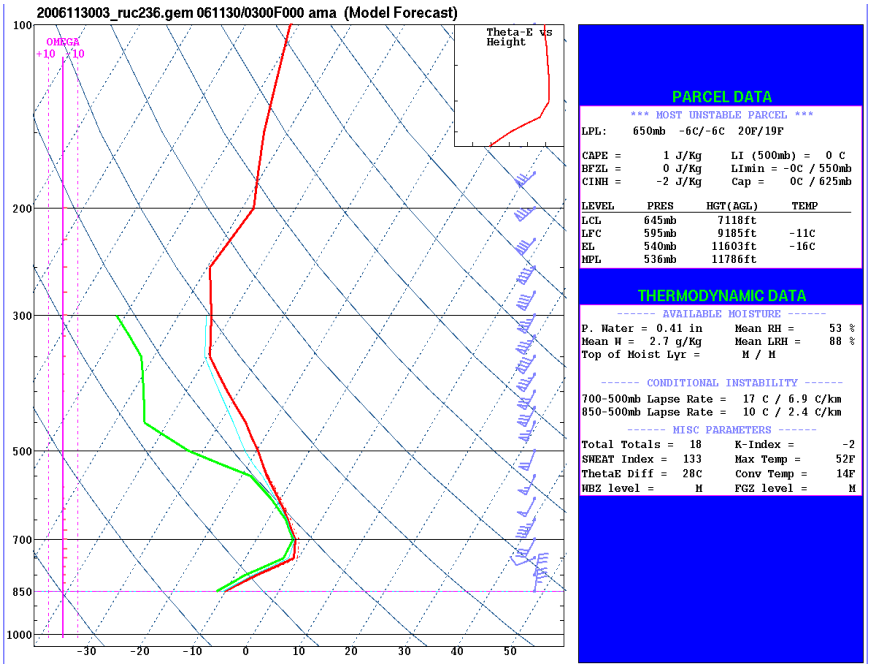

Figure 6.9: A skew-T analysis valid at 0300 UTC 30 November 2006 from the KAMA initiation site using the initial forecast fields produced by the 40-km RUC model.

spanning almost 48 hours between 28 February 2007 - 2 March 2007, a detached, area of cold sector lightning activity was present across seven states that mainly favored an axis stretching from extreme northeastern KS to the upper peninsula of MI (not shown). Consistent with the late November/early December event discussed previously, cooperative stations (Fig. 6.10) with the greatest accumulating snowfall (often 12 inches or more) were generally found to overlap with this described stretch of land, just north of the rapidly, intensifying center of low pressure. Another recurrent characteristic was the negative polarity present in the electrical nature of the storms, as first shown in Fig. 6.2 and once more recently in Fig. 6.11. This distinction was further highlighted by Pettegrew et al. (2007) as they found that only 14 percent of *all* CG strokes in the winter precipitation (for this particular storm system) were positively charged. More considerable evidence for this type of polarity outside of this one occurrence of TSSN was also provided by an overall climatology of several recent convective snowfall events by Becker et al. (2007).

The surface analyses in Figs. 6.12 and 6.13 depicted the main, 997-hPa cyclone center situated over the panhandle of OK with a connected trough of low pressure stretching northward into western SD, where the slow east to northeastward progression of the storm system into south central KS transpired between 1100 UTC to 1400 UTC 28 February 2007. During this time frame, the 1000-500hPa thickness pattern became more amplified downstream as warm air advanced farther poleward into the northern Plains and upper Midwest. Still, the 5400-gpm contour line stayed just south of the area of interest, such that the lone, earliest CG flash occurred near O'Neill, NE (KONL; compare Fig. 6.13 to Fig. 6.11). Accordingly, the partial thickness evaluation and RUC surface temperatures from Fig. 6.11 supported the occurrence of winter precipitation. Although copious amounts of water vapor were prevalent south and east of the primary disturbance, modest bright shading in the satellite imagery suggested

decent cloud development within the subfreezing airmass as well (Figs. 6.12 and 6.13). Underneath this latter region, light precipitation generally in the form of snow was reported from a combination of METARs and radar for portions of ND, SD, and NE (Figs. 6.14 and 6.15). The 25-35dBZ reflectivity values near the place and time of thunderstorm initiation coincided with a cluster of cells, unlike the more organized, banded arrangement discussed for 0300 UTC 30 November 2006. With minimal convection in the beginning, only a few inches in accumulations were recorded over northeastern NE (Fig. 6.11). Still, greater snowfall totals were observed within a few hundred kilometers often in conjunction with later incidents of TSSN. Consequently, this purported close relationship initially put forward by Crowe et al. (2006) has been reinforced by two examples of vigorous, cold-season ETCs and the explicit identification of CG lightning from the NLDN.

The RUC upper-air analysis at 1400 UTC 28 February 2007 in Fig. 6.16 was more complex compared to that at 0300 UTC 30 November 2006 in Fig. 6.7. Two separate disturbances were influencing weather conditions over the central United States, the dominant circulation connected to a broad, long-wave trough over the four corners region and the secondary counterpart apparently due to an embedded, negatively tilted short-wave trough located in eastern MT (e.g., Figs. 6.16a,c). Dynamic and thermodynamic forcing from the combination of both features was aiding in large-scale ascent over a vast area east of the Rocky Mountains. In particular, jet stream diffluence was evident (Fig. 6.16d), several geostrophic, cyclonic vorticity centers were propagating within the 500-hPa southwesterly flow (Fig. 6.16c), and lower to middle tropospheric warm air advection was concurrent with two distinct trowal airstreams (Figs. 6.16a,b). The increase in temperature advections with height near KONL and the orientation of the convective initiation site to the right of the θ_e ridge apex were consistent with both Figs. 6.7 and 5.2 as well as the example offered in Melick et al. (2008;

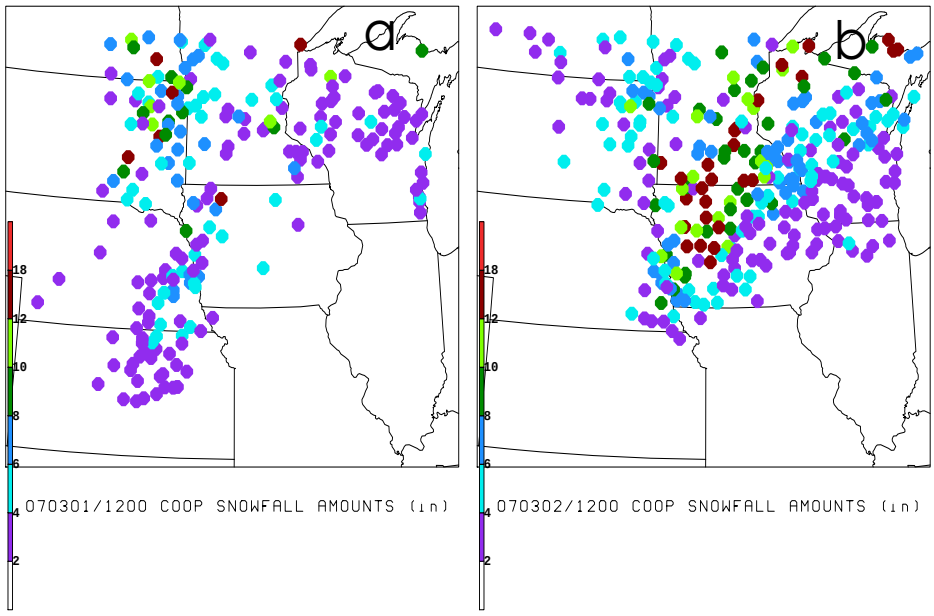

Figure 6.10: As in Fig. 6.1 except for snowfall accumulations ending on (a) 01 March 2007 and (b) 02 March 2007.

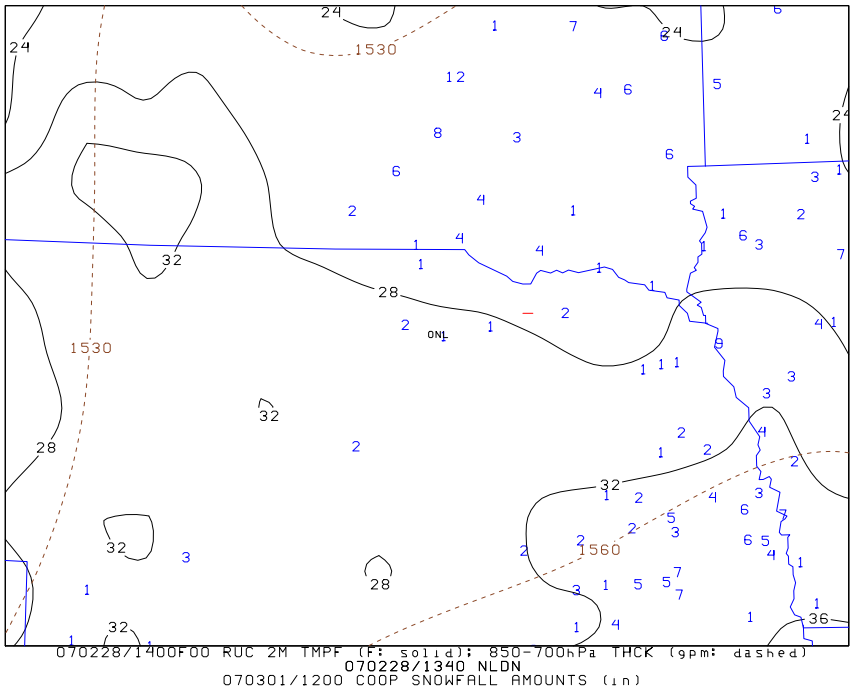

Figure 6.11: Cooperative (24-hr) snowfall accumulations ending at approximately 1200 UTC on 01 March 2007 and 1400 UTC 28 February 2007 40-km RUC 2-meter temperature (^0F, solid lines) with 850-700hPa thickness (gpm, dashed lines). The National Lightning Detection Network (NLDN) analysis of cloud-to-ground lightning flashes valid at 1340 UTC 28 February 2007.

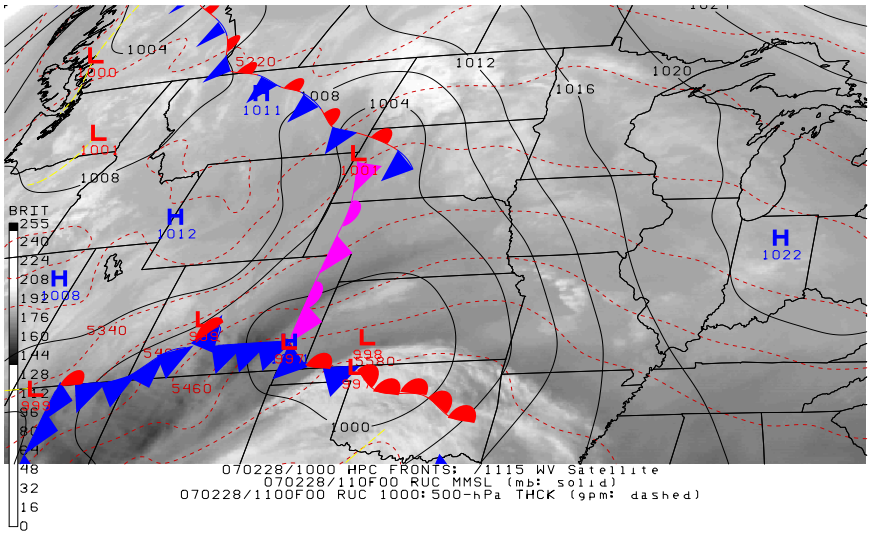

Figure 6.12: As in Fig. 6.3 except valid for about 1100 UTC 28 February 2007 using a combination of 1000 UTC HPC frontal depictions, 1115 UTC water vapor imagery, and 1100 UTC 40-km RUC sea level pressure (hPa; solid lines) with 1000-500hPa thickness (gpm; dashed lines).

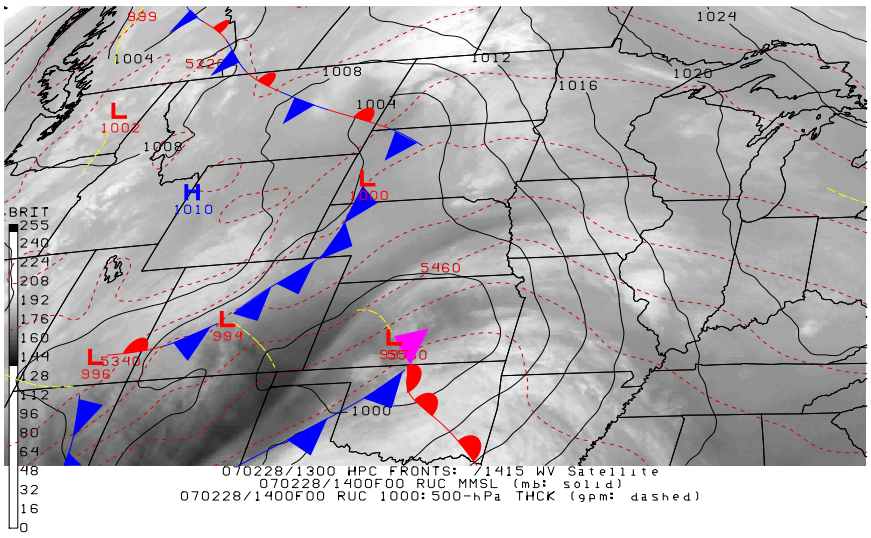

Figure 6.13: As in Fig. 6.3 except valid for about 1400 UTC 28 February 2007 using a combination of 1300 UTC HPC frontal depictions, 1415 UTC water vapor imagery, and 1400 UTC 40-km RUC sea level pressure (hPa; solid lines) with 1000-500hPa thickness (gpm; dashed lines).

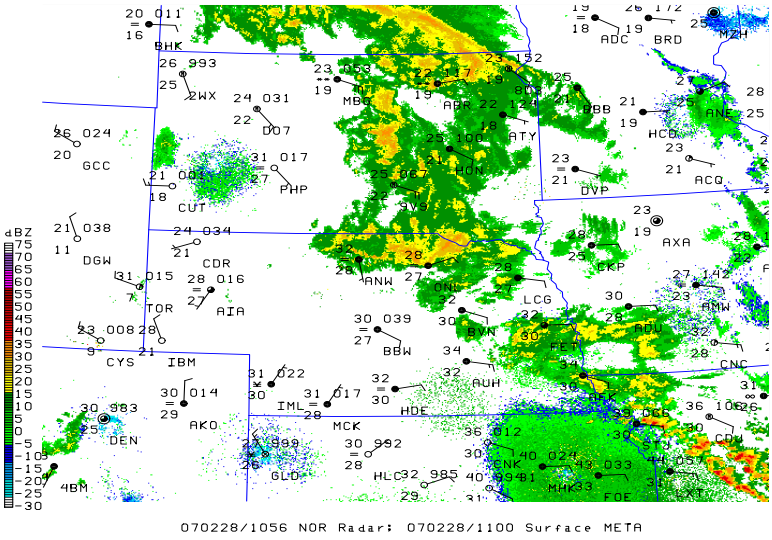

Figure 6.14: As in Fig. 6.5 except valid for about 1100 UTC 28 February 2007. The 1056 UTC radar reflectivity patterns obtained from several WSR-88D sites surrounding initiation location (KONL) in conjunction with 1100 UTC standard plotted METAR observations.

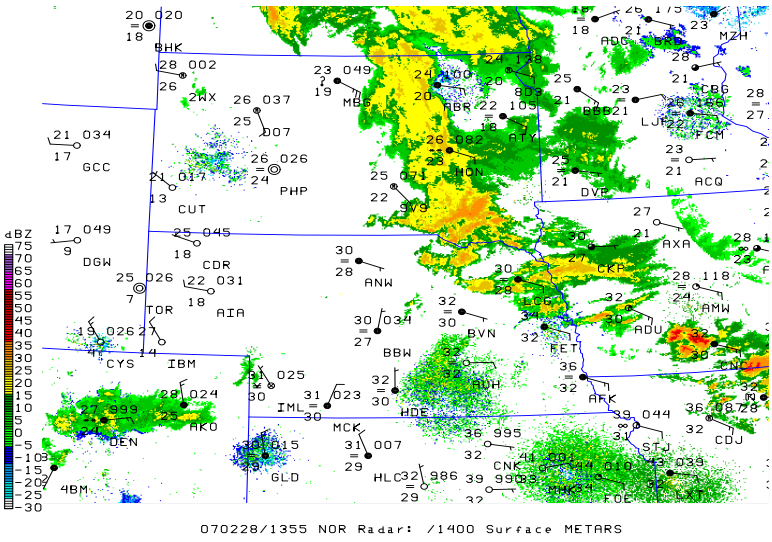

Figure 6.15: As in Fig. 6.5 except valid for about 1400 UTC 28 February 2007. The 1355 UTC radar reflectivity patterns obtained from several WSR-88D sites surrounding initiation location (KONL) in conjunction with 1400 UTC standard plotted METAR observations.

see their Fig. 3). Thus, it is intriguing to note that while each TSSN environment is not exactly identical (e.g., magnitude of ETC and characteristics of related meteorological phenomena), certain signals in the background synoptic plots were systematic. Given the deterministic nature of anticipating convection in the midst of snowstorms, forecasters could become aware of these trends in the analyses and ultimately would be of value in deciding whether to issue severe winter weather outlooks.

6.1.2.2 Growth rates, sounding examination, and type of instability

The structure of the radar reflectivity and attributes of the lightning activity were different for 1400 UTC 28 February 2007 compared to 0300 UTC 30 November 2006. In the hour following initiation, this case study was distinct in only having one CG flash occur in the area of freezing temperatures and the lack of banding in the precipitation surrounding KONL (e.g., Fig. 6.15). While σ^2 (3-D EPV) increased (decreased) leading up to the first report of TSSN (Fig. 6.17a,b), the distribution of positive growth rates had less of a linear framework against that in Fig. 6.8a,b. An inspection of frontogenesis in plan and cross-sectional views (not shown) featured a layer of positive results above and near the area of interest in both scenarios, but the strength of the signal tended to be weaker and more spread out as opposed to the tight, banded nature in the late November/early December instance. Thus, the exact interaction of mesoscale forcing, abundant moisture, convective instability, and destabilization determined the strength and likelihood of elevated thunderstorms in the winter precipitation events. While these combined factors in the RUC diagnostics were more robust with the numerous CG flashes in the earlier episode, the necessary, overlapping ingredients accurately captured the timing and spatial properties in the observations (i.e. northeast NE at 1400 UTC 28 February 2007). Unlike the banded TSSN scenario, the magnitudes of σ^2 were lower and only slightly positive at

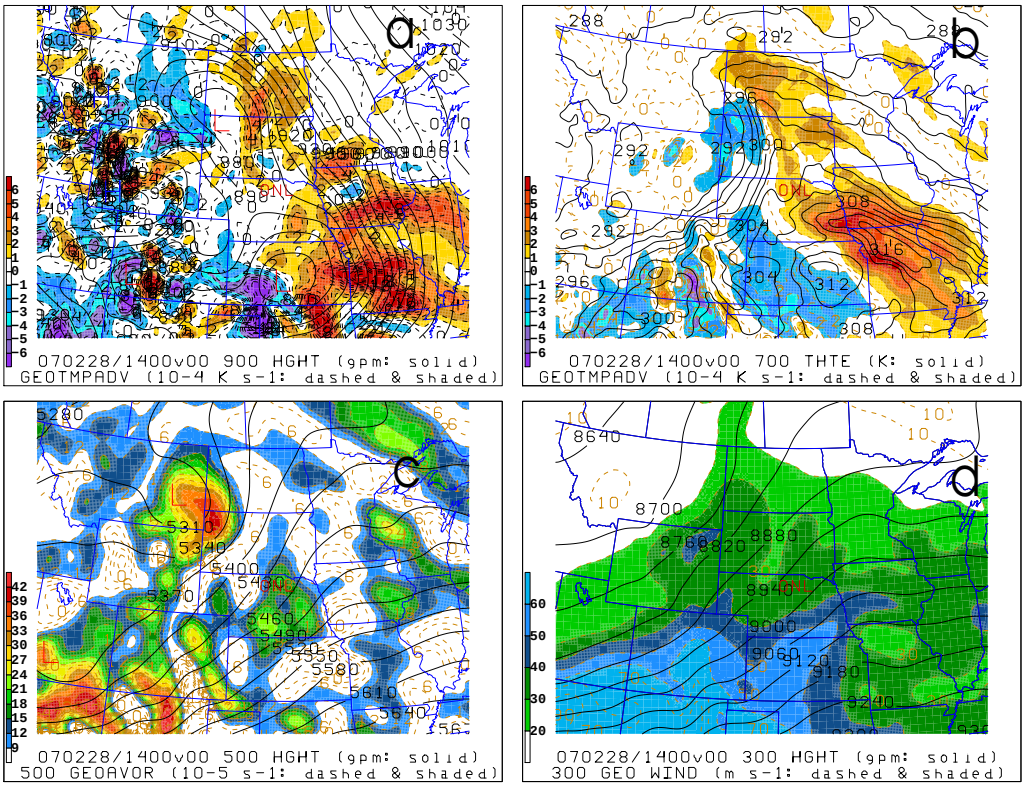

Figure 6.16: As in Fig. 6.7 except for 1400 UTC 28 February 2007. Location of initiation site is represented by surface station identifier KONL (O'Neill, NE).

the initiation site (compare Fig. 6.17b to Fig. 6.8b). The other difference is the fact that the type of instability at the LHSGR was convective, something revealed by the θ_e decrease and the 33 Jkg^{-1} of CAPE in the sounding at 750 hPa (Fig. 6.18). Otherwise, the MULI, 700-500hPa lapse rates, intensity of the vertical velocities, wind profile, and temperature inversion were either identical or very similar to the KAMA representation in Fig. 6.9. Thus, the characteristics outlined in these two examples of convective snowfall were largely consistent with the standard conditions of TSSN presented in the composite results from the preceding chapters.

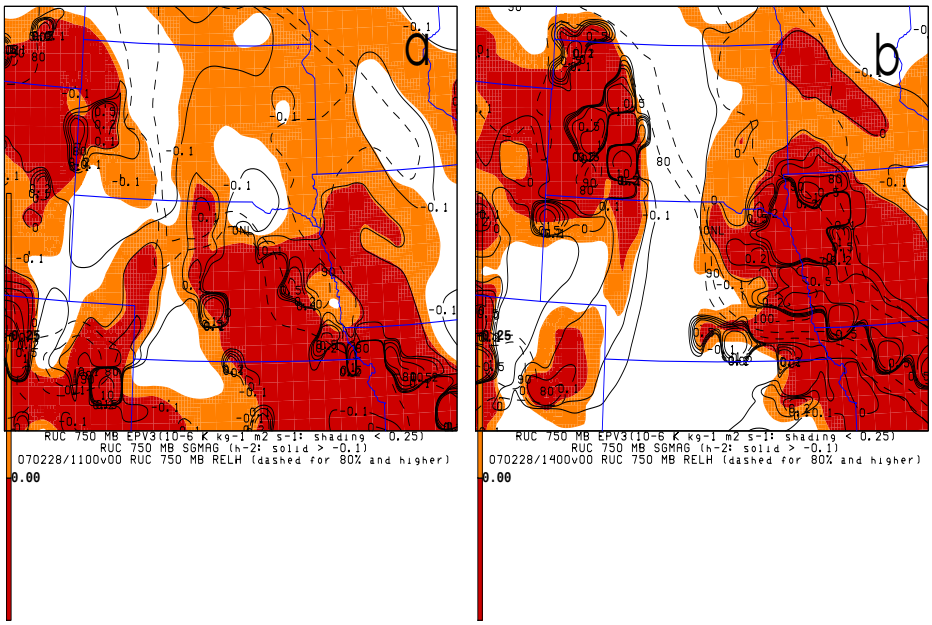

Figure 6.17: As in Fig. 6.8 except for the left panel (a) being valid at 1100 UTC 28 February 2007 and the right panel (b) valid at 1400 UTC 28 February 2007. Location of initiation site is represented by surface station identifier KONL (O'Neill, NE).

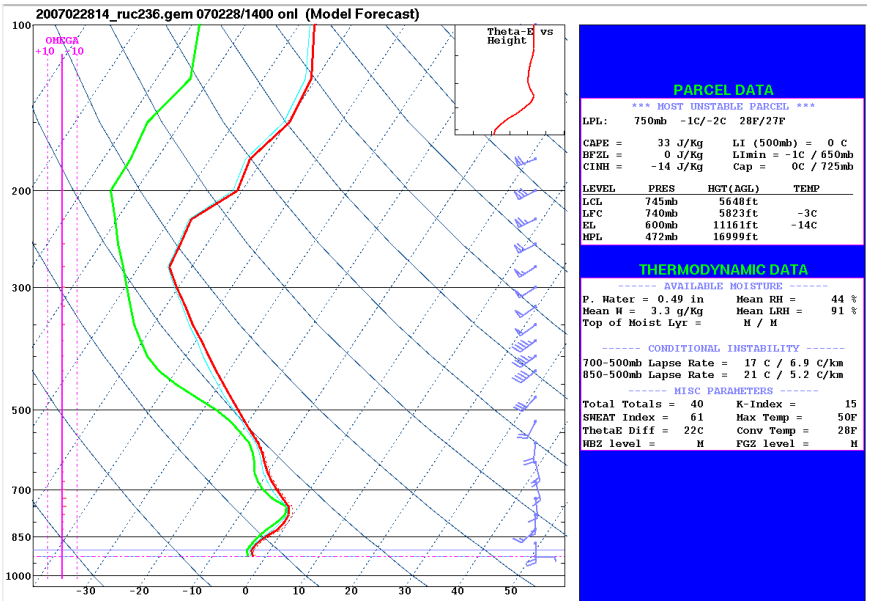

Figure 6.18: As in Fig. 6.9 except for the skew-T analysis for KONL valid at 1400 UTC 28 February 2007.

6.2 non-TSSN Events

6.2.1 01 February 2002

Numerous states in the Upper Midwest experienced several inches of snowfall over the first couple of days in February 2002 (Fig. 6.19) from a parent ETC that did not contain any thunderstorms within the colder air. Unlike the two that did have evidence of lightning activity, the precipitation was generally weaker and resulted in a smaller area reporting twelve inch and greater totals (compare Figs. 6.1 and 6.10 to Fig. 6.19). The central pressure of the surface closed circulation, initially 1002 hPa and situated in southwestern MI at 0900 UTC 01 February 2002, intensified and began to occlude as it traversed northeastward by 1200 UTC (Figs. 6.20 and 6.21). Surface METARs across WI and MI indicated temperatures to be in the lower 20s with light snow predominantly occurring, the latter supported by the elongated pattern of 15-25dBZ reflectivity values in

Figs. 6.22 and 6.23. The intrusion of dry air northward over Lake Michigan in the midlevels, as noted in the satellite perspective, acted to effectively delineate the wrap-around moisture behind the cold front (e.g., Fig. 6.20 and Fig. 6.21). The RUC analysis of 700-hPa streamlines and mixing ratios particularly substantiate this evaluation (not shown) and the 1000-500hPa thickness plots showed lower average tropospheric temperatures in the vicinity of the winter precipitation compared to that of 30 November 2006 (e.g., Fig. 6.4) and 28 February 2007 (e.g., Fig. 6.13). The colder environment was accompanied by the absence of warm air advection and the displacement of the θ_e ridge axis farther east (Fig. 6.24a,b), this configuration not conducive to supporting and enhancing upward vertical motions. Farther aloft, the trough axis at 1200 UTC was coincident with the area of interest near Green Bay, WI (KGRB), where prolonged snowfall had occurred *but* without the presence of CG flashes (Fig. 6.24c,d). From a QG approach, the favorable dynamics for lift were advanced by the translation of the associated, strong positive vorticity maximum and the slight downstream placement of the strongest winds in the jet stream.

Figure 6.25 displayed a combined examination of 3-D EPV, σ^2, and RH for the 2002 February 01, similar to that in Figs. 6.8 and 6.17. However, in this non-TSSN example, the LHSGR estimates portrayed a nearly saturated atmosphere preconditioned toward greater stability in the 0900-1200 UTC time frame. In particular, moist slantwise/upright convection was more likely toward the northern portions of MI and Lake Michigan (Fig. 6.25a), with this region shifting eastward in three hours (Fig. 6.25b). In the vicinity of KGRB, on the other hand, values for growth rates (EPV) were slightly negative (slightly positive) initially and had a downward (upward) trend. Furthermore, unlike the two TSSN case studies, lapse rates of θ_e were strongly positive up through 600 hPa (compare Fig. 6.26 to Figs. 6.9 and 6.18). While the representative sounding revealed upward vertical velocities on the same order of magnitude, the potential for lightning production

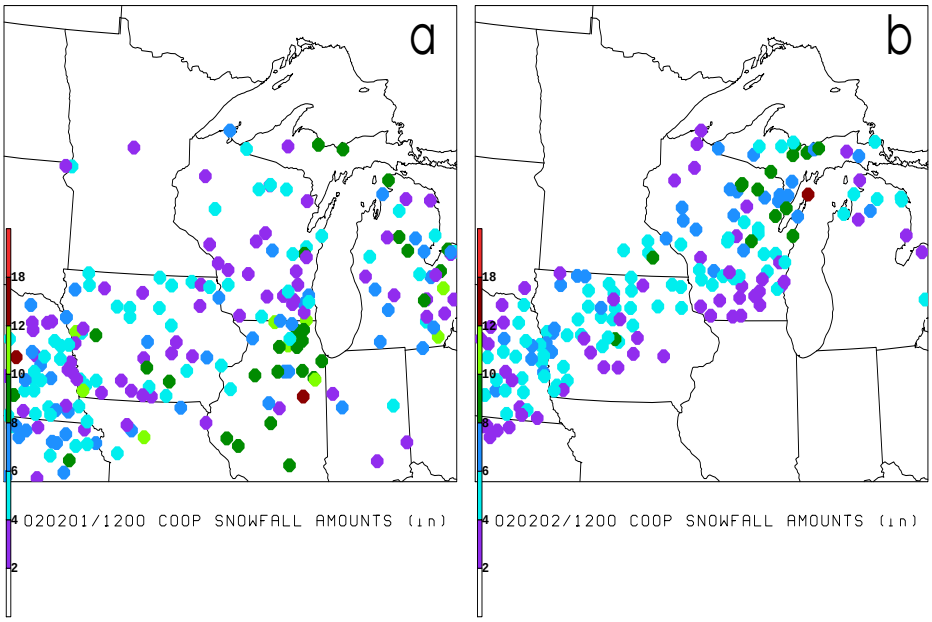

Figure 6.19: As in Fig. 6.1 except for snowfall accumulations ending at approximately 1200 UTC on (a) 01 February 2002 and (b) 02 February 2002.

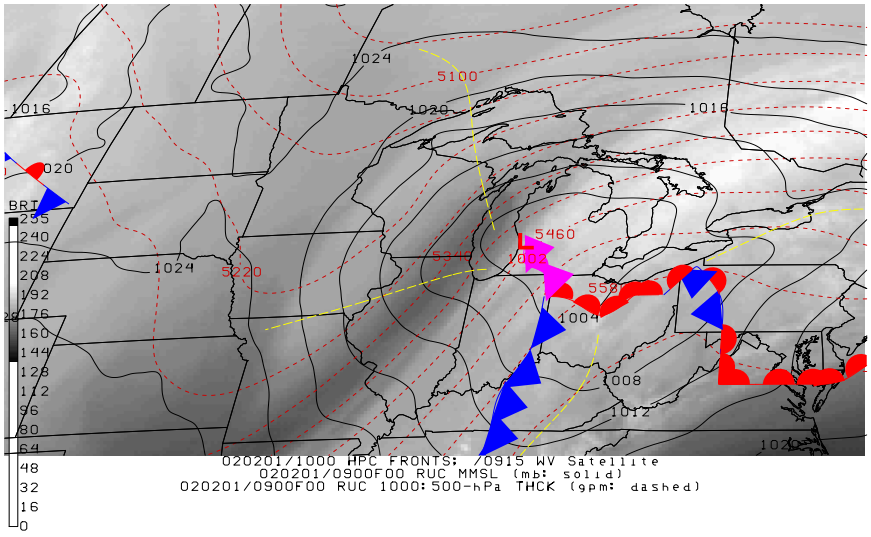

Figure 6.20: As in Fig. 6.3 except valid for about 0900 UTC 01 February 2002 using a combination of 1000 UTC HPC frontal depictions, 0915 UTC water vapor imagery, and 0900 UTC 40-km RUC sea level pressure (hPa; solid lines) with 1000-500hPa thickness (gpm; dashed lines).

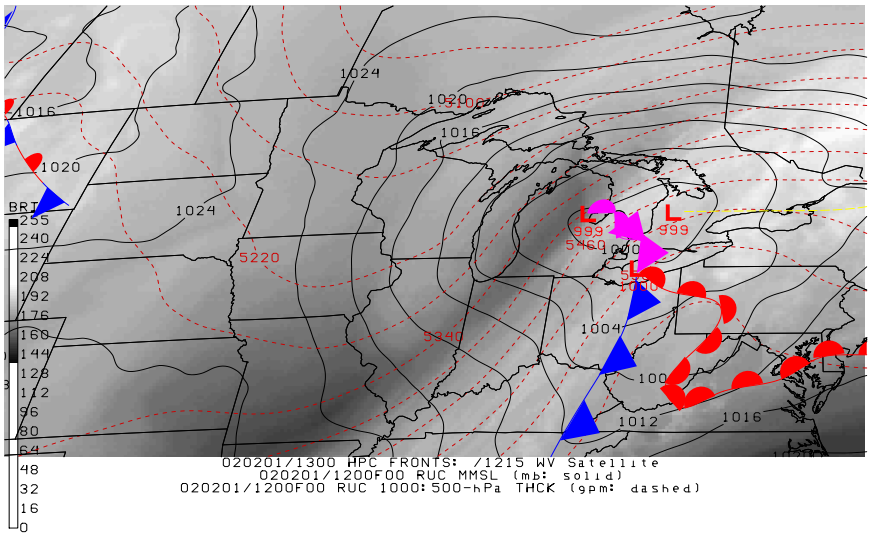

Figure 6.21: As in Fig. 6.3 except valid for about 1200 UTC 01 February 2002 using a combination of 1300 UTC HPC frontal depictions, 1215 UTC water vapor imagery, and 1200 UTC 40-km RUC sea level pressure (hPa; solid lines) with 1000-500hPa thickness (gpm; dashed lines).

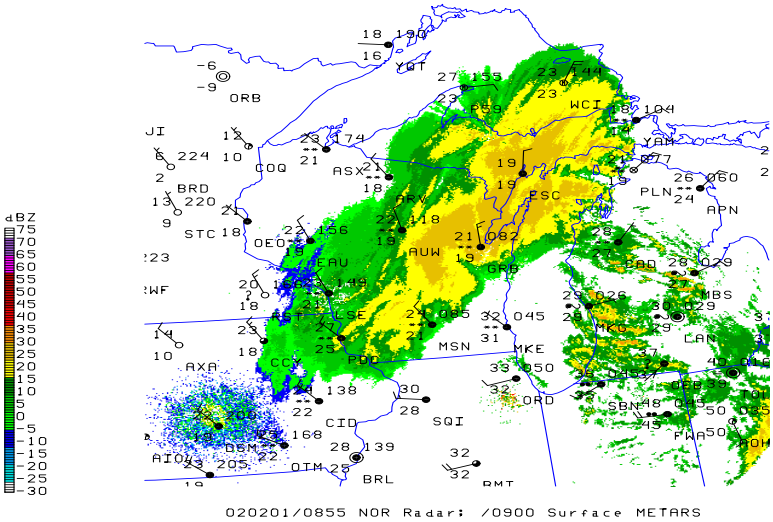

Figure 6.22: As in Fig. 6.5 except valid for about 0900 UTC 01 February 2002. The 0855 UTC radar reflectivity patterns obtained from several WSR-88D sites surrounding midpoint location (KGRB) in conjunction with 0900 UTC standard plotted METAR observations.

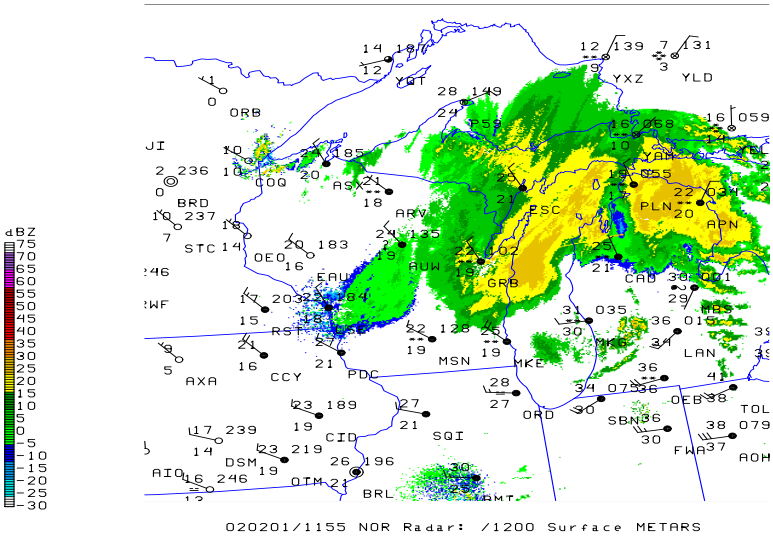

Figure 6.23: As in Fig. 6.5 except valid for about 1200 UTC 01 February 2002. The 1155 UTC radar reflectivity patterns obtained from several WSR-88D sites surrounding midpoint location (KGRB) in conjunction with 1200 UTC standard plotted METAR observations.

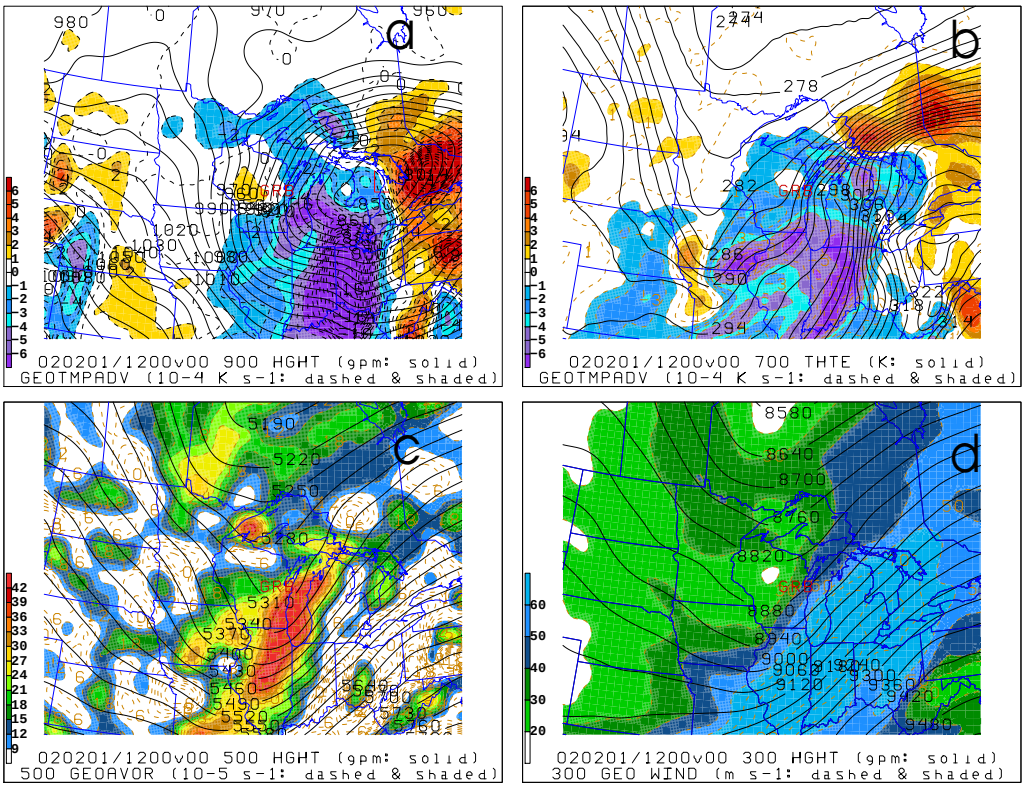

Figure 6.24: As in Fig. 6.7 except for 1200 UTC 01 February 2002. Location of midpoint site is represented by surface station identifier KGRB (Green Bay, WI).

was diminished as temperatures were too cold to allow an abundant concentration of supercooled water droplets below the MULPL (e.g., Bright et al. 2005; Van Den Broeke et al. 2005). Similar to the statistical evaluation reached by Smith (2006), the altitude of the -10^0C level in this particular event was below that of the two prior soundings with CG flashes nearby (compare Fig. 6.26 to Figs. 6.9 and 6.18). More importantly, this height failed to reach the minimum criteria of 1.4 km proposed by Michimoto (1993) where the temperature at the high MULPL (550 hPa) for KGRB had declined to a -23^0C reading. Finally, the absence of MUCAPE, slightly more elevated MULI of 2, and the less than aspiring (i.e. 5.1 Kkm^{-1}) 700-500hPa lapse rates combined to also provide further demonstration to the stable stratification at 1200 UTC 01 February 2002.

6.2.2 24 February 2003

Observations from cooperative stations on 23 February 2003 and 24 February 2003 showed widespread snowfall affecting a sizable portion of the central United States but predominantly having the greatest impact on southwest MO, southeast KS, and north-central to northeast OK where amounts tended to be 8 inches and higher (Fig. 6.27). Satellite, HPC, and RUC-2 analyses around 2100 UTC 23 February 2003 depicted the presence of a 1004-hPa cyclone situated near Texarkana, TX with attendant surface fronts, the 5400 gpm thickness isopleth displaced just a short distance to the west and north of the surface disturbance, and the best supply of water vapor residing over the Midwest into the subfreezing airmass (Fig. 6.28). Unlike the earlier occurring non-TSSN event, Fig. 6.29 revealed reflectivity values over 25 dBZ occurring in tandem with moderate to heavy snowfall diagnosed from various METARs (e.g., Emporia, KS [KEMP]; Fort Leonard Wood, MO [KTBN]; Joplin, MO [KJLN]; Springfield, MO [KSGF]; Wichita, KS [KICT]). In this specific domain, temperatures varied more as well with the warmest readings near 30^0F. In a short period, the low pressure center

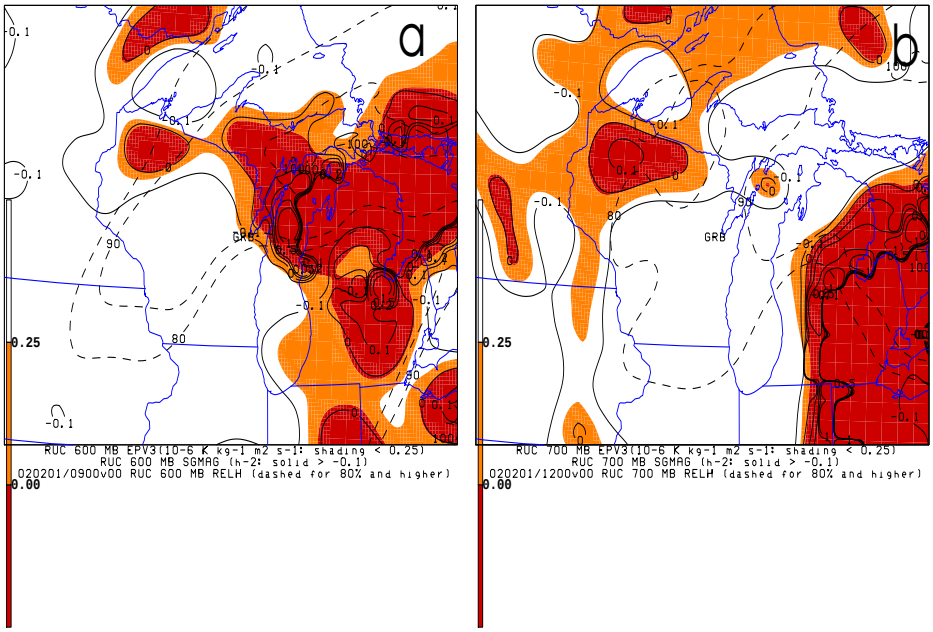

Figure 6.25: As in Fig. 6.8 except for the left panel (a) being valid at 0900 UTC 01 February 2002 and the right panel (b) valid at 1200 UTC 01 February 2002. Location of midpoint site is represented by surface station identifier KGRB (Green Bay, WI).

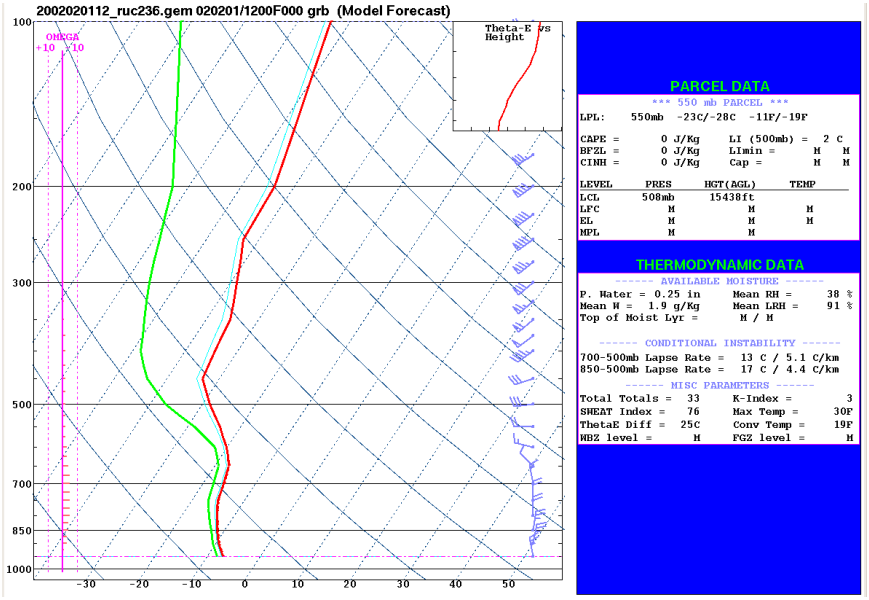

Figure 6.26: As in Fig. 6.9 except for the skew-T analysis for KGRB valid at 1200 UTC 01 February 2002.

decreased in intensity and progressed into southeastern AR, wherein the satellite and radar imagery also indicated a similar movement in the cloud and precipitation shield by 0000 UTC 24 February 2003 (Figs. 6.30 and 6.31). In addition, the conventional upper-air plots for this case study (Fig. 6.32) resembled that of the non-TSSN composites in terms of less developed upper-level features (Fig. 5.4). The 900-hPa and 700-hPa QG diagnosis of cold air advection at KGRB (Fig. 6.32a,b) coexisted with a 500-hPa, broad, open shortwave just upstream (Fig. 6.32c). The trowal airstream was pronounced but situated in a less than favorable position to the right of the southwestern MO area by 0000 UTC, where 700-hPa frontolysis was present (not shown). Further aloft, however, the synoptic scale examination once again portrayed the appropriate cyclonic horizontal shear and divergence relative to the area of interest to aid in upward vertical motions (Fig. 6.32c,d).

Resistance to moist parcel displacements and a tendency toward greater sta-

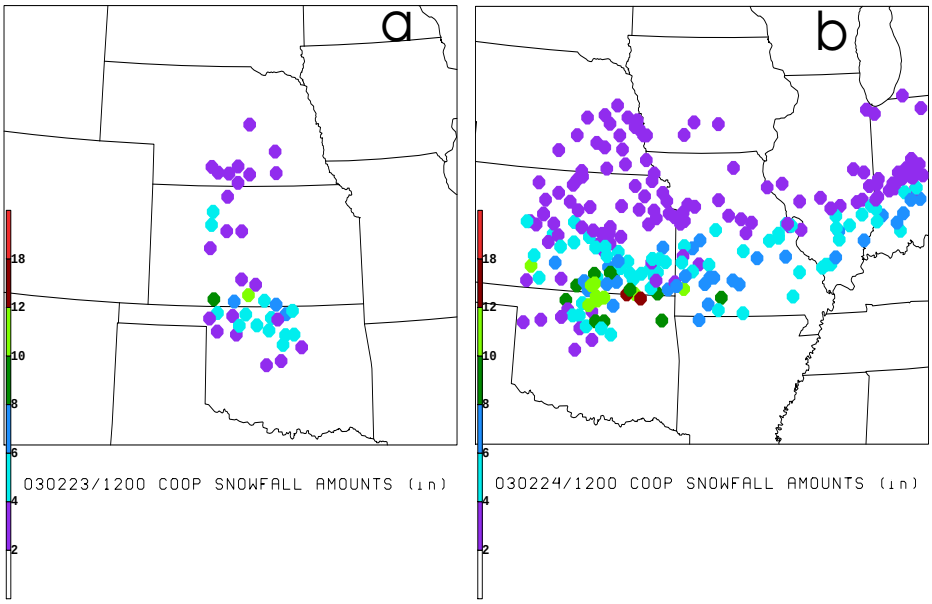

Figure 6.27: As in Fig. 6.1 except for snowfall accumulations ending on (a) 23 February 2003 and (b) 24 February 2003.

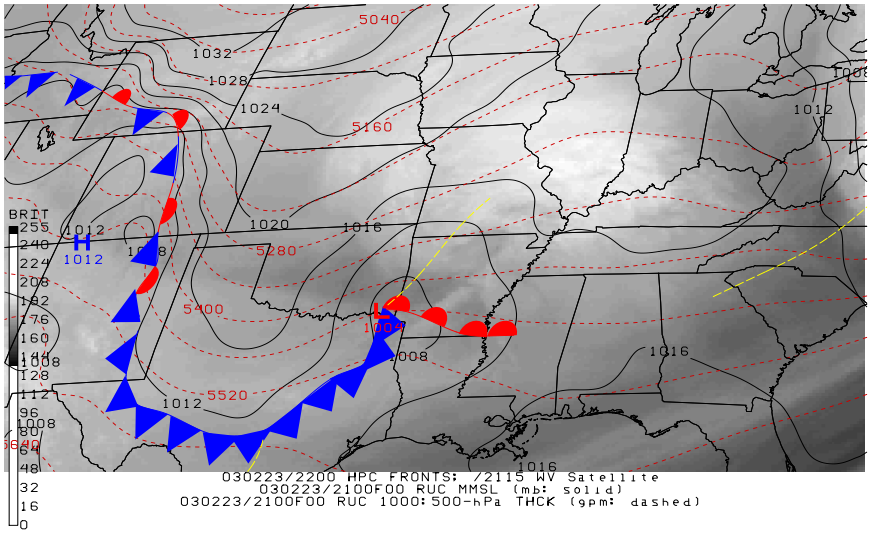

Figure 6.28: As in Fig. 6.3 except valid for about 2100 UTC 23 February 2003 using a combination of 2200 UTC HPC frontal depictions, 2115 UTC water vapor imagery, and 2100 UTC 40-km RUC sea level pressure (hPa; solid lines) with 1000-500hPa thickness (gpm; dashed lines).

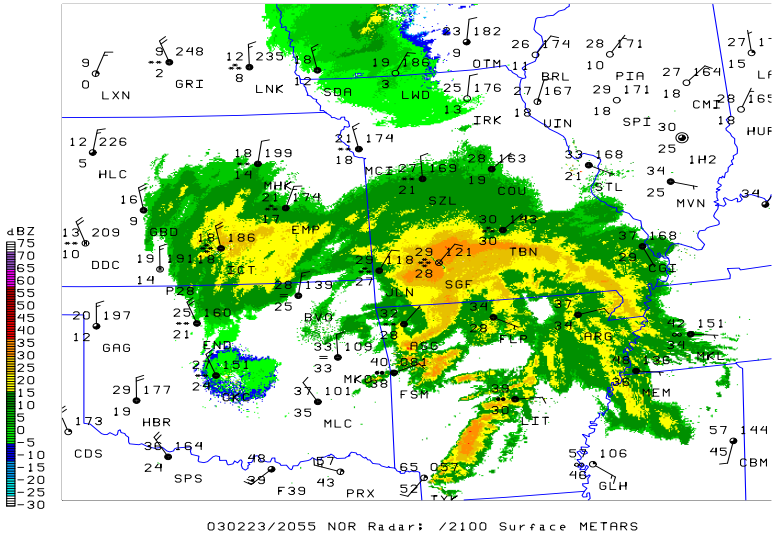

Figure 6.29: As in Fig. 6.5 except valid for about 2100 UTC 23 February 2003. The 2055 UTC radar reflectivity patterns obtained from several WSR-88D sites surrounding midpoint location (KSGF) in conjunction with 2100 UTC standard plotted METAR observations.

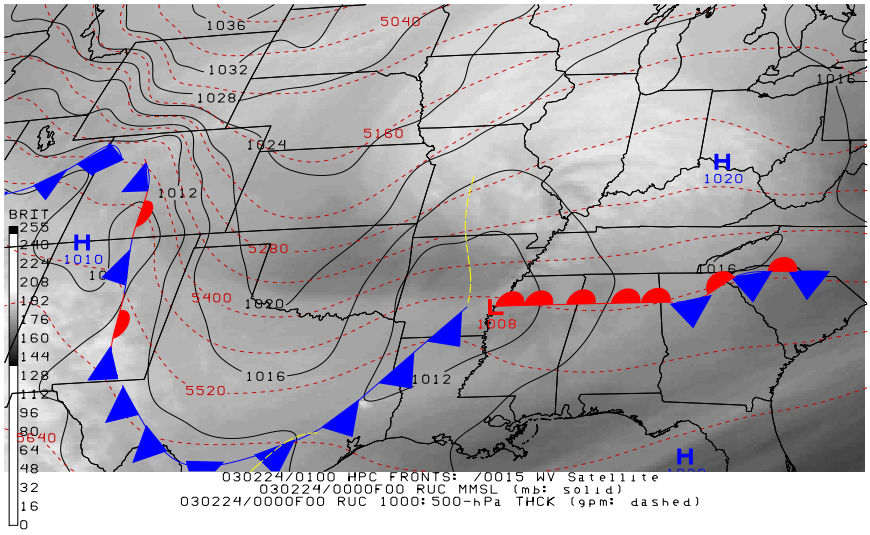

Figure 6.30: As in Fig. 6.3 except valid for about 0000 UTC 24 February 2003 using a combination of 0100 UTC HPC frontal depictions, 0015 UTC water vapor imagery, and 0000 UTC 40-km RUC sea level pressure (hPa; solid lines) with 1000-500hPa thickness (gpm; dashed lines).

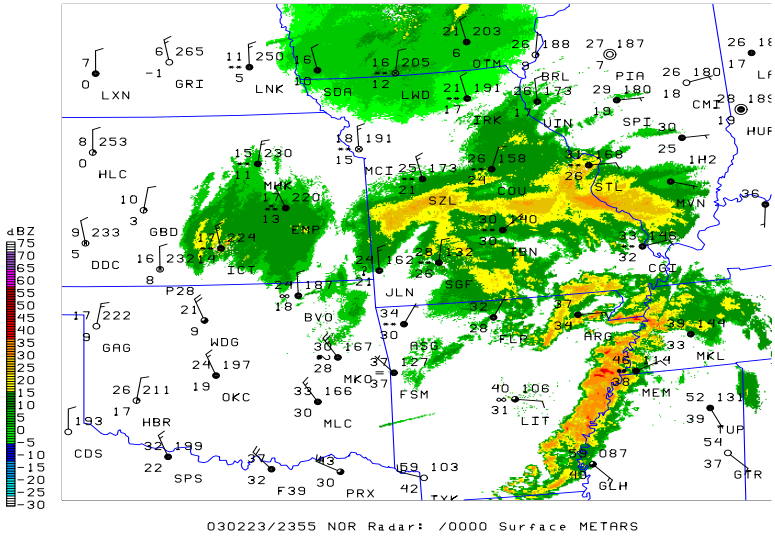

Figure 6.31: As in Fig. 6.5 except valid for about 0000 UTC 24 February 2003. The 2355 UTC 23 February 2003 radar reflectivity patterns obtained from several WSR-88D sites surrounding midpoint location (KSGF) in conjunction with 0000 UTC standard plotted METAR observations.

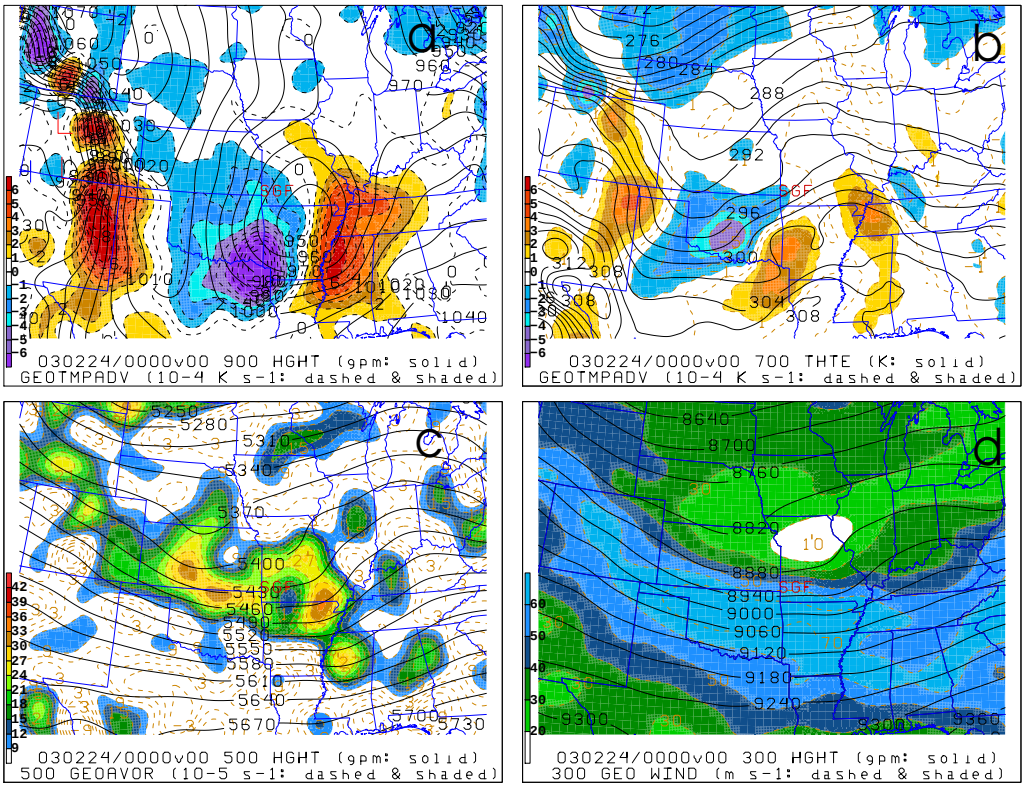

Figure 6.32: As in Fig. 6.7 except for 0000 UTC 24 February 2003. Location of midpoint site is represented by surface station identifier KSGF (Springfield, MO).

bility characterized the environment in the area of interest (Fig. 6.33). Between 2100 UTC (Fig. 6.33a) and 0000 UTC (Fig. 6.33b), the preferred conditions for convective development were displaced predominantly to the east and south, where an above freezing airmass was present. Instead, the values of LHSGR 3-D EPV and σ^2 were generally greater than 0.25 $10^{-6} K kg^{-1} m^2 s^{-1}$ and less than -0.10 h^{-2}, respectively, in southwestern MO. It should also be stressed the weak frontogenesis to frontolysis gave the impression that mesoscale forcing was going to be ineffective in encouraging a narrowing and strengthening of the ageostrophic circulation (not shown). On the other hand, the explicit evaluation of omega from the KSGF sounding portrayed values of about -10 $\mu bars\ s^{-1}$ in the 850-650hPa layer, which was more robust than any of the other stations analyzed (compare Fig. 6.34 to Figs. 6.9, 6.18, and 6.26). The discrepancy might, however, reside with the appropriateness of using the QG approach, something that was suspect to some extent in all TSSN and non-TSSN events with an ETC in close proximity. For instance, the veering in the observed wind direction with height in Fig. 6.34 implied warm air advection in the lower troposphere, an obvious distinction from the simplified diagnosis reached in Fig. 6.32.

From a stability standpoint, the results of a few standard indices (i.e. midlevel lapse rates, MULI) were nearly consistent with those from snowstorms exhibiting evidence of lightning. Nonetheless, these encouraging signs for thunderstorm development were offset by the relatively, strong increase in θ_e with height, the higher MULPL, and the associated temperature being too cold (i.e. $-16^0 C$) to allow for the necessary electrical charge separation within the parent cloud (Fig. 6.34). Even though both non-TSSN events investigated contained no appearance of CAPE within the sounding, this would not necessarily be a fair discriminator seeing that many of the TSSN composite cases displayed the same characteristic (Section 4.2.3). Thus, in summary, the forcing and moisture requirements were satisfied in all of the examples considered in this chapter. Yet,

the crucial instability factor was not as convincing in the typical snowstorms without CG lightning flashes.

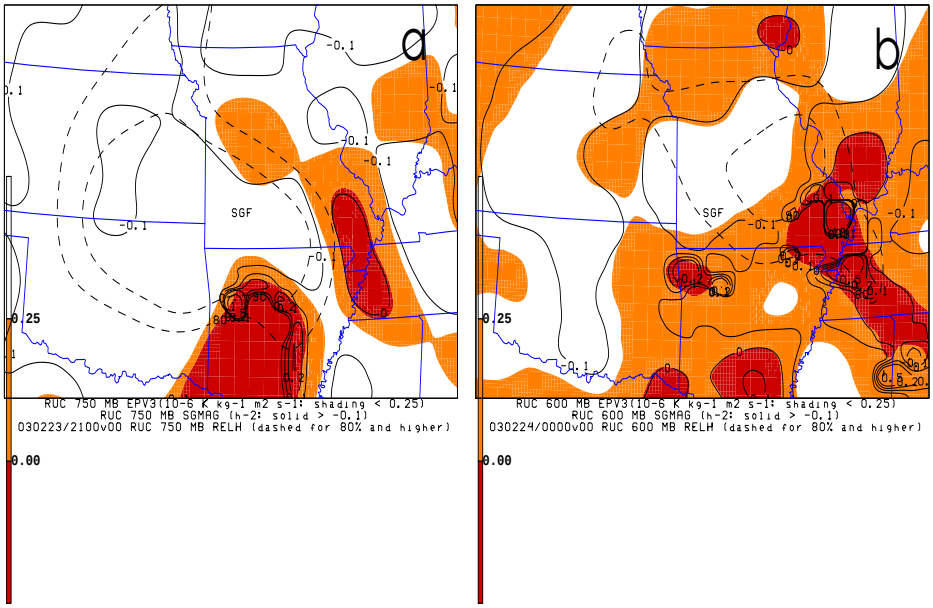

Figure 6.33: As in Fig. 6.8 except for the left panel (a) being valid at 2100 UTC 23 February 2003 and the right panel (b) valid at 0000 UTC 24 February 2003. Location of midpoint site is represented by surface station identifier KSGF (Springfield, MO).

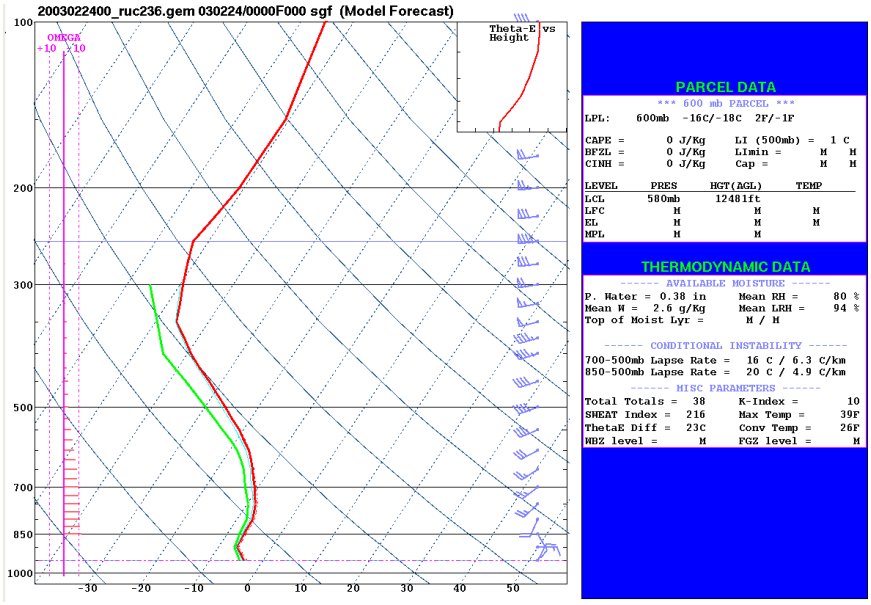

Figure 6.34: As in Fig. 6.9 except for the skew-T analysis for KSGF valid at 0000 UTC 24 February 2003.

Chapter 7

Summary and Conclusions

7.1 Summary

Throughout the current investigation, the main goal was to make a detailed examination of stability characteristics associated with wintertime, elevated thunderstorms immediately leading up to convective initiation. From this additional insight, the strict intention was to discover unique criteria and formulate more accurate strategies for forecasters to predict such phenomena in a nowcasting framework. The tightly, interdependent presence of forcing, moisture, and an unstable environment were crucial to the development of TSSN, as has been first speculated by Schultz and Schumacher (1999), and then recently advanced by Market et al. (2006) and Smith (2006). Several different methods for gauging the atmosphere's response to vertical and slantwise displacements were explored, such as traditional stability indices. Yet, the unconventional application of σ^2 (and its tendency) served as the primary motivation for the dissertation. The diagnosis was accomplished by utilizing two seasons (2003-04 and 2004-05) worth of data while determining tabular point values and creating spatial composite analyses. Given the small sample size, the Mann-Whitney rank sum test was employed to quantify the statistical significance in the stability patterns near the convective initiation site. The importance of the results for the

collection of convective snowstorms was emphasized by the incorporation of a set of non-thundering events. Finally, external case studies to the composite dataset were identified and discussed to check the value of the average findings against *all* events and demonstrate the effectiveness of an ingredients-based methodology by comparing various RUC analyses to observations, particularly concentrating on the sign, magnitudes, trends, and distribution of growth rates.

7.2 Conclusions

The research sought to resolve several inquiries first raised in Section 1.3.1:

1. How substantial are departures from geostrophy in thundersnow events? In other words, is it appropriate or accurate to diagnose the momentum equations of mesoscale features by imposing thermal wind balance on the background environment?

   The short reply is that the geostrophic constraints would not be suitable for the amplified trough attending most winter convection. Still, the legitimacy in the approximation varied considerably from one event to the next. From the more realistic extended growth rates, pronounced departures from this balanced state often did occur in TSSN (and even non-TSSN) episodes. Regardless, the crude representation of the atmosphere was often a quality, first approximation, whereby the placements of features for both σ^2 and σ_e^2 were similar even if not identical. As the effects of curved flow became more enhanced in well developed ETCs, the ageostrophic component to the shear could not be neglected. Specifically, the estimates of R_o were often at least in the intermediate range and would sometimes exceed unity. Ultimately, the net effect on destabilization in convective snow events was an underestimate of its strength from the original theory proposed by Bennetts and Hoskins (1979) and Bennetts and Sharp (1982).

2. Can the approximate location and timing of lightning and thunder in snowstorms be identified immediately beforehand by examining a suite of stability parameters and their trends? Is there general agreement in the various techniques?

   Most of the methods used to evaluate instability and the changes to it with time in instances of TSSN were successful in isolating when and where convection would occur right before initiation. Trends in the traditional stability indices were small but the actual values at either time step were favorable (e.g., MULPL often in the 700-600hPa layer, MULI near 1, 700-500hPa lapse rates at least approaching moist adiabatic) as compared to those obtained in Market et al. (2006) and Smith (2006). While not always present and limited in magnitude, identification of MUCAPE ≤ 50 Jkg^{-1} in the various analyses and near the area of interest meant that the occasional source of elevated convective energy could be realized. Upon comparison with Ri_{sc}, the critical instability criterion was often satisfied in a sizeable number of the snowstorms with lightning activity, this being validated by the mean (-11.85) and median (1.15) MV calculated. The temporal changes, however, were minimal for this stability parameter. More importantly, the establishment of an atmosphere becoming more susceptible to stronger vertical/slantwise motions was also substantiated by the usual downward (upward) trend in 3-D EPV (σ^2 and σ_e^2) and the subsequent, beneficial emergence of negative (positive) results at the end of the short time frame. In a prognostic sense, the preconditioning toward higher growth rates in the near future was especially advanced by the noticeably, high tendencies in σ^2 from both plots and tabular statistics. Although these indications suggested an atmosphere inclined toward destabilization, the large standard deviations in the results does demand some caution in speculating that *all* TSSN scenarios will show the same favorable charac-

teristics.

3. Along those lines, is it possible to predict banding in these events from the growth rate parameter, such as what was accomplished in Bennetts and Sharp (1982)? What is the best way to do this?

   Precipitation banding was repeatedly identified by tracking structures in the plots of growth rates, conforming to the original recommendation in Bennetts and Sharp (1982). While bandedness in the reflectivity pattern tended to become more likely with higher, positive σ^2, the specific 0.2 h^{-1} threshold alone was insufficient for discriminating the type of convection to expect. Instead, a more accurate means was required to recognize shapes in the 2-D analyses of σ^2, an objective not possible with single interpolated estimates. In this regard, a clear distinction was noted in the banded and nonbanded composites and case study examples. From the plan view and cross-section perspective, the growth rates tended to be higher in the portion of the TSSN dataset with precipitation banding and take on a narrow, elongated feature similar to the orientation in the radar pattern. On the other hand, relatively lower values of σ^2 occurred at the initiation site in situations with cellular convection. Accordingly, the RUC analyses tended to show evidence of circular shaped features near the area of interest. Through both tabular and graphical means, greater success was found in obtaining estimates at the LHSGR, something which was not obtained with the set pressure level of 700 hPa utilized by Bennetts and Sharp (1982). This selection was physically more reasonable compared to restricting the analysis to one level in all the thundersnow events since a more ideal situation for convective development is usually where the least resistance to convection was observed.

4. What type of instability is most common in convective snowstorms?

TSSN events were typically found to be stable with respect to pure upright displacements, yet more susceptible to slantwise motions from CSI. In order to determine the type of instability, a term-by-term analysis of σ^2 and an inspection of Ri_{sc} was utilized. Repeatedly, lapse rates in θ_w (or θ_e) were small but positive and baroclinicity was pronounced near where the first CG flash occurred. By assuming nearly geostrophic conditions for both of these approaches, the often similar magnitudes in the effects of shear and buoyancy meant that conditions of either WSS or CSI would be fulfilled. Fluctuations from case to case in the stratification allowed for the occasional presence of CI. By partitioning the TSSN occurrences into banding and nonbanding subsets, greater susceptibility to upright/slantwise convection in the case of the former was implied by the results from the stability diagnostics. In this context, however, the development of frontal convection from symmetric instability automatically assumes a non-evolving, inviscid state, under which the geostrophic shear was unidirectional. Besides the inclusion of ageostrophic influences in σ^2, the application of the M_g - θ_e relationship showed this approximation to be unrealistic, as around 70 % of the total convective snowstorms had distinct curvature in the flow regime. Given the nearly neutral static stability, more complex, localized slantwise updrafts would still be possible from the 3-D treatment described by Jones and Thorpe (1992) and Gray and Thorpe (2001).

5. How much do stability regimes in thundersnow events differ from those in non-thundersnow events? Are there statistically significant thresholds?

   The main conclusion reached here follows that of Market et al. (2006) and Smith (2006), in which the diagnostics imply an environment more unstable in occurrences of TSSN compared to an otherwise comparable collection of non-TSSN events. For example, calculations of σ^2 and 3-D EPV produced greater and reduced outcomes, respectively, for snowstorms

with evidence of lightning activity. The unfavorable results from the traditional stability indices in those wintertime systems without thunderstorms was also justified by the higher altitude MULPL, slightly lower (greater) MULI (MUCAPE), and decidedly smaller midlevel lapse rates. Also, the relevant criteria of $Ri_{sc} \leq 1$ marginally succeeded more frequently in TSSN events. The strong relationship between forcing and the response to that mechanism was particularly illustrated by various contributions (e.g., frontogenesis, static stability tendency) to σ^2 tendency. As a result, the multiscale inspection of dynamic and thermodynamic processes also revealed more amplified, robust features associated with convective, ageostrophic circulations. Overall, the collective action of all three essential factors for the onset of elevated thunderstorms was established conclusively to be accurate.

Considering that Smith (2006) already determined statistically significant discriminators for two limited datasets using the t-test routine, a more sound numerical analysis was conducted on the grid point domain. The nonparametric, Mann-Whitney rank-sum evaluation was capable of testing for discernible features in the model fields. Beyond the qualitative inspection, a few combinations of stability diagnostics were applied to reveal the *relatively*, more favorable features near the convective initiation site. Overall, the results from the Mann-Whitney test, however, were unexpected and would be sensitive to how the data samples were defined, something which the author found to not be clearly stipulated. Consequently, there were no strict physical guidelines pertaining to meteorology and different assumptions were open to be tested. Even though the "convective area of interest" was found to be more stable compared to a comparably sized domain in the non-TSSN episodes, it was speculated that a more beneficial assessment might be obtained if the mesoscale analysis of lightning activity

covered a smaller territory. Ultimately, pattern recognition appeared to be the means to accurately identify regions which might be deemed susceptible to constricted and enhanced updrafts.

6. Does the surrogate airstream analysis offer any significant, additional information on the distinguishing marks of snowstorms with lightning compared to those without?

   Inductive reasoning for airstreams showed some initial, promising evidence that TSSN events were indeed distinct. The abbreviated examination relied primarily on the position and movement of σ^2 features at different vertical levels in the atmosphere. The isolated, cellular spots of high growth rates obtained in the assortment of plots tended to give a less smooth quality product compared to Bennetts and Sharp (1982); however, some of the contradiction could be explained by the course resolution in the model (approximately 100-km) of the prior work compared to that of the RUC-2 architecture. Nonetheless, the contoured domain of more favorable results from this stability parameter were continuous enough, especially near and close to the convective initiation site, for tracking to be permitted. Even though the current work did not fully investigate the detailed, 3-D nature of the atmosphere in the way that trajectories would entail, the horizontal depictions from 700 hPa and the LHSGR (as well as the vertical cross-sections) provided a simplified means to fulfill this objective.

   Since CSI was generally the reason for positive values of σ^2, especially for those TSSN events where banding was present, the associated atmospheric conditions in these regions would implicitly indicate the appropriate juxtaposition and interaction between the cold conveyor belt (CCB), warm conveyor belt (WCB), and dry conveyor belt (DCB; e.g., see Carlson 1980; Elkins 1987; Martin 1998, 1999; Oravetz 2003; Moore et al. 2005b). Moore et al. (2005b) utilized trajectories to illustrate that the formation of heavy

snowbands resulted from the presence of these three airstreams (see their Fig. 2). For instance, the area of EPV reduction (and often related growth rate increase) found near the first report of winter convection in the late November/early December case study could be due to the superposition of the upper branch of the DCB over the warm, moist air of the WCB (Moore et al. 2005b). In addition, the relatively lower ascending CCB acts to maintain a temperature profile cold enough to support snowfall. Similar schematic representations of the atmosphere can also be obtained in Elkins (1987) or Oravetz (2003). This essential relationship in the Lagrangian framework, thus, can be approximately identified by the more organized, favorable zones of σ^2. These susceptible regions for thunderstorm development (and usually greater snowfall totals) were restricted spatially in all directions as the patterns evolved, thereby offering a means to monitor specific portions of the country for the possibility of significant winter precipitation.

In conclusion, some of the techniques employed by this work could be useful for routine implementation in an operational environment. Since episodes of convective snowfall often produce intense rates of precipitation over a concise time period and small spatial scale, which can often result in hazardous traveling conditions, more precise and accurate means of anticipating significant wintertime weather events are always needed by forecasters. Similar to what was recommended by Bennetts and Sharp (1982), σ^2 and its terms could be computed easily using simple scripts with output generated from fine resolution models. Further, by combining the growth rates with other measures of stability (such as EPV), the areal extent and temporal duration of potential elevated convection could be narrowed down. Of course, this does not detract from the usual cold-season weather process of checking for sufficient causes for ascent, adequate

moisture content, and the necessary near to subfreezing temperature profiles. After completion, the relatively new product would hopefully provide another tool to help forecasters in predicting the likelihood of banded precipitation and determining the type of instability present. Finally, other complementary procedures considered in the present work, such as Ri_{sc}, could then be implemented to fine tune and increase confidence in any potential outlook region issued.

7.3 Future research

Many aspects in this dissertation, some discussed briefly, could be expanded in future projects either partially by the author or possibly other graduate students. Some of these topics include:

1. Verifying the results obtained from the RUC-2 solution by utilizing a different modeling framework that exhibits a finer resolution, such as the Weather Research and Forecast (WRF) model (Skamarock et al. 2005).

2. Developing more fully the case study examples introduced in Chapter 6. For example, additional time periods might be incorporated along with more measures of stability dealt with in the point value and composite statistics. In addition, explicit trajectory calculations would serve as a true, rigorous evaluation of the type and magnitude of airstream interactions evident in TSSN versus non-TSSN episodes.

3. Examining more completely the connection of snowfall totals against lightning activity by focusing on the entire time period of TSSN reports in several case studies. Perhaps, objective gridded analyses would be generated utilizing the Barnes scheme found within the GEMPAK software. These plots could then be overlaid with only those CG flashes from the NLDN that occurred in regions with sufficiently cold thermal profiles for frozen precipitation.

Appendix A

List of TSSN and non-TSSN events

Table A.1: Information on subset of convective snow case studies examined. Location of thundersnow onset is given along with surface weather station identifier when possible. Onset time indicates year, month, date, and closest hour (UTC) for which the first report occurred. As described in the text, the level with the highest significant growth rates [LHSGR(hPa)] is determined for each event at initiation as well as 3-hours prior.

Location of TSSN onset	Onset Time	LHSGR(hPa) (Onset,Prior)
Salina, Kansas (KSLN)	03/11/23 0400	(700,800)
Beatrice, Nebraska (KBIE)	03/12/09 1500	(600,700)
Tulsa, Oklahoma (KRVS)	03/12/10 0400	(600,800)
Marion, Illinois (KMWA)	04/01/27 0400	(750,None)
Mountain Home, Arkansas (KBPK)	04/02/05 0300	(550,600)
Near Eau Claire, Wisconsin (44.6N;90.9W)	04/03/05 0700	(550,650)
Hutchinson, Minnesota (KHCD)	04/03/13 1300	(700,550)
Amarillo, Texas (KAMA)	04/11/02 0900	(550,600)
Kansas City, Missouri (KMKC)	04/11/24 0700	(650,700)
Cape Girardeau, Missouri (KCGI)	04/12/22 0900	(600,550)
Owensboro/Davies, Kentucky (KOWB)	04/12/23 0200	(800,800)
Near Watertown, South Dakota (45.1N; 96.9W)	05/01/01 1600	(700,600)
Near Terre Haute, Indiana (39.88N; 87.26W)	05/01/08 0600	(550,550)
Lincoln, Illinois (KAAA)	05/01/22 0800	(650,750)
Benton Harbor, Michigan (KBEH)	05/02/20 1700	(600,800)
Near Albert Lea, Minnesota (43.5N; 92.45W)	05/03/18 1100	(550,550)
Goodland, Kansas (KGLD)	05/04/11 0400	(700,750)

Table A.2: Information on subset of non-thundering snow case studies examined. The time given is year, month, date, and hour of the midevent period. The location is distinguished by station identifier. Similar to Table A.1, the LHSGR(hPa) is determined for each event at the midpoint as well as 3-hours prior.

Non-TSSN Location	Midpoint Time	LHSGR(hPa) (Midpoint, Prior)
Green Bay, WI (KGRB)	02/04/02 1200	(700,600)
Springfield, MO (KSGF)	03/01/16 1200	(750,800)
Omaha/Eppley, NE (KOMA)	03/02/15 1200	(700,700)
Omaha/Eppley, NE (KOMA)	04/03/15 1200	(550,550)
Green Bay, WI (KGRB)	05/01/06 1200	(650,550)
Green Bay, WI (KGRB)	05/01/22 1200	(800,650)
Green Bay, WI (KGRB)	05/02/14 1200	(550,800)

Appendix B

Rawinsonde Balloon Flights for RUC-2 Verification

Table B.1: Locations of rawinsonde balloon flights, as well as the dates and times on which the data were collected. Times marked with an asterisk were not used in the statistical measures of the u and v wind components discussed in Tables 3.1 and 3.2.

LOCATION	**DATE**	**TIME(UTC)**
Mineral Point, WI	20 Feb 2005	0700
	20 Feb 2005	0800
	20 Feb 2005	0900
	20 Feb 2005	1000
	20 Feb 2005	1100
	20 Feb 2005	1200
	20 Feb 2005	1300
	20 Feb 2005	1400
Madison, IN	24 Feb 2005	0800
	24 Feb 2005	0900
	24 Feb 2005	1100
	24 Feb 2005	1200
	24 Feb 2005	1300
Dumas, TX	15 Mar 2005	1000
	15 Mar 2005	1100*
	15 Mar 2005	1200
	15 Mar 2005	1300
	15 Mar 2005	1400
	15 Mar 2005	1500
	15 Mar 2005	1600
	15 Mar 2005	1700*
	15 Mar 2005	1800
St. James, MN	18 Mar 2005	0800
	18 Mar 2005	0900
	18 Mar 2005	1000*
	18 Mar 2005	1500
	18 Mar 2005	1900

Appendix C

Acronyms

This list in not meant to be complete, but rather only emphasizes the acronyms that occurred the most often and/or the author felt were most important:

1. B — Banded
2. CAPE — Convective Available Potential Energy
3. CCB — Cold Conveyor Belt
4. CG — Cloud-to-Ground
5. CI — Conditional Instability
6. CSI — Conditional Symmetric Instability
7. DCB — Dry Conveyor Belt
8. DTJ — Dry Tongue Jet
9. EPV — Equivalent Potential Vorticity
10. ETC — Extratropical Cyclone
11. GEMPAK — GEneral Meteorological PAcKage

12. GOES — Geostationary Observational Environmental Satellite
13. LHSGR — Level of Highest Significant Growth Rate
14. LMV — Level of Minimum Value
15. LTG DSNT — Distant Lightning
16. MAV — Mean Absolute Value
17. MULI — Most Unstable Lifted Index
18. MULPL — Most Unstable Level for Lifting a Parcel
19. MV — Minimum Value
20. NAM — North American Mesoscale (NCEP model)
21. NCEP — National Centers for Environmental Prediction
22. NCM — Norwegian Cyclone Model
23. NLDN — National Lightning Detection Network
24. NSHARP — Skew-T Hodograph Analysis and Research Program
25. PI — Potential Instability
26. PSI — Potential Symmetric Instability
27. QG — Quasi-Geostrophic
28. RUC — Rapid Update Cycle (NCEP model)
29. RH — Relative Humidity
30. VCTSSN — Thundersnow in the Vicinity

31. WATADS — WSR-88D Algorithm Testing and Display System

32. WB — Weakly Banded

33. WCB – Warm Conveyor Belt

34. WDSS-II — Warning Decision Support System - Integrated Information

References

American Meteorological Society, 2000: *Glossary of Meteorology.* 2^{nd} ed. Amer. Meteor. Soc., 855 pp.

Barnes, S.L., F. Caracena, and A. Marroquin, 1996: Extracting synoptic-scale diagnostic information from mesoscale models: The Eta model, gravity waves, and quasigeostrophic diagnostics. *Bull. Amer. Meteor. Soc.*, **77**, 519-528.

Benjamin, S.G., J.M Brown, K.J. Brundage, B.E. Schwartz, T.G. Smirnova, T.L. Smith, and L.L. Morone, 1998: RUC-2 - The Rapid Update Cycle Version 2. NWS Technical Procedures Bulletin No. 448. NOAA/NWS, 18 pp. [Available online at: `http://maps.fsl.noaa.gov/ruc2.tpb.html`.]

———, G.A. Grell, J.M. Brown, T.G. Smirnova, and R. Bleck, 2004a: Mesoscale weather prediction with the RUC hybrid isentropic-terrain-following coordinate model. *Mon. Wea. Rev.*, **132**, 473-494.

———, D. Dévényi, S.S. Weygandt, K.J. Brundage, J.M. Brown, G.A. Grell, D. Kim, B.E. Schwartz, T.G. Smirnova, T.L. Smith, and G.S. Manikin, 2004b: An hourly assimilation-forecast cycle: The RUC. *Mon. Wea. Rev.*, **132**, 495-518.

Becker, A.E., C.J. Melick, B.P. Pettegrew, R. Holle, N.W.S. Demetriades, and P. Market, 2007: Lightning and radar reflectivity signatures in banded snow events. *National Weather Association* 32^{nd} *Annual Meeting*, Reno, NV, 15 October 2007.

Bennetts, D.A., and B.J. Hoskins, 1979: Conditional symmetric instability - a possible explanation for frontal rainbands. *Quart. J. Roy. Meteor. Soc.*, **105**, 945-962.

———, and J.C. Sharp, 1982: The relevance of conditional symmetric instability to the prediction of mesoscale frontal rainbands. *Quart. J. Roy. Meteor. Soc.*, **108**, 595-602.

Bjerknes, J., and H. Solberg, 1922: Life cycle of cyclones and the polar front theory of atmospheric circulation. *Geophys. Publ.*, **3**, 3-18.

Black, T.L., 1994: The new NMC mesoscale Eta model: Description and forecast examples. *Wea. Forecasting*, **9**, 265-278.

Bluestein, H., 1986: Fronts and jet streaks: A theoretical perspective. *Mesoscale Meteorology and Forecasting*, P.S. Ray, Ed., Amer. Meteor. Soc., 173-215.

Branick, M.L., 1997: A climatology of significant winter-type weather events in the contiguous United States, 1982-94. *Wea. Forecasting*, **12**, 193-207.

Bright, D.R., M.S. Wandishin, R.E. Jewell, and S.J. Weiss, 2005: A physically based parameter for lightning prediction and its calibration in ensemble forecasts. Preprints, *Conf. on Meteorological Applications of Lightning Data*, San Diego, CA, Amer. Meteor. Soc., CD-ROM, 4.3.

Brook, M., M. Nakano, P. Krehbiel, T. Takeuti, 1982: The electrical structure of the Hokuriku winter thunderstorms. *J. Geophys. Res.*, **87**, 1207-1215.

Brown, R.A., 1993: A compositing approach for preserving significant features in atmospheric profiles. *Mon. Wea. Rev.*, **121**, 874-880.

Browne, R.F., and R.J. Younkin, 1970: Some relationships between 850-millibar lows and heavy snow occurrences over the central and eastern United States. *Mon. Wea. Rev.*, **98**, 399-401.

Browning, K.A., 1990: Organization of clouds and precipitation in extratropical cyclones. *Extratropical Cyclones, The Erik Palmén Memorial Volume*, C.W. Newton and E.O. Holopainen, Eds., Amer. Meteor. Soc., 129-153.

Burk, S.D., and W.T. Thompson, 1989: A vertically nested regional numerical prediction model with second-order closure physics. *Mon. Wea. Rev.*, **117**, 2305-2324.

Byrd, G.P., 1989: A composite analysis of winter season overrunning precipitation bands over the Southern Plains of the United States. *J. Atmos. Sci.*, **46**, 1119-1132.

Carlson, T.N., 1980: Airflow through midlatitude cyclones and the comma cloud pattern. *Mon. Wea. Rev.*, **108**, 1498-1509.

———, 1998: *Mid-Latitude Weather Systems*. Amer. Meteor. Soc., 507 pp.

Changnon, S.A., D. Changnon, and T.R. Karl, 2006: Temporal and spatial characteristics of snowstorms in the contiguous United States. *J. Appl. Meteor. Climatol.*, **45**, 1141-1155.

Clark, J.H.E., R.P. James, and R.H. Grumm, 2002: A reexamination of the mechanisms responsible for banded precipitation. *Mon. Wea. Rev.*, **130**, 3074-3086.

Colman, B.R., 1990a: Thunderstorms above frontal surfaces in environments without positive CAPE. Part I: A climatology. *Mon. Wea. Rev.*, **118**, 1103-1121.

_____, 1990b: Thunderstorms above frontal surfaces in environments without positive CAPE. Part II: Organization and instability mechanisms. *Mon. Wea. Rev.*, **118**, 1123-1144.

Court, A., and J.F. Griffiths, 1986: Thunderstorm climatology. *Thunderstorms: Vol. 2: Thunderstorm Morphology and Dynamics*. Second ed. revised and enlarged, E. Kessler, Ed., University of Oklahoma Press, 9-39.

Crowe, C., P. S. Market, B. Pettegrew, C. Melick, and J. Podzimek, 2006: An investigation of thundersnow and deep snow accumulations. *Geophys. Res. Lett.*, **33**, L24812, doi:10.1029/2006GL028214.

Curran, J.T., and A.D. Pearson, 1971: Proximity soundings for thunderstorms with snow. Preprints, 7^{th} *Conf. on Severe Local Storms*, Kansas City, MO, Amer. Meteor. Soc., 118-119.

Davis, J.C., 2002: *Statistics and data analysis in geology, 3rd edition.* John Wiley and Sons, Inc., 638 pp.

desJardins, M.L., K.F. Brill, and S.S. Schotz, 1991: Use of GEMPAK on Unix workstations, *Proc.* 7^{th} *International Conf. on Interactive Information and Processing Systems for Meteorology, Oceanography, and Hydrology*, New Orleans, LA, Amer. Meteor. Soc., 449-453.

Doswell, C.A., III, 1987: The distinction between large-scale and mesoscale contribution to severe convection: A case study example. *Wea. Forecasting*, **2**, 3-16.

Dudhia, J., 1989: Numerical study of convection observed during the winter monsoon experiment using a mesoscale two-dimensional model. J. Atmos. Sci., **46**, 3077-3107.

Elkins, H.A., 1987: Thunderstorms with snow: a comprehensive, empirical study of their occurrence, development and structure. M.S. Thesis, Department of Earth and Atmospheric Sciences, Saint Louis University, 79 pp.

Emanuel, K.A., 1983a: On assessing local conditional symmetric instability from atmospheric soundings. *Mon. Wea. Rev.*, **111**, 2016-2033.

_____, 1983b: The Lagrangian parcel dynamics of moist symmetric stability. *J. Atmos. Sci.*, **40**, 2368-2376.

_____, 1985: Frontal circulations in the presence of small moist symmetric stability. *J. Atmos. Sci.*, **42**, 1062-1071.

———, 1986: Overview and definition of mesoscale meteorology. *Mesoscale Meteorology and Forecasting*, P.S. Ray, Ed., Amer. Meteor. Soc., 1-17.

Goree, P.A., and R.J. Younkin, 1966: Synoptic climatology of heavy snowfall over the central and eastern United States. *Mon. Wea. Rev.*, **94**, 663-668.

Gray, S.L., and A.J. Thorpe, 2001: Parcel theory in three dimensions and the calculation of SCAPE. *Mon. Wea. Rev.*, **129**, 1656-1672.

Grell, G.A., 1993: Prognostic evaluation of assumptions used by cumulus parameterizations. *Mon. Wea. Rev.*, **121**, 764-787.

———, J. Dudhia, and D.R. Stauffer, 1994: A description of the fifth-generation Penn State/NCAR Mesoscale Model (MM5). NCAR Technical Note, NCAR/TN-398 + STR, 138 pp.

Halcomb, C.E., 2001: Case studies of midwestern thundersnow events. M.S. Thesis, Department of Soil and Atmospheric Sciences, University of Missouri-Columbia, 101 pp. [Available online at: `http://weather.missouri.edu/ROCS/pub/Halcomb-thesis.pdf`]

———, and P.S. Market, 2003: Forcing, instability, and equivalent potential vorticity in a midwest USA convective snowstorm. *Meteorol. Appl.*, **10**, 273-280.

Hane, C.E., 1986: Extratropical squall lines and rainbands. *Mesoscale Meteorology and Forecasting*, P.S. Ray, Ed., Amer. Meteor. Soc., 359-389.

Hart, J.A., and W. Korotky, 1991: The SHARP workstation v1.50 users guide. National Weather Service, 30 pp. [Available from NWS Eastern Region Headquarters, 630 Johnson Ave., Bohemia, NY 11716.]

Heppner, P.O.G., 1992: Snow versus rain: Looking beyond the "magic" numbers. *Wea. Forecasting*, **7**, 683-691.

Holle, R.L., J.V. Cortinas, and C.C. Robbins, 1998: Winter thunderstorms in the United States. Preprints, 16^{th} *Conf. on Weather Analysis and Forecasting*, Phoenix, AZ, Amer. Meteor. Soc., 118-119.

Holton, J.R., 2004: *An Introduction to Dynamic Meteorology.* 4^{th} ed. Elsevier Academic Press, 529 pp.

Hoskins, B.J., and F.P. Bretherton, 1972: Atmospheric frontogenesis models: Mathematical formulation and solution. *J. Atmos. Sci.*, **29**, 11-37.

———, I. Draghici, and H.C. Davies, 1978: A new look at the ω-equation. *Quart. J. Roy. Meteor. Soc.*, **104**, 31-38.

Houze, R.A., Jr., P.V. Hobbs, K.R. Biswas, and W.M. Davis, 1976: Mesoscale rainbands in extratropical cyclones. *Mon. Wea. Rev.*, **104**, 868-878.

Hunter, S.M., S.J. Underwood, R.L. Holle, and T.L. Mote, 2001: Winter lightning and heavy frozen precipitation in the southeast United States. *Wea. Forecasting*, **16**, 478-490.

Jascourt, S.D., S.S. Lindstrom, C.J. Seman, and D.D. Houghton, 1988: An observation of banded convective development in the presence of weak symmetric stability. *Mon. Wea. Rev.*, **116**, 175-191.

Johns, R.J., and C.A. Doswell III, 1992: Severe local storms forecasting. *Wea. Forecasting.*, **7**, 588-612.

Jones, S.C., and A.J. Thorpe, 1992: The three-dimensional nature of 'symmetric' instability. *Quart. J. Roy. Meteor. Soc.*, **118**, 227-258.

Jurewicz, M.L., and M.S. Evans, 2004: A comparison of two banded, heavy snowstorms with very different synoptic settings. *Wea. Forecasting.*, **19**, 1011-1028.

Lakshmanan, V., T. Smith, G. Stumpf, and K. Hondl, 2007: The Warning Decision Support System - Integrated Information. *Wea. Forecasting*, **22**, 596-612.

Lilly, D.K., 1986: Instabilities. *Mesoscale Meteorology and Forecasting*, P.S. Ray, Ed., Amer. Meteor. Soc., 259-271.

MacGorman, D.R., and W.D. Rust, 1998: *The Electrical Nature of Storms*. Oxford University Press, 422 pp.

Market, P.S., C.E. Halcomb, and R.L. Ebert, 2002: A climatology of thundersnow events over the contiguous United States. *Wea. Forecasting*, **17**, 1290-1295.

_____, A.M. Oravetz, D. Gaede, E. Bookbinder, R. Ebert, and C. Melick, 2004: Upper air constant pressure composites of midwestern thundersnow events. Preprints, 20^{th} *Conf. on Weather Analysis and Forecasting*, Seattle, WA, Amer. Meteor. Soc., CD-ROM, P4.6.

_____, _____, _____, _____, A.R. Lupo, C.J. Melick, L.L. Smith, R. Thomas, R. Redburn, B.P. Pettegrew, and A.E. Becker, 2006: Proximity soundings of thundersnow in the central United States. *J. Geophys. Res.*, **111**, D19208, doi:10.1029/2006JD007061.

Martin, J.E., 1998: The structure and evolution of a continental winter cyclone. Part II: Frontal forcing of an extreme snow event. *Mon. Wea. Rev.*, **126**, 329-348.

_____, 1999: Quasigeostrophic forcing of ascent in the occluded sector of cyclones and the trowal airstream. *Mon. Wea. Rev.*, **127**, 70-88.

McCann, D.W., 1995: Three-dimensional computations of equivalent potential vorticity. *Wea. Forecasting*, **10**, 798-802.

Melick, C.J., 2003: A comparison of vertical motions obtained from different forms of the omega equation. M.S. Thesis, Department of Earth and Atmospheric Sciences, Purdue University, 47 pp.

_____, L.L. Smith, B.P. Pettegrew, A.E. Becker, P.S. Market, and A.R. Lupo, 2008: Investigation of stability characteristics of cold-season convective precipitation events by utilizing the growth rate parameter. *J. Geophys. Res.*, **113**, D08108, doi:10.1029/2007JD009063.

McNulty, R.P., 1995: Severe and convective weather: A Central Region fore casting challenge. *Wea. Forecasting*, **10**, 187-202.

Mellor, G.L., and T. Yamada, 1982: Development of a turbulence closure model for geophysical fluid problems. *Rev. Geophys. Space. Phys.*, **20**, 851-875.

Michimoto, K., 1991: A study of radar echoes and their relationship to lightning discharge of thunderclouds in the Hokuriku District. Part I: Observation and analysis of thunderclouds in summer and winter. *J. Meteor. Soc. Japan*, **69**, 327-335.

_____, 1993: A study of radar echoes and their relationship to lightning discharge of thunderclouds in the Hokuriku District. Part II: Observation and analysis of "single-flash" thunderclouds in midwinter. *J. Meteor. Soc. Japan*, **71**, 195-204.

Moore, J. T., and P. D. Blakely, 1988: The role of frontogenetical forcing and conditional symmetric instability in the Midwest snowstorm of 30-31 January 1982. *Mon. Wea. Rev.*, **116**, 2155-2171.

_____, and T.E. Lambert, 1993: The use of equivalent potential vorticity to diagnose regions of conditional symmetric instability. *Wea. Forecasting*, **8**, 301-308.

_____, F.H. Glass, C.E. Graves, S.M. Rochette, and M.J. Singer, 2003: The environment of warm-season elevated thunderstorms associated with heavy rainfall over the central United States. *Wea. Forecasting*, **18**, 861-878.

_____, C.E. Graves, S. Ng, and J.L. Smith, 2005a: A process-oriented methodology towards understanding the organization of an extensive mesoscale snow band: A diagnostic case study of 4-5 December 1999. *Wea. Forecasting*, **20**, 35-50.

_____, S. Ng, and C.E. Graves, 2005b: The role of conveyor belts in organizing processes associated with heavy banded snowfall. Preprints, 21^{st} *Conf. on Weather Analysis and Forecasting*, Washington D.C., Amer. Meteor. Soc., CD-ROM, 10A.1.

Mote, T.L., D.W. Gamble, S.J. Underwood, and M.L. Bentley, 1997: Synoptic-scale features common to heavy snowstorms in the southeast United States. *Wea. Forecasting*, **12**, 5-23.

Mudrick, S.E., 1974: A numerical study of frontogenesis. *J. Atmos. Sci.*, **31**, 869-892.

Nicosia, D.J., and R.H. Grumm, 1999: Mesoscale band formation in three major northeastern United States snowstorms. *Wea. Forecasting*, **14**, 346-368.

NOAA, cited 2008: Systems and equipment. Rawinsonde and Pibal Observations, Federal Meteorological Handbook No. 3. [Available online at: `http://www.ofcm.gov/fmh3/text/chapter2.htm`.]

Novak, D.R., L.F. Bosart, D. Keyser, and J.S. Waldstreicher, 2004: An observational study of cold season-banded precipitation in Northeast U.S. cyclones. *Wea. Forecasting*, **19**, 993-1010.

Oravetz, A.M., 2003: Composite analysis of thundersnow events in the central United States. M. S. Thesis, Department of Soil and Atmospheric Sciences, University of Missouri-Columbia, 141 pp. [Available online at: `http://weather.missouri.edu/ROCS/pub/Oravetz-thesis.pdf`.]

Orville, R.E. and G.R. Huffines, 2001: Cloud-to-ground lightning in the United States: NLDN results in the first decade, 1989-98. *Mon. Wea. Rev.*, **129**, 1179-1193.

Parsons, D.B., and P.V. Hobbs, 1983: The mesoscale and microscale structure and organization of clouds and precipitation in midlatitude cyclones. XI: Comparisons between observational and theoretical aspects of rainbands. *J. Atmos. Sci.*, **40**, 2377-2397.

Pettegrew, B.P., P.S. Market, R.L. Holle, and N.W.S. Demetriades, 2007: Analysis of cloud and cloud-to-ground lightning with winter precipitation. Preprints, 22^{nd} *Conf. on Weather Analysis and Forecasting*, Park City, UT, Amer. Meteor. Soc., CD-ROM, P1.18.

Petterssen, S., 1956: *Weather Analysis and Forecasting. Vol. I, Motion and Motion Systems*, 2nd ed., McGraw-Hill, 428 pp.

Reisner, J., R.M. Rasmussen, and R.T. Bruintjes, 1998: Explicit forecasting of supercooled liquid water in winter storms using the MM5 mesoscale model. *Quart. J. Roy. Meteor. Soc.*, **142**, 1071-1107.

Sanders, F., and L.F. Bosart, 1985: Mesoscale structure in the Megalopolitan snowstorm of 11-12 February 1983. Part I: Frontogenetical forcing and symmetric instability. *J. Atmos. Sci.*, **42**, 1050-1061.

Schultz, D.M., 1999: Lake-effect snowstorms in northern Utah and western New York with and without lightning. *Wea. Forecasting*, **14**, 1023-1031.

_____, and C.F. Mass, 1993: The occlusion process in a midlatitude cyclone over land. *Mon. Wea. Rev.*, **121**, 918-940

_____, and P.N. Schumacher, 1999: The use and misuse of conditional symmetric instability. *Mon. Wea. Rev.* **127**, 2709-2732.

_____, D. Keyser, and L.F. Bosart, 1998: The effect of large-scale flow on low-level frontal structure and evolution in midlatitude cyclones. *Mon. Wea. Rev.*, **126**, 1767-1791.

_____, P.N. Schumacher, and C.A. Doswell III, 2000: The intricacies of instability. *Mon. Wea. Rev.*, **128**, 4143-4148.

Schumacher, R.S., and D.M. Schultz, 2001: Inertial instability: Climatology and possible relationship to severe weather predictability. Preprints, 9^{th} *Conf. on Mesoscale Processes*. Ft. Lauderdale, FL, Amer. Meteor. Soc., 372-375.

Seltzer, M.A., R.E. Passarelli, and K.A. Emanuel, 1985: The possible role of symmetric instability in the formation of precipitation bands. *J. Atmos. Sci.*, **42**, 2207-2219.

Shapiro, M.A., and S. Grønås, Eds., 1999: *The Life Cycles of Extratropical Cyclones.* Amer. Meteor. Soc., 359pp.

Skamarock, W.C., J.B. Klemp, J. Dudhia, D.O. Gill, D.M. Barker, W. Wang, and J.G. Powers, 2005: A description of the Advanced Research WRF, Version 2. NCAR Tech. Note., NCAR/TN-468+STR, 88 pp. [Available from UCAR Communications, P.O. Box 3000, Boulder, CO 80307 and online at: `http://www.mmm.ucar.edu/wrf/users/docs/arw_v2.pdf`.]

Smith, L.L., 2006: Investigating stability evolution of snow storms featuring lightning. M. S. Thesis, Department of Soil, Environmental, and Atmospheric Sciences, University of Missouri-Columbia, 136 pp. [Available online at: `http://weather.missouri.edu/ROCS/pub/Smith-thesis.pdf`.]

_____, C.J. Melick, and P.S. Market, 2005a: Examination of thundersnow cases in the United States utilizing NLDN data. Preprints, *Conf. on Meteorological Applications of Lightning Data*, San Diego, CA, Amer. Meteor. Soc., CD-ROM, P2.13.

_____, B.P. Pettegrew, C.J. Melick, and P.S. Market, 2005b: Investigating stability evolution of two winter storms using mobile GAUS data. Preprints, it 21^{st} Conf. on Weather Analysis and Forecasting, Washington D.C., Amer. Meteor. Soc., CD-ROM, 9.1.

Snook, J.S., 1992: Current techniques for real-time evaluation of conditional symmetric instability. *Wea. Forecasting*, **7**, 430-439.

Takahashi, T., 1978: Riming electrification as a charge generation mechanism in thunderstorms. *J. Atmos. Sci.*, **35**, 1536-1548.

Thorpe, A.J., and K.A. Emanuel, 1985: Frontogenesis in the presence of small stability to slantwise convection. *J. Atmos. Sci.*, **42**, 1809-1824.

Tsou, C.-H., P.J. Smith, and P.M. Pauley, 1987: A comparison of adiabatic and diabatic forcing in an intense extratropical cyclone system. *Mon. Wea. Rev.*, **115**, 763-786.

Van Den Broeke, M.S., D.M. Schultz, R.H. Johns, J.S. Evans, and J.E. Hales, 2005: Cloud-to-ground lightning production in strongly forced, low-instability convective lines associated with damaging wind. *Wea. Forecasting*, **20**, 517-530.

Wallace, J.M., and P.V. Hobbs, 1977: *Atmospheric Science: An Introductory Survey.* Academic Press, 467 pp.

Walters, M.K., 2001: A simple example of Galilean invariance in the omega equation. *Bull. Amer. Meteor. Soc.*, **82**, 463-472.

WATADS (WSR-88D Algorithm Testing and Display System) 2000: Reference guide for Version 10.2. [Available from Storm Scale Applications Division, National Severe Storms Laboratory, 1313 Halley Circle, Norman, OK 73069.]

Wetzel, S.W., and J.E. Martin, 2001: An operational ingredients-based methodology for forecasting midlatitude winter season precipitation. *Wea. Forecasting*, **16**, 156-167.

Wiesmueller, J.L., and S.M. Zubrick, 1998: Evaluation and application of conditional symmetric instability, equivalent potential vorticity, and frontogenetical forcing in an operational forecasting environment. *Wea. Forecasting*, **13**, 84-101.

Wilks, D.S., 1995: *Statistical methods in the atmospheric sciences.* Academic Press, 467 pp.

Wolfsberg, D.G., K.A. Emanuel, and R.E. Passarelli, 1986: Band formation in a New England Winter Storm. *Mon. Wea. Rev.*, **114**, 1552-1569.

Zipser, E.J., and K.R. Lutz, 1994: The vertical profile of radar reflectivity of convective cells: A strong indicator of storm intensity and lightning probability? *Mon. Wea. Rev.*, **122**, 1751-1759.

VITA

Christopher James Melick was born on May 1^{st}, 1975 in Indianapolis, IN to James and Linda Melick. He experienced a rather normal and actually blessed childhood growing up with his younger brother, Travis, whom courageously battled a rare from of cancer off an on for more than a decade. Unfortunately, Travis lost his battle in April 1990 at the young age of 13. Within two years of his death, Chris's parents split and eventually divorced; both still reside in the northern suburbs of Indianapolis. During this time, Chris would graduate from North Central High School in 1993.

The pursuit of Atmospheric Science as a major almost never began for Chris. At an early age, weather was seen mainly as just a general curiosity in the natural environment. Going into college, Chris had many ideas of what to study but no true passion or direction. After a conversation with his grandmother and some deep thought, Chris had a revelation that his true love would be to become a meteorologist. This career went into full gear once the author transferred to Purdue University in 1996, graduating with a Bachelor of Science in 2000, and eventually returned to obtain his Masters in 2003 under the direction of Dr. Phillip J. Smith. For the latter, the written thesis dealt with the topic of synoptic-scale dynamics, with the research focusing on comparing vertical motion estimates from various forms of the omega equation.

For more than four years afterward, Chris continued his doctoral study at the University of Missouri-Columbia in order to inspect aspects of thundersnow across the Central United States with the support of a National Science Foundation grant. Dr. Patrick S. Market served as adviser and principal investigator for the research project, with the results from these investigations presented at various regional, national, and international conferences. In addition, a few peer-reviewed journal articles were eventually published. Along these lines, the title for the author's dissertation centered on the synoptic and mesoscale organization of mid-latitude, continental convective snow events. After obtaining several scholastic honors over the years, Chris finally moved on to his first career job at Baron Services as a research meteorologist in Spring 2008, shortly before graduating with his PhD that May.